2007

Two-dimensional Guided Mode Resonant Structures For Spectral Filtering Applications

Sakoolkan Boonruang
University of Central Florida

TWO-DIMENSIONAL GUIDED MODE RESONANT STRUCTURES FOR SPECTRAL FILTERING APPLICATIONS

by

SAKOOLKAN BOONRUANG
B.S. King Mongkut's Institute of Technology Ladkrabang, 2000
M.S. University of Central Florida, 2004

A dissertation submitted in partial fulfillment of the requirements
for the degree of Doctoral of Optics
in the College of Optics and Photonics/CREOL
at the University of Central Florida
Orlando, Florida

Fall Term
2007

Major Professor: M.G.Moharam

ABSTRACT

Guided mode resonant (GMR) structures are optical devices that consist of a planar waveguide with a periodic structure either imbedded in or on the surface of the structure. The resonance anomaly in GMR structures has many applications as dielectric mirrors, tunable devices, sensors, and narrow spectral band reflection filters. A desirable response from a resonant grating filter normally includes a nearly 100% narrowband resonant spectral reflection (transmission), and a broad angular acceptance at either normal incidence or an oblique angle of incidence.

This dissertation is a detailed study of the unique nature of the resonance anomaly in GMR structures with two-dimensional (2-D) periodic perturbation. Clear understanding of the resonance phenomenon is developed and novel 2-D GMR structures are proposed to significantly improve the performance of narrow spectral filters. In 2-D grating diffraction, each diffracted order inherently propagates in its distinct diffraction plane. This allows for coupled polarization dependent resonant leaky modes with one in each diffraction plane. The nature of the interaction between these non-collinear guides and its impact on spectral and angular response of GMR devices is investigated and quantified for 2-D structures with rectangular and hexagonal grids. Based on the developed understanding of the underlying phenomenon, novel GMR devices are proposed and analyzed.

A novel controllable multi-line guided mode resonant (GMR) filter is proposed. The separation of spectral wavelength resonances supported by a two-dimensional GMR structure can be coarse or fine depending on the physical dimensions of the structure and not the material properties. Multiple resonances are produced by weakly guided modes individually propagating along multiple planes of diffraction. Controllable two-line and three-line narrow-band reflection

filter designs with spectral separation from a few up to hundreds of nanometers are exhibited using rectangular-lattice and hexagonal-lattice grating GMR structures, respectively.

Broadening of the angular response of narrow band two-dimension guided mode resonant spectral filters, while maintaining a narrow spectral response, is investigated. The angular response is broadened by coupling the diffracted orders into multiple fundamental guided resonant modes. These guided modes have the same propagation constant but propagating in different planes inherent in multiple planes of diffraction of the 2-D gratings. The propagation constants of the guided resonant modes are determined from the physical dimensions of the grating (periodicity and duty cycle) and the incident direction. A five-fold improvement in the angular tolerance is achieved using a grating with strong second Bragg diffraction in order to produce a crossed diffraction. A novel dual grating structure with a second grating located on the substrate side is proposed to further broaden the angular tolerance of the spectral filter without degrading its spectral response. This strong second Bragg backward diffraction from the substrate grating causes two successive resonant bands to merge producing a resonance with symmetric broad angular response.

To my parents and family

ACKNOWLEDGMENTS

I would like first to thank my advisor, Dr. M. G. Moharam, for his continuous support and guidance during my period of study in CREOL. He had provided me with a great research environment and a continuous help and valuable advices that facilitate my progress towards finishing my thesis work. I also would like to acknowledge my colleagues Dr. Don Jacob, Dr. Andy Greenwell, and George Siganakis for the constructive discussions.

I want to thank my parents and family back in Thailand for their never-ending emotional support that eased the harshness of being away from them, especially at the beginning. Also, I want to thank my new family, Dr. Waleed Mohammed, who always believed in me and gave me lots of help in research and life, and my friends who made me feel home.

Finally, I would like to thank NECTEC who supported my fellowship and Dr. Sarun Sumriddetchkajorn for recommending me CREOL.

TABLE OF CONTENTS

LIST OF FIGURES xi

LIST OF TABLES xx

LIST OF ACRONYMS/ABBREVIATIONS xxi

CHAPTER 1 : INTRODUCTION 1

CHAPTER 2 : BACKGROUND 11

2.1 The diffraction theory of the gratings 11

2.1.1 One-dimensional (1-D) grating 13

2.1.2 Two-dimensional (2-D) grating 14

2.1.3 Three-dimensional rigorous coupled wave analysis (3-D RCWA) 16

2.1.3.a Three-dimensional coupled wave equations (3-D CWE) 18

2.1.3.b Boundary condition: transmission matrix approach (TMA) 22

2.1.3.c Permittivity/permeability expansions 25

2.1.3.d RCWA formulation for a finite beam 26

2.2 Dielectric slab waveguide 29

2.2.1 Multilayer slab waveguide mode solving method 31

2.2.2 Field distribution 36

2.3 Dielectric grating-waveguide structures 37

2.3.1 Scattering matrix approach 39

2.3.2 Bloch mode approach 41

CHAPTER 3 : RESONANT ANOMALY IN GUIDED MODE RESONANT (GMR) STRUCTURES 45

3.1 Principle of resonance anomaly in GMR....45
3.2 Resonances in 1-D GMR....51
3.3 Coupling into a single-diffracted order resonant mode in 1-D GMR....56
3.3.1 GMR with Lorentzian resonant response....58
3.3.2 De-phasing manners at off-resonant wavelength and off-resonant angle....62
3.4 Coupling into a two-diffracted order resonant mode in 1-D GMR at in-plane mounting...64
3.4.1 At normal incidence....64
3.4.2 At oblique incidence....68
3.5 Coupling into a two-diffracted order resonant mode in 1-D GMR at conical mounting....70
3.6 Summary....75
CHAPTER 4 : ANALYSIS OF TWO DIMENSIONAL-GUIDED MODE RESONANT (2-D GMR) STRUCTURES....78
4.1 Resonances in 2-D GMR....78
4.2 2-D GMR using rectangular-lattice grating....81
4.2.1 Coupling of resonant modes at normal incidence....81
4.2.2 Coupling of resonant modes at oblique incidence....87
4.3 2-D GMR using arbitrary crossed grating....92
4.4 2-D GMR using hexagonal-lattice grating....96
4.4.1 Coupling of resonant modes at normal incidence....97
4.4.2 Coupling of resonant modes at oblique incidence....105
4.5 Calculations of the leaky mode dispersion....110
4.6 Summary....116

CHAPTER 5 : MULTI-LINE GMR FILTERS 118
5.1 Overview 118
5.2 Multi-line 1-D GMR Filters 120
5.2.1 Design of controllable multi-line 1-D GMR filters 123
5.3 Multi-line 2-D GMR Filters 125
5.3.1 Design of controllable multi-line 2-D GMR filters 129
5.3.2 Results and discussion 131
5.3.2.a Controllable two-line 2-D GMR filters using a rectangular-lattice grating 132
5.3.2.b Controllable three-line 2-D GMR filters using a hexagonal-lattice grating 136
5.4 Fabrication tolerances of Multi-line 2-D GMR Filters 139
5.5 Summary 145
CHAPTER 6 : BROADENING THE ANGULAR TOLERANCES IN 2-D GMR AT OBLIQUE INCIDENCE 147
6.1 Overview 147
6.2 Coupling characteristics to enhance the angular tolerances of 2-D GMR 149
6.3 Multiple resonant modes with the same β in 2-D GMR at oblique incidence 151
6.3.1 Three resonant modes with the same β in a rectangular-lattice grating 152
6.3.2 Four resonant modes with the same β in a hexagonal-lattice grating 154
6.3.3 Results and discussions 156
6.4 Broadening the angular tolerances in a single- grating 2-D GMR 160
6.5 Broadening the angular tolerances in a dual- grating 2-D GMR 167
6.6 Summary 175

CHAPTER 7 : CONCLUSION 177

LIST OF REFERENCES 181

LIST OF FIGURES

Figure 2.1: Configuration of the grating and the diffraction directions.....12

Figure 2.2: Diffraction in 1-D grating at (a) in- plane (b) fully conical (c) conical mounting.....14

Figure 2.3: A general two-dimensional crossed diffraction grating and the diffraction pattern....15

Figure 2.4: Configurations of (a) a Gaussian beam at arbitrary incident (θ_0 and φ_0) and its polarization (b) Gaussian beam's parameters.....28

Figure 2.5: (a) configurations of three-layer slab waveguide (b)-(d) plots of the field amplitudes of the first three vertically guided modes, m=0,1, and 2 30

Figure 2.6: Configuration of multilayer slab waveguide 31

Figure 2.7: Field distribution of fundamental mode in a multilayer slab waveguide with (a) single (b) two-layer of high index 37

Figure 2.8: Configurations of (a) the corrugated slab waveguide (b) the grating waveguide 38

Figure 2.9: (a) an artificial periodicity used in Bloch mode approach (b) a unit-cell computation of the grating-waveguide structure. 42

Figure 3.1: Configurations of GMR devices (a) refractive index modulated waveguide (b) surface-relief grating coupler (c) coated dielectric grating.....46

Figure 3.2: The configurations of phase matching conditions in the GMR structure at resonance47

Figure 3.3: The configurations of (a) 1-D GMR, (b) 2-D GMR, (c) GMR structure considered as multilayer waveguide when applying the HWA 50

Figure 3.4: Diffraction/guidance planes and phase matching diagrams of the resonant modes in 1-D GMR at in-plane mounting (a) single-propagation (b)/(c) counter-propagation and (d) two resonant modes at conical mounting. 53

Figure 3.5: (a) Plot of resonances (calculated by the HWA) versus the film thickness (t_f), and the spectral responses (calculated by the RCWA) of resonances in1-D GMR (b) t_f=0.25 μm (c)/(d) t_f=0.594 μm 55

Figure 3.6: Scattering of the single-diffracted order resonant mode in 1-D GMR at oblique incidence 57

Figure 3.7: Plots of resonance response approximately calculated by Eq. (3.10) 58

Figure 3.8: Contour plots of R_0 and η_d versus grating depth and filling factor.....59

Figure 3.9: (a) plots of R_0 and η_d versus grating depth when f=0.85 (b) Spectral responses of 1-D GMR with the grating A (t_g=0.05 μm, t_f= 0.532 μm), B (t_g=0.13 μm, t_f= 0.528 μm) and C (t_g=0.19 μm, t_f= 0.527μm). 60

Figure 3.10: (a) Configurations of the multilevel AR grating (b) plots of R_0 and η_d versus the N-level (c) Spectral responses of 1-D GMR with the 1-, 4-, 7-, and 10-level AR grating61

Figure 3.11: Scattering fields of a single-diffracted order resonant mode in 1-D GMR (a) at-off resonant wavelength (b) at off-resonant angle (c)/(d) spectral and angular responses62

Figure 3.12: Scattering of the two-diffracted order resonant mode in 1-D GMR at normal incidence 65

Figure 3.13: Scattering fields of a two-diffracted order resonant mode in 1-D GMR (a) at-off resonant wavelength (b) at off-resonant angle (c)/(d) spectral and angular responses66

Figure 3.14: Contour plots of R_0, η_d, and η_B versus grating depth and filling factor.....67

Figure 3.15: (a) plots of R_0, η_d, and η_B versus grating depth for 0.4-filling factor (b) plots of angular/spectral linewidth ratio, $\frac{\Delta\theta_{FWHM}}{\Delta\lambda_{FWHM}/\lambda_0}$, versus the grating depth 68

Figure 3.16: Scattering of a two-diffracted order resonant mode in 1D-GMR at oblique incidence69

Figure 3.17: (a) Scattering fields of two-diffracted order resonant modes with different β in 1-D GMR at off-resonant angle (b) comparison of the angular responses of resonances .70

Figure 3.18: (a) Configurations of the guiding planes and related resonant modes in 1-D GMR at conical mounting (b) HWA calculations of resonances versus the shift of incident plane ($\theta_{inc} = 10^{\circ}, \varphi_{inc}$) in 1-D GMR (Figure 3.5) with t_f=0.5 μm.....71

Figure 3.19: (a) Spectral responses of 1-D GMR at conical mounting $\theta_{inc} = 10^{\circ}, \varphi_{inc} = 45^{\circ}$ (b) Deviation of reflectivities at resonances plotted versus incident polarization 72

Figure 3.20: Phase matching diagram and decomposition of TE and TM incident beam corresponding to TE and TM resonant mode for a fully conical mounting 73

Figure 3.21:(a) Spectral responses of 1-D GMR at conical mounting $\theta_{inc} = 10^{\circ}, \varphi_{inc} = 90^{\circ}$ (b) plots of the field magnitude ($|E|$) of the diffracted waves versus the θ_{inc} for the TE and TM polarized beam. 74

Figure 3.22: Spectral responses of 1-D GMR at conical mounting $\theta_{inc} = 50^{\circ}, \varphi_{inc} = 90^{\circ}$ versus the deviation of filling factor (FF) ($\Lambda_a = 0.61\ \mu m$.) 75

Figure 4.1: 2-D GMR structure configuration 79

Figure 4.2: First-order diffraction/guidance planes in 2-D GMR with (a) rectangular- (b) arbitrary- (c) hexagonal-lattice grating 80

Figure 4.3: Scattering of field inside the structure with a rectangular-lattice grating at resonance (a) forward diffraction (b) backward and crossed diffraction. 82

Figure 4.4: (a) Phase matching diagram of TE resonant mode (β_1) for an unpolarized incident beam (b) plots of normalized powers dissipated to the normal ($\eta_{d,\perp}$) and in-plane ($\eta_{d,//}$) field components by a square-lattice grating versus ψ_{inc} 84

Figure 4.5: RCWA calculations (a) spectral response for ψ_{inc}= 0°, 45°, 90°; (b) and (c) polarization rotation ($\Delta\psi_R = \psi_R - \psi_{inc}$) and phase ($\Delta\phi_R$) of the reflected beam at TM_0 resonance. 84

Figure 4.6: (a) Phase matching diagram of TE resonant mode (β_1) for an unpolarized incident beam, when $\Lambda_a > \Lambda_a$ (b) plots of resonances versus shift of period Λ_a, calculated by HWA. 85

Figure 4.7: Comparison between reflectivity (R) at $TE_{0,\beta l}$ resonance calculated by RCWA and $|\cos(\psi_{inc})|^2$ versus ψ_{inc} 86

Figure 4.8: Reflectivity spectrum of GMR with rectangular-lattice grating ($\Lambda_a > \Lambda_b$) 87

Figure 4.9: Phase matching diagram of the resonant modes in 2-D GMR with a square-grid grating at oblique incidence (a) $\varphi_{inc} = 0^\circ$; (b) $\varphi_{inc} = 45^\circ$ 88

Figure 4.10: Plots of resonances in of GMR with square-lattice grating ($\Lambda_a = \Lambda_b$) at $\varphi_{inc} = 45^\circ$ versus θ_{inc} , calculated by homogeneous waveguide approach. 89

Figure 4.11: Reflectivity spectrum of GMR with square-lattice grating ($\Lambda_a = \Lambda_b$) at $(\theta_{inc}, \varphi_{inc}) = (10^\circ, 45^\circ)$ 90

Figure 4.12: Closed-up plots of reflectivity spectrum in Figure 4.11 (a) $TM_{0,\beta 1}$ (b) $TE_{0,\beta 1}$ (c) $TM_{0,\beta 2}$ (d) $TE_{0,\beta 2}$ resonance 91

Figure 4.13: Comparison of deviation of grating coupling strengths ($\Delta\eta_d$) for TE and TM incident beam when coupling to the same mode (solid-line: TM mode, dash-line: TE mode) (a) $\varphi_{inc} = 0^\circ$; (b) $\varphi_{inc} = 45^\circ$ 92

Figure 4.14: (a) First-order diffraction/guidance planes by an arbitrary crossed grating; phase matching diagram (b) $\zeta < 30^\circ$ (c) $\zeta = 30^\circ$ and (d) $\zeta > 30^\circ$, when $\Lambda_a = \Lambda_b$ 93

Figure 4.15: Phase matching diagram of TE resonant mode in 2-D GMR with an arbitrary crossed grating ($\Lambda_a = \Lambda_b, \zeta \neq 30^\circ$) at normal incidence (a) $\psi_{inc} = 0^\circ$ (b) $\psi_{inc} = 90^\circ$ 94

Figure 4.16: Plots of (a) phase mismatches of wave (-1,0) (b) the deviation of the coupling strength, when applying the TE and TM polarized beam, versus the air-hole radius (r)of the crossed grating with $\zeta = 20^\circ$ in comparison to the square-lattice grating ($\zeta = 0^\circ$) 95

Figure 4.17: (a) Plot of the film thickness (t_f) for achieving the TE resonance at $\lambda_0 = 0.475\mu m$ versus the change of the air-hole radius (r) of the crossed grating with $\zeta = 20^\circ$ (b) spectral response when r=0.095 μm and t_f = ~0.108 μm.....96

Figure 4.18: Scattering of field inside the structure with a hexagonal-lattice grating at resonance (a) forward diffraction (b) backward and crossed diffraction. 98

Figure 4.19: Phase matching diagram of TE resonant modes (β_1) in 2-D GMR using a regular hexagonal-lattice grating for the unpolarized beam 99

Figure 4.20: Plots of (a) polarization direction and (b) normalized powers dissipated to first-order waves by the regular hexagonal-lattice grating at normal incidence versus ψ_{inc} 100

Figure 4.21: Spectral responses versus the polarization direction ψ_{inc} = 0° to 90° (a) TE_0 resonance: $t_f \sim 0.107\mu m$ (b) TM_0 resonance: $t_f \sim 0.155\mu m$ 101

Figure 4.22: Plot of (a) polarization rotation ($\Delta\psi_R = \psi_R - \psi_{inc}$) and (b) phase ($\Delta\phi_R = \phi_{E_{r,//}} - \phi_{E_{r,\perp}}$) of the reflected beam at λ_0 versus ψ_{inc} 102

Figure 4.23: (a) Phase matching diagram of TE resonant mode (β_1) for an unpolarized incident beam, when $\Lambda_a < \Lambda_a$ (b) plots of resonances versus shift of period Λ_a, calculated by HWA.....103

Figure 4.24: Spectral responses of the structure in Figure 4.19b having $\Lambda_a < \Lambda_a$, when incident polarization is ψ_{inc}=0º and 90º 104

Figure 4.25: (a) Symmetric planes of incidence; phase matching diagram of the resonant modes in 2D-GMR with a regular hexagonal-lattice grating at oblique incidence (b) $\varphi_{inc} = 0^\circ$; (c) $\varphi_{inc} = 90^\circ$ 105

Figure 4.26: Plots of resonances in of GMR with hexagonal-lattice grating ($\Lambda_a = \Lambda_b$) at (a) $\varphi_{inc} = 0^\circ$ (b) $\varphi_{inc} = 90^\circ$ versus θ_{inc}, calculated by HWA.....106

Figure 4.27: Reflectivity spectrum of GMR with hexagonal-lattice grating ($\Lambda_a = \Lambda_b$) at $(\theta_{inc}, \varphi_{inc}) = (10^\circ, 90^\circ)$ 107

Figure 4.28: Phase matching diagram of four resonant modes in 2-D GMR using an irregular lattice grating at oblique incidence $\varphi_{inc} = 90^\circ$ and coupling characteristics for (a) TE and (b) TM polarized beam 108

Figure 4.29: Plots of TE_0 resonant wavelengths as a contribution of waves (1,0)/(-1,0) and (0,1)/(-1,1) versus the incident angle θ_{inc} in 2-D GMR using an irregular hexagonal-lattice grating ($\Lambda_a = 0.25\mu m$ and $\Lambda_a = 0.27\mu m$) 109

Figure 4.30: Reflectivity spectrum of GMR in Figure 4.29 at (a) $\theta_{inc} = 10^\circ$ (b) $\theta_{inc} 10.45^\circ$ and (c) $\theta_{inc} = 11^\circ$ 110

Figure 4.31: Unit cells of 2D-GMR with a rectangular-lattice grating (rectangular-shape hole)112

Figure 4.32: Dispersion of leaky modes (a) normalized $\Re\{n_{eff}\}$ $\mathrm{Re}\{n_{eff}\}$ (b) normalized $\Im\{n_{eff}\}$ of TM_0 guided modes (c) normalized $\Im\{n_{eff}\}$ of TE_0 guided modes 113

Figure 4.33: Spectral response of the resonances at (a) normal incidence/(c) at $(\varphi_{inc}, \theta_{inc}) = (45^\circ, 9.14^\circ)$ and (b) band diagram of structure in Figure 4.32 115

Figure 4.34: (a) Spectral response and (b) matching plots of normalized modal index (TE_0/TM_0) and the normalized ±1 waves (calculated from Eq.(4.3)) at $(\theta_{inc}, \varphi_{inc}) = (10^\circ, 0^\circ)$, and TE-polarized beam.....115

Figure 5.1: The spectral response of the two-line 1-D GMR filter at normal incidence: grating (n_g=1.5, Λ_a=320 nm FF=0.6, t_g=105 nm), high index film (n_f =1.7, t_f=353 nm), an AR coating ($n_{AR} = \sqrt{n_f n_s}$, $t_{AR} = \lambda_1 / 4n_{AR}$), a substrate (n_s=1.47), and an air superstrate (n_c=1).....121

Figure 5.2: Resonance separation ($\Delta\lambda/\lambda_1$) calculations of TE_0 and TE_1 resonances in two-line 1D-GMR filters (Figure 5.1) versus period of the grating (Λ_a) and film thickness (t_f) (a) film index (n_f)=1.7 (b) film index (n_f)=2.5 124

Figure 5.3: Resonance separation ($\Delta\lambda/\lambda_1$ for both exact and approximated Eq. (5.5) for two-line 1D-GMR filters (in Figure 5.1) versus film refractive index (n_f) and film thickness (t_f).....125

Figure 5.4: Resonances separation ($\Delta\lambda/\lambda_1$) calculations of TE_0 and TM_0 resonances in 2-D GMR filters using a square-grid grating versus grating period and film thickness (t_f) (a) film index (n_f)=1.7 (b) film index (n_f)=2.5 128

Figure 5.5: Spectral response of the two-line 2-D GMR filters with a rectangular-lattice structure. (a) Λ_b/Λ_a= 0.89; (b) Λ_b/Λ_a = 0.96; (c) Λ_b/Λ_a = 1.03; (d) Λ_b/Λ_a = 1.1 133

Figure 5.6: (a) Shift in the location of the second resonance (b) resonance locations in two-line 2-D GMR filters with a rectangular-lattice structure versus the ratio of grating periods ($\Lambda_a = 281\,nm$).....134

Figure 5.7: Resonance locations in two-line 2-D GMR filters with a rectangular-lattice structure versus the ratio of grating periods ($\Lambda_a = 220\,nm$) 136

Figure 5.8: (a) The change of the grating periods Λ_b versus Λ_a to fix two resonances (λ_1 and λ_2), while shift the other (λ_3). (b) The location of resonances in three-line 2-D GMR filters using a hexagonal-lattice grating versus the ratio of the two grating periods (Λ_b/Λ_a).....137

Figure 5.9: Spectral response of the three-line 2-D GMR filters using a hexagonal-lattice structure (a.) Λ_b/Λ_a= 0.96; (b.) Λ_b/Λ_a= 1.07; (c.) Λ_b/Λ_a= 1.14; (d.) Λ_b/Λ_a= 1.21 ..138

Figure 5.10: Deviation of the resonant wavelengths while changing one of each structure dimension from the design (a) TM_0 resonance (b) TE_0 resonance 140

Figure 5.11: Deviation of the spectral linewidth while changing one of each structure dimension from the design (a) TM_0 resonance (b) TE_0 resonance.....142

Figure 5.12: Contour plot of the shift (nm) of TM_0 resonance (a) deviation of grating depth (Δt_g) and air-hole radius (Δr) (b) deviation of high index film thickness (Δt_f) and air-hole radius (Δr). 143

Figure 5.13: (a) A configuration of the grating with slanted side wall (b) the contour plot of the shift (nm) of TM_0 resonance with the change of air-hole radius (Δr) and slanted side wall angle ($\Delta\theta$).....144

Figure 6.1: Configurations of diffraction/guidance planes at oblique incidence and phase matching diagram of resonant modes with the same β in the 2-D GMR with (a) a rectangular-(b) a hexagonal-lattice grating.....150

Figure 6.2: Configurations of diffraction/guidance plane and phase matching diagram of three resonant modes at off-resonant angle (a) on- (b) off-incident plane. 153

Figure 6.3: Configurations of diffraction/guidance plane and phase matching diagram of four resonant modes at off-resonant angle (a) on- (b) off-incident plane. 155

Figure 6.4: (a) Phase matching conditions (b) spectral (c) and (d) angular resonant response along and perpendicular to plane of incidence of 2-D GMRs in Table 6.1 158

Figure 6.5: Comparison of de-phasing compensations in GMR#1 and GMR#2 (Figure 6.4) calculated from Eqs. (6.3)-(6.6) (a) on- incident plane (b) at off-incident plane 159

Figure 6.6: (a) Scattering of four resonant modes at resonance (A: forward diffraction, B: a crossed diffraction) and de-phasing manners of a crossed diffraction at off-resonance (b) $\theta_0+\Delta\theta$ (c) $\varphi_0+\Delta\varphi$ 161

Figure 6.7: η_B and η_d of the grating structure of GMR#2 in Table 6.1 versus the grating depth, where grating has r=0.13 μm, λ_0=0.98μm θ_{inc}~10.4º.....163

Figure 6.8: (a)/(e) Angular responses of four TM_0 resonant modes located at λ_0=0.98μm, θ_{inc}=10.4º and dispersion plots calculated by RCWA (a)-(b) t_g=0.05 μm, t_f=0.503 μm and (e)-(d) when t_g=0.15 μm, t_f= 0.44μm (c) dispersion plot calculated by HWA for t_g=0.05 μm 164

Figure 6.9: Resonant band diagram of the structure in Table 6.2 calculated by RCWA and angular responses at λ_0, (a)-(d) t_g=0.25 μm, (b)-(e) t_g=0.35 μm, and (c)-(f) t_g=0.55 μm 165

Figure 6.10: The angular -wavelength linewidth ratio vs. grating depth.....166

Figure 6.11: Dual-grating 2-D GMR configuration.....167

Figure 6.12: (a) Scattering of four resonant modes at resonance (A: forward diffraction, B: a crossed diffraction by the substrate grating) and de-phasing manners of a crossed diffraction (B) at off-resonance (b) $\theta_0+\Delta\theta$ (c) $\varphi_0+\Delta\varphi$ 169

Figure 6.13: The angular-wavelength linewidth ratio vs. substrate grating depth, t_{g2}, (resonances in Table 6.3).....170

Figure 6.14: Resonant band diagram of the structure in Table 6.3 calculated by RCWA (a) t_{g2}=0.15 μm (b) t_{g2}=0.25 μm (c) t_{g2}=0.34 μm (d) plot of angular responses at λ_0 of the structures with t_{g2}= 0.25-0.4 μm 171

Figure 6.15: The angular-wavelength linewidth ratio vs. substrate grating depth, t_{g2}, (resonances in Table 6.4).....173

Figure 6.16: Resonant band diagram of the structure in Table 6.4 calculated by RCWA (a) t_{g2}=0.05 μm (b) t_{g2}=0.25 μm (c) t_{g2}=0.4 μm (d) plot of angular responses at λ_0 of the structures with t_{g2}= 0.35-0.45 μm.....174

LIST OF TABLES

Table 6.1: Spectral and angular linewidth of resonances (λ_0=0.98 μm) by a counter-propagation resonant mode in 2D-GMR at oblique incidence 157

Table 6.2: Spectral and angular linewidth of resonances (λ_0= 0.98 μm) in a hexagonal-lattice grating resonance structures (Λ_a =0.55 μm, Λ_b=0.6 μm, and r =0.13 μm) at oblique incidence (φ_0=90º, ψ_0=0º).....165

Table 6.3: Spectral and angular linewidth of resonances (λ_0=0.98 μm) in a dual hexagonal-lattice grating resonance structures (Λ_a = 0.55 μm, Λ_b=0.6 μm, superstrate grating: nH/nL=2/1, t_{g1}=0.55 μm, r_1 =0.13 μm, substrate grating: nH/nL=2/1.47, r_2=0.21 μm) at oblique incidence (φ_0=90º, ψ_0=0º, θ_0=14 º) 170

Table 6.4: Spectral and angular linewidth of resonances (λ_0=0.98 μm) in a dual hexagonal-lattice grating resonance structures (Λ_a = 0.55 μm, Λ_b=0.6 μm, superstrate grating: nH/nL=2/1, t_{g1}=0.35 μm, r_1 =0.13 μm, substrate grating: nH/nL=2/1.47, r_2=0.21 μm) at oblique incidence (φ_0=90º, ψ_0=0º).....172

LIST OF ACRONYMS/ABBREVIATIONS

1-D	One-Dimensional
2-D	Two-Dimensional
3-D	Three-Dimensional
CWE	Coupled Wave Equations
GMR	Guided Mode Resonant
HWA	Homogeneous Waveguide Approach
RCWA	Rigorous Coupled Wave Analysis
S-matrix	Scattering matrix
TE	Transverse Electric
TM	Transverse Magnetic
TMA	Transmission Matrix Approach

CHAPTER 1 : INTRODUCTION

History of resonance anomaly in a grating-waveguide structure developed from the discovery of a discrete spectrum in the higher-order diffraction reflected waves by R.W. Wood in 1902 [1.]. Although, the theory of grating diffraction was well established, the unexpected phenomenon could not be explained at that time. Since then, several researchers [2-9] have attempted to explain the effect, the so-called "Wood's anomalies."

Lord Rayleigh in 1907 showed that the passing off or the emergence of a higher diffracted order results in the redistribution of energy manifested itself as a singularity in one or more of the propagating diffraction orders. The wavelengths corresponding to this transition of the diffracted orders from evanescent-to propagating are now known as the Rayleigh wavelengths [2.] However, Wood in 1912 [3] observed a different type of anomalies not associated with Rayleigh wavelengths. Wood attributed the anomalies, which was observed light polarized perpendicular to the grating groove (S polarization), to a resonant effect within the grating grooves. In 1938, Fano described the lineshape of the anomalies and his approach was based on the existence of surface waves in a metallic grating [4]. This was the first step in better physical understanding of the resonant phenomena. In 1952, Palmer found the anomalies when the incident beam is polarized in the plane parallel to the grating grooves (P polarization) for the first time [5]. He showed that P anomalies disappear when the grating groove depth is much less than the wavelength. This explained why the theoretical descriptions up to that time cannot predict the P-polarization anomalies. Lippmann later verified this discussion by analyzing the effect of Rayleigh's approximation for the deep grating [6.] Through the 1950's and early 1960,

the theoretical works focused on clarifying the anomalies using multiple scattering approaches [7-8] after the well-developed treatments of electromagnetic scattering from various obstacles.

In 1965, a new understanding the Wood's anomalies based on the influence of the guided wave was presented by Hessel and Oliner [9.] They identified for the first time two mechanisms for Wood's anomalies. The first is the well-known Rayleigth's wavelength type. The second is associated with the coupling of the diffracted order to excite of weakly guided modes supported by the structure. The fields leaked from the structure remains in phase and constructively interferes thereby producing the anomaly. This is clearly a resonant effect (as Wood suspected). The Hessel and Oliner's work was further extended by Nievere in 1972. He investigated the resonances associated with dielectric coated metallic gratings [10]. The resonances of P polarization were observed in a shallow grating with a dielectric layer. The resonances were related to the modes supported in the structure when a dielectric film is introduced. Later, he proposed a rigorous formalism for grating coupler waveguide system and associated the complex poles and zeros with the maxima and minima of the approximated Lorentzian resonance spectra [11-12.]

In 1986, Popov and Mastev were the first to theoretically report a 100% efficient resonance in the reflected zero order as a result of the guided mode excitation in coated dielectric gratings [13]. Later, Avrutsky and Sychugov related the radiative loss in the structure to the resonance spectral and angular linewidths [14]. In 1990, Magnusson and Wang's investigation of a planar dielectric grating waveguide using rigorous coupled wave analysis (RCWA) also demonstrated 100% efficient narrowband spectral peaks in the reflected zero order [15]. The spectral linewidths were shown to be directly proportional to the grating modulated amplitude.

The device was referred to as "guided mode resonance (GMR) filter." In 1992, they suggested a potential use of these structures as polarization elements, electro-optic switches and narrowband filters [16]. After these investigations, a number of researchers have analyzed the resonance characteristics [17-24], related resonances to the structure parameters [21-22, 25], attempted to fabricate devices [26-28] and improved the responses [29-34].

In the last few years, dielectric GMR devices were extensively investigated. Norton *et al.* [17] formulated an approximate closed-form expression for the radiative coupling loss of the planar dielectric grating waveguide using the coupled mode theory. The radiative coupling losses along with the approximated Lorentzian function resonance response established by Neviere [10] were shown to accurately predict the spectral/angular linewidth expression verified by the RCWA. Its inverse expression as well defined minimum size of the structure required a 100% reflectivity. A better physical understanding of the resonance characteristics were later introduced by Sharon using the interference approach [18-19.] The approach was used to investigate the scattering/absorption loss on the resonance lineshape and shift of the resonances in lossy dielectric structure. Rosenblatt [20] demonstrated broaden and flat angular responses of resonances at normal incidence by using coupled wave approach together with the ray picture model to study the impact of the coupling strength of the two counter-propagating fields on the angular response. Combining the studies of Sharon [18-19] and Rosenblatt [20], Jacob *et al.* proposed two new separate models, based on the interference-waveguide approach, for a structure at oblique [21] and at normal incidence [22]. Resonance responses were connected to the grating coupling strengths associating with the grating physical dimensions. Other approaches to investigate the resonance effect include: examining the field and power flux inside

the grating using rigorous modal solution of the scattering problem by Tamir and Zhang [23], and addressing the leaky stop bands associated with resonant structures [24.]

Several GMR multilayer configurations were investigated and proposed for spectral filtering applications which require a symmetric narrow spectral lineshape and low baseline reflection [29-38]. Due to the high dependence of the filter response on the structure properties and the direction of incident angle, the GMR applications extended include sensors, rotational tunable filters, electro-optic tunable filters and also optical switches [39-43]. The numerical and experimental results were intensively reported.

While GMR filters have been observed to possess a very narrow spectral response, there angular response may not broad enough to operation with finite beams. The divergence nature of finite beams results in reduced peak reflection at resonance due to the narrow acceptance angle of the device. This is particularly more pronounced at oblique incidence. Increasing the resonance angular acceptance requires engineering the coupling characteristics of the leaky mode. Lemarchand *et al.*[44] was the first to propose a structure with double-period gratings in 1998. Using this configuration, the coupling between the counter-propagating modes was strengthened and therefore broadening the angular linewidth at normal incidence. To reduce the fabrication process complexity, the configuration was later re-modified to bi-atom or asymmetric grating [45]. They recently applied this structure at oblique incidence [46]. Another study by Jacob *et al.* [22] reported the increment of the angular tolerance at normal incidence by optimizing the grating dimensions to have a strong second Bragg diffraction. He also proposed a new approach by coupling the incident beam to a higher-order mode in order to minimize the dependency of the spectral and the angular linewidths [22].

While the resonance anomaly in the grating-waveguide structure was thoroughly investigated in the past twenty years, most of the studies focused on the field scattering and the modal index in one-dimensional (1-D) grating structure. Only few studies referred to the influences of the double diffraction using two-dimensional (2-D) grating structure on the resonances. The first study was experimentally demonstrated by Peng *et al.* in 1995 [49]. He later theoretically investigated the scattering of the field inside the structure at resonance using the three-dimensional (3-D) rigorous coupled wave analysis [50]. Two potential applications were proposed to benefit from the double periodicity at normal incidence: polarization-independent narrow-band filter and dual narrow band filter. Mizutani *et al.* [51] proposed a rhombic-lattice grating structure as a non-polarizing GMR filter at oblique incidence without explaining the mechanism of the filter. Fehrembach and Sentenac later presented a phenomenological theory of diffraction gratings made by perturbing a planar waveguide [52-53]. They considered the Hermitian reflection matrix of the second order linking the orthogonal polarized magnitudes of the reflected order and the incident wave. Two uncoupled Eigen modes were presented but do not exist at the same wavelength for the orthogonal polarized incident waves. The unpolarized filter requires simultaneous excitation of both Eigen modes using a certain value of the Fourier coefficient of the permittivity, or a grating geometry, for a particular incident direction [53.] This explained the mechanism of the unpolarized filter proposed by Mizutani [51.] Fehrembach and Sentenac combined their studies of polarization independence [53] and the broadening of the angular linewidth [46] of the resonances at oblique incidence and proposed an unpolarized structure with high angular tolerances. The structure using the square-lattice grating with non-uniform grating-groove size was designed to have two pairs of first-order diffracted waves

simultaneously coupled to two guided modes having different propagation constant [54]. Recently, Clausnitzer *et al.* [55] fabricated an unpolarized filter based on the design presented by Mizutani [51.] To increase the design tolerance, he used a double-sided crossed grating instead. The experimental results were in agreement to the numerical models.

Two-dimensional crossed gratings diffract the incident light into multiple diffracted orders in conical configuration with each diffracted order occupying a distinct diffraction plane. Therefore, the incident beam could be coupled to the multiple polarization-dependent leaky modes each in its own plane (that associated with relevant diffracted). The capability in producing of the various symmetric/asymmetric coupling configurations for a certain incident direction allows engineering both resonance location and response directly through the grating parameters (duty cycle and periodicity.) This offers a huge advantage of the two dimensional structures where resonances are less dependent on the structure material properties. However, a clear through - understanding of the resonant coupling characteristics in the two-dimensional structure has not been provided.

The objective of this dissertation is to provide a detailed study of the unique nature of the resonance anomaly in GMR structures with two-dimensional (2-D) periodic perturbation. Clear understanding of the resonance phenomenon is developed and novel 2-D GMR structures are proposed to significantly improve the performance of narrow spectral filters. The focus will be on investigating and quantifying nature of coupling between the polarization dependent resonant leaky modes, each in its plane. The impact of this coupling on spectral and angular response of GMR devices with rectangular and hexagonal grid 2-D grating structures will be investigated.

Based on the developed understanding of the underlying phenomenon, novel GMR devices are proposed and analyzed.

In the next chapter, the basics elements of resonance anomaly in GMR structures: diffraction and wave guiding will be discussed to provide the background for the analysis of GMR devices. The theory of the grating diffraction with different grating geometries, the wave guiding characteristics of multilayer homogenous slab waveguides, and the wave guiding/scattering in the grating-waveguide structures are presented. The numerical tool used to determine the field magnitude of the diffraction waves namely the exact three-dimensional rigorous coupled wave analysis (3-D RCWA) [56-59] will be described. The numerically stable transmission matrix approach (TMA) [60] used for grating stacked will be presented. Extension of the formulation to finite beams is included. Formulation for the analysis multilayer slab wave guiding structures will be developed. The nature of leaky modes in e grating-waveguide structure is investigated using the scattering matrix method [10-12] and the Bloch mode approach [61-62.] Formulations for the two techniques will be presented.

In Chapters 3, the general concept of the resonant anomaly based on the scattering and coupling characteristics of the resonant modes in GMR devices having the one-dimensional grating structure will be reviewed. An approach where the homogenous waveguide approach (HWA) [21], which does not account for the leaky mode, is used to develop a very good estimate for the structure dimension and the resonance location, and the rigorous coupled analysis (RCWA) to determine the exact structure parameters will be developed. The impact of the structure parameters and grating coupling strengths will be studied to develop a conceptual understanding that can be used how to control the spectral and angular lineshapes. The analysis

will help evaluating the capability and the limitation of the filter due to the restriction of the modes in a common plane at in-plane incidence. The polarization dependency of resonances is investigated in the conical mount and GMR filters for unpolarized light will be demonstrated.

In Chapter 4, the resonance anomaly in the GMR structure using a 2-D grating will be studied. The effect of the inherent multiple diffraction/guidance planes on the resonance is investigated in details. Three 2-D GMR grid structures, rectangular lattice, arbitrary cross lattice, and hexagonal lattice will be considered. The field scattering and the phase matching condition at resonance are studied in order to gain a better understanding of the coupling characteristics including the impact of light polarization and the effect of the grating coupling strengths on the resonance responses. The Bloch mode approach is used to calculate the actual complex modal index related to the formation of the resonances in the 2-D GMR. Investigating the resonances of unpolarized light can be simplified by the decomposition of the incident beam into two components each associated with a polarization-dependent leaky mode in its diffraction planes. The developed understanding of the coupling mechanisms through the incident direction and the grating vectors introduces the concept in order to achieve 100% reflection for the polarized and unpolarized beam. As will be shown in the chapter, achieving the total reflection and polarization independent resonances requires at least two resonance modes to which both orthogonal polarized beams can be coupled and the structure having the appropriate grating dimensions (duty cycle.) Hexagonal-lattice grating are shown to provide better characteristics for unpolarized filters. A novel structure is proposed for the first time where the incident beam is coupled into four resonant modes having the same propagation constant. A polarization independence of the resonance at oblique incidence is achieved without the requirement of

changing the grating duty cycle. At the end of the chapter, the resonance phenomenon in the GMR structure will be investigated utilizing the complex modal indices determined by the Bloch mode approach. The dispersion of the leaky resonant modes counter-propagating along the diffraction planes will be produced and this indicates the interaction of resonant modes and hence the structure set up required for the formation of specific resonances.

In Chapters 5, a novel 2-D GMR structures will be proposed as a controllable multi-line passive optical filter [63]. Multiple spectral resonances are obtained by phase matching the first diffracted orders at specified spectral locations to weakly guided modes propagating along different planes of diffraction each with its distinct propagation constant. The location and the separation between the resonances are directly controlled via the physical dimensions of the structures: the grating periods, and the geometric shape of the unit cell. Controllable two-line and three-line narrow-band reflection filter designs with spectral separation from few up to hundreds nanometers are demonstrated using rectangular-lattice and hexagonal-lattice grating GMR structures, respectively. The strong dependency of resonance locations on the grating period requires a good control of the fabrication processes. The fabrication tolerance and the impact of each structure dimension on the resonance locations as well as the resonance linewidths are characterized at the end of the chapter.

In Chapter 6, broadening of the angular tolerance in two dimensional GMR spectral filters at oblique incidence, while maintaining the narrow spectral linewidth, is investigated. Symmetric and broad angular responses are demonstrated by phase matching the first order diffraction to four fundamental resonant modes having the same propagation constant in a hexagonal grating structure. The angular linewidth can be increased by a factor of two

comparing to when coupling to higher-order modes with unequal magnitude of propagation constant. A five-fold improvement in the angular tolerance is achieved using a grating with strong second Bragg diffraction in order to produce a crossed diffraction. A novel dual grating structure with a second grating located on the substrate side is proposed to further broaden the angular tolerance of the spectral filter without degrading its spectral response. This strong second Bragg backward diffraction from the substrate grating causes two successive resonant bands to merge producing a resonance with symmetric broad angular response.

CHAPTER 2 : BACKGROUND

In this chapter, two phenomena participating in guided mode resonant devices, diffraction and leaky mode in wave guiding structure are discussed. The diffraction part focuses on the effect of the grating geometry/periodicity to the diffracted waves where the diffracted field magnitudes are analyzed using the exact three-dimensional rigorous coupled wave analysis (3-D RCWA) [56-59] together with the transmission matrix approach [60] in the linear regime. The formulations of the approaches are summarized for both a plane wave and a finite beam. They are also mainly used to investigate the resonances in GMR structure in this dissertation. For the waveguide section, the content includes the mode solving approaches in both multilayer slab (homogeneous) waveguides and the grating-waveguide structure. Two approaches, the scattering matrix approach [10-12] and the Bloch mode approach [61-62], are briefly reviewed in order to solve the complex propagation constant in the GMR structure.

2.1 The diffraction theory of the gratings

Gratings are periodic structures with modulated permittivity (a volume/phase grating), absorption (an amplitude grating), or surface (a surface relief grating). Gratings diffracts incident light into multiple directions depending on the grating vectors. Each diffraction order corresponds to the direction where the scattered waves constructively interfere regardless of the grating type [64.]

In general, when an incident light with a tangential wave vector, $\vec{k}_{inc,\tan}$, is modulated by a periodic structure with a tangential grating vector, $\vec{K}_{\tan}$, the tangential wave vectors of the p^{th} diffracted order ($\vec{k}_{p,\tan}$) is written as

$$\vec{k}_{p,\tan} = \vec{k}_{inc,\tan} - p\vec{K}_{\tan} \tag{2.1}$$

The diffraction directions defined in Eq. (2.1) are demonstrated in Figure 2.1, where the diffracted waves have tangential wave vectors $k_{p,\tan} < k_0 n_{1,2}$ (k_0 is the free space wave vector and $n_{1,2}$ is the refractive indices of the media *1* and *2* outside the grating region.) The number of diffracted waves is limited by both the incident direction and the tangential grating vector ($\vec{K}_{\tan}$.)

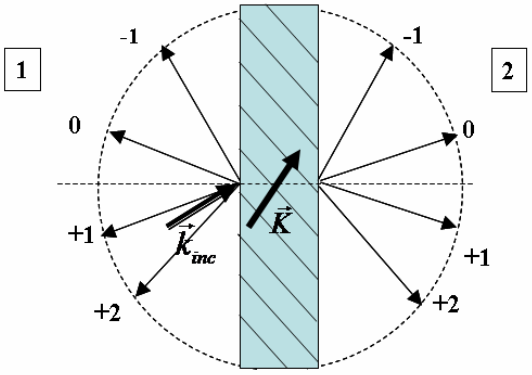

Figure 2.1: Configuration of the grating and the diffraction directions

The grating diffracts light in the desired directions with a proper periodicity as will be shown for the one- and two-dimensional grating cases in Section 2.1.1 and 2.1.2, respectively. The diffraction efficiencies are determined using the rigorous coupled wave analysis (RCWA). The

calculation technique in Section 2.1.3 and the discussion follows support the surface relief grating case which is mainly utilized in this dissertation.

2.1.1 One-dimensional (1-D) grating

For the one-dimensional grating in Figure 2.2, the structure is periodic along the x-axis with a period Λ_a. The grating vector ($\vec{K}$) along the k_x-axis, then, has a magnitude $2\pi/\Lambda_a$. For this setting, the diffraction equations (2.1) are generally represented as follows.

$$k_{x,p} = k_0 n_{inc} \sin\theta_{inc} \cos\varphi_{inc} - p\frac{2\pi}{\Lambda_a},$$

$$k_{y,p} = k_0 n_{inc} \sin\theta_{inc} \sin\varphi_{inc}. \qquad (2.2)$$

where $k_{x,p}$ and $k_{y.p}$ are the wave vector components (tangential to the boundary) of the *p*-th diffracted order, respectively. $(\theta_{inc}, \varphi_{inc})$ are the radial incident angles. n_{inc} is the refractive index of the incident medium. The directions of the diffracted waves can be written as

$$\theta_p = \tan^{-1}\left\{\frac{\sqrt{k_{x,p}^2 + k_{y,p}^2}}{k_{z,p}}\right\},$$

$$\varphi_p = \tan^{-1}\left\{\frac{k_{y,p}}{k_{x,p}}\right\},$$

and $$k_{z,p} = \sqrt{(k_0 n_{out})^2 - k_{x,p}^2 - k_{y,p}^2}. \qquad (2.3)$$

where $k_{z,p}$ is the wave vector of the p-th diffracted order normal to the boundary (x-y). As shown, the directions of the diffracted waves depend on the output region (refractive index n_{out}.) The diffracted waves can be within the common plane at the in-plane mounting (Figure 2.2a), or individual planes at conical mounting (Figures. 2.2b and c show the rotation of the diffracted planes with respect to the incident plane). The drawings in Figure 2.2 show the diffraction planes when assuming that the diffraction occurs only in the transmitted medium.

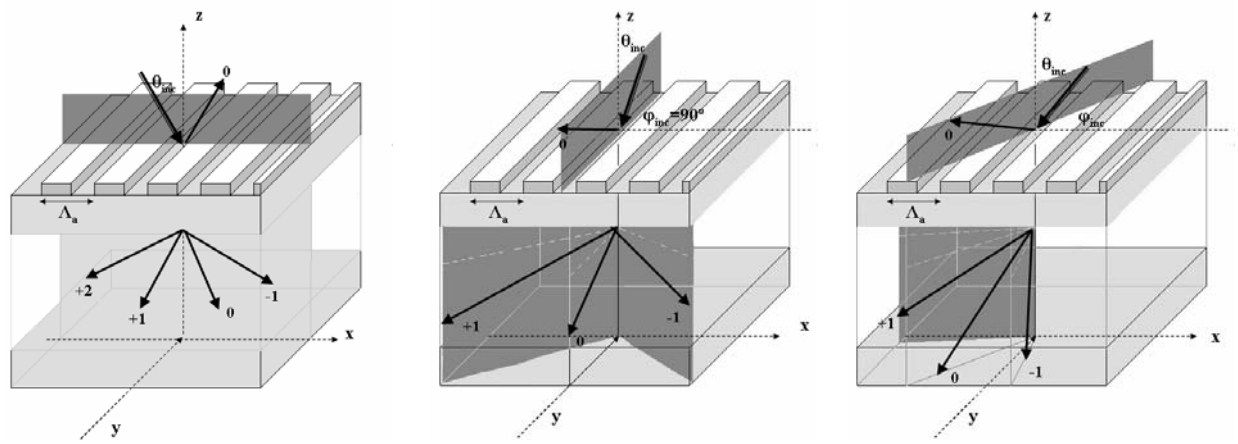

(a) (b) (c)

Figure 2.2: Diffraction in 1-D grating at (a) in- plane (b) fully conical (c) conical mounting

2.1.2 Two-dimensional (2-D) grating

For a crossed grating, the structure is periodic along two directions with periods Λ_a and Λ_b as illustrated in Figure 2.3a. The diffraction pattern is along reciprocal planes [65] designated in Figure 2.3b with unit lengths C_a and C_b. In this structure, the grating vectors are written as

$$\vec{K} = C_a \vec{a} + C_b \vec{b} \tag{2.4}$$

The diffraction orders, p and q, are defined as harmonics along grating vectors $\vec{C}_a$ and $\vec{C}_b$, respectively.

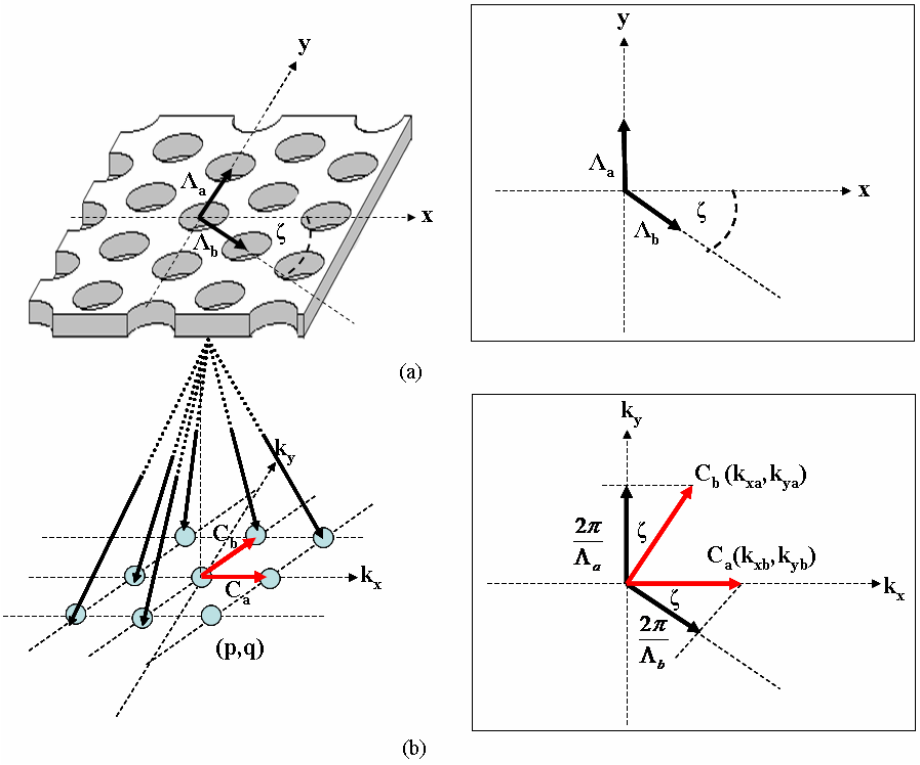

Figure 2.3: A general two-dimensional crossed diffraction grating and the diffraction pattern

For the generalized case, the grating vectors are rotated along $\vec{k}_x$ and $\vec{k}_y$ direction as follows

$$\vec{C}_{a,p} = p\frac{2\pi}{\Lambda_b \cos(\zeta)}\vec{k}_x, \text{ and} \qquad \vec{C}_{b,q} = q\frac{2\pi}{\Lambda_a}\tan(\zeta)\vec{k}_x + q\frac{2\pi}{\Lambda_a}\vec{k}_y. \tag{2.5}$$

The grating vectors in the new coordinates are

$$\begin{aligned}\vec{K}_{pq} &= K_{x,pq}\vec{k}_x + K_{y,pq}\vec{k}_y \\ &= \left\{p\frac{2\pi}{\Lambda_b \cos(\zeta)} + q\frac{2\pi}{\Lambda_a}\tan(\zeta)\right\}\vec{k}_x + q\frac{2\pi}{\Lambda_a}\vec{k}_y\end{aligned} \tag{2.6}$$

The wave vectors of the diffracted waves are determined from the two-dimensional grating equations.

$$k_{x,pq} = k_{x,inc} - \left(p\frac{2\pi}{\Lambda_b}\sec(\zeta) + q\frac{2\pi}{\Lambda_a}\tan(\zeta) \right) \tag{2.7}$$

and,

$$k_{y,pq} = k_{y,inc} - \left(q\frac{2\pi}{\Lambda_a} \right). \tag{2.8}$$

where $k_{x,y,pq}$ is the wave vector component (tangential to the boundary) of a diffracted order designated by p in a-direction and q in b-direction.

Unlike the 1-D grating at conical mounting, the crossed diffraction grating (Figure. 2.3b) diffracts the incident beam more symmetrically. In two-dimensional grating structures, the diffracted orders are in multiple planes of diffraction and multiple waves can propagate in the common plane. Eq's (2.7) and (2.8) show that each plane contains all the diffracted orders designated by $-\infty < p < \infty$ for a given value of q.

2.1.3 Three-dimensional rigorous coupled wave analysis (3-D RCWA)

Field magnitudes of each diffracted wave are accurately calculated using the rigorous coupled wave analysis (RCWA) [56-59]. This technique is based on plane wave expansion and it is an exact solution of Maxwell's equations in the frequency domain. Then, the accuracy relies on the convergence of the solutions and hence the number of harmonics under calculations. The space harmonics of the tangential electric and magnetic field Eigen modes are calculated within the grating region from the coupled wave equations, and then proper boundary conditions are

applied through the transmission matrix approach [60] to calculate the field outside the structure. The calculations here are carried for the orthogonal Cartesian coordinate systems, however to serve the arbitrary (non-orthogonal) grating periodicities, the grating vectors are modified corresponding to the calculating coordinate as in Eq. (2.6). The approach determines an incident plane wave. The response of a finite beam is investigated by the plane wave decomposition [65] as will be presented by the end of this section.

The normalized incident electric field is written as

$$\vec{E}_{inc} = \vec{u}\exp\left[-j\left(k_{x,inc}x + k_{y,inc}y + k_{z,inc}z\right)\right] \quad , \quad \vec{u}\bullet\vec{k} = 0 \tag{2.9}$$

where $\vec{u}$ is normalized incident electric field vector.

The electromagnetic fields inside the periodic media are represented by summations of the space-harmonic components (p,q).

$$\vec{E}_g = \sum_p \sum_q \vec{S}_{pq}(z) e^{-j\left(k_{x,pq}x + k_{y,pq}y\right)} \tag{2.10}$$

and,

$$\vec{H}_g = -j\eta_0^{-1} \sum_p \sum_q \vec{U}_{pq}(z) e^{-j\left(k_{x,pq}x + k_{y,pq}y\right)} . \tag{2.11}$$

where, $\vec{S}_{pq}(z)$ and $\vec{U}_{pq}(z)$ are the z-spatial components of the normalized electric and magnetic fields respectively, and $\eta_0 = \sqrt{\mu_0/\varepsilon_0}$, $\mu_0 = 4\pi\times10^{-7}\,H/m$ is permeability of free space , $\varepsilon_0 = 8.854\times10^{-12}\,F/m$ is permittivity of free space.

The reflected ($\vec{E}_R$) and transmitted ($\vec{E}_T$) fields are also written as summations of the space harmonics,

$$\vec{E}_R = \sum_p \sum_q \vec{E}_{r,pq} \exp\left[-j\left(k_{x,pq}x + k_{y,pq}y - k_{1,z,p,q}z\right)\right] \tag{2.12}$$

$$\vec{E}_T = \sum_p \sum_q \vec{E}_{t,pq} \exp\left[-j\left(k_{x,pq}x + k_{y,pq}y + k_{2,z,pq}z\right)\right] \tag{2.13}$$

where, $k_{1,z,pq}$ and $k_{2,z,pq}$ are the wave vector normal components of the diffracted orders in the incident medium and the substrate respectively. $\vec{E}_{r,pq}$ and $\vec{E}_{t,pq}$ are the electric field of the reflected and transmitted waves. The calculations of these fields will be presented in the following sections.

2.1.3.a Three-dimensional coupled wave equations (3-D CWE)

The first step of calculating the transmitted and reflected fields using this approach is determining the field Eigen modes inside the grating through the coupled wave equations. In general 3-D CWE deals with all three vector components of both electric and magnetic fields. Formulating the couple wave equations is important to the convergence rates of the solutions. The equations are implemented to preserve the continuity of the EM fields along the discontinuity of the grating's permittivity/permeability. Therefore, they are reformulated for the non-magnetic material as a form [59.]

$$\begin{bmatrix} \dfrac{\partial \mathrm{S_y}}{\partial(k_0 z)} \\ \dfrac{\partial \mathrm{S_x}}{\partial(k_0 z)} \end{bmatrix} = \begin{bmatrix} \mathrm{K_y E^{-1} K_x} & \mathrm{I - K_y E^{-1} K_y} \\ -\mathrm{I + K_x E^{-1} K_x} & -\mathrm{K_x E^{-1} K_y} \end{bmatrix} \begin{bmatrix} \mathrm{U_y} \\ \mathrm{U_x} \end{bmatrix},$$

and

$$\begin{bmatrix} \dfrac{\partial U_y}{\partial(k_0 z)} \\ \dfrac{\partial U_x}{\partial(k_0 z)} \end{bmatrix} = \begin{bmatrix} K_y K_x & E_x - K_y^2 \\ K_x^2 - E_y & K_x K_y \end{bmatrix} \begin{bmatrix} S_y \\ S_x \end{bmatrix}. \tag{2.14}$$

Matrices $E_y = \alpha_1 E + (1-\alpha_1) A^{-1}$ and $E_x = \alpha_2 A^{-1} + (1-\alpha_2) E$ are written as the average of the harmonic coefficient matrices of the relative permittivity E and inverse relative permittivity A addressing the uniformity of the tangential electric field at the grating-groove surfaces. Factors α_1 and α_2 are the two positive numbers in the interval [0, 1.] They indicate the relative strength between matrix E and A. With the proper values of α_1 and α_2, the convergence rate is maximized and that reduces the minimum number of space harmonics, M, under the calculations for the accurate results. $I_{M\times M}$ is an identity matrix. K_x and K_y are diagonal matrices of the tangential wave vectors $k_{x,pq}$ and $k_{y,pq}$ (Eqs. (2.7) and (2.8)), respectively.

Here, to simplify the formulation, the tangential components of the fields are analyzed along new coordinates parallel (//) and perpendicular ($\perp$) to the planes of diffraction. Using these new coordinates, the coupled wave equations, in terms of the electric and magnetic field harmonics (tangential components) can be written as follows.

$$\begin{bmatrix} \dfrac{\partial S_\perp}{\partial(k_0 z)} \\ \dfrac{\partial S_{//}}{\partial(k_0 z)} \end{bmatrix} = \begin{bmatrix} A_{\perp,\perp} & A_{\perp,//} \\ A_{//.\perp} & A_{//,//} \end{bmatrix} \begin{bmatrix} U_\perp \\ U_{//} \end{bmatrix},$$

$$A_{\perp,\perp} = 0, \qquad A_{\perp,//} = I,$$

$$A_{//.\perp} = K_n E^{-1} K_n - I, \text{ and} \qquad A_{//,//} = 0. \tag{2.15a}$$

$$\begin{bmatrix} \dfrac{\partial \mathrm{U}_{\perp}}{\partial(k_0 z)} \\ \dfrac{\partial U_{//}}{\partial(k_0 z)} \end{bmatrix} = \begin{bmatrix} \mathrm{B}_{\perp,\perp} & \mathrm{B}_{\perp,//} \\ \mathrm{B}_{//,\perp} & \mathrm{B}_{//,//} \end{bmatrix} \begin{bmatrix} \mathrm{S}_{\perp} \\ \mathrm{S}_{//} \end{bmatrix},$$

$$\mathrm{B}_{\perp,\perp} = \mathrm{K}_{\mathrm{y}}^{'}\mathrm{E}_{\mathrm{y}}\ \mathrm{K}_{x}^{'} - \mathrm{K}_{x}^{'}\ \mathrm{E}_{\mathrm{x}}\ \mathrm{K}_{\mathrm{y}}^{'}, \qquad \mathrm{B}_{\perp,//} = \mathrm{K}_{\mathrm{y}}^{'}\ \mathrm{E}_{\mathrm{y}}\ \mathrm{K}_{\mathrm{y}}^{'} + \mathrm{K}_{\mathrm{x}}^{'}\ \mathrm{E}_{\mathrm{x}}\ \mathrm{K}_{\mathrm{x}}^{'},$$

$$\mathrm{B}_{//,\perp} = \mathrm{K}_{\mathrm{n}}^{2} - \mathrm{K}_{\mathrm{x}}^{'}\ \mathrm{E}_{\mathrm{y}}\ \mathrm{K}_{\mathrm{x}}^{'} - \mathrm{K}_{\mathrm{y}}^{'}\ \mathrm{E}_{\mathrm{x}}\ \mathrm{K}_{\mathrm{y}}^{'}, \text{ and } \quad \mathrm{B}_{//,//} = -\mathrm{K}_{\mathrm{x}}^{'}\ \mathrm{E}_{\mathrm{y}}\ \mathrm{K}_{\mathrm{y}}^{'} + \mathrm{K}_{\mathrm{y}}^{'}\ \mathrm{E}_{\mathrm{x}}\ \mathrm{K}_{\mathrm{x}}^{'}. \quad (2.15b)$$

In (2.15a) and (2.15b), $\mathrm{K}_{\mathrm{x}}^{'}$, $\mathrm{K}_{y}^{'}$, and $\mathrm{K}_{n}^{'}$ are the diagonal matrices : $\mathrm{K}_{\mathrm{x}}^{'} = \left[\dfrac{k_{x,pq}}{\sqrt{k_{x,pq}^2 + k_{y,pq}^2}} \right]_{M \times M}$,

$\mathrm{K}_{\mathrm{y}}^{'} = \left[\dfrac{k_{y,pq}}{\sqrt{k_{x,pq}^2 + k_{y,pq}^2}} \right]_{M \times M}$, and $\mathrm{K}_{\mathrm{n}} = \left[\dfrac{\sqrt{k_{x,pq}^2 + k_{y,pq}^2}}{k_0} \right]_{M \times M}$

Combining the two coupled wave equations in (2.15a) and (2.15b), the second-order differential matrix equations are

$$\begin{bmatrix} \dfrac{\partial^2 \mathrm{S}_{\perp}}{\partial(k_0 z)^2} \\ \dfrac{\partial^2 \mathrm{S}_{//}}{\partial(k_0 z)^2} \end{bmatrix} = \begin{bmatrix} \mathrm{A}_{\perp,\perp} & \mathrm{A}_{\perp,//} \\ \mathrm{A}_{//,\perp} & \mathrm{A}_{//,//} \end{bmatrix} \begin{bmatrix} \mathrm{B}_{\perp,\perp} & \mathrm{B}_{\perp,//} \\ \mathrm{B}_{//,\perp} & \mathrm{B}_{//,//} \end{bmatrix} \begin{bmatrix} \mathrm{S}_{\perp} \\ \mathrm{S}_{//} \end{bmatrix} = [\mathrm{A}][\mathrm{B}] \begin{bmatrix} \mathrm{S}_{\perp} \\ \mathrm{S}_{//} \end{bmatrix} \qquad (2.16)$$

That can be re-written in a form of an Eigen –value problem

$$\mu^2 \begin{bmatrix} \mathrm{S}_{\perp} \\ \mathrm{S}_{//} \end{bmatrix} = [\mathrm{A}][\mathrm{B}] \begin{bmatrix} \mathrm{S}_{\perp} \\ \mathrm{S}_{//} \end{bmatrix} \qquad (2.17)$$

Based on the solutions of the Eigen-value problem in (2.17), the space harmonics of electric fields ($\vec{S}(z)$) can be written as

$$\begin{bmatrix} S_{\perp} \\ S_{//} \end{bmatrix} = \begin{bmatrix} W_1 e^{-k_0 \mu z} & W_1 e^{k_0 \mu (z-d)} \\ W_2 e^{-k_0 \mu z} & W_2 e^{k_0 \mu (z-d)} \end{bmatrix} \begin{bmatrix} C^{+} \\ C^{-} \end{bmatrix} \tag{2.18}$$

where $\left[\mu^2\right]_{2M \times 2M}$ is the Eigen value matrix and $[W] = \begin{bmatrix} W_1 \\ W_2 \end{bmatrix}_{2M \times 2M}$ is the Eigen vector matrix. The space harmonics of magnetic fields $\vec{U}(z)$ are

$$\begin{bmatrix} U_{\perp} \\ U_{//} \end{bmatrix} = \begin{bmatrix} -V_1 e^{-k_0 \mu z} & V_1 e^{k_0 \mu (z-d)} \\ -V_2 e^{-k_0 \mu z} & V_2 e^{k_0 \mu (z-d)} \end{bmatrix} \begin{bmatrix} C^{+} \\ C^{-} \end{bmatrix},$$

and

$$[V] = \begin{bmatrix} V_1 \\ V_2 \end{bmatrix}_{2M \times 2M} = [A]^{-1}[\mu][W] \tag{2.19}$$

In Eqs. (2.18) and (2.19), C^{+} and C^{-} represent the magnitude coefficients of the electric fields when propagating in the forward and backward directions inside the periodic medium with thickness d. $\mu_{pq} = k_{z,pq,grating} / k_0$ indicates the propagating waves inside the grating region (when μ_{pq} is purely imaginary). The effective indices of the subwavelength grating for the incident beam polarized normal to ($n_{\perp}$) and in ($n_{//}$) the plane of incidence are directly estimated by μ_{00} [59, 67.] The two unknown parameters, C^{+} and C^{-}, will be subtracted when applying the boundary condition to estimate the diffracted field outside the grating.

2.1.3.b Boundary condition: transmission matrix approach (TMA)

For a single-level grating, the tangential components of electromagnetic fields at interfaces z=0 and z=d can be written as

$$\begin{bmatrix} E_{inc,\perp}\delta_{00} \\ Z_{1,00}\eta_0 H_{inc,\perp}\delta_{00} \\ j\eta_0 H_{inc,\perp}\delta_{00} \\ Y_{1,00}\eta_0 E_{inc,\perp}\delta_{00} \end{bmatrix} + \begin{bmatrix} I & 0 \\ 0 & jZ_{1,pq} \\ 0 & I \\ jY_{1,pq} & 0 \end{bmatrix} \begin{bmatrix} E_{r,pq,\perp} \\ j\eta_0 H_{r,pq,\perp} \end{bmatrix} = \begin{bmatrix} W_1 & W_1 X \\ W_2 & W_2 X \\ -V_1 & V_1 X \\ -V_2 & V_2 X \end{bmatrix} \begin{bmatrix} C^+ \\ C^- \end{bmatrix}, \quad \text{at z=0,}$$

and

$$\begin{bmatrix} W_1 X & W_1 \\ W_2 X & W_2 \\ -V_1 X & V_1 \\ -V_2 X & V_2 \end{bmatrix} \begin{bmatrix} C^+ \\ C^- \end{bmatrix} = \begin{bmatrix} I & 0 \\ 0 & -jZ_{2,pq} \\ 0 & I \\ -jY_{2,pq} & 0 \end{bmatrix} \begin{bmatrix} E_{t,pq,\perp} \\ j\eta_0 H_{t,pq,\perp} \end{bmatrix}, \text{ at z=d} \qquad (2.20)$$

where X, $Z_{\ell,pq}$, and $Y_{\ell,pq}$ are the diagonal matrices: $X = \left[e^{-k_0 \mu d} \right]_{2M\times 2M}$, $Z_{\ell,pq} = \left[k_{\ell,z,pq} / k_0 n_\ell^2 \right]_{M\times M}$, and $Y_{\ell,pq} = \left[k_{\ell,z,pq} / k_0 \right]_{M\times M}$ (ℓ=1 and 2 represent the reflected and transmitted regions.) $[\delta_{00}]_{M\times M}$ is Kronecker delta function matrix.

As shown, calculating the diffracted fields ($\vec{E}_{pq}$ and $\vec{H}_{pq}$) confronts the operation of inverse matrices. That may cause numerical instability, especially for a deep grating having very small exponential term X. This can be avoided using the transmission matrix approach[39] which eliminates the use of X^{-1} from the calculations. For an N-level grating structure, the calculations initially separate the X_N^{-1} from the main inverse matrix $[A]_N^{-1}$ (Eq.(2.21)) Therefore, the final matrix equation of the tangential electromagnetic fields is modified as follow.

$$\begin{bmatrix} I & 0 & I & 0 \\ 0 & -jZ_{1,0} & 0 & jZ_{1,0} \\ 0 & I & 0 & I \\ -jY_{1,0} & 0 & jY_{1,pq} & 0 \end{bmatrix} \begin{bmatrix} E_{inc,\perp}\delta_{0,0} \\ j\eta_0 H_{inc,\perp}\delta_{0.0} \\ E_{r,pq,\perp} \\ j\eta_0 H_{r,pq,\perp} \end{bmatrix} = \begin{bmatrix} W_1 & W_1X \\ W_2 & W_2X \\ -V_1 & V_1X \\ -V_2 & V_2X \end{bmatrix}_1 \underbrace{\begin{bmatrix} X & 0 \\ 0 & II \end{bmatrix}_1^{-1} \begin{bmatrix} W_1 & W_1 \\ W_2 & W_2 \\ -V_1 & V_1 \\ -V_2 & V_2 \end{bmatrix}_1^{-1}}_{[A]_1^{-1}} \cdots$$

$$\cdots \begin{bmatrix} W_1 & W_1X \\ W_2 & W_2X \\ -V_1 & V_1X \\ -V_2 & V_2X \end{bmatrix}_N \begin{bmatrix} X & 0 \\ 0 & II \end{bmatrix}_N^{-1} \begin{bmatrix} W_1 & W_1 \\ W_2 & W_2 \\ -V_1 & V_1 \\ -V_2 & V_2 \end{bmatrix}_N^{-1} \cdots$$

$$\cdots \underbrace{\begin{bmatrix} I & 0 \\ 0 & -jZ_{2,pq} \\ 0 & I \\ -jY_{2,pq} & 0 \end{bmatrix} \begin{bmatrix} E_{t,pq,\perp} \\ j\eta_0 H_{t,pq,\perp} \end{bmatrix}}_{\begin{bmatrix} f \\ g \end{bmatrix}_{N+1} T_{N+1}} \qquad (2.21)$$

where II is an identity matrix with dimensions $2M \times 2M$.

The right hand side of Eq (2.21) is then reduced to $\begin{bmatrix} f \\ g \end{bmatrix}_1 [T]_1$, where sub-matrices $[f]_1$ and $[g]_1$ are calculated from known $[f]_{N+1}$ and $[g]_{N+1}$ as defined in Eq. (2.21). That can be written as follows, assuming that $T_{N+1} = a_N^{-1} X_N T_N$ in order to eliminate X_N^{-1}.

$$\begin{bmatrix} f \\ g \end{bmatrix}_N T_N = \begin{bmatrix} W_1 & W_1X \\ W_2 & W_2X \\ -V_1 & V_1X \\ -V_2 & V_2X \end{bmatrix}_N \begin{bmatrix} X^{-1} & 0 \\ 0 & II \end{bmatrix}_N \begin{bmatrix} a \\ b \end{bmatrix}_N T_{N+1} = \begin{bmatrix} W_1 & W_1X \\ W_2 & W_2X \\ -V_1 & V_1X \\ -V_2 & V_2X \end{bmatrix}_N \begin{bmatrix} I \\ b_N a_N^{-1} X_N \end{bmatrix} T_N ,$$

and

$$\begin{bmatrix} a \\ b \end{bmatrix}_N = \begin{bmatrix} W_1 & W_1 \\ W_2 & W_2 \\ -V_1 & V_1 \\ -V_2 & V_2 \end{bmatrix}_N^{-1} \begin{bmatrix} f \\ g \end{bmatrix}_{N+1}. \tag{2.22}$$

Substituting $[f]_l = \begin{bmatrix} f_{1,1} & f_{1.2} \\ f_{1.3} & f_{1.4} \end{bmatrix}$, and $[g]_l = \begin{bmatrix} g_{1,1} & g_{1.2} \\ g_{1.3} & g_{1.4} \end{bmatrix}$ in Eq. (2.21), the matrix T_1 is written as

$$T_1 = \begin{bmatrix} E_{t,1,\perp} \\ j\eta_0 H_{t,1,\perp} \end{bmatrix} = \begin{bmatrix} g_{1,2} - jY_{1,pq} f_{1,1} & g_{1,4} - jY_{1,pq} f_{1,3} \\ f_{1,2} - jZ_{1,pq} g_{1,1} & f_{1,4} - jZ_{1,pq} g_{1,3} \end{bmatrix}^{-1} \begin{bmatrix} -2jY_{1,p,q} E_{inc,\perp} \delta_{0,0} \\ 2Z_{1,p,q} \eta_0 H_{inc,\perp} \delta_{0,0} \end{bmatrix} \tag{2.23}$$

And hence, the reflected and transmitted fields are

$$T_{N+1} = \begin{bmatrix} E_{t,pq,\perp} \\ j\eta_0 H_{t,pq,\perp} \end{bmatrix} = a_N^{-1} X_N a_{N-1}^{-1} X_{N-1} a_{N-2}^{-1} X_{N-2} \ldots a_1^{-1} X_1 T_1,$$

and

$$\begin{bmatrix} E_{r,pq,\perp} \\ j\eta_0 H_{r,pq,\perp} \end{bmatrix} = \begin{bmatrix} f_{1,1} E_{t,1,\perp} + f_{1,3} j\eta_0 H_{t,1,\perp} - E_{inc,\perp} \delta_{0,0} \\ g_{1,1} E_{t,1,\perp} + g_{1,3} j\eta_0 H_{t,1,\perp} - H'_{inc,\perp} \delta_{0,0} \end{bmatrix}. \tag{2.24}$$

For a normalized power, $E_{inc,\perp} = \cos\psi$ and $j\eta_0 H_{inc,\perp} = jn_{inc} \sin\psi$, where ψ is the polarization of the incident field with respect to an axis normal to the plane of incident. The diffraction efficiencies of the reflected and transmitted waves are

$$DER = \left| E_{r,pq,\perp} \right|^2 \mathrm{Re}\left\{ \frac{k_{1,z,pq}}{k_{1,z,00}} \right\} + \left| j\eta_0 H_{r,pq,\perp} \right|^2 \mathrm{Re}\left\{ \frac{k_{1,z,pq}}{n_1^2 k_{1,z,00}} \right\} \tag{2.25}$$

$$DET = \left| E_{t,pq,\perp} \right|^2 \mathrm{Re}\left\{ \frac{k_{2,z,pq}}{k_{1,z,00}} \right\} + \left| j\eta_0 H_{t,pq,\perp} \right|^2 \mathrm{Re}\left\{ \frac{k_{2,z,pq}}{n_2^2 k_{1,z,00}} \right\} \tag{2.26}$$

2.1.3.c Permittivity/permeability expansions

As these calculations assume that the periodic structure is infinite along x- and y–axis, the space harmonic coefficients of both permittivity, $\varepsilon(x,y)$, and inverse permittivity, $1/\varepsilon(x,y)$, of a binary 2-D grating with any unit cell can be expanded in two-dimensional Fourier series of the form [65]

$$f(x,y)=\sum_i\sum_j d_{ij}\, e^{j\left(K_{x,ij}\,x+K_{y,ij}\,y\right)},$$

and

$$d_{ij}=\frac{1}{A}\int_A f(x,y)\,e^{-j\left(K_{x,ij}\,x+K_{y,ij}\,y\right)}\,dx\,dy. \qquad (2.27)$$

In Eq. (2.27), A is the area of the unit cell. $d_{i,j}$ is the $\left(i^{th},j^{th}\right)$ Fourier component of the function $f(x,y)$ which identifies the grating's groove/permittivity profile within the unit cell. In the coupled wave equations (Section 2.1.3a), the harmonics (i,j) in Eq. (2.27) are replaced by $(p-p',q-q')$ corresponding to each field harmonic (p,q) where $p'=[p(1)...p(M)]$ and $q'=[q(1)...q(M)]$. For a skew periodic function, the spatial frequencies ($K_{x,ij}$, $K_{y,ij}$) are defined as in Eq. (2.6).

For the surface relief grating, the same approach as a binary grating can be applied after slicing the grating into multiple levels [60,] where each level has a constant fill factor. The permittivity/inverse permittivity expansion, hence, is proportional to the grating profile. The coupled wave calculations are solved for each level individually. The numbers of the levels increases the accuracy of the calculations.

2.1.3.d RCWA formulation for a finite beam

In practice, the incident beam is finite with certain divergence angle. The above formulations are not sufficient unless the beam is perfectly collimated. Theoretically, the finite beam is a composition of plane waves with symmetric angular components around the direction of propagation of the beam. Using Fourier analysis, the magnitudes of each plane wave are determined [66.] The reflected/ transmitted fields of each plane wave with scaled magnitude are individually calculated using RCWA. The total field is calculated by recombining the reflected/transmitted fields through the inverse Fourier transform.

Here, the plane wave decomposition is carried by determining the Fourier transform of the incident beam. Assuming that the incident beam $E_{inc}(x,y)$ is initially sampled in spatial domain by N points along x and y with Δx and Δy sampling spacing, the sampled incident beam is then $E_{inc}(x_{n_x}, y_{n_y})$, where $x_{n_x} = n_x \Delta x$, and $y_{n_y} = n_y \Delta y$. In the angular domain, the field is sampled by M points along k_x and k_y with Δk_x and Δk_y sampling spacing. The angular components of the incident beam are calculated using the discrete Fourier transform.

$$\mathrm{E}_{inc}\left(m_x \Delta k_x, m_y \Delta k_y\right) = \sum_{n_y=-N_y/2}^{N_y/2} \sum_{n_x=-N_x/2}^{N_x/2} E_{inc}\left(x_{n_x}, y_{n_y}\right) e^{-j\left(m_x \Delta k_x x_{n_x} + m_y \Delta k_y y_{n_y}\right)} \Delta x \, \Delta y \qquad (2.28)$$

It is worth mentioning that the sampling theory [65] is satisfied in our calculations ($L_u \le 2\pi/\Delta k_u$ and $K_u \le 2\pi/\Delta u$, where L_u and K_u are the calculation range of the spatial and angular domain, and u represents x and y). The reflection and transmission of each scaled plane wave is then calculated using RCWA. The total reflected/transmitted beams at distance z away

from the structure surface (superstrate or substrate) are finally reconstructed by initially combining the multiple reflected/transmitted waves, $E_{r/t,pq}$, for each angular component and then composing them to the spatial domain through the numerical inverse Fourier transform.

$$E_{R/T}\left(x_{n_x}, y_{n_y}, z\right) = \frac{1}{(2\pi)^2} \sum_{m_x=-M_x/2}^{M_x/2} \sum_{m_y=-M_y/2}^{M_y/2} \mathrm{E}_{R/T}\left(m_x\Delta k_x, m_y\Delta k_y\right) e^{j\left(m_x\Delta k_x\, x_{n_x} + m_y\Delta k_y\, y_{n_y}\right)} \Delta k_x\, \Delta k_y\,,$$

and

$$\mathrm{E}_{R/T}\left(m_x\Delta k_x, m_y\Delta k_y\right) = \sum_p \sum_q \mathrm{E}_{r/t,pq}\, e^{-j\left(k_{x,pq}x_{n_x} + k_{y,pq}y_{n_y} \pm k_{z,pq}z\right)}. \qquad (2.29)$$

The composition can be individually performed at z=0 interface for each diffracted wave (p,q) when calculating the diffraction efficiencies.

In this chapter, we consider the incident beam with Gaussian profile. Eq. (2.30) shows a general expression for an obliquely incident normalized Gaussian beam (Figure. 2.4) at the structure surface (z=0)

$$\vec{E}(x, y, z=0) = \exp\left\{-\left(\frac{x^2}{w_{0x}^2} + \frac{y^2}{w_{0y}^2}\right)\right\} \exp\left\{-j\left[k_x y + k_y y\right]\right\} \cdot \vec{u}$$

Where, the beam radii are

$$\begin{aligned} w_{0x} &= w_{0x'} \cos\theta_0 \cos\varphi_0 - w_{0y'} \sin\varphi_0 \\ w_{0y} &= w_{0x'} \cos\theta_0 \sin\varphi_0 + w_{0y'} \cos\varphi_0 \end{aligned} \qquad (2.30)$$

The sub-plane waves have angular components defined as

$$k_{x,m_x} = m_x\Delta k_x + k_0\, n \sin\theta_0 \cos\varphi_0\,,$$

and $$k_{y,m_y} = m_y \Delta k_y + k_0 \; n \sin\theta_0 \sin\varphi_0 \qquad (2.31)$$

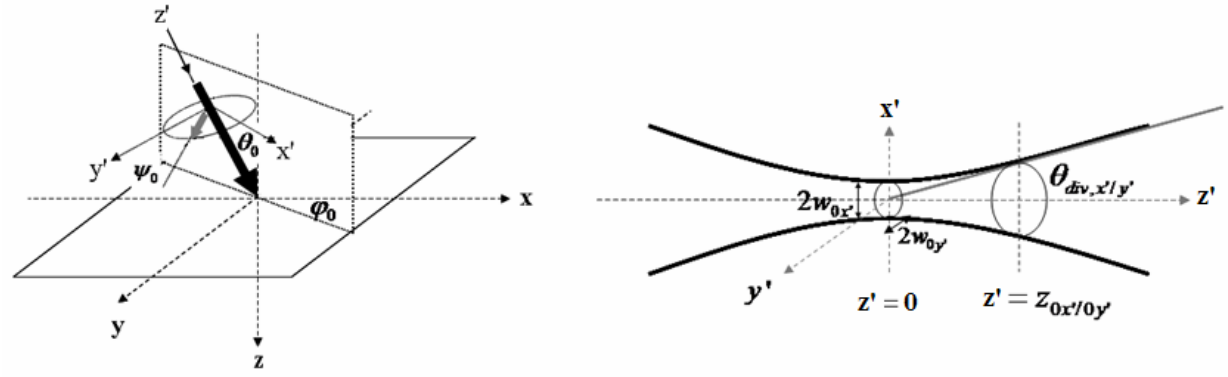

(a) (b)

Figure 2.4: Configurations of (a) a Gaussian beam at arbitrary incident (θ_0 and φ_0) and its polarization (b) Gaussian beam's parameters

The polarization of the sub-plane waves remains the same as that of the beam. Rotating the incident polarization along the incident plane of each sub-plane wave, the polarization can be written as

$$\psi_{m_x,m_y} = \tan^{-1}\left(\frac{u^{//}_{m_x,m_y}}{u^{\perp}_{m_x,m_y}}\right),$$

$$u^{//}_{m_x,m_y} = u_0^x \cos\varphi_{m_x,m_y} \cos\theta_{m_x,m_y} + u_0^y \sin\varphi_{m_x,m_y} \cos\theta_{m_x,m_y} - u_0^z \sin\theta_{m_x,m_y},$$

and $$u^{\perp}_{m_x,m_y} = -u_0^x \sin\varphi_{m_x,m_y} + u_0^y \cos\varphi_{m_x,m_y}. \qquad (2.32)$$

In Eq. (2.32), u_0^x, u_0^y, and u_0^z are the unit vectors of the incident beam ($\vec{u}_0 = u_0^x \hat{x} + u_0^y \hat{y} + u_0^z \hat{z}$). These vectors can be written s follows.

$$u_0^x = \sin\psi_0 \cos\theta_0 \cos\varphi_0 - \cos\psi_0 \sin\varphi_0,$$

$$u_0^y = \sin\psi_0 \cos\theta_0 \sin\varphi_0 + \cos\psi_0 \cos\varphi_0,$$

$$u_0^z = -\sin\psi_0 \sin\theta_0. \tag{2.33}$$

Here, ψ_0 is the polarization of the incident beam.

In this section, we have explained briefly the diffraction analysis of the general 2-D surface relief grating part of the GMR structure. As mentioned earlier, the resonance effect in GMR structures rely on both diffraction by the grating and guidance in the slab waveguide layer beneath the grating. In the following section, we will highlight the guiding calculation in general dielectric slab waveguide structures.

2.2 Dielectric slab waveguide

Wave guiding in planar slab waveguide is achieved when light propagates in a region surrounded by lower -refractive index media, and it interacts to each interface with an angle larger than the critical angle ($\theta_c = \sin^{-1}(n_2/n_1)$, where n_1 and n_2 are refractive indices of the surrounding and guiding media respectively). Once the multiple total reflected waves are constructively interfered, light is perfectly bounded within the guiding region. The simple waveguide structure, called *"three-layer slab waveguide"*, is demonstrated Figure 2.5a.

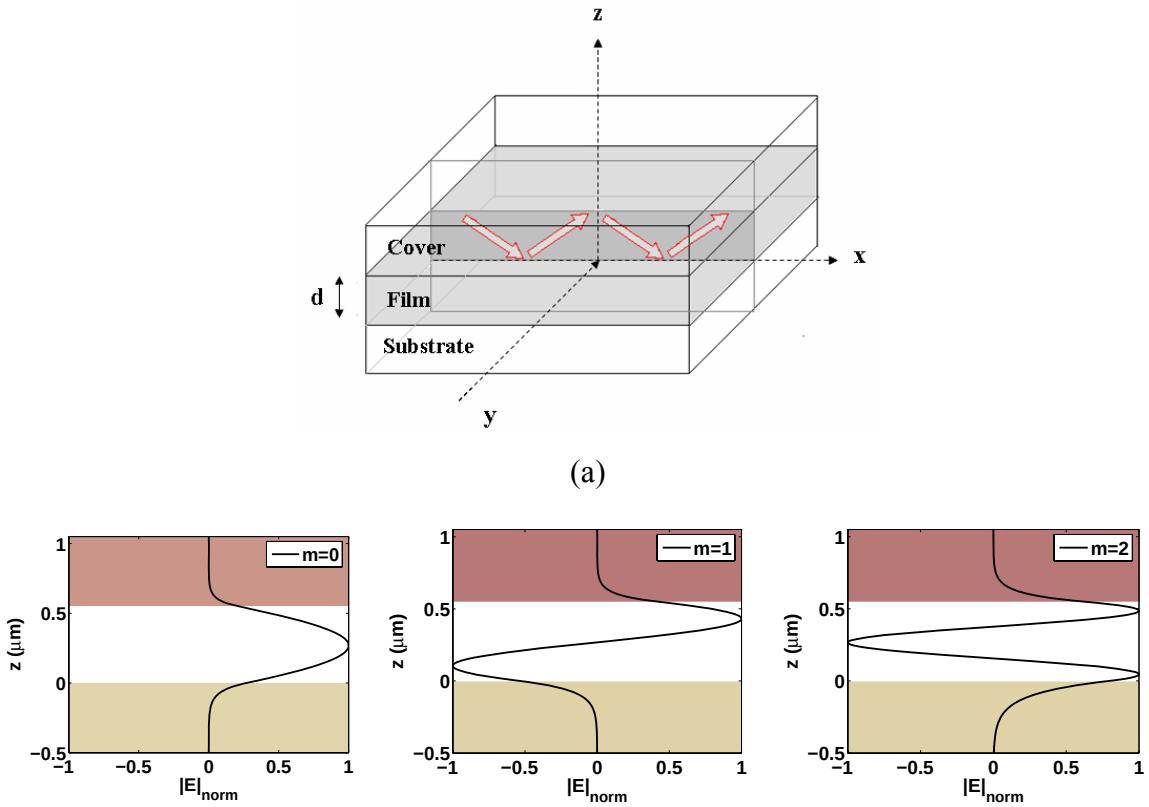

Figure 2.5: (a) configurations of three-layer slab waveguide (b)-(d) plots of the field amplitudes of the first three vertically guided modes, m=0,1, and 2

In the structure, light is vertically confined in the film region (only along z-direction) when assuming that the structure is infinite in x- and y-direction. The guided waves propagate from the upper film interface to the lower film interface and reflects back again with a total phase shift of $2m\pi$ (m is an integer number). These discrete waves form the so-called guided modes (m). The first three guided modes field profiles are plotted in Figures 2.5b-d. Based on these conditions, the characteristic equation for the slab waveguide is expressed as [68]

$$2\kappa_m d - 2\phi_s - 2\phi_c = 2m\pi \qquad m = 0,1,2,3,\ldots, \tag{2.34}$$

In Eq. (2.34), $\beta_m = k_0 n_{eff,m}$ is the modal propagation constant, $\kappa_m = \sqrt{(k_0 n_f)^2 - \beta_m^2}$ is the transverse propagation constant within the film. $2\phi_c$ and $2\phi_s$ are the phase shifts due to the total reflection at the film-cover and film-substrate interfaces, respectively. The formulation is more involved when the structure comprises of composite cover and composite substrate, referred to as *"multilayer slab waveguide."*

2.2.1 Multilayer slab waveguide mode solving method

For an *N*-layer slab waveguide (as illustrated in Figure 2.6,) the structure may comprise of single or multiple high index layers.

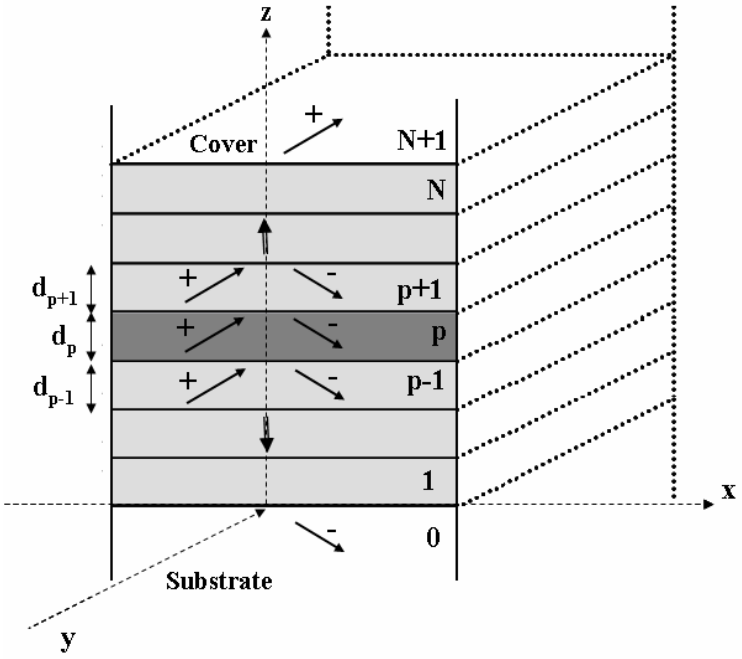

Figure 2.6: Configuration of multilayer slab waveguide

The waveguide modes can be determined using the same approach, where the guiding region is the highest index layer, *-p*. The phases gained by the total reflection at upper/lower interfaces (*p-1/p* and *p/p+1*) are calculated from the amplitude reflection coefficients, which are determined by applying the boundary condition to match the tangential fields from the outmost interfaces, *0/1* and *N/N+1*, towards the inner interfaces, *p-1/p* and *p/p+1*, respectively.

As depicted in Figure 2.6, the fields in each layer bounce upward and downward with magnitude coefficients designated as C^{+} and C^{-}. For the TE-case, the tangential fields at each layer are defined as

$$E_{y,i} = \begin{cases} C_0^{-} e^{\gamma_0 z} e^{-j\beta x}, \quad for\ z < 0 \\ \left.\begin{array}{c} C_i^{+}\left(e^{-\gamma_i z_i} + c_i X_i e^{\gamma_i (z_i - d_i)}\right) e^{-j\beta x} \\ or\ C_i^{-}\left(e^{\gamma_i (z_i - d_i)} + s_i X_i e^{-\gamma_i z_i}\right) e^{-j\beta x} \end{array}\right\}, \quad for \quad 0 \le z_1 < d_1,\ \sum_{i=1}^{i=p-1} d_i \le z < \sum_{i=1}^{i=p} d_i \\ C_{N+1}^{+} e^{-\gamma_{N+1} z_{N+1}} e^{-j\beta x}, \quad for \quad x \ge \sum_{i=1}^{i=N} d_i \end{cases}$$

(2.35a)

and,

$$H_{x,i} = \begin{cases} C_0^- \left(-j \dfrac{\gamma_0}{\omega \mu_{x,0}} \right) e^{\gamma_0 z_0} e^{-j\beta x}, \quad for\ z_0 < 0 \\ \left. \begin{array}{l} C_i^+ \left[-j \dfrac{\gamma_i}{\omega \mu_{x,i}} \left(-e^{-\gamma_i z_i} + c_i X_i e^{\gamma_i (z_i - d_i)} \right) \right] e^{-j\beta x} \\ or\ C_i^- \left[-j \dfrac{\gamma_i}{\omega \mu_{z,i}} \left(e^{\gamma_i (z_i - d_i)} - s_i X_i e^{-\gamma_i z_i} \right) \right] e^{-j\beta x} \end{array} \right\}, \quad for\ 0 \le z_1 < d_1,\ \sum_{ii=1}^{ii=i-1} d_{ii} \le z_i < \sum_{i=1}^{ii=i} d_{ii} \\ C_{N+1}^+ \left(j \dfrac{\gamma_{N+1}}{\omega \mu_0 \mu_x} \right) e^{-\gamma_{N+1} z_{N+1}} e^{-j\beta x}, \quad for\ z_{N+1} \ge \sum_{ii=1}^{ii=N} d_{ii} \end{cases}$$

(2.35b)

The fields are written as a function of the magnitude reflection coefficients, $c_i \equiv C_i^- / C_i^+ X_i$ at the upper interface, and $s_i \equiv C_i^+ / C_i^- X_i$ at the lower interface, where $X_i = e^{-\gamma_i d_i}$. d_i and n_i are the thickness and the refractive index of each layer. μ_i is the relative permeability of each interface. γ_i ($\gamma_i^2 = \beta^2 - k_0^2 n_i^2$) is the transverse propagation constant within each layer.

At the i^{th}-layer, matching the tangential fields (Φ) at the lower interface, $\Phi_{i-1}(d_{i-1}) = \Phi_i(0)$, and at the upper interface, $\Phi_i(d_i) = \Phi_{i+1}(0)$, the amplitude reflection coefficient at the left and right interfaces (s_i and c_i) are

$$s_i = \frac{\gamma_i / \mu_{x,i} - \gamma_{i-1}^s / \mu_{x,i-1}}{\gamma_i / \mu_{x,i} + \gamma_{p-1}^s / \mu_{x,i-1}} \qquad , \qquad \gamma_{i-1}^s = \gamma_{i-1} \frac{\left(1 - s_{i-1} X_{i-1}^2\right)}{\left(1 + s_{i-1} X_{i-1}^2\right)} \tag{2.36}$$

and,

$$c_i = \frac{\gamma_i / \mu_{x,i} - \gamma_{i+1}^c / \mu_{x,i+1}}{\gamma_i / \mu_{x,i} + \gamma_{i+1}^c / \mu_{x,i+1}} \quad , \quad \gamma_{i+1}^c = \gamma_{i+1} \frac{\left(1 - c_{i+1} X_{i+1}^2\right)}{\left(1 + c_{i+1} X_{i+1}^2\right)} \tag{2.37}$$

Since there is no upward wave in the substrate ($C_0^+ = 0$ and $s_0 = 0$), s_p is successively calculated from s_0 to s_{p-1}. Meanwhile, there is no downward wave in the cover ($C_{N+1}^- = 0$ and $c_{N+1} = 0$), c_p is consecutively calculated from c_{N+1} to c_{p+1}. At the calculated guiding layer,-*p*, $\gamma_p = j\sqrt{k_0^2 n_p^2 - \beta^2} = j\kappa_p$. Therefore, the amplitude reflection coefficients at the guiding interfaces are

$$s_p = \frac{j\kappa_p / \mu_{x,p} - \gamma_{p-1}^s / \mu_{x,p-1}}{j\kappa_p / \mu_{x,p} + \gamma_{p-1}^s / \mu_{x,p-1}} = e^{-j2\phi_{s,TE}},$$

and

$$c_p = \frac{j\kappa_p / \mu_{x,p} - \gamma_{p+1}^c / \mu_{x,p+1}}{j\kappa_p / \mu_{x,p} + \gamma_{p+1}^c / \mu_{x,p+1}} = e^{-j2\phi_{c,TE}} \tag{2.38}$$

where, the phase shift due to the total internal reflection at the film-composite substrate and film-composite cover interfaces are

$$\phi_{s,TE} = \tan^{-1}\left(\frac{\kappa_p / \mu_{x,p}}{\gamma_{p-1}^s / \mu_{x,p-1}}\right) \quad \text{,and} \quad \phi_{c,TE} = \tan^{-1}\left(\frac{\kappa_p / \mu_{x,p}}{\gamma_{p+1}^c / \mu_{x,p+1}}\right) \tag{2.39}$$

For the TM-guided modes, the formulations are similar to the TE case. After applying the boundary conditions, the amplitude reflection coefficient s_i and c_i are

$$s_i = \frac{\dfrac{\gamma_i}{\varepsilon_{x,i}} - \dfrac{\gamma_{i-1}^s}{\varepsilon_{x,i-1}}}{\dfrac{\gamma_i}{\varepsilon_{x,i}} + \dfrac{\gamma_{i-1}^s}{\varepsilon_{x,i-1}}} \qquad , \qquad \gamma_{i-1}^s = \gamma_{i-1}\frac{\left(1 - s_{i-1}X_{i-1}^2\right)}{\left(1 + s_{i-1}X_{i-1}^2\right)} \tag{2.40}$$

and,

$$c_i = \frac{\dfrac{\gamma_i}{\varepsilon_{x,i}} - \dfrac{\gamma_{i+1}^c}{\varepsilon_{x,i+1}}}{\dfrac{\gamma_i}{\varepsilon_{x,i}} + \dfrac{\gamma_{i+1}^c}{\varepsilon_{x,i+1}}} \qquad , \qquad \gamma_{i+1}^c = \gamma_{i+1}\frac{\left(1 - c_{i+1}X_{i+1}^2\right)}{\left(1 + c_{i+1}X_{i+1}^2\right)} \tag{2.41}$$

Therefore, the amplitude reflection coefficients at the guiding interfaces are

$$s_p = \frac{j\kappa_p \Big/ \varepsilon_{x,p} - \gamma_{p-1}^s \Big/ \varepsilon_{x,p-1}}{j\kappa_p \Big/ \varepsilon_{x,p} + \gamma_{p-1}^s \Big/ \varepsilon_{x,p-1}} = e^{-j2\phi_{s,TM}} ,$$

and

$$c_p = \frac{j\kappa_p \Big/ \varepsilon_{x,p} - \gamma_{p+1}^c \Big/ \varepsilon_{x,p+1}}{j\kappa_p \Big/ \varepsilon_{x,p} + \gamma_{p-1}^c \Big/ \varepsilon_{x,p+1}} = e^{-j2\phi_{c,TM}} \tag{2.42}$$

The phase shifts, due to the total internal reflection at the lower and upper interfaces, are

$$\phi_{s,TM} = \tan^{-1}\left(\frac{\kappa_p / \varepsilon_{x,p}}{\gamma^s_{p-1} / \varepsilon_{x,p}}\right) \quad \text{,and} \quad \phi_{c,TM} = \tan^{-1}\left(\frac{\kappa_p / \varepsilon_{x,p}}{\gamma^c_{p+1} / \varepsilon_{x,p+1}}\right) \tag{2.43}$$

where, ε_i is the relative permittivity of each interface.

2.2.2 Field distribution

To determine the field distribution of the guided mode (*m*), it is necessary to define the initial magnitude coefficients, either C_p^+ or C_p^-, of the field inside the calculated guiding layer,-*p*. Based on these values, the field magnitude coefficients $C_i^{+/-}$ of the other layers are consecutively estimated by applying the proper boundary conditions as mentioned earlier.

Therefore, the field coefficients of the layers above the guiding layer, $i = p+1,..., N$, are written as

$$C_{i+i}^+ = C_i^+ \frac{X_i\left(1+c_i\right)}{\left(1+c_{i+1}X_{i+1}^2\right)} \tag{2.44}$$

And those of the layers beneath the guiding layer, $i = 0,..., p-1$, are written as

$$C_{i-i}^- = C_i^- \frac{X_i\left(1+s_i\right)}{\left(1+s_{i-1}X_{i-1}^2\right)} \tag{2.45}$$

The plots in Figure 2.7 show the field distribution of the fundamental mode in multilayer slab waveguide with single (Figure 2.7a) and multiple (Figure 2.7b) high index layers using this approach.

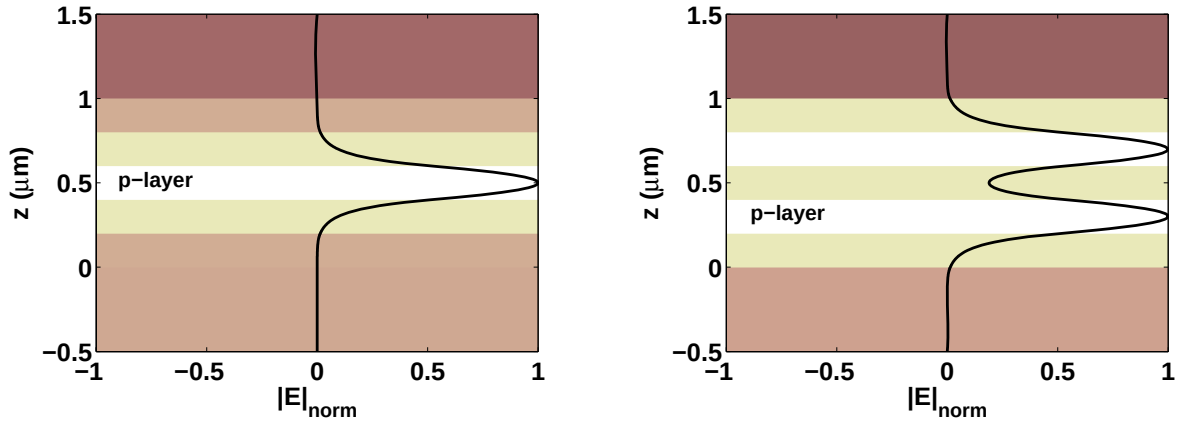

Figure 2.7: Field distribution of fundamental mode in a multilayer slab waveguide with (a) single (b) two-layer of high index

In general, dielectric slab waveguides with uniform dielectric layers confine the guided mode in the higher index layer(s). Introducing non-uniformity in the guiding region or in the surrounding layers would cause light to leak outside the structure and hence reduce its confinement. This effect will be briefly illustrated in the following section.

2.3 Dielectric grating-waveguide structures

Slab waveguides comprised of corrugated surface, as illustrated in Figure 2.8a, or with inhomogeneous waveguide in Figure.2.8b, are referred to as *"grating-waveguide structures."* Due the presence of the modulated surface or permittivity the guided mode in these structures is scattered outside by the grating. Hence the mode is not perfectly bound as it was for the slab waveguide in Section 2.2. This type of mode is called *"a leaky mode."* The power confined in

the guiding region is slowly reduced along the direction of propagation. The leaky mode, as a result, has a complex propagation constant, $\beta = \beta' - j\beta''$, where the imaginary term(β'') indicates the leakage, and hence $1/\beta''$ defined as the distance which the leaky mode propagates in the structure before being completely scattered outside. Hence it indicates the minimum size of the GMR structure, will be discussed in Chapter 3, required to achieve total reflection at resonances.

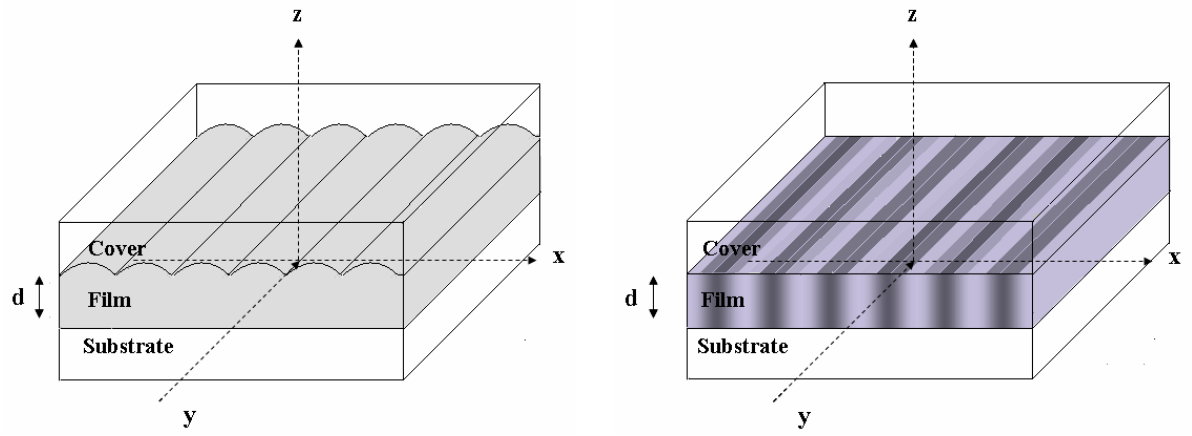

(a) (b)

Figure 2.8: Configurations of (a) the corrugated slab waveguide (b) the grating waveguide

Solving the leaky modes in this type of structure requires including the scattering by the grating in the calculations. Forming a characteristic equation as in Section 2.2 is not sufficient. Hence, two calculation approaches are presented here: scattering matrix approach [10-12, 69] and the Bloch mode approach [61-62.]

2.3.1 Scattering matrix approach

The formulations are based on applying the boundary conditions at each layer interface as it is the case in Section 2.2. In spite of forming the characteristic equations, the formulations group the matching of the tangential fields from the first (*0/1*) to the last (*N/N+1*) interfaces in a form of a scattering matrix $[S]$[69.] For the N-layer structure depicted in Figure 2.6, the field equation is written as

$$\begin{bmatrix} C_0^- \\ C_{N+1}^+ \end{bmatrix} = [S(\beta)] \begin{bmatrix} C_{N+1}^- \\ C_0^+ \end{bmatrix} \quad \rightarrow \quad [S(\beta)]^{-1} \begin{bmatrix} C_0^- \\ C_{N+1}^+ \end{bmatrix} = \begin{bmatrix} C_{N+1}^- \\ C_0^+ \end{bmatrix} \tag{2.46}$$

Without an external excitation from the substrate nor the cover ($\begin{bmatrix} C_{N+1}^- \\ C_0^+ \end{bmatrix} = 0$), non-zero solutions, which indicate the presence of modes, can exist if

$$\left| S^{-1}(\beta) \right| = 0 \tag{2.47}$$

In equation (2.46), C^+ and C^- are the amplitude coefficients of the forward and backward propagations along each layer, where subscript *-0* and *-N+1* represent the substrate and cover, respectively. $\left| S^{-1} \right|$ denotes the determinant of the inverse of the S-matrix.

For the grating-waveguide structures, the fields within the structure are scattered due to the perturbation by the grating. To form the S-matrix, the scattering fields along each layer are initially determined by solving the coupled-wave equations (2.14) to (2.19) in Section 2.1.3. For the homogenous layer, the Eigen vector matrix $[W]$ is the identity matrix and each element of the

Eigen value matrix $\left[q_{pq}^2\right]$ is $n_h^2 - k_{\tan,pq}^2 / k_0^2$, where n_h is the refractive index of the homogeneous layer.

Then, proper boundary conditions are applied at each interface. For the interface of layers –*a* and -*b*, the S-matrix [69] is written as

$$\begin{bmatrix} C_a^- \\ C_b^+ \end{bmatrix} = [S_{ab}] \begin{bmatrix} C_b^- \\ C_a^+ \end{bmatrix} \quad \rightarrow \quad [S_{ab}] = \begin{bmatrix} A_{ab} & B_{ab} \\ C_{ab} & D_{ab} \end{bmatrix}$$

$$\begin{aligned} A_{ab} &= \left[\left(V_b^{-1}V_a + W_b^{-1}W_a\right)^{-1}\left(2X_b\right)\right] \\ B_{ab} &= \left[\left(V_b^{-1}V_a + W_b^{-1}W_a\right)^{-1}\left(V_b^{-1}V_a X_a - W_b^{-1}W_a X_a\right)\right] \\ C_{ab} &= \left[\left(V_a^{-1}V_b + W_a^{-1}W_b\right)^{-1}\left(V_a^{-1}V_b X_b - W_a^{-1}W_b X_b\right)\right] \\ D_{ab} &= \left[\left(V_a^{-1}V_b + W_a^{-1}W_b\right)^{-1}\left(2X_a\right)\right] \end{aligned} \tag{2.48}$$

Where, the matrices $[W]$, $[V]$, and $[X]$ have been defined in Section 2.1.3.

The S-matrix of the entire structure (covering from first to final interfaces) is the (*) product of all sub-S matrices.

$$[S] = [S_{0,1}] * [S_{1,2}] * \ldots * [S_{N,N+1}] \tag{2.49}$$

Where the (*) is referred as the S-matrix multiplication defined as

$$[S] = [S_{ab}] * [S_{bc}] = \begin{bmatrix} A & B \\ C & D \end{bmatrix}$$

$$\begin{aligned} A &= \left\{\left(A_{ab}A_{bc}\right) - \left(A_{ab}B_{bc}\right)\left(C_{ab}B_{bc} - I\right)^{-1}\left(C_{ab}A_{bc}\right)\right\} \\ B &= \left\{\left(B_{ab}\right) - \left(A_{ab}B_{bc}\right)\left(C_{ab}B_{bc} - I\right)^{-1}\left(D_{ab}\right)\right\} \\ C &= \left\{\left(C_{bc}\right) - \left(D_{bc}C_{ab}\right)\left(B_{bc}C_{ab} - I\right)^{-1}\left(A_{bc}\right)\right\} \\ D &= \left\{\left(D_{bc}D_{ab}\right) - \left(D_{bc}C_{ab}\right)\left(B_{bc}C_{ab} - I\right)^{-1}\left(B_{bc}D_{ab}\right)\right\} \end{aligned} \tag{2.50}$$

Here I is a unity matrix with dimensions $2M \times 2M$ (M is the total number of harmonics).

Since the structure is periodic, the solutions are applied via the tangential wave vectors as defined by grating equations. For a 1-D grating case, the complex solutions can be written as[7]

$$\beta_p = \left(\beta' - p \frac{2\pi}{\Lambda} \right) - j\beta'' \tag{2.51}$$

β' and β'' are the real and imaginary terms of the propagation constant of the leaky mode. Λ is the grating period.

Achieving the complex solutions in this approach requires smart root finding computation, otherwise it is a time consuming procedure. Besides, the numerical instability exists due to the inverse S-matrix operation. These drawbacks can be avoided when using the Bloch mode approach.

2.3.2 Bloch mode approach

In this approach, the actual propagation constants of the guided or leaky mode are calculated via the Bloch mode (periodic mode) formulations [61-62.] An artificial periodicity is formed in the direction of the mode confinement as depicted in Figure 2.9a. The interaction between the modes from these adjacent waveguides is eliminated by inserting a perfect matched layer (PML) [70] between them.

Using the plane wave expansion as it is the case for RCWA, the Eigen modes (Bloch modes) are determined. Within the propagation length Λ_x, only the modes with null imaginary part of propagation constant are guided.

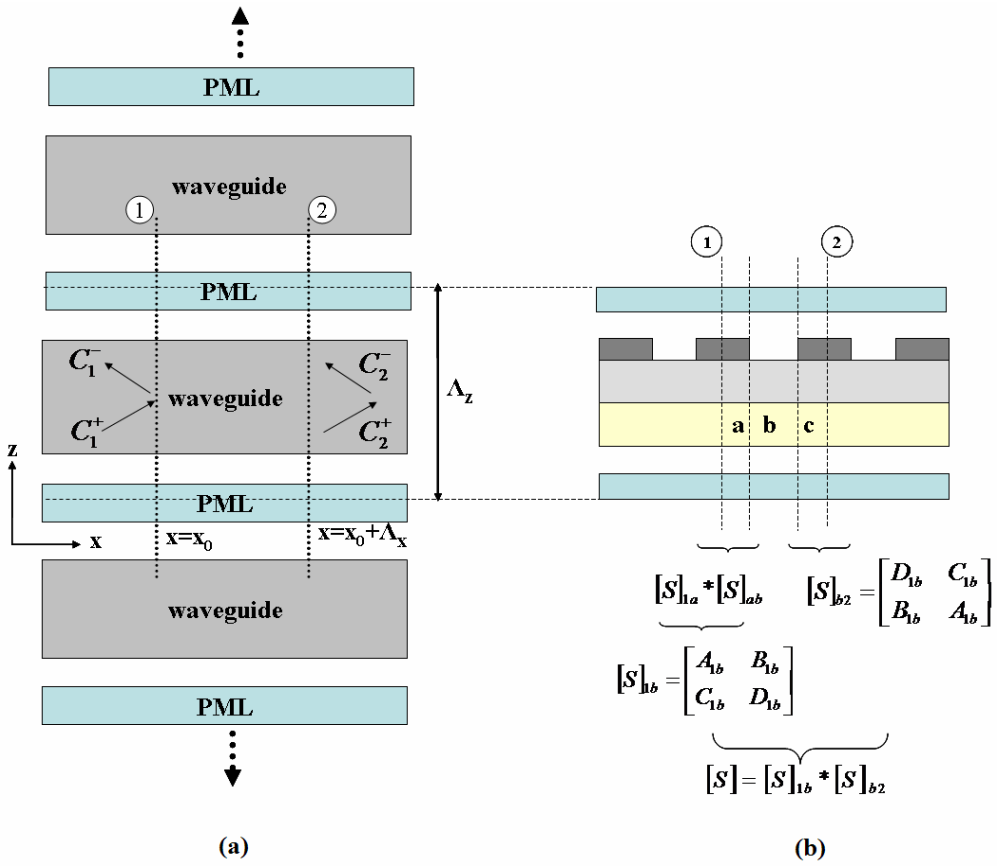

Figure 2.9: (a) an artificial periodicity used in Bloch mode approach (b) a unit-cell computation of the grating-waveguide structure.

The guided mode formulations start with forming a scattering matrix along the propagation length, interface 1 and 2 in Figure 2.9a, where modes at each interface experiences the same medium. For the grating-waveguide structure, the computation takes place along a symmetric unit cell as illustrated in Figure 2.9b. That reduces the S–matrix multiplication by a factor $\frac{N}{2}-1$, where N is the total number of interfaces in the unit cell. The S-matrix is written as

$$\begin{bmatrix} C_1^- \\ C_2^+ \end{bmatrix} = \begin{bmatrix} S_1 & S_2 \\ S_3 & S_4 \end{bmatrix} \begin{bmatrix} C_2^- \\ C_1^+ \end{bmatrix} \tag{2.52}$$

Since each mode propagates for a distance Λ_x, each one of them will accumulate a phase of $\beta \Lambda_x$. Here, β is the propagation constant of each mode. Therefore, the scattering matrix in Eq.(2.52) is rearranged as follows

$$\begin{bmatrix} I & -S_2 \\ 0 & S_4 \end{bmatrix} \begin{bmatrix} C_1^- \\ C_1^+ \end{bmatrix} = \mu \begin{bmatrix} S_1 & 0 \\ -S_3 & I \end{bmatrix} \begin{bmatrix} C_1^- \\ C_1^+ \end{bmatrix} \tag{2.53}$$

where $\mu = e^{-j\beta\Lambda_x}$. The propagation constant of each Bloch mode is then calculated from the Eigen values (μ). In general, the propagation constant is considered to be complex ($\beta = \beta' + j\beta''$). Hence, $\mathrm{Im}\{\beta\}$ is directly determined by the magnitude of the Eigen value and $\mathrm{Re}\{\beta\}$ is calculated from the phase of the Eigen values (ϕ).

$$\beta'' = \frac{\ln|\mu|}{\Lambda_x}, \quad \text{and} \quad \beta' = \begin{cases} \dfrac{\phi + 2\pi}{\Lambda_x}, & \textit{forward propagation modes} \\ \dfrac{\phi - 2\pi}{\Lambda_x}, & \textit{backward propagation modes} \end{cases} \tag{2.54}$$

Finally, the guided modes are the ones which have the real part of the propagation constants, (β'), within the cut off range ($\max[k_0 n_{\text{superstrate}}, k_0 n_{\text{substrate}}] < |\beta'| < k_0 n_{\text{high index film}}$). A mode with null imaginary part (β'') is a bound mode. Otherwise it is a leaky mode.

Using this approach, the exact propagation constants of both guided and leaky modes can be accurately determined with no numerical instability. This approach is utilized in this

dissertation to determine the complex propagation constant of the leaky modes in the grating-waveguide structures which will be analyzed in this dissertation.

CHAPTER 3 : RESONANT ANOMALY IN GUIDED MODE RESONANT (GMR) STRUCTURES

As mentioned earlier in Chapter 1, guided mode resonant (GMR) structures produce a very narrowband resonance as a consequence of phase matching between diffracted waves and slowly leaky modes. The structures suit for a narrowband spectral filtering applications. In this chapter, the structure geometry and the resonance mechanism are presented and investigated mainly in a one-dimensional GMR structure. That constructs the main concept of achieving and controlling the desired resonance responses. An approximated computation, homogeneous waveguide approach (HWA,) is developed and used to relate resonances to the waveguide modes. That leads to a better understanding of the coupling configurations. The design techniques to improve the resonance performances (symmetric spectral response with low base-line and narrow linewidth, large angular tolerance, and the polarization independence) are presented and discussed for the specific use.

3.1 Principle of resonance anomaly in GMR

Guided mode resonant (GMR) structures are optical devices that consist of a planar waveguide with a periodic structure. In general, GMR structures are categorized into three configurations as depicted in Figure 3.1 for the grating imbedded in, on the surface and on both surface and substrate side of the structure. Like the structure mentioned in Section 2.3, the waveguide modes existing in the GMR structure are not perfectly bounded due to the scattering by the grating. The

amount of energy leaked out from the structure is proportional to the grating coupling strength. Hence, the mode has complex propagation constant.

$$\beta = \beta' - j\beta'' \tag{3.1}$$

The leaky modes are mainly guided in the inhomogeneous layer for the first geometry in Figure 3.1a. For the other two geometries (Figure 3.1and 3.1b), the leaky modes are guided in the homogeneous high index layer.

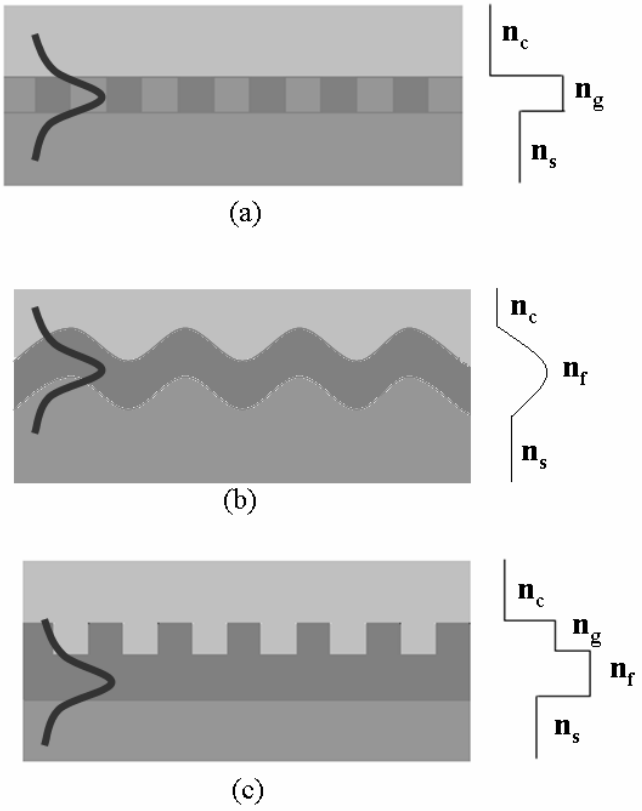

Figure 3.1: Configurations of GMR devices (a) refractive index modulated waveguide (b) surface-relief grating coupler (c) coated dielectric grating

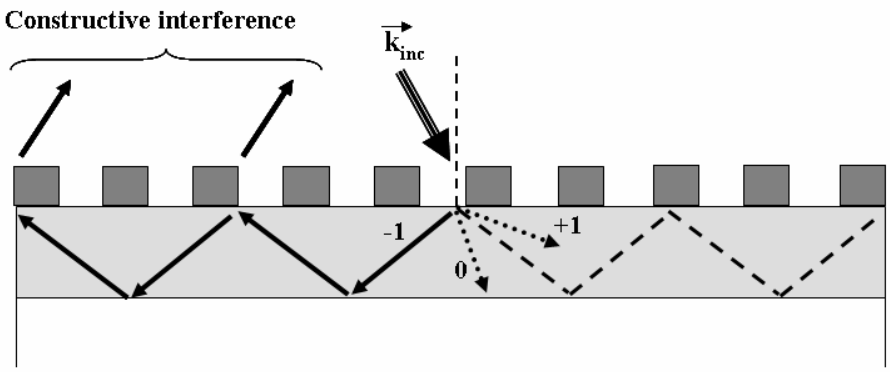

Figure 3.2: The configurations of phase matching conditions in the GMR structure at resonance

To achieve a 100% reflection at resonance, the grating has to be in the subwavelength scale and diffracts only first-order waves inside the guiding region, not outside the structure. Therefore, at resonance, the diffracted waves are phase matched to the waveguide mode. The leaking fields in the incident region hence constructively interfere and the incident beam is totally reflected. The phase matching condition at resonance is depicted by the ray model in Figure 3.2 when -1 diffracted wave is phase matched to the waveguide mode.

In general, the phase matching condition between the first-order diffracted waves and the waveguide modes at resonance can be approximately written as

$$\beta' \approx k_{diff,1^{st}} \tag{3.2}$$

where $k_{diff,1^{st}}$ is the tangential wave vector of the first-order diffracted waves which are defined by the grating vectors and the direction of the incident beam as discussed in Section 2.1.

The resonance location can be directly predicted if the modal propagation constant (β') is known from the grating equations (2.2) for a 1-D grating structure and Eqs. (2.7)-(2.8) for a 2-

D grating structure. The imaginary part of the modal propagation constant (β'') represents the leakage of the waveguide mode. This does not only determine the propagation length of the modes but the resonance linewidths as well. The connection of β'' and the resonance linewidths ($\Delta\lambda_{FWHM}$ and $\Delta\theta_{FWHM}$) can be determined by using an approximate Lorentzian expression of the reflectivity [10, 17], while maintaining the resonance as a complex pole. The reflectivity is then written as

$$R = \frac{|c|^2}{\left[k_{inc,\tan} - \left(2\pi/\Lambda_a - \beta'\right)\right]^2 + \left[\beta''\right]^2}. \tag{3.3}$$

where *c* is an arbitrary constant. The angular linewidth can be directly formulated from Eq. (3.3) as

$$\Delta\theta_{FWHM} \approx \frac{2\beta''}{k_0 n_{inc}\cos\theta_0}. \tag{3.4}$$

θ_0 is the direction of the incident beam at resonance.

To determine the spectral linewidth, the reflectivity in equation (3.3) is written as a function of the wavelength [17.]

$$R = \frac{|c|^2\left(\Lambda_a\lambda_0/2\pi\right)^2}{\left[\lambda - \Lambda_a\left(\sin\theta_0 - n'\right)\right]^2 + \left[\Lambda_a n''\right]^2}. \tag{3.5}$$

where λ_0 is the resonant wavelength. n' and n'' are the real part and imaginary part of the complex modal index at the resonant wavelength. Then, the spectral linewidth is defined as the following.

$$\Delta\lambda_{FWHM} \approx \beta'' \frac{\lambda_0 \Lambda_a}{\pi}, \tag{3.6}$$

The resonance linewidths in Eq. (3.4) and (3.6) may not be accurate when the resonance lineshape is not Lorentzian, especially when coping with the multiple resonant modes. For this case, the resonance responses depend on the coupling characteristics. That will be investigated in the next sections for the 1-D GMR and in Chapter 4 for the 2-D GMR. The resonance responses however are exactly determined using the RCWA calculations as discussed in Section 2.1

Avoiding the involved computations of the complex propagation constant, the waveguide mode (TE_m, or TM_m) propagation constant can be determined using the homogeneous waveguide approach (HWA) [21.] As this approach does not include the scattering by the grating, only the real part of the propagation constant is determined which give a very good approximation for the location of resonances. Considering the GMR structure as the homogeneous slab waveguide in Figure 3.3 where the grating, both 1-D and 2-D cases, is replaced by a homogeneous film with an effective refractive index (n_g). The accuracy of the approach then increases by determining the grating effective index using the RCWA. The error is significant when dealing with the grating with the strong coupling strength.

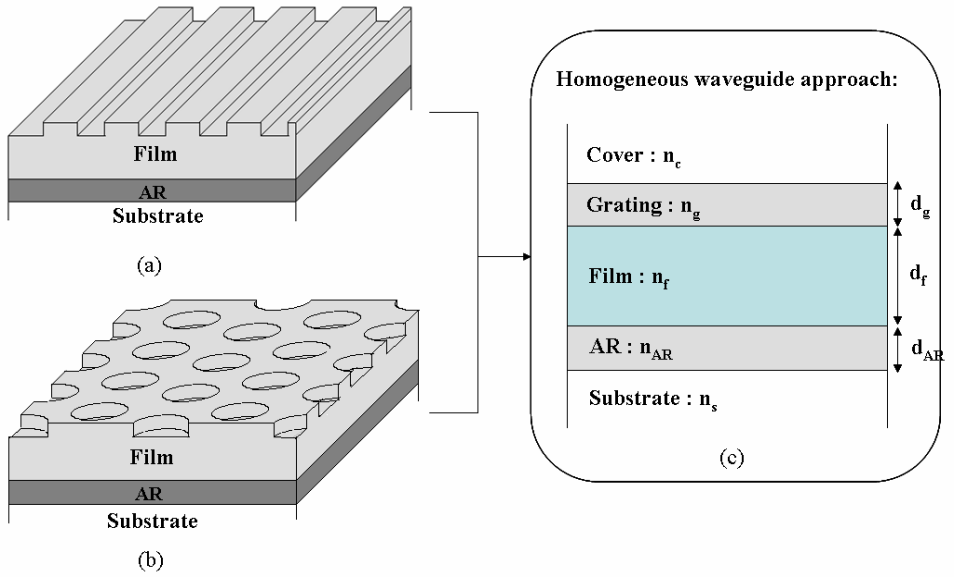

Figure 3.3: The configurations of (a) 1-D GMR, (b) 2-D GMR, (c) GMR structure considered as multilayer waveguide when applying the HWA

The mode solving method applies the formulations in Section 2.2. The phase, $2\phi_s$, accumulated by the total reflection at film-composite substrate interface in Section 2.2 can be simplified as follows

$$\phi_s = \tan^{-1}\left(A \frac{\kappa}{\gamma_{AR}^s} \right), \qquad \gamma_{AR}^s = \gamma_{AR}\left(\frac{1 - s_{AR} e^{-2\gamma_{AR} d_{AR}}}{1 + s_{AR} e^{-2\gamma_{AR} d_{AR}}} \right), \text{ and } \qquad s_{AR} = \frac{A_s \gamma_{AR} - \gamma_s}{A_s \gamma_{AR} + \gamma_s}. \quad (3.7)$$

The total reflection phase $2\phi_c$ at the film-composite cover interface is written as follow:

$$\phi_c = \tan^{-1}\left(B \frac{\kappa}{\gamma_g^c} \right), \qquad \gamma_g^c = \gamma_g\left(\frac{1 - c_g e^{-2\gamma_g d_g}}{1 + c_g e^{-2\gamma_g d_g}} \right), \text{ and } \qquad c_g = \frac{B_c \gamma_g - \gamma_c}{B_c \gamma_g + \gamma_c}. \quad (3.8)$$

The coefficients in Eq. (3.7) and (3.8) are defined for TE modes as $A = A_s = 1$, and $B = B_c = 1$. For the TM modes, $A = \varepsilon_{AR}/\varepsilon_f$, $A_s = \varepsilon_s/\varepsilon_{AR}$, $B = \varepsilon_g/\varepsilon_f$, and $B_c = \varepsilon_c/\varepsilon_g$. For the subscripts -*AR*, -*s*, -*f*, and -*g* represent the anti-reflection (AR) film, the substrate, the guiding layer, and the grating, respectively. The rest of the parameters have been designated in Section 2.2.

Due to the simple and fast computations, the HWA is used in this dissertation to estimate the location of resonances and obtain a very good estimation of the structure parameters. The RCWA is then used to refine the structure parameters and to determine the spectral and angular responses of the resonance.

In next sections, the discussion focuses on the resonances in 1-D GMR structure. Based on the coupling characteristics, the resonance modes are classified and investigated using the HWA and the RCWA. Later, the phase configurations of each resonance modes type at on- and off- resonance are discussed and related to the resonance responses.

3.2 Resonances in 1-D GMR

For 1-D GMR structure, the first-order diffraction is limited along two waves (±1) propagating within a common plane at in-plane mounting (Figure 2.2a) or separated planes at conical mounting (Figure 2.2b/c). Satisfying the resonant condition, the grating period must meet three requirements. First, there is no diffracted order outside the structure; second, an incident beam diffracts only first order waves in the guiding region which refractive index n_f and finally, the first order waves is above the cut-off range of the waveguide mode. Therefore, the minimum and maximum limits of the grating period (Λ_a) are written as follow:

$$\Lambda_{a,\min} = \frac{\lambda_0}{\sqrt{n_s^2 + \left[n_{inc} \sin\theta_{inc} \sin\varphi_{inc}\right]^2} + n_{inc} \sin\theta_{inc} \cos\varphi_{inc}},$$

and

$$\Lambda_{a,\max} = \frac{\lambda_0}{\sqrt{n_f^2 + \left[n_{inc} \sin\theta_{inc} \sin\varphi_{inc}\right]^2} + n_{inc} \sin\theta_{inc} \cos\varphi_{inc}}. \quad (3.9)$$

Where n_f and n_s are the refractive indices of the film and the substrate, and λ_0 is the resonance wavelength.

Hence, the resonant modes in 1-D GMR structure are classified into three categories when resonance is a contribution of a single-diffracted order resonant mode (Figure 3.4a), two-diffracted order resonant mode in a common plane (Figure 3.4b at normal incidence and Figure 3.4c at oblique incidence), and two-diffracted order resonant mode in the separated planes (Figure 3.4d).

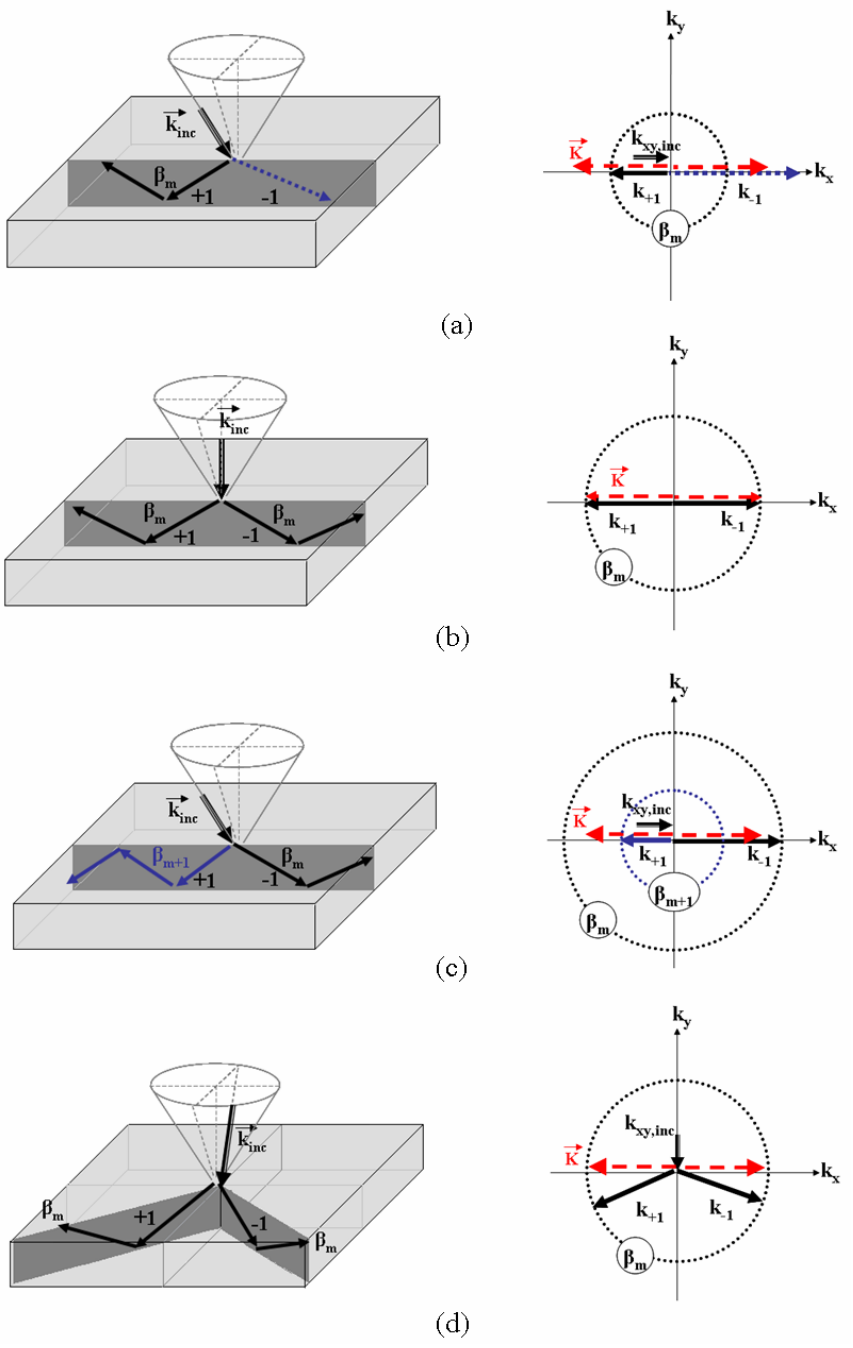

Figure 3.4: Diffraction/guidance planes and phase matching diagrams of the resonant modes in 1-D GMR at in-plane mounting (a) single-propagation (b)/(c) counter-propagation and (d) two resonant modes at conical mounting.

Using the HWA approach, structure dimensions needed to achieve each type of these resonances are estimated. The exact resonance responses are then determined by the RCWA. As an illustration, resonances due to the phase matching condition of +1 and -1 diffracted waves to the waveguide modes are calculated and plotted versus the film thickness (t_f) in Figure 3.5a. The calculations are considered at the in-plane oblique incidence $(\theta_{inc}, \varphi_{inc}) = (10^\circ, 0^\circ)$ for a resonance wavelength $\lambda_0 \approx 0.98 \mu m$. The structure has a film which refractive index 2 deposited on a substrate which refractive index 1.47. The 1-D binary grating with a fill factor of 0.5 and 0.1-μm depth is directly fabricated on the film. The grating period calculated from Eq. (3.9) is limited within the range of $0.45 \le \Lambda_a \le 0.59 \mu m$. Here, the grating period is selected to be $0.55 \mu m$ and hence the resonant spectral range of interest is $0.95 \le \lambda \le 1.15 \mu m$.

As shown, the resonances of a single-propagation mode by +1 diffracted wave are located at two different wavelengths for the phase matching of TM_0 and TE_0 waveguide modes. They are individually excited when the incident beam is TM and TE polarized, respectively. That can be seen in the resonance responses in Figure 3.5b, where the structure (t_f=0.25 μm) supports only fundamental modes. The resonances shift towards longer wavelengths when increasing the film thickness. For the multimode structure, the +1-diffracted wave is also phase matched to the higher order modes and it introduces the resonances located at the shorter wavelengths. The resonance responses plotted in Figure 3.5c show the resonances relating to the waveguide modes for the cases of TM (solid lines) and TE (dash lines) incident beams.

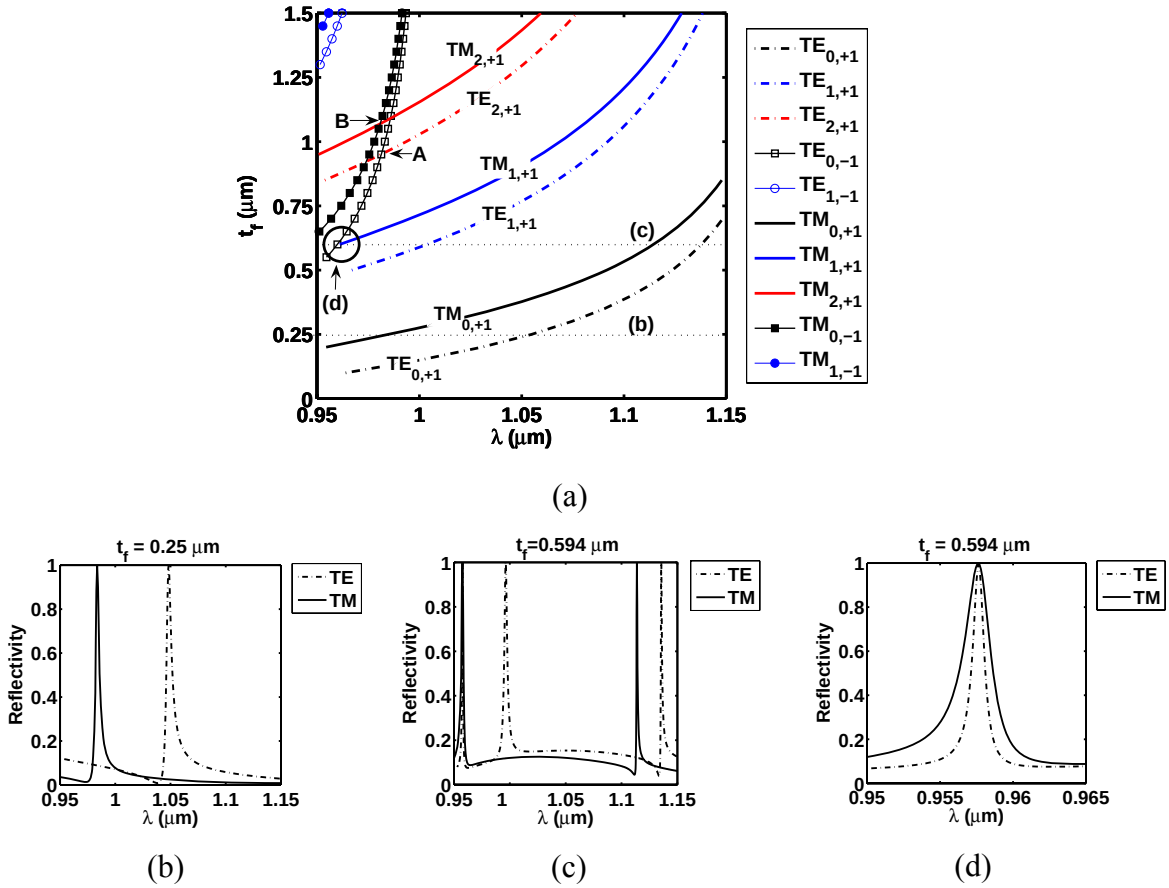

Figure 3.5: (a) Plot of resonances (calculated by the HWA) versus the film thickness (t_f), and the spectral responses (calculated by the RCWA) of resonances in1-D GMR (b) t_f=0.25 μm (c)/(d) t_f=0.594 μm

Resonant modes by -1 diffracted wave with larger propagation constants can be formed when the film is adequately thick. In benefit of the resonance responses (will be discussed in next section), resonances by -1 diffracted wave can be located at the same wavelength as the ones by +1 diffracted wave when designing the structure properly. That can be seen in Figure 3.5a, where resonances in design A (TE mode) and B (TM mode) are for the two-diffracted order resonant modes in a common plane. For the single-diffracted order resonant mode in design (d), resonance becomes polarization independent. The resonant mode is coupled along +1 diffracted wave by

the TM polarized beam. For the TE polarized beam, the resonant mode is excited by -1 diffracted wave and it is located at the same wavelength ($\lambda_0 \sim 0.957 \mu m$). In spit the fact that the resonances of each polarization are at the same wavelength, the resonance responses plotted in Figure 3.5d do not completely overlap due to the difference in the phase matching conditions.

It has shown here that the resonance location and type can be efficiently estimated using the HWA approach. However, the coupling configurations and the field scattering have an effect on the resonance responses (resonance linewidths, resonance lineshape, the spectral side lobes and the polarization sensitivity.) The effect of the scattering field for each type of resonance modes and the design methodologies to improve the resonance responses in 1-D GMR will be discussed in the next sections.

3.3 Coupling into a single-diffracted order resonant mode in 1-D GMR

The scattering of the field within the 1-D GMR structure, when +1 diffracted wave satisfies the resonance condition at oblique incidence, is shown in Figure 3.6. In the figure, the propagating diffraction orders are presented inside the film. Only the solid arrows, representing the first-order diffracted wave (+1,) are totally reflected at the film/substrate interface and accumulate the constructive phases of the waveguide modes. As it interacts with the grating, the mode is partially leaked out from the structure and also diffracted back to the film. The existence of other scattering fields, the non-diffracted wave (0) and the -1 diffracted wave, contributes to the three sources of Fresnel reflections (R_0 at the cover/grating interface, $R_{f\,0}$ and $R_{f\,1}$ at high index film/substrate interface). These reflections deform the resonance response and cause asymmetric lineshape and high base line [21].

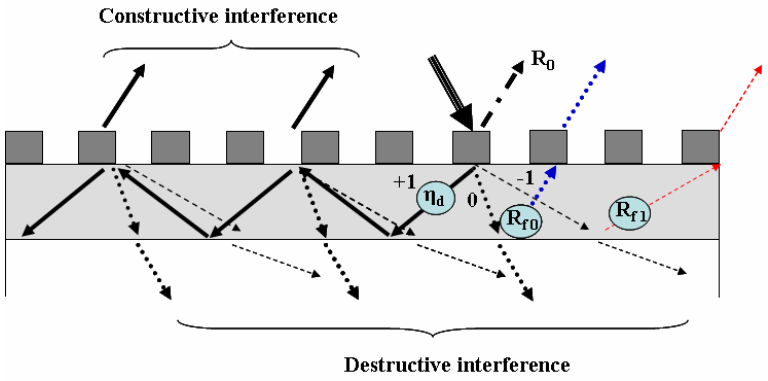

Figure 3.6: Scattering of the single-diffracted order resonant mode in 1-D GMR at oblique incidence

Without these unwanted scatterings, the leaking fields of the +1 diffracted wave are interfered and hence the reflectivity, when the 1-D GMR has an infinite size, can be written as [21]

$$R = \frac{\eta_d^2}{\eta_d^2 + 4(1-\eta_d)\sin^2\left(\frac{\phi}{2}\right)} \tag{3.10}$$

The constant η_d, referred to here as the grating strength, is defined as the normalized power that is coupled to the resonant mode and it is the leaking power at each individual round trip. ϕ is the phase gained each round-trip propagation. As seen, the reflectivity is unity at resonance or $\phi = 2m\pi$. The resonance response, on the other hand, has a phase linewidth $\Delta\phi_{FWHM} = 4\sin^{-1}\left(\eta_d / 2\sqrt{1-\eta_d}\right)$ which is directly proportional to the grating strength (η_d).

Figure 3.7 presents the resonance response of the structure for various values of η_d. The graph shows the Lorentzian resonance response having a high phase selectivity and low base line when the grating strength is small.

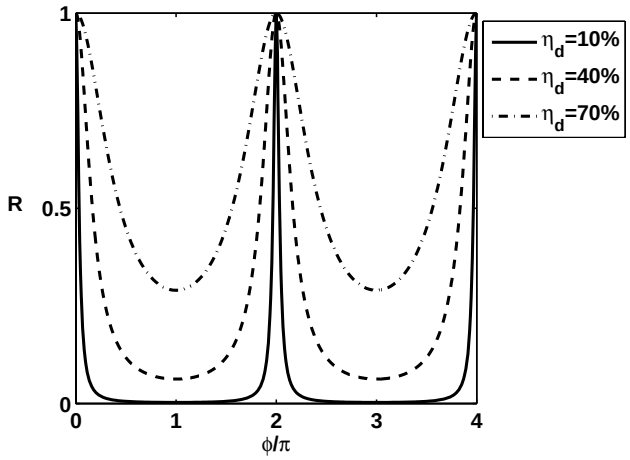

Figure 3.7: Plots of resonance response approximately calculated by Eq. (3.10)

Here, the grating strength, η_d, is the main parameter that influences both the spectrum base line and linewidth as it is the case in the Fabry Perot cavity. Therefore, the GMR structure is considered as an inverted Fabry Perot cavity [75.]

3.3.1 GMR with Lorentzian resonant response

It is desirable for GMR structure to have a symmetric spectral response, narrow resonant linewidth and low baseline reflection. This can be achieved by using the grating that produces a small η_d and a small Fresnel reflection R_0 at the cover/grating interface (Figure 3.6.). An anti-reflection film is inserted at the high index film/substrate interface to eliminate the Fresnel reflections R_{f0} and R_{f1}.

Before applying the HWA to estimate the film thickness, the grating is designed to produce the minimized coupling strength and Fresnel reflection at the resonance wavelength. The diffraction efficiencies of diffracted and non-diffracted waves by the grating are determined

while the film is considered as a half-space. As defined by the drawing in Figure 3.8, the Fresnel reflection R_0 and the grating strength η_d are the diffraction efficiencies of reflected 0^{th} wave and transmitted $+1^{st}$ wave, respectively. For the binary grating of the GMR considered earlier in Section 3.2, the R_0 and η_d are determined using the RCWA and plotted versus the change of the grating fill factor (f) and the grating depth (t_g) in Figure 3.8.

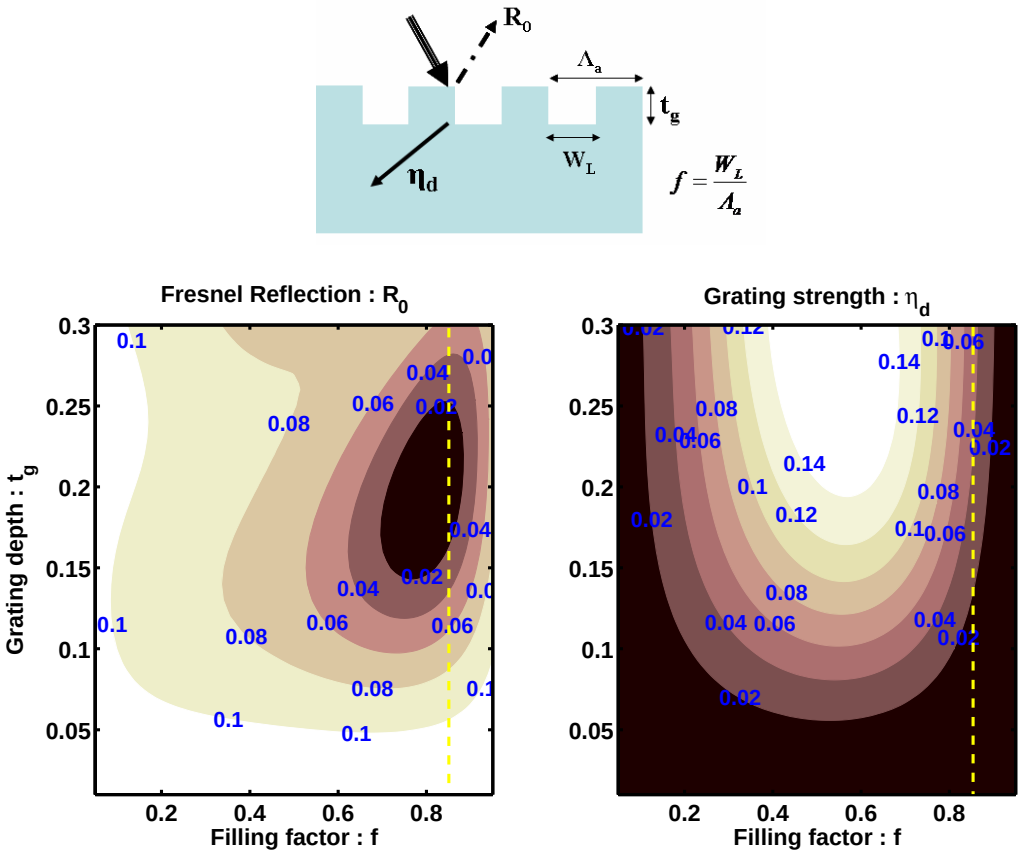

Figure 3.8: Contour plots of R_0 and η_d versus grating depth and filling factor

The contour plots show that for a filling factor between 0.8 and 0.9 (that may not be feasible to fabricate) and depth between 0.15 and 0.25 μm, the grating efficiencies are minimized (R_0< 0.02 and η_d < 0.08.) Here, the objective is to show the impact of the grating efficiencies on the

resonance responses. A 1-D GMR structures with a 0.85-filling factor grating is used in the investigation. As shown in the graph (Figure 3.9a,) the Fresnel reflection R_0 is gradually reduced when increasing the grating depth. In contrary, the grating strength becomes stronger. As a result, the resonances in the structure with shallower grating are expected to have narrower resonant linewidth, but they have the high baseline reflection. Applying three grating designs with depths A, B, and C (reported in Figure 3.9a), the structure dimensions can be estimated for each design in order to achieve the resonance due to the same TE_1 resonant mode. The spectral responses plotted in Figure 3.8b show that the spectral responses are proportional to the grating efficiencies as discussed earlier.

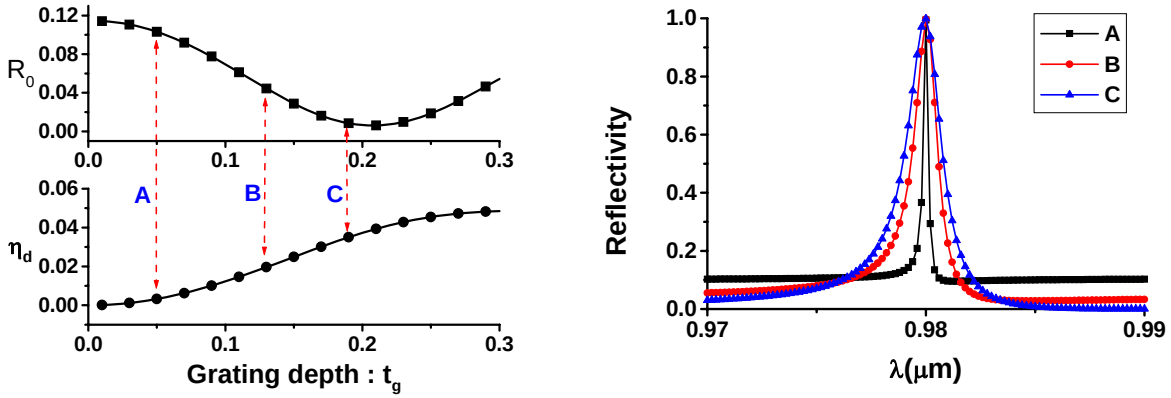

(a) (b)

Figure 3.9: (a) plots of R_0 and η_d versus grating depth when f=0.85 (b) Spectral responses of 1-D GMR with the grating A (t_g=0.05 μm, t_f= 0.532 μm), B (t_g=0.13 μm, t_f= 0.528 μm) and C (t_g=0.19 μm, t_f= 0.527μm).

A second approach to reduce the Fresnel reflection R_0 is to have the grating behaving as a multi-level AR subwavelength structure [67] as depicted in Figure 3.9a. Using the formulations based on Chebyshev polynomial [72], the effective refractive index of each grating level is determined,

and that defines the fill factor, where each grating level is a quarter-wave thick. Increasing the number of levels broadens the anti-reflection band. That allows achieving resonances with large spectral separations and negligible base-line reflection between resonances. Similar to the binary grating, removing the Fresnel reflection confronts the fact that the grating strength (η_d) increases as well as the resonances linewidth.

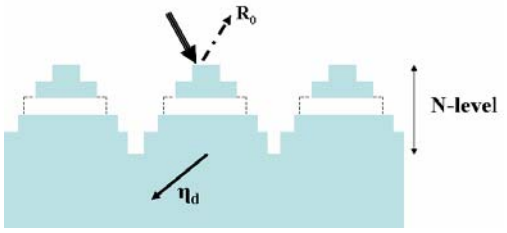

(a)

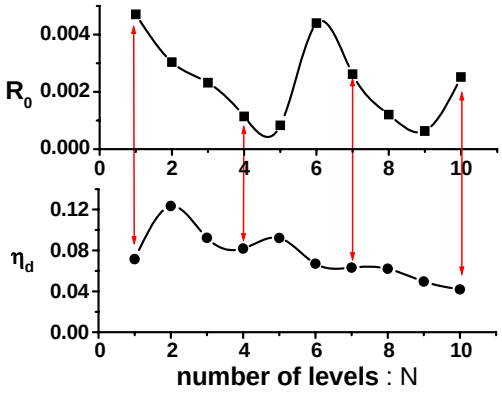

(b)

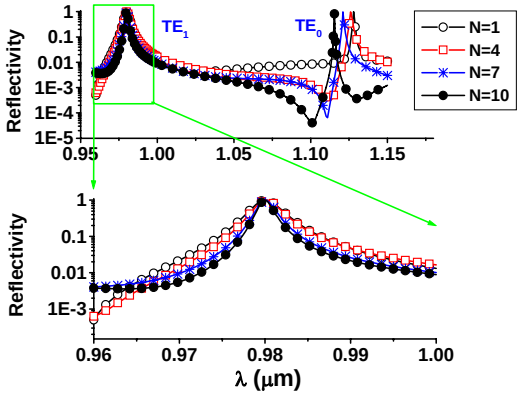

(c)

Figure 3.10: (a) Configurations of the multilevel AR grating (b) plots of R_0 and η_d versus the N-level (c) Spectral responses of 1-D GMR with the 1-, 4-, 7-, and 10-level AR grating

For the GMR using a multilevel AR grating, it appears that the effective grating strength is reduced when the number of the grating levels is increased. The Fresnel reflection however does not significantly increase. Comparing the spectral linewidths of TE_1 resonance in GMRs

with 1-, 4-, 7-, and 10-level AR grating, Figure 3.10c shows narrower and more symmetric lineshape when increasing the number of levels. In addition, the baseline reflection between resonances is also minimized due to the broader anti-reflection band as demonstrated in Figure 3.10c.

3.3.2 De-phasing manners at off-resonant wavelength and off-resonant angle

For coupling of one diffracted order into the waveguide mode, the de-phasing characteristics have observed similar behavior for the deviation of either wavelength or the incident angle.

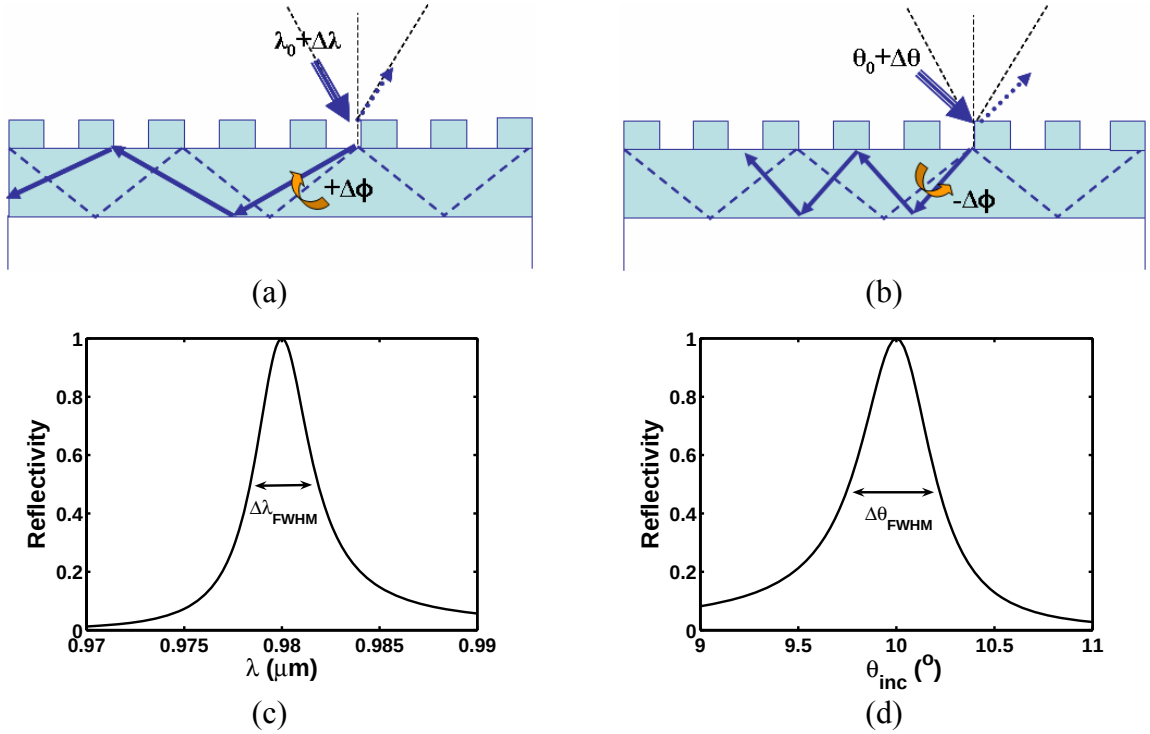

Figure 3.11: Scattering fields of a single-diffracted order resonant mode in 1-D GMR (a) at-off resonant wavelength (b) at off-resonant angle (c)/(d) spectral and angular responses

Figures 3.11a and 3.11b show that the +1 diffracted wave accumulates a de-phasing of $|\Delta\phi_{+1}|$ at both off-resonant wavelength ($\lambda_0 + \Delta\lambda$) and off-resonant angle ($\theta_0 + \Delta\theta$) but in opposite signs.

Hence, both spectral and angular responses have a Lorentzian lineshape, as plotted in Figure 3.11c and 3.11d, respectively.

The de-phasing rates ($\Delta\phi/\Delta\lambda$ and $\Delta\phi/\Delta\theta$) indicate the reduction of the reflectivity at off-resonance. Therefore, in addition to the mode leakage (β'') or the grating strength (η_d), the spectral/angular linewidths of this resonance type are directly proportional to the de-phasing rates as follows [21.]

$$\left|\frac{d\phi}{d\theta_{inc}}\right| \approx \frac{d\beta}{d\theta_{inc}}\frac{d\phi}{d\beta} \approx k_0 \cos\theta_0 \left|\frac{d\phi}{d\beta}\right|,$$

$$\left|\frac{d\phi}{d\lambda}\right| \approx \frac{k_0}{\Lambda_a}\left|\frac{d\phi}{d\beta}\right| + 2d_f\sqrt{(k_0 n_f)^2 - \beta_0^2},$$

where
$$\frac{d\phi}{d\beta} \approx -2\frac{\beta_0}{\kappa}\left\{d_f + \frac{1}{\gamma_c} + \frac{1}{\gamma_s}\right\}. \qquad (3.11)$$

Assuming that $\beta \approx k_{+1}$ and the structure is a simple three-layer slab waveguide excluding the grating and the AR film from the calculations, the resonant mode has a phase ϕ defined by Eqs. (3.7) and (3.8). The parameters in Eq. (3.11) are designated as in Eqs. (3.7) and (3.8).

Eq. (3.11) clarifies the dependence of the de-phasing rates and hence the spectral and angular linewidths in a single-diffracted order resonant mode. Both linewidths are directly proportional to the direction of the incident beam and also the modal propagation constant. Exciting a higher-order mode requires thicker film and hence the resonance has narrower

linewidths. The dependency of both linewidths ($\Delta\lambda_{FWHM}$, $\Delta\theta_{FWHM}$) become stronger when using shorter grating period. That can be written as [21]

$$\Delta\theta_{FWHM} \approx \frac{\Delta\lambda_{FWHM}}{\Lambda_a \cos\theta_0} \tag{3.12}$$

Where θ_0 is the incident angle at resonance. Therefore, achieving very narrow-band resonances by a single propagation mode confronts a limited angular tolerance.

3.4 Coupling into a two-diffracted order resonant mode in 1-D GMR at in-plane mounting

A different resonance behavior is observed when two first-order diffracted waves (±1) are phase matched to two resonant guided modes propagating within a common plane. At normal incidence, the diffraction is symmetric and the two counter-propagating resonant modes have the same propagation constant. For this type of resonance behavior at oblique incidence, each one of the first-order waves is coupled to a different waveguide mode.

3.4.1 <u>At normal incidence</u>

The scattering of the resonant mode at normal incidence is demonstrated in Figure 3.12. The two sources of Fresnel reflections are the non-diffracted waves, R_0 and R_{f0}. As shown, the small leakages with constructive phases are a contribution of two modes with the same propagation constants along +1 and -1 waves. The backward scattering by the grating (long-dash red arrow) causes these two modes to interact influencing the resonance responses as will be discussed later

in the section. The strength of the interaction increases when the grating has stronger second Bragg diffraction (η_B) [22.]

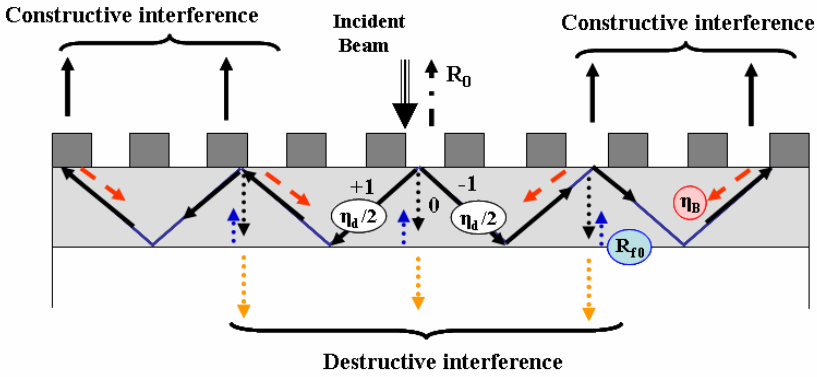

Figure 3.12: Scattering of the two-diffracted order resonant mode in 1-D GMR at normal incidence

To achieve a symmetric and low side-lobe spectral lineshape, the same approach used in the case of the single-diffracted order resonant mode is utilized. However, the grating strength (η_d) is a combination of the diffraction efficiency of both +1 and -1. The calculation in Eq. (3.10) is valid only if the interaction between modes is negligible.

At off-resonant wavelength (Figure 3.13a), both modes are de-phased in the same direction. The spectral lineshape in Figure 3.13c then remains the same as in the case of a single-diffracted order resonant mode (Figure 3.11c). At off-resonant angle, on the other hand, the modes are de-phased with opposite signs, as shown in Figure 3.13b (solid-blue arrows). This de-phasing compensation of these two modes at off-resonant angle produces a gradual reduction of the reflectivity at off-resonant angle.

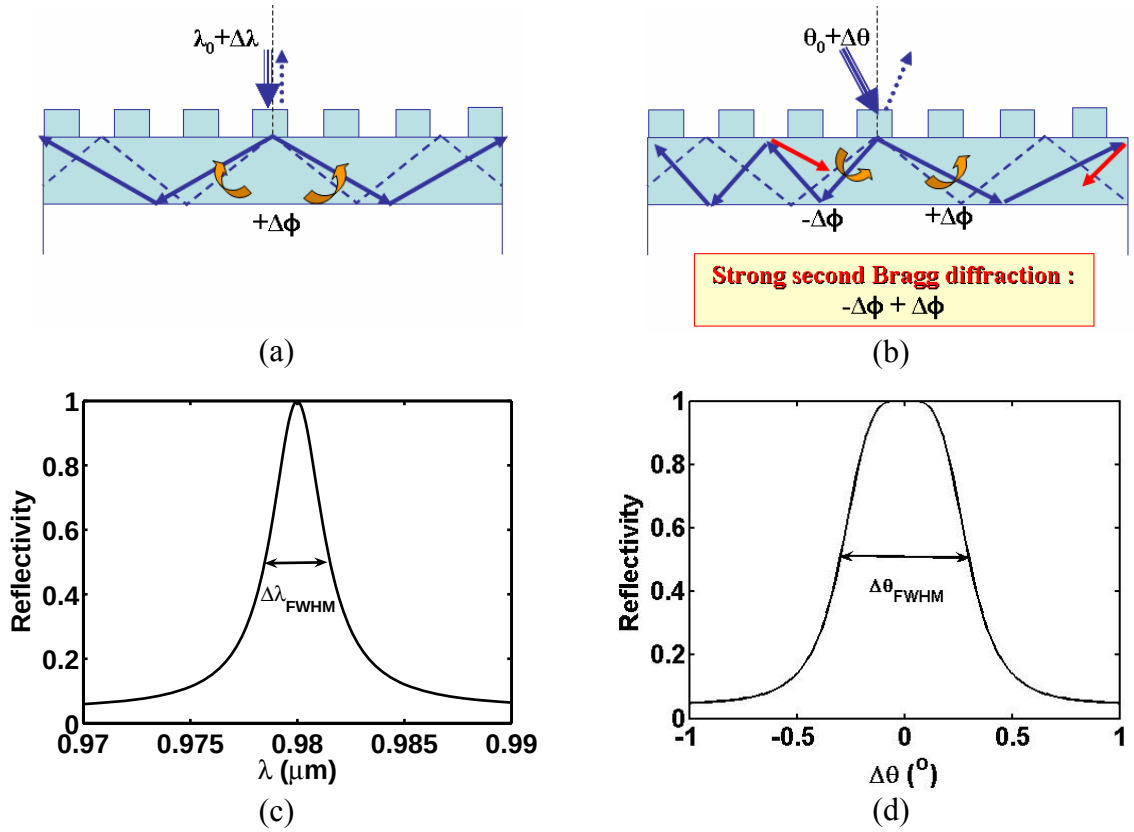

Figure 3.13: Scattering fields of a two-diffracted order resonant mode in 1-D GMR (a) at-off resonant wavelength (b) at off-resonant angle (c)/(d) spectral and angular responses

Therefore, the angular lineshape has a flat-top and broader linewidth (Figure 3.13d). That makes the resonance by this type more angularly tolerant. In addition, the de-phasing compensation can be further improved when the grating has a strong second Bragg diffraction [22]. As a result, the angular linewidth is expected to be even broader and more independent on the spectral linewidth.

Strengthening the second Bragg diffraction or the backward grating strength, η_B, might impact the grating strength, η_d, and the Fresnel reflection, R_0, as demonstrated in Figure 3.14. The contour plots of these grating diffraction efficiencies are calculated based on the deviation of the grating depth and filling factor when applying the structure in Section 3.3. In order to maintain $\Re\{\beta\}$ of the resonant mode, the grating at normal incidence has a period of 0.62-μm.

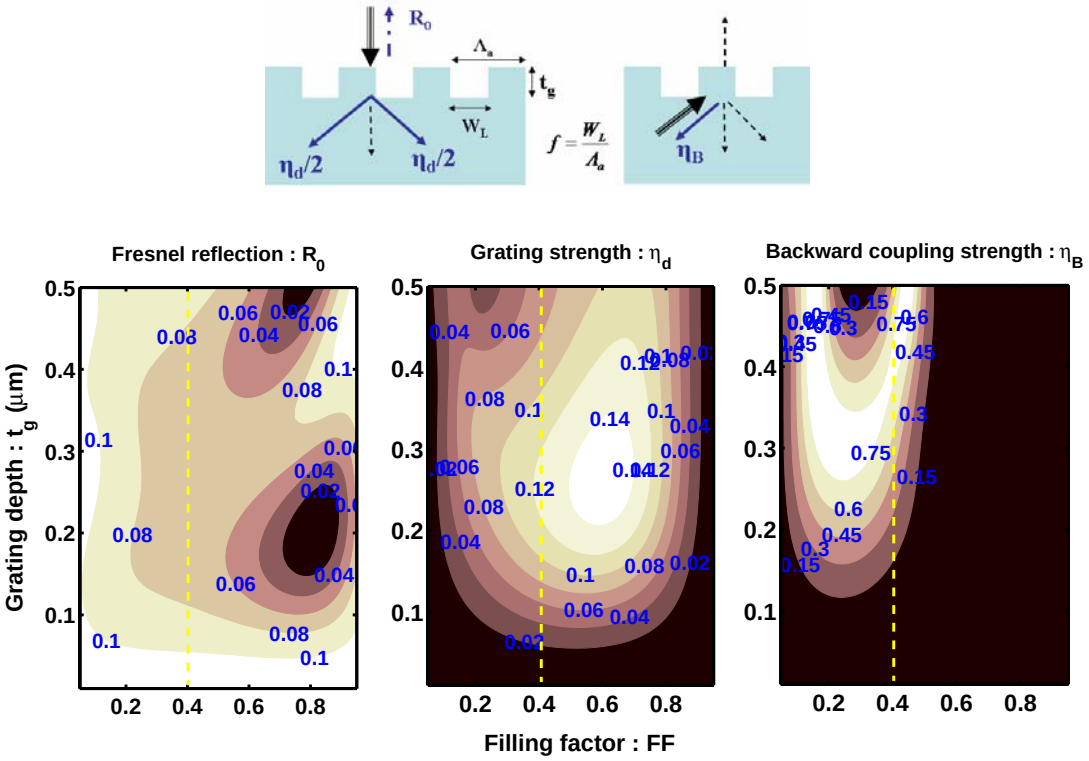

Figure 3.14: Contour plots of R_0, η_d, and η_B versus grating depth and filling factor

In comparison, the leakage of the counter-propagating modes increases roughly twice of that of the single propagation mode. Strengthening η_B in this structure results in a high R_0 causing asymmetric and high sidelobe resonant lineshape. That occurs when the grating has < 0.5-filling factor and > 0.1-μm thickness.

To demonstrate the improvement of the resonant response due to the interaction of two counter-propagating modes, the TE_1 resonance response of GMR structures with gratings of 0.4-filling factor are calculated when increasing the depth from 0.05 to 0.5 μm.

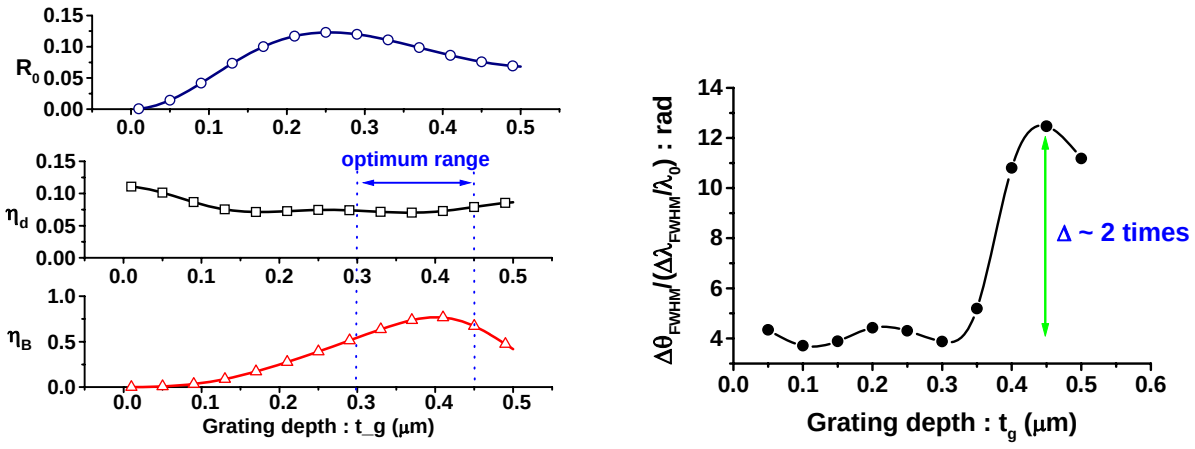

(a) (b)

Figure 3.15: (a) plots of R_0, η_d, and η_B versus grating depth for 0.4-filling factor (b) plots of angular/spectral linewidth ratio, $\frac{\Delta\theta_{FWHM}}{\Delta\lambda_{FWHM}/\lambda_0}$, versus the grating depth

The grating diffraction efficiencies are plotted in Figure 3.15a. The graphs in Figure 3.15b depict the angular/spectral linewidth ratio versus the grating depth. It is shown that when the grating has sufficiently strong second Bragg diffraction (t_g~0.3-0.45 μm), the dependency of spectral/ angular linewidth is significantly reduced. The optimum design shows an improvement of the angular/spectral ratio by a factor of two.

3.4.2 At oblique incidence

The scattering of the resonant modes at oblique incidence depicted in Figure 3.16 represents the phase matching of two first-order (±1) waves to two different waveguide modes. The -1 wave is coupled to the lower-order mode with a larger propagation constant. The leakages from both modes contribute to the resonance. Therefore, the resonant linewidths are directly proportional to

the summation of the grating strengths $\eta_{d,+1}$ and $\eta_{d,-1}$. The two grating strengths may not be identical.

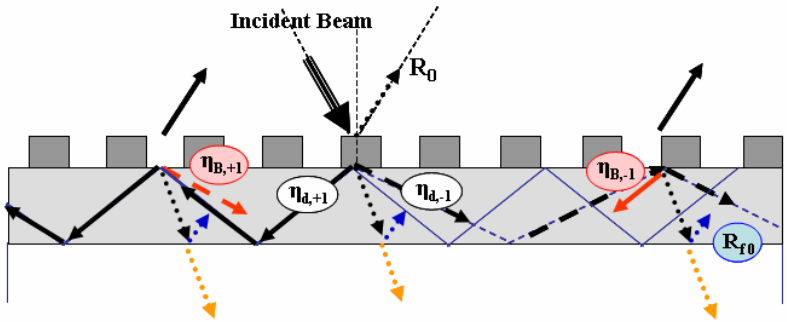

Figure 3.16: Scattering of a two-diffracted order resonant mode in 1D-GMR at oblique incidence

At off-resonance, each resonant mode accumulates de-phasing in the same manner as the one at normal incidence. However, the de-phasing of these counter-propagation modes performs asymmetrically at off resonant angle as depicted in Figure 3.17a. This is due to the deviation of the propagation constant ($\Delta\beta$). This mismatch ($\Delta\phi_{+1}/\Delta\theta \neq \Delta\phi_{-1}/\Delta\theta$) degrades the de-phasing compensation and hence the angular linewidth. Based on Eq. (3.11), the de-phasing compensation can be approximately written as

$$\frac{\Delta\phi_{+1}}{\Delta\theta} - \frac{\Delta\phi_{-1}}{\Delta\theta} \approx -2\left\{\frac{\kappa\Delta\beta - \beta\Delta\kappa}{\kappa^2}\left(t_f + \frac{1}{\gamma_c} + \frac{1}{\gamma_c}\right) + \frac{\beta}{\kappa}\left(-\frac{\Delta\gamma_c}{\gamma_c^2} - \frac{\Delta\gamma_s}{\gamma_s^2}\right)\right\} k_0 \cos\theta_{inc} \quad (3.13)$$

Eq. (3.13) shows that de-phasing mismatch increases with the propagation constant difference ($\Delta\beta$) and the film thickness (t_f). However, the angular lineshape remains the same but with narrower linewidth compared to the case at normal incidence. Likewise, the angular linewidth is also broadened due to the strong second Bragg diffraction.

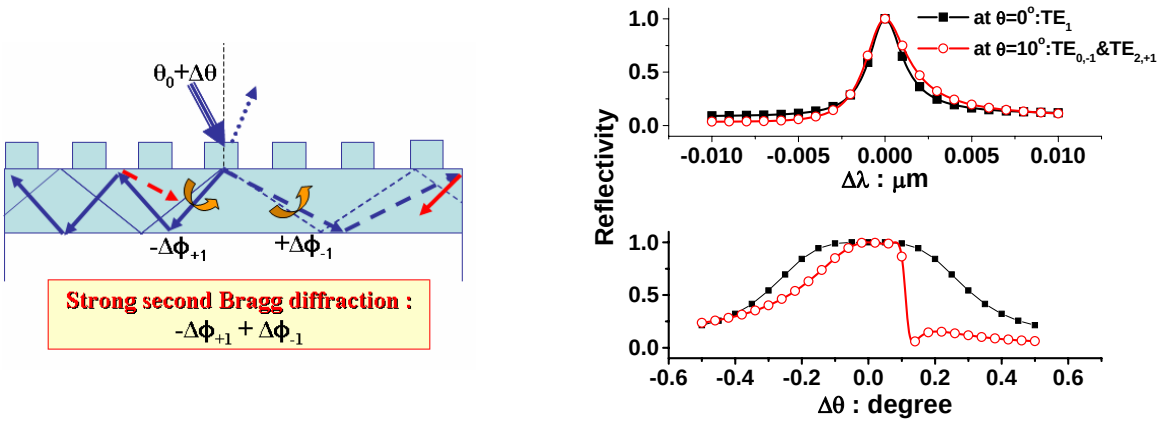

(a) (b)

Figure 3.17: (a) Scattering fields of two-diffracted order resonant modes with different β in 1-D GMR at off-resonant angle (b) comparison of the angular responses of resonances

Achieving this type of resonance requires the proper grating period and the film thickness for the desired resonance. The structure dimension can be estimated using the HWA approach demonstrated in Figure 3.5a. As seen, the resonance in design A is a contribution of the phase matching of -1 and +1 waves to TE_0 and TE_2 mode, respectively. Using the RCWA, the spectral and angular linewidths of this resonance are plotted in Figure 3.17b compared to the one with similar spectral response at normal incidence. It is noticeable that the angular linewidth is reduced by a factor of two. The angular response appears to be asymmetric since the resonance is located near the cut off range of the -1 wave. This can be avoided using a longer grating period.

3.5 Coupling into a two-diffracted order resonant mode in 1-D GMR at conical mounting

At conical mounting, the first-order diffraction waves do not share the same plane as demonstrated in Figure 3.18a. Due to the fact that the resonant modes propagate along two tilted planes, both TE and TM modes could be excited simultaneously. However, it is not guaranteed

that the incident beam is totally reflected at resonances. This depends on the ratio of the field components coupled to each mode and hence the incident beam polarization. The resonant modes propagating in two different planes could be simultaneously excited at the same wavelength once the structure is set at fully conical mounting ($\varphi_{inc} = 90^0$). Otherwise, resonances relating to modes with different propagation constants (β_{+1} and β_{-1}) cause a shift in wavelengths. This is shown in Figure 3.18b using the HWA.

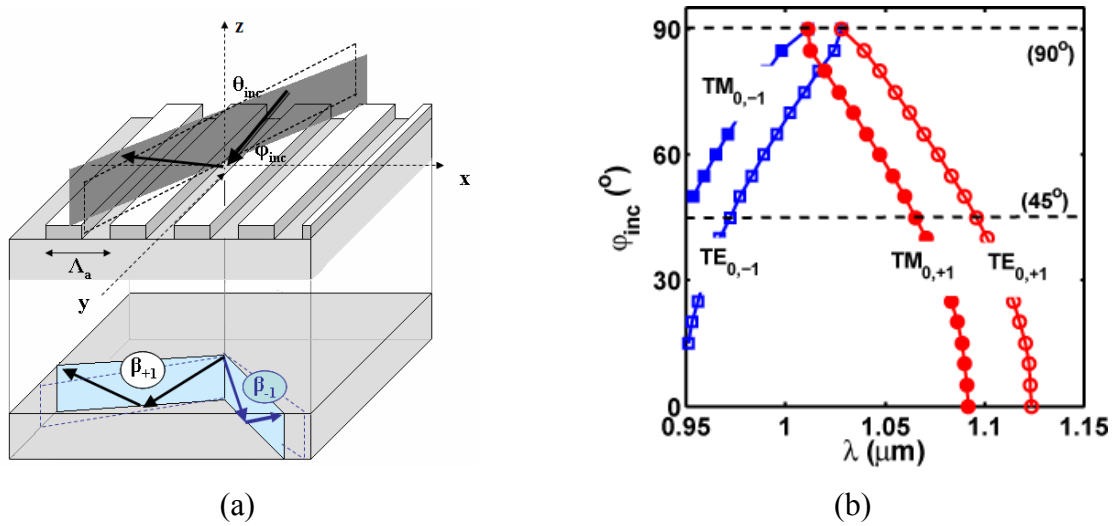

(a) (b)

Figure 3.18: (a) Configurations of the guiding planes and related resonant modes in 1-D GMR at conical mounting (b) HWA calculations of resonances versus the shift of incident plane ($\theta_{inc} = 10^\circ, \varphi_{inc}$) in 1-D GMR (Figure 3.5) with t_f=0.5 μm.

Resonances due to modes $TE_{m,p}$ and $TM_{m,p}$ are plotted versus the shift of the incident plane, φ_{inc}, away from the grating vector. The subscript *-p* represents the diffraction wave which phase matches to the mode *–m*.

For the case of $\varphi_{inc} \neq 90^\circ$, resonances are individually formed by single-propagation modes. At resonance, the incident beam is totally reflected only if it is polarized perpendicular or parallel to the related diffraction plane. The resonance linewidths are proportional to the power

dissipated normal to or within the plane of diffraction for TE and TM mode, respectively. In Figure 3.19a, the resonant responses are calculated using the RCWA when $\varphi_{inc} = 45^{\circ}$. Resonances with partial reflections occur at the locations with correspondence to Figure 3.17b, when the incident beam is TE ($\psi_{inc} = 0^{\circ}$) and TM ($\psi_{inc} = 90^{\circ}$) polarized. The reflectivity is proportional to the incident beam polarization. Figure 3.19b demonstrates the change of reflectivity at each resonance when rotating the incident beam polarization.

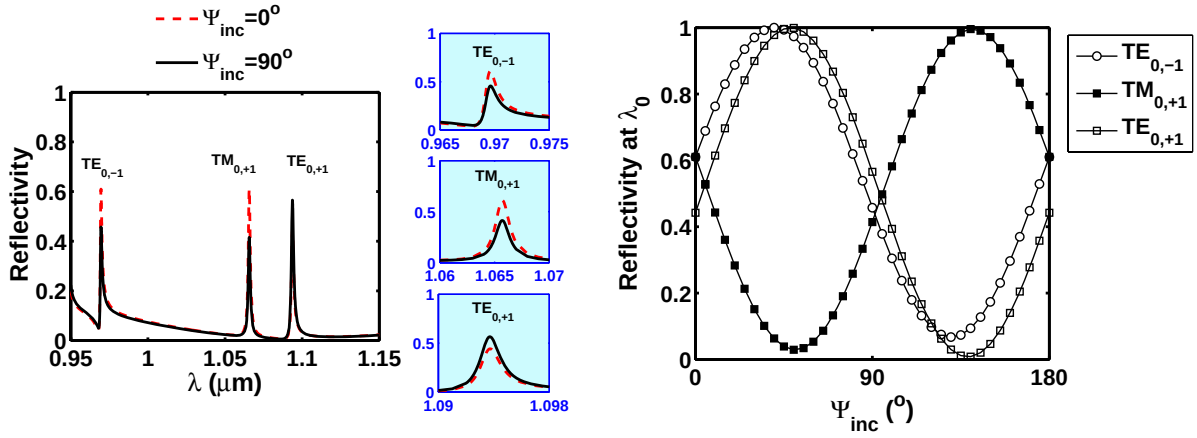

(a) (b)

Figure 3.19: (a) Spectral responses of 1-D GMR at conical mounting $\theta_{inc} = 10^{\circ}, \varphi_{inc} = 45^{\circ}$ (b) Deviation of reflectivities at resonances plotted versus incident polarization

For the case of $\varphi_{inc} = 90^{\circ}$, the incident beam diffracts along two waves symmetrically tilted away from the incident plane. Therefore, resonances are formed due to the phase matching of two resonant modes with the same propagation constant. At this setting, the polarized incident beam is totally reflected at resonances independent of the polarization [35.] However, the phase matching of the resonant modes for the TE and TM beam performs differently as the demonstration in Figure 3.20, which is based on the field decomposition. This will produce the

shift of resonances. Resonances are formed by anti-symmetric modes ($E_{\perp,-1} = -E_{\perp,+1}$) when coupling the incident beam to a mode with cross polarization (phase matching of TM incident beam and TE waveguide mode, for example.) Otherwise, resonance satisfies the phase matching of symmetrical modes ($E_{\perp,-1} = E_{\perp,+1}$). That may introduce a phase mismatch and hence shifts the resonances as plotted in Figure 3.21a for the structure calculated in Figure 3.18 at $\varphi_{inc} = 90^{\circ}$.

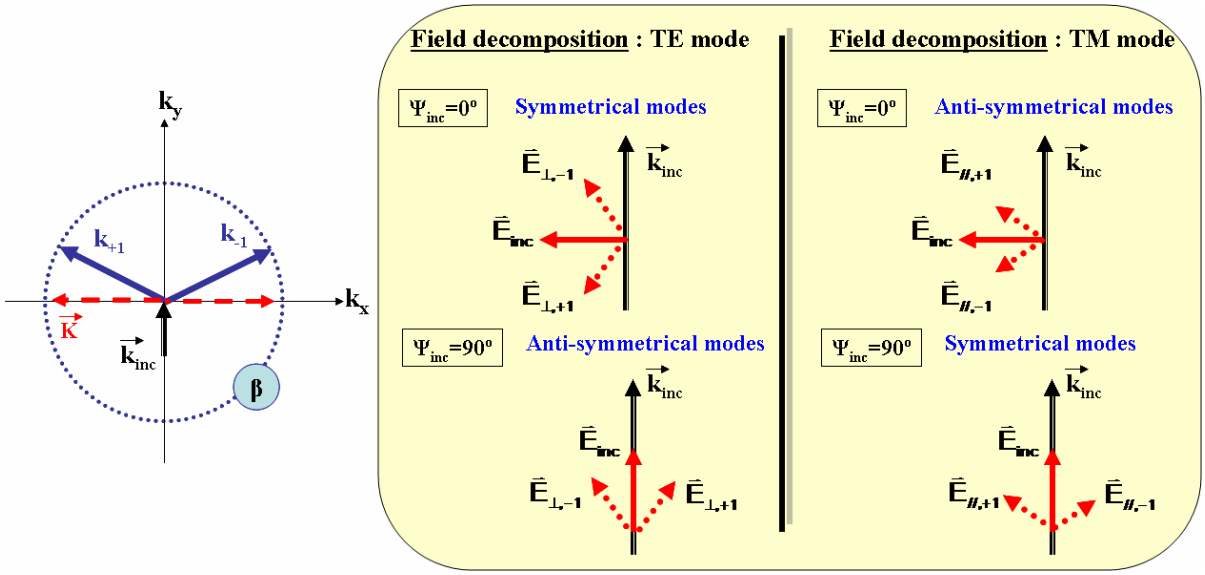

Figure 3.20: Phase matching diagram and decomposition of TE and TM incident beam corresponding to TE and TM resonant mode for a fully conical mounting

As seen, the spectral responses do not only shift both resonances (TM_0 and TE_0) under TE (red dash-line) and TM (black solid-line) incident beams, but also differs in the spectral linewidths as well. That is explained in the calculations of the field magnitudes of the diffracted waves in Figure 3.21b. The results indicate stronger grating strength when coupling the incident beam to the anti-symmetric mode. The differences are however less significant when operating the

structure at larger angle. Achieving almost identical leakage for both symmetric and anti-symmetric modes requires phase matching of TM mode for the structure at $\theta_{inc} > 50^{\circ}$.

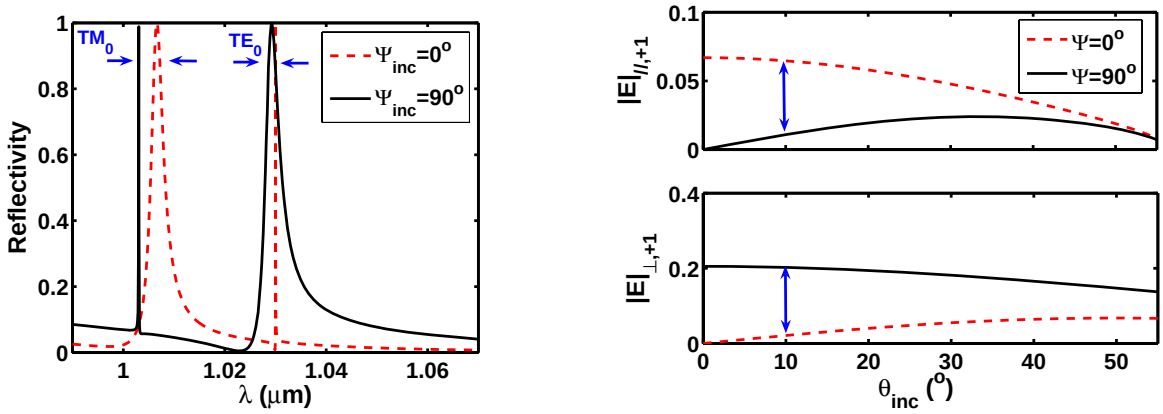

(a) (b)

Figure 3.21:(a) Spectral responses of 1-D GMR at conical mounting $\theta_{inc} = 10^{\circ}, \varphi_{inc} = 90^{\circ}$ (b) plots of the field magnitude ($|E|$) of the diffracted waves versus the θ_{inc} for the TE and TM polarized beam.

Although the resonances at fully conical mounting are sensitive to the incident polarization due to the phase mismatch of the symmetric and anti-symmetric modes, the slight shift of the resonance can be compensated by optimizing the grating filling factor, which directly compensates the phase mismatch. When properly designing the grating, the resonances are overlapped at the same wavelength as seen in the calculation results in Figure 3.22. Here, the structure is set at $\theta_{inc} = 50^{\circ}$ and the 1-D grating period is adjusted to be 0.61 μm in order to achieve the similar resonances as in the previous calculations at $\theta_{inc} = 10^{\circ}$ keeping the other parameters constant.

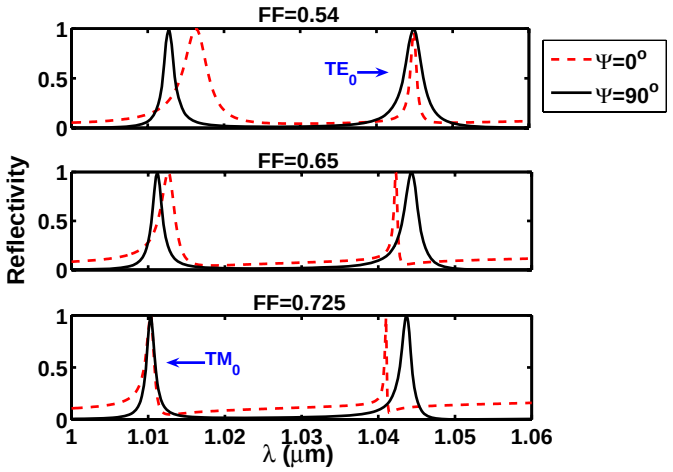

Figure 3.22: Spectral responses of 1-D GMR at conical mounting $\theta_{inc} = 50^{\circ}, \varphi_{inc} = 90^{\circ}$ versus the deviation of filling factor (FF) ($\Lambda_a = 0.61\ \mu m$.)

As shown, optimizing the structure to remove the polarization dependency can be individually done for each resonance (FF=0.54 for TE_0 resonance and FF=0.725 for TM_0 resonance) but not both in the same structure. Besides, the resonance performance is better when matching the TM mode, where the spectral responses are almost completely overlapped.

3.6 Summary

In this chapter, the concepts of resonant anomaly within the GMR structure were presented. GMR structures are investigated for the desired resonances using the RCWA together with the HWA. The resonant response is directly related to the scattering of the resonant modes and the de-phasing characteristics at off resonance.

In general, the resonance response is symmetric with low side lobes when the leaking fields are purely a contribution of the resonant mode. The linewidth is on the other hand dependent on the grating strength (η_d). The grating was properly designed to have negligible

Fresnel reflection and meanwhile low grating strength in order to achieve the narrow band resonances. To do so, GMR with the multi-level AR grating was shown to serve the requirements.

For 1-D GMR at in-plane mounting, the first-order diffraction is limited along a single plane. Therefore, resonance is sensitive to the incident polarization. At oblique incidence, resonances formed by the single-diffracted order resonant mode appear to have strong dependency on the angular and spectral linewidths. Resonances due to the two-diffracted order resonant modes are more desirable. Both modes gain de-phasing in opposite directions at off-resonant angle. The de-phasing compensations reduce the degradation of reflectivity. De-phasing can be further reduced when the grating has a strong second Bragg diffraction and the resonant modes are more laterally confined. That introduces broader angular linewidth and less dependency to the spectral linewidth. However, coupling into the two-diffracted order resonant modes at oblique incidence confronts a de-phasing mismatch due to matching of different waveguide modes. The angular linewidth is then not as broad as the one at normal incidence. Polarization independent resonance is feasible. Resonances are formed by coupling each one of the counter-propagation waves to different polarized modes at the same wavelength when the structure is set at oblique incidence.

For 1-D GMR at conical mounting, the resonant mode propagates along two planes. In general, resonance is a contribution of a single diffracted wave, unless it is fully conical mounting ($\varphi_{inc} = 90^{\circ}$.) In advantage, it is possible to excite the same resonant mode when using TE and TM beam. However, there exists a slight shift of resonance due to the phase mismatch of

symmetric and anti-symmetric modes. For the proper grating design, the shift is removed and that makes resonances at this setting polarization independent.

CHAPTER 4 : ANALYSIS OF TWO DIMENSIONAL-GUIDED MODE RESONANT (2-D GMR) STRUCTURES

In this chapter, the resonance anomaly in the GMR structure using a 2-D grating is studied. The effect of the inherent multiple diffraction/guidance planes on the resonance is investigated in details. The field scattering and the phase matching condition at resonance are studied in order to gain better understanding of the coupling characteristics including the impact of light polarization and the effect of the grating coupling strengths on the resonance responses. The Bloch mode approach is used to calculate the actual complex modal index related to the formation of the resonances in the 2-D GMR.

4.1 Resonances in 2-D GMR

For 2-D GMR (Figure 4.1), the diffracted orders, and hence the guiding planes, intrinsically propagate in multiple planes due to the double periodicity of the 2-D grating as discussed in Section 2.1.2. Phase matching of a diffracted wave to a guided resonant mode can be achieved in various configurations (planes) depending on the periodicity of the structure and the direction of the incident wave.

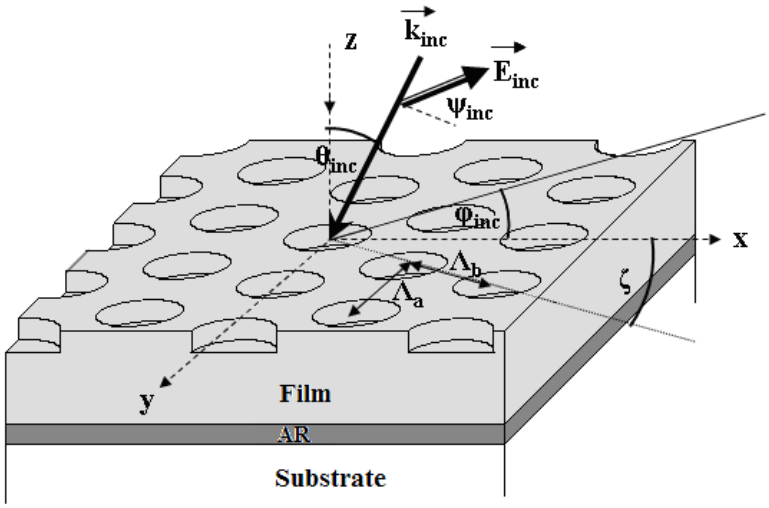

Figure 4.1: 2-D GMR structure configuration

In general, the GMR structure comprises of a subwavelength grating. For a 2-D grating, the range of the grating periods that meets the resonance condition is determined from the grating equations (2.7) and (2.8). For the period Λ_a, the range is simplified in the form of 1-D grating as in Eq. (3.8). The maximum and minimum values of Λ_b can be written as follows

$$\Lambda_{b,\min} = \frac{\lambda_0 \sec(\zeta)}{\sqrt{n_s^2 + [n_{inc} \sin\theta_{inc} \sin\varphi_{inc}]^2} + n_{inc} \sin\theta_{inc} \cos\varphi_{inc}}$$

and

$$\Lambda_{b,\max} = \frac{\lambda_0 \sec(\zeta)}{\sqrt{n_f^2 + [n_{inc} \sin\theta_{inc} \sin\varphi_{inc}]^2} + n_{inc} \sin\theta_{inc} \cos\varphi_{inc}}. \qquad (4.1)$$

Where n_s and n_f are the refractive indices of the substrate and the film respectively. The other parameters in Eq. (4.1) are designated in Figure 4.1

Since the coupling characteristics rely on the first-order diffraction, for the 2-D grating in Figure 4.1, the periodicity can be classified into three categories (rectangular-, arbitrary-, and

hexagonal-lattice crossed grating.) These classifications are based on the grating skew angle (ζ .) The fundamental first-order diffraction of each pattern is depicted in Figure 4.2.

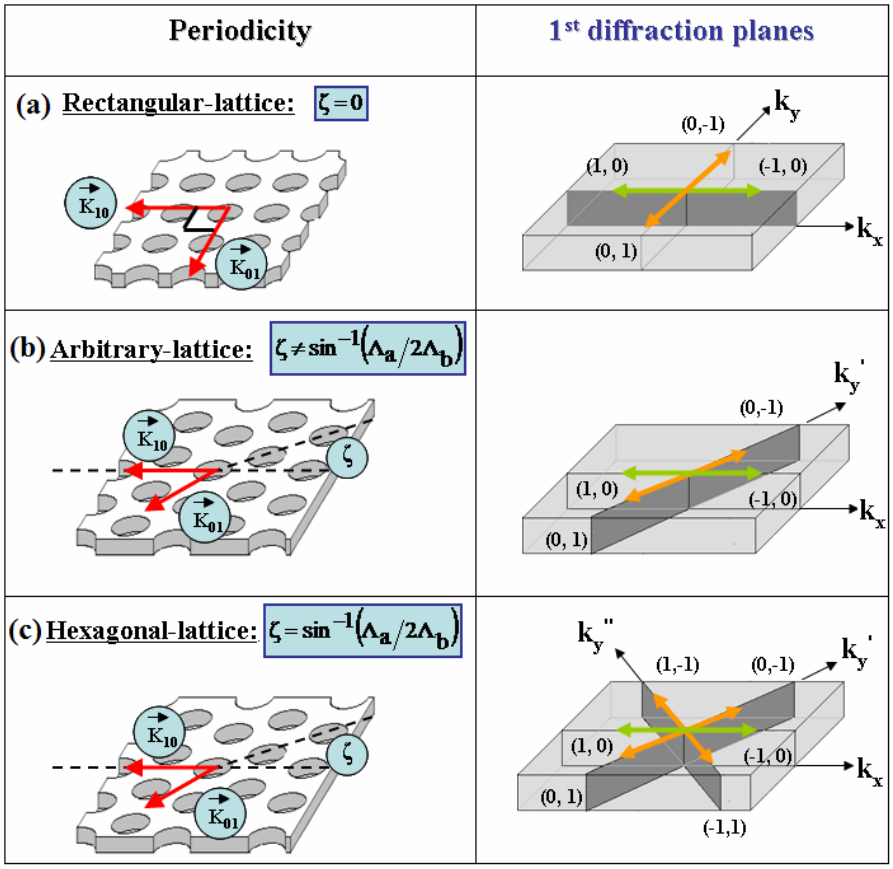

Figure 4.2: First-order diffraction/guidance planes in 2-D GMR with (a) rectangular- (b) arbitrary- (c) hexagonal-lattice grating

Resonance locations relating to each first-order wave are individually estimated using the HWA approach. These resonance locations are shifted from the actual ones obtained by the RCWA as the homogeneous waveguide approach does not include the scattering by the 2-D grating. This scattering and the multiplicity of the diffraction and guidance in 2-D structure stress three important parameters impacting the resonances characteristics; the related first-order diffracted waves, polarization of the incident beam and the polarization of the leaky mode. In next sections,

the resonance characteristics in 2-D structures will be analyzed based on the scattering of the field relating to resonances at both normal and oblique incidence when applying different grating patterns. The resonant responses will be discussed and the advantages of having the higher-order fundamental multiple planes will be shown to allow for new GMR devises to improve the resonant performances.

4.2 2-D GMR using rectangular-lattice grating

The existence of two orthogonal grating vectors ($\zeta = 0^\circ$) in the rectangular-lattice grating (Figure 4.2a) allows the first-order diffraction to be along four waves (p,q) = (0,1), (0,-1), (1,0), and (-1,0). The tangential wave vectors of these wave, reduced from Eqs. (2.7) and (2.8), can be written as

$$k_{x,pq} = k_{x,inc} - p\frac{2\pi}{\Lambda_b}, \quad \text{and} \qquad k_{y,pq} = k_{y,inc} - q\frac{2\pi}{\Lambda_a}. \tag{4.2}$$

The incident directions $(\theta_{inc}, \varphi_{inc})$ and the grating periods (Λ_a, Λ_b) define the wave vectors, and hence the propagation constant of the weak leaky resonant mode ($\mathrm{Re}\{\beta\} \cong \sqrt{k_{x,pq}^2 + k_{x,pq}^2}$).

4.2.1 Coupling of resonant modes at normal incidence

At normal incidence, the incident beam is symmetrically diffracted along two orthogonal fundamental planes as depicted in Figure 4.3a. Each plane sustains two counter-propagating first-order waves with the same propagation constant that phase matches the leaky waveguide mode at resonance. However, it is not guaranteed that resonances are always a contribution of four

resonant modes at the same wavelength. This is defined by the incident beam polarization as will be discussed later. In all cases, at each round trip a backward diffraction with the same amplitudes of the wave vectors as well as a crossed diffraction is produced due to the symmetric diffraction as demonstrated in Figure 4.3b. The influence of these diffractions will be considered when investigating a structure with broad angular tolerance in Chapter 6.

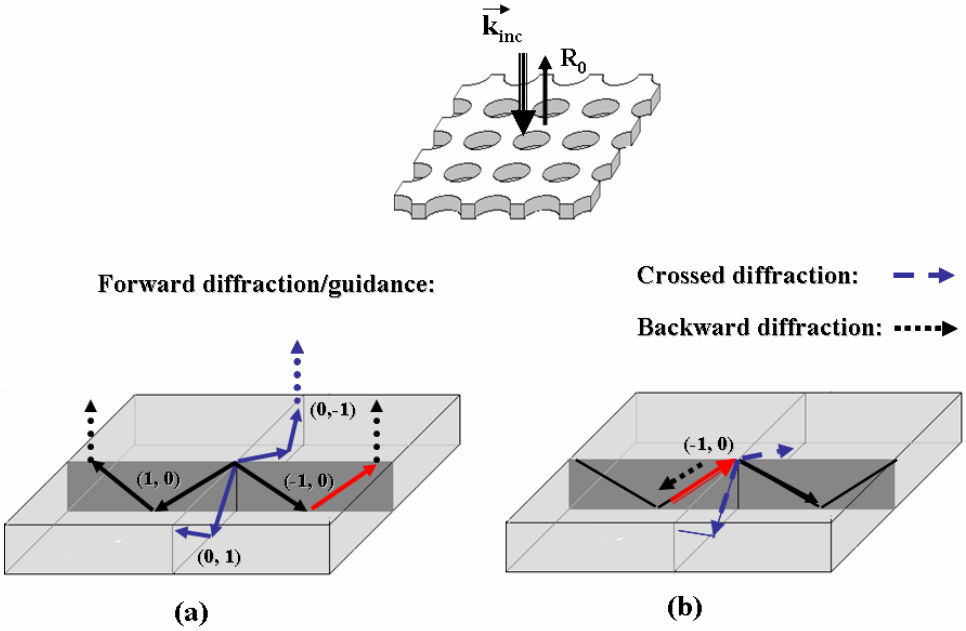

Figure 4.3: Scattering of field inside the structure with a rectangular-lattice grating at resonance (a) forward diffraction (b) backward and crossed diffraction.

The orthogonal planes of diffraction/guidance make resonances a contribution of both TE and TM resonant modes. These two modes are decoupled when the incident beam is linearly polarized along one of these grating vectors. Then, at least two fundamental resonances from TE_0 and TM_0 modes are expected. Coupling to both polarized modes propagating along two orthogonal planes does not prevent the total reflection to be formed at resonances as in the case of 1-D GMR. The wave vector of each mode defines the resonance wavelength. The spectral

linewidths are proportional to the power dissipated to the field normal ($\eta_{d,\perp}$) and in-plane ($\eta_{d,//}$) components relating to TE and TM resonances, respectively. In advantage, the double diffraction reduces the power dissipated to each resonant mode. Hence, resonances in 2-D GMR may have narrower linewidths than the ones in 1-D GMR.

Using a square-lattice grating ($\Lambda_a = \Lambda_b$) with symmetric filling factors, four resonant modes have the same propagation constant. Therefore, phase matching of both polarized modes can be accomplished in both planes. That produces resonances which are independent of the incident beam polarization. The diffraction/coupling characteristics relating to the TE resonant mode is demonstrated in Figure 4.4a based on the decomposition of the incident beam along each plane, $\vec{E}_{inc} = E_x\ \vec{x} + E_y\ \vec{y}$. $\vec{E}_x$ is coupled to the resonant modes counter-propagating along the diffracted waves (0, 1) and (0,-1), while $\vec{E}_y$ is coupled to the resonant modes via the diffracted waves (1, 0) and (-1, 0) and vice versa for the TM resonant mode. The power coupling to each diffracted wave deviates corresponding to the incident beam polarization (ψ_{inc}) as shown in Figure 4.4b. The total power coupling to each polarized mode however remains constant. That results in the conservation of both resonant location and resonant linewidth.

The analysis is verified using the RCWA as shown in Figure 4.5. The structure has an air-hole grating pattern fabricated on a dielectric film with a refractive index of 2. The grating has periods Λ_a=Λ_b=250 nm, depth t_g = 50 nm, and hole-radius 100 nm. A high index film has a refractive index of n_f =2.5 and a thickness t_f=~85 nm. An anti-reflection film (n_{AR}= $\sqrt{n_f n_s}$, t_{AR}= 475/4n_{AR} nm.) is inserted at the high index film/substrate (n_s=1.47) interface. The graphs show an invariant resonance response, while the incident beam is polarized from 0 to 90 degree with

respect to the incident plane for TM_0 resonant mode. In addition, the polarization of the reflected beam maintains the same direction and state as that of the incident beam.

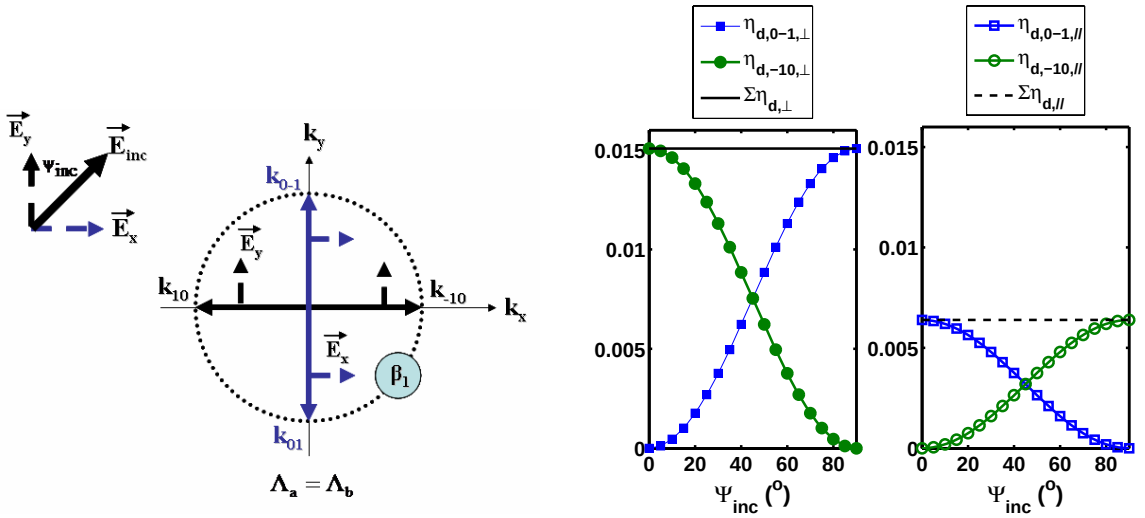

(a) (b)

Figure 4.4: (a) Phase matching diagram of TE resonant mode (β_1) for an unpolarized incident beam (b) plots of normalized powers dissipated to the normal ($\eta_{d,\perp}$) and in-plane ($\eta_{d,//}$) field components by a square-lattice grating versus ψ_{inc}

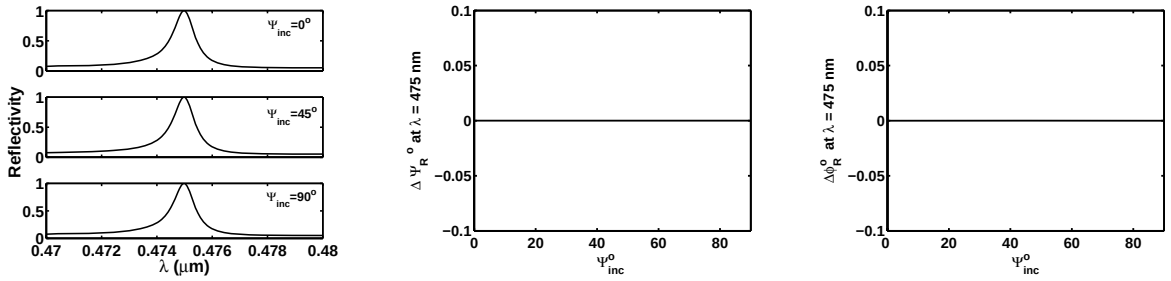

(a) (b) (c)

Figure 4.5: RCWA calculations (a) spectral response for $\psi_{inc} = 0^o, 45^o, 90^o$; (b) and (c) polarization rotation ($\Delta\psi_R = \psi_R - \psi_{inc}$) and phase ($\Delta\phi_R$) of the reflected beam at TM_0 resonance.

In contrary, partial reflection is expected at resonance for a rectangular-lattice grating GMR, $\Lambda_a \neq \Lambda_b$, unless the incident beam is linearly polarized along one of the diffraction planes. The phase matching diagram in Figure 4.6a shows the possible modes with two different propagation constants (β_1 and β_2).

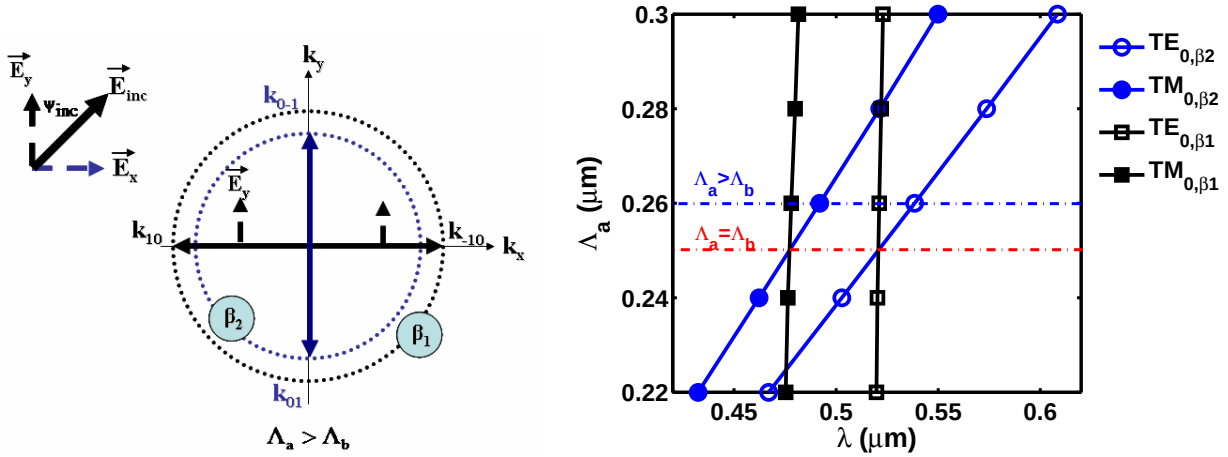

(a) (b)

Figure 4.6: (a) Phase matching diagram of TE resonant mode (β_1) for an unpolarized incident beam, when $\Lambda_a > \Lambda_a$ (b) plots of resonances versus shift of period Λ_a, calculated by HWA.

Therefore, four resonances corresponding to these fundamental modes may be formed. Resonances calculated by HWA are plotted versus the shift of period Λ_a in Figure 4.6b. That mainly impacts the propagation constant (β_2) of the resonant modes propagating along waves ($0,\pm 1$.) The calculation results demonstrate the relocation of the resonances to the longer wavelength due to the decrement of the modal propagation constant (larger period), while the other resonances (β_1) remain almost at the same wavelengths. The incident beam polarization defines the coupling characteristics as discussed. Here, resonances of TE resonant mode with

propagation constant β_1 is a contribution of only $\vec{E}_y$ coupled along diffracted waves $(\pm 1,0)$ as in Figure 4.6a. Hence, the incident beam is partially reflected at resonance where the reflectivity is proportional to the polarization angle ψ_{inc} as an approximated form $\left|\cos(\psi_{inc})\right|^2$. In comparison to the actual reflectivity, the difference appears more significant when polarization angle is larger as in the graph Figure 4.7.

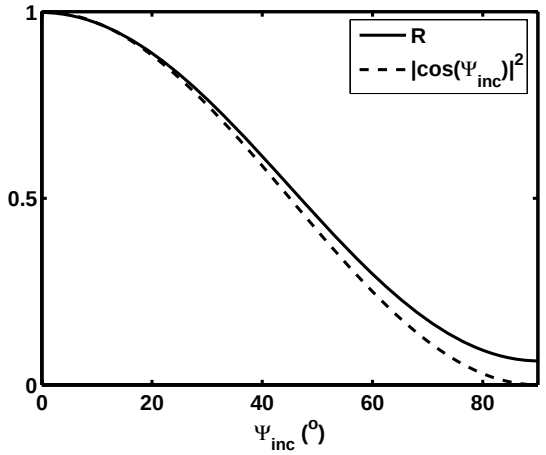

Figure 4.7: Comparison between reflectivity (R) at $TE_{0,\beta 1}$ resonance calculated by RCWA and $\left|\cos(\psi_{inc})\right|^2$ versus ψ_{inc}

The resonance response of a structure with $\Lambda_a = 260\ nm$ is plotted in Figure 4.8, when the incident beam polarization is set at 0, 45 and 90 degrees. As seen, resonances are polarization dependent. The separation between the resonances can be changed over a wide range by changing the input polarization. The resonance locations are adjustable by changing the period as demonstrated in the graph in Figure 4.6b.

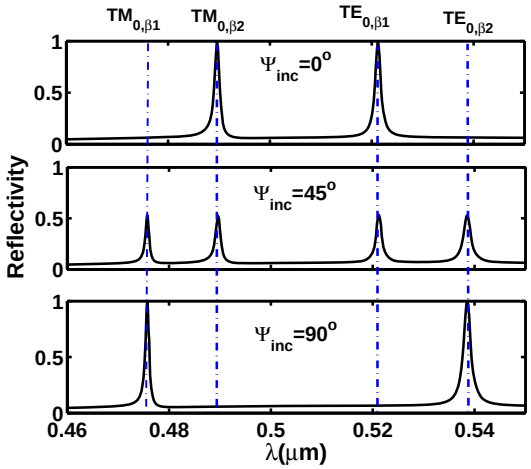

Figure 4.8: Reflectivity spectrum of GMR with rectangular-lattice grating ($\Lambda_a > \Lambda_b$)

4.2.2 Coupling of resonant modes at oblique incidence

At oblique incidence, the symmetry of the first-order diffraction is broken. The leaky mode can be coupled by any of the four first-order diffracted waves that match its propagation constant ($\sim \mathrm{Re}\{\beta\}$ of the leaky mode.) The tangential wave vectors of the diffracted orders can be completely different. As discussed in Section 3.5 for 1-D GMR at conical mounting, total reflection is achieved when the incident beam is perfectly polarized normal to or along a diffraction plane. Total reflection happens also when all the components of an unpolarized incident beam are coupled to the resonant modes without phase mismatch. At least two resonant modes having the same propagation constant propagate symmetrically around the plane of incidence. That can be accomplished when the incident plane is set at $\varphi_{inc} = 0^\circ$ and $\varphi_{inc} = 45^\circ$ as demonstrated in Figure 4.9 for structure with square-lattice grating.

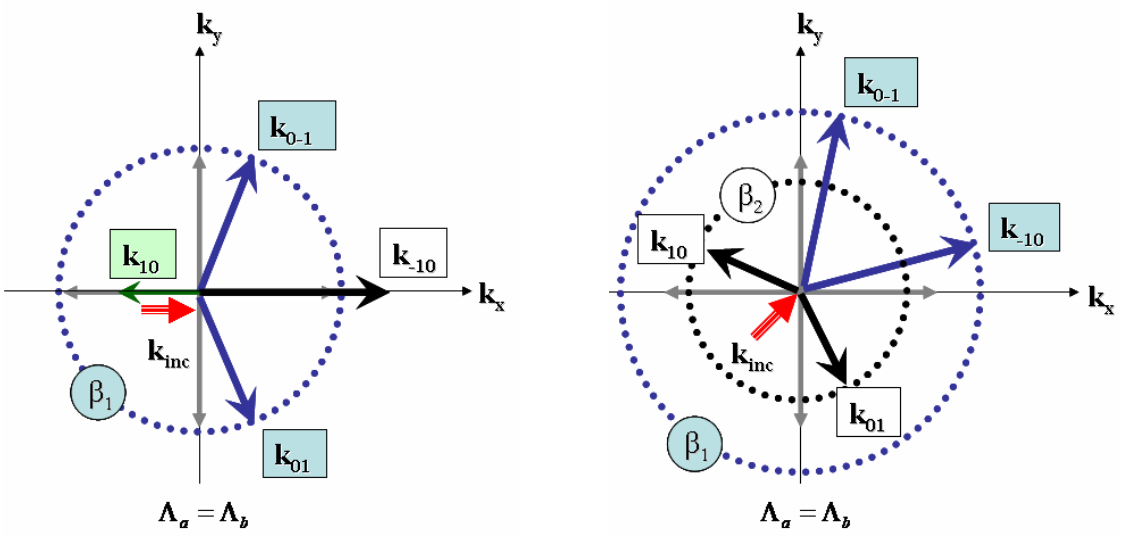

Figure 4.9: Phase matching diagram of the resonant modes in 2-D GMR with a square-grid grating at oblique incidence (a) $\varphi_{inc} = 0^{\circ}$; (b) $\varphi_{inc} = 45^{\circ}$

Although total reflection forms at resonance for TE and TM polarized beam, resonances occur at different wavelengths due to the phase mismatches between the symmetric and anti-symmetric modes, thus degrading this reflectivity for an unpolarized beam. This difference in the resonance location can be eliminated by changing the grating dimensions (filling factor and period.)

For 2-D GMR with square-lattice grating ($\Lambda_a = \Lambda_b$), having two orthogonal fundamental planes of diffraction/guidance makes it possible to achieve four fundamental resonances with total reflection at oblique incidence. For example, when the incident plane is set at $\varphi_{inc} = 45^{\circ}$, as displayed in Figure 4.9b, two pairs of first-order waves, (0,-1)/(-1,0) and (0,1)/(1,0), diffract symmetrically around the incident plane and phase match to resonant modes with shifted propagating constants β_1 and β_2, respectively. Using HWA, resonances corresponding to the resonant modes are approximately determined.

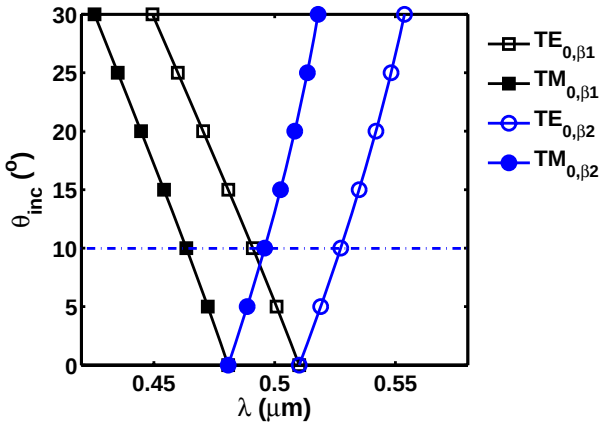

Figure 4.10: Plots of resonances in of GMR with square-lattice grating ($\Lambda_a = \Lambda_b$) at $\varphi_{inc} = 45^\circ$ versus θ_{inc} , calculated by homogeneous waveguide approach.

The calculation results in Figure 4.10 demonstrate the fundamental resonances locating at four different wavelengths. Tilting the structure with large angle (θ_{inc}) results in the increment of β_1 and hence related resonances moving toward the shorter wavelength. In contrary, resonances of modes with the smaller β_2 are located at the longer wavelengths. The structure considered here has the same material as in Section 4.2.1. The grating has a square-lattice pattern with period 230 nm, hole-radius 109 nm, and depth t_g = 50 nm. A high index film has a thickness t_f=127 nm.

Unlike the structure with rectangular-lattice grating at normal incidence, all of the four fundamental resonances are formed and have a total reflection when the incident beam is TE or TM polarized, as demonstrated in Figure 4.11. The structure is calculated at $\theta_{inc} = 10^\circ$. Like the 1-D GMR at oblique incidence, the shift of resonances by orthogonal polarized beams is expected unless the grating is well optimized to remove the phase mismatch of the symmetric and anti-symmetric modes. As the optimum grating dimension is suitable for individual

resonances, achieving all resonances independent to the incident polarization is not feasible at oblique incidence.

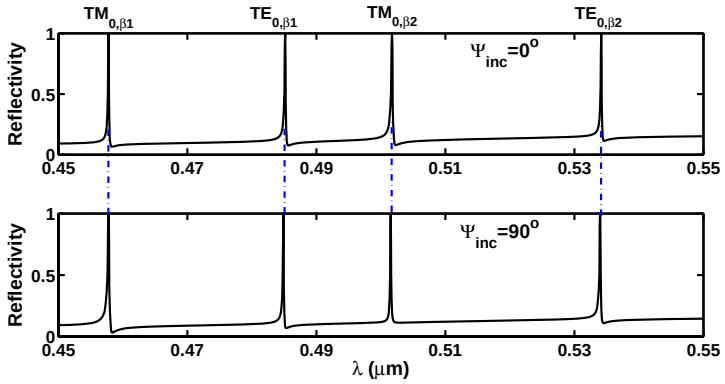

Figure 4.11: Reflectivity spectrum of GMR with square-lattice grating ($\Lambda_a = \Lambda_b$) at $(\theta_{inc}, \varphi_{inc}) = (10^\circ, 45^\circ)$

The enlarged spectra in Figure 4.12 indicate that only TM_0 resonance due to the β_1 resonant modes ((0,-1)/(-10)) is polarization independent, while the other three resonances are not. The appearance of the slight shift (~2-3 nm) between the orthogonal polarization beam components results in the partial reflection and deformed spectral lineshapes (Figure 4.12b to d: red-solid plots) when using an unpolarized beam.

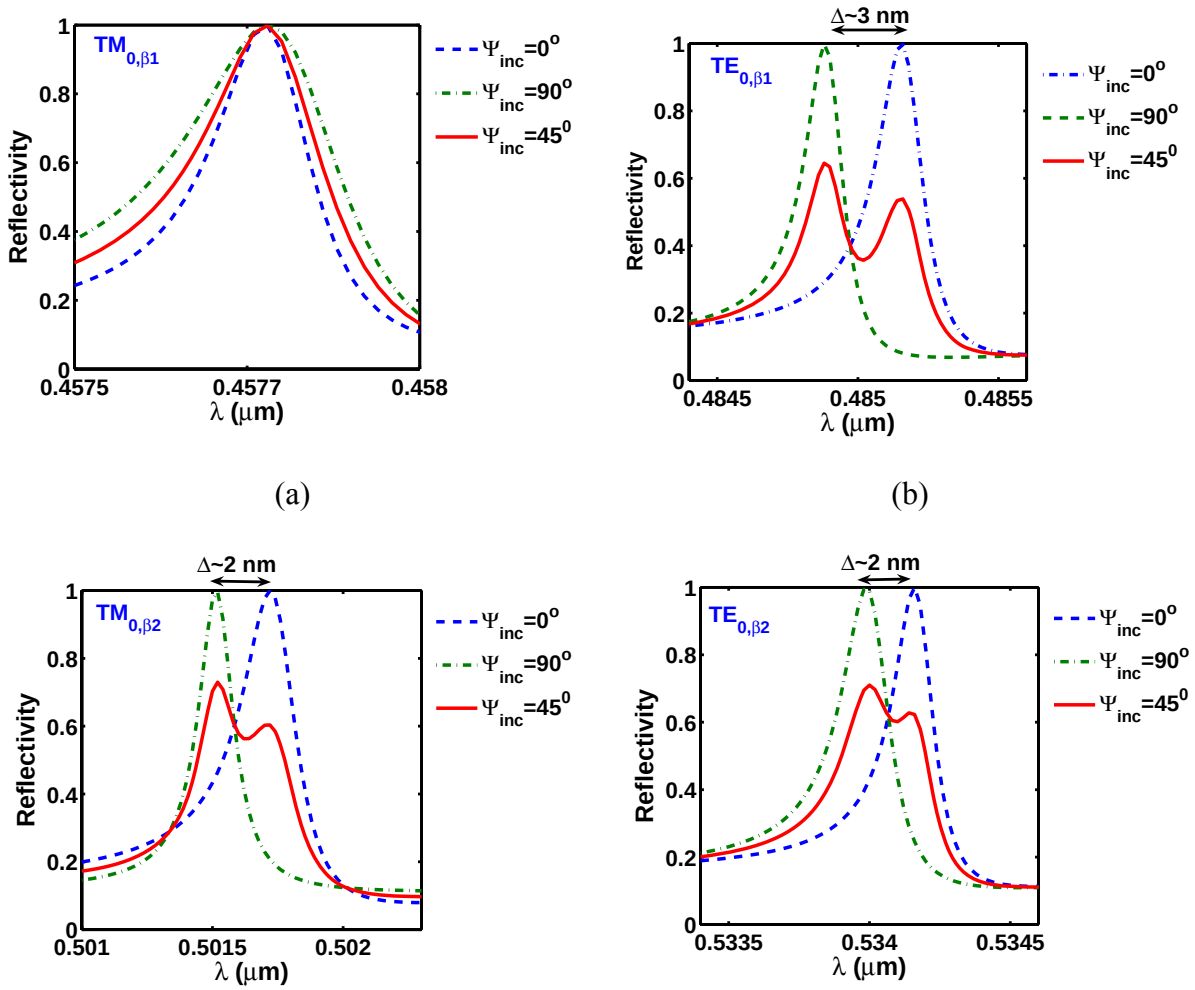

Figure 4.12: Closed-up plots of reflectivity spectrum in Figure 4.11 (a) $TM_{0,\beta 1}$ (b) $TE_{0,\beta 1}$ (c) $TM_{0,\beta 2}$ (d) $TE_{0,\beta 2}$ resonance

For unpolarized GMR filter, it is important to equalize the grating coupling strength for the symmetric and the anti-symmetric modes so that resonant linewidths are similar and the lineshape remains unchanged. Even though the spectra may not be completely overlapped due to the Fresnel reflections, the spectral lineshape for an unpolarized beam is not deformed. The calculation results in Figure 4.13 indicate that the structure setting at $\varphi_{inc} = 45^{\circ}$ is more

desirable. The deviation of power leakages ($\Delta\eta_d = \eta_d\big|_{\psi_{inc}=0^\circ} - \eta_d\big|_{\psi_{inc}=90^\circ}$) is significantly reduced to roughly 3 times of the one at $\varphi_{inc} = 0^\circ$. Achieving resonances with identical linewidths at $\varphi_{inc} = 0^\circ$ is still possible when coupling to TM resonant modes but at the large incident angle nearby the cut-off limit.

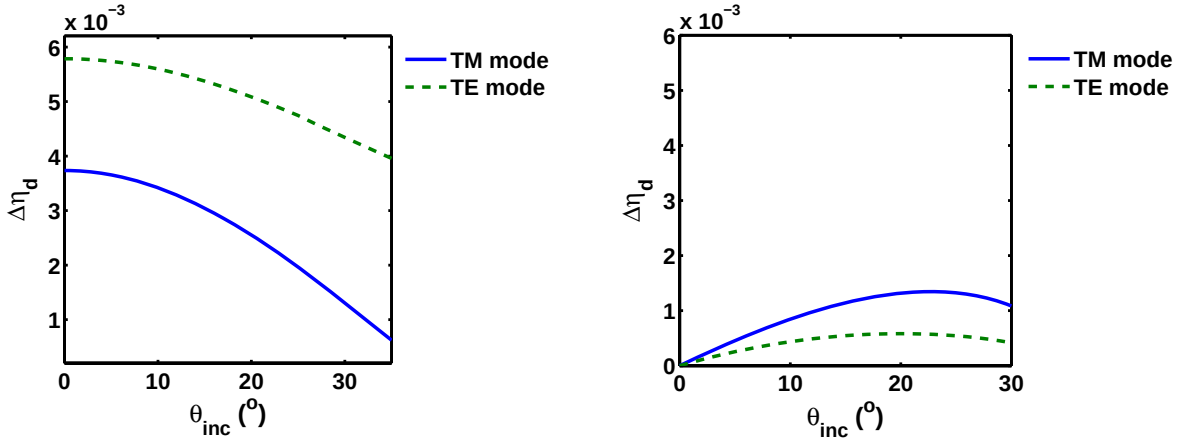

(a) (b)

Figure 4.13: Comparison of deviation of grating coupling strengths ($\Delta\eta_d$) for TE and TM incident beam when coupling to the same mode (solid-line: TM mode, dash-line: TE mode) (a) $\varphi_{inc} = 0^\circ$; (b) $\varphi_{inc} = 45^\circ$

4.3 2-D GMR using arbitrary crossed grating

Having two non-orthogonal grating vectors as in the arbitrary crossed-grating (Figure 4.2b) produces four first-order diffracted waves within two tilted planes. The higher-order diffracted waves (1,-1) and (-1,1), in Figure 4.14a, will have smaller tangential wave vectors (defined in Eq. (2.7) and (2.8)) when the grating skew angle increases (Figures 4.14b-d.). Therefore, the higher order modes might phase-match to the leaky mode and hence contribute the resonances.

Having resonant modes propagating along three tilted planes, coupling characteristics are more complicated than the previous case as will be discussed in the next section.

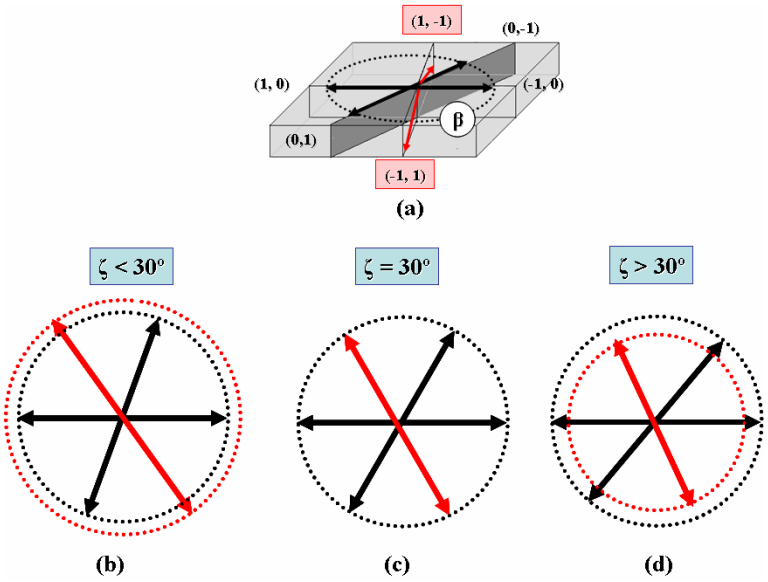

Figure 4.14: (a) First-order diffraction/guidance planes by an arbitrary crossed grating; phase matching diagram (b) $\zeta < 30^\circ$ (c) $\zeta = 30^\circ$ and (d) $\zeta > 30^\circ$, when $\Lambda_a = \Lambda_b$

For a 2-D GMR using a crossed grating with skew angle $\zeta < 30^\circ$, the higher-order waves (1,-1) and (-1,1) are cut off. In this case, the presence of two tilted fundamental diffraction planes makes the coupling characteristics at normal incidence similar to a structure using an orthogonal-lattice grating at oblique incidence. Therefore, this configuration does not improve the resonant performances and resonance with total reflection is still limited by the beam polarization. Decreasing the polarization dependence requires symmetric diffraction around the plane of incidence when coupling to resonant modes having the same propagation constant. Otherwise, the plane of incident has to be aligned along one of the grating vectors. Then, the active resonant modes will propagate along a direction overlapping with the incident plane as in the case of a rectangular-lattice grating.

The coupling characteristics of the TE resonant mode at normal incidence are demonstrated in Figure 4.15 for the cases of TE and TM incident beams when the crossed grating has identical periods ($\Lambda_a = \Lambda_b$). As seen, the incident beams in both cases are symmetrically coupled to each wave vector. However, only normal components of the diffracted waves contribute to the TE resonant mode.

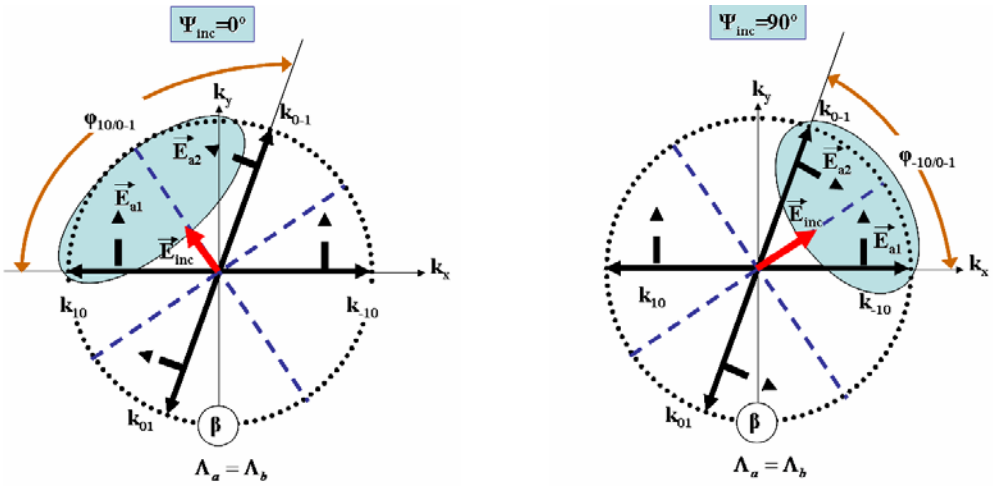

(a) (b)

Figure 4.15: Phase matching diagram of TE resonant mode in 2-D GMR with an arbitrary crossed grating ($\Lambda_a = \Lambda_b, \zeta \neq 30^\circ$) at normal incidence (a) $\psi_{inc} = 0^\circ$ (b) $\psi_{inc} = 90^\circ$

The decomposition of the TE and TM polarized beam with respect to the diffraction planes performs similarly to the square-lattice grating case. Due to coupling to the tilted planes, beams with orthogonal polarizations are individually coupled to the anti-symmetric or symmetric modes via different pairs of first-order waves while the diffraction angles between them ($\varphi_{10/0-1}$ for TE beam, and $\varphi_{-10/0-1}$ for TM beam, as in Figure 4.15 when coupling to anti-symmetric modes) are deviated proportionally to the polarization direction. As a result, the first-order diffracted waves accumulate phase mismatches and hence the resonance is located at different wavelengths for the

TE and TM beam. As discussed earlier, the phase mismatches can be removed when the grating parameters are optimized.

The graph in Figure 4.16a shows the phase mismatch of the first order wave (-1,0) caused by a crossed grating with skew angle $\zeta = 20^\circ$ in comparison to the one caused by a square-lattice grating when changing the grating filling factor. At the optimum grating parameters (r~ 0.01 and 0.088 μm), there exists no phase mismatch. Resonances in the structure then are expected to be polarization independent. Nevertheless, the deviation of the coupling strengths in Figure 4.16b is considerably large, and hence it prevents the spectral responses to be perfectly overlapped as will be seen in Figure 4.17b for the structure using the grating with 0.095-μm air-hole radius.

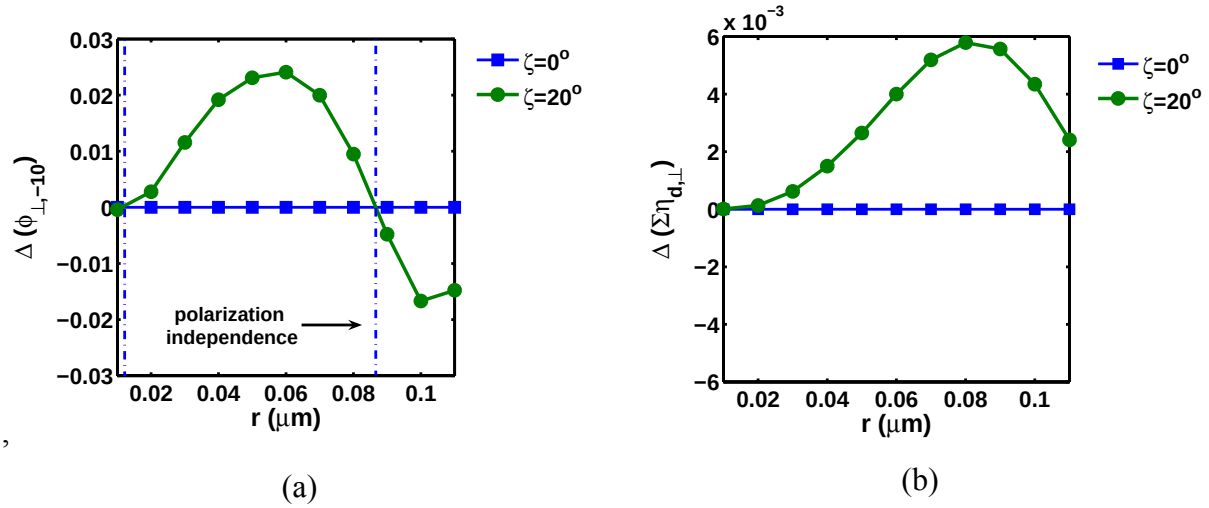

(a) (b)

Figure 4.16: Plots of (a) phase mismatches of wave (-1,0) (b) the deviation of the coupling strength, when applying the TE and TM polarized beam, versus the air-hole radius (r)of the crossed grating with $\zeta = 20^\circ$ in comparison to the square-lattice grating ($\zeta = 0^\circ$)

Figure 4.17a shows the fill factor (hole size) and film thickness that will produce resonances at a specific wavelength for two orthogonal polarizations. It is shown that for a grating with the proper parameters simultaneous resonance is located at the same wavelength for

both polarizations and therefore unpolarized light. The shift of resonances agrees with the phase mismatches when adjusting the grating fill factor in Figure 4.16a.

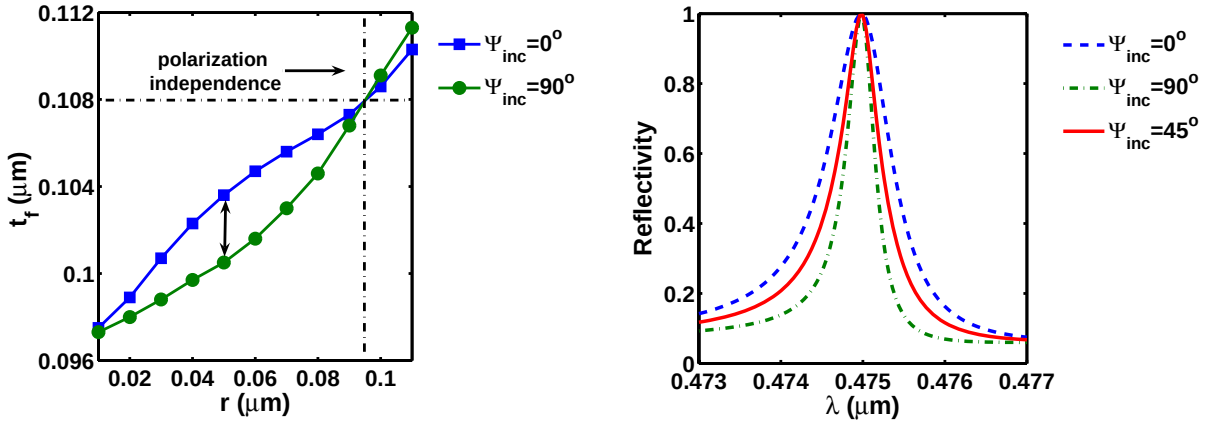

Figure 4.17: (a) Plot of the film thickness (t_f) for achieving the TE resonance at $\lambda_0 = 0.475\mu m$ versus the change of the air-hole radius (r) of the crossed grating with $\zeta = 20^\circ$ (b) spectral response when r=0.095 μm and t_f = ~0.108 μm

4.4 2-D GMR using hexagonal-lattice grating

Hexagonal-lattice grating is formed when the periodicity has a skew angle $\zeta = \sin^{-1}(\Lambda_a / 2\Lambda_b)$, as shown in Figure 4.2c. The grating generates fundamental diffraction along three crossed planes; two of them are equally slanted around the other. This configuration produces six first-order diffracted waves (p,q) =(0,1), (0,-1), (1,0), (-1,0), (-1,1), and (1,-1). The tangential first-order wave vectors are written as

$$k_{x,pq} = k_{x,inc} - \left(p\frac{4\pi}{\sqrt{4\Lambda_b^2 - \Lambda_a^2}} + q\frac{2\pi}{\sqrt{4\Lambda_b^2 - \Lambda_a^2}} \right), \text{ and } k_{y,pq} = k_{y,inc} - \left(q\frac{2\pi}{\Lambda_a} \right). \quad (4.2)$$

The diffracted waves have the same length once both periods are identical. In the case of equal periods the grating is referred to as *"regular-hexagonal lattice."* Otherwise, the tangential wave vectors of four waves ((0,1), (0,-1), (-1,1), and (1,-1)) along the symmetrically tilted planes are equal but different than the other two ((1,0) and (-1,0)). This grating configuration is referred to as *"irregular-hexagonal lattice."*

4.4.1 Coupling of resonant modes at normal incidence

The symmetric diffraction by the hexagonal-lattice grating at normal incidence results in phase matching the resonant modes with the same propagation constants counter-propagating along the common plane. Due to the higher-order fundamental diffraction, coupling to this type of resonant modes could occur in the three crossed planes, as demonstrated by the field scattering at resonance in Figure 4.18. Likewise, the backward and the additional crossed diffractions maintain the same paths as the forward diffractions. That increases the interaction between the modes and hence improving the resonance angular tolerance.

As the diffraction/guidance planes are not orthogonal, resonances in this structure are a contribution of resonant modes propagating within at least two crossed planes. Nonetheless, coupling to the counter-propagation resonant modes within only one plane can be obtained when using an irregular hexagonal-lattice grating.

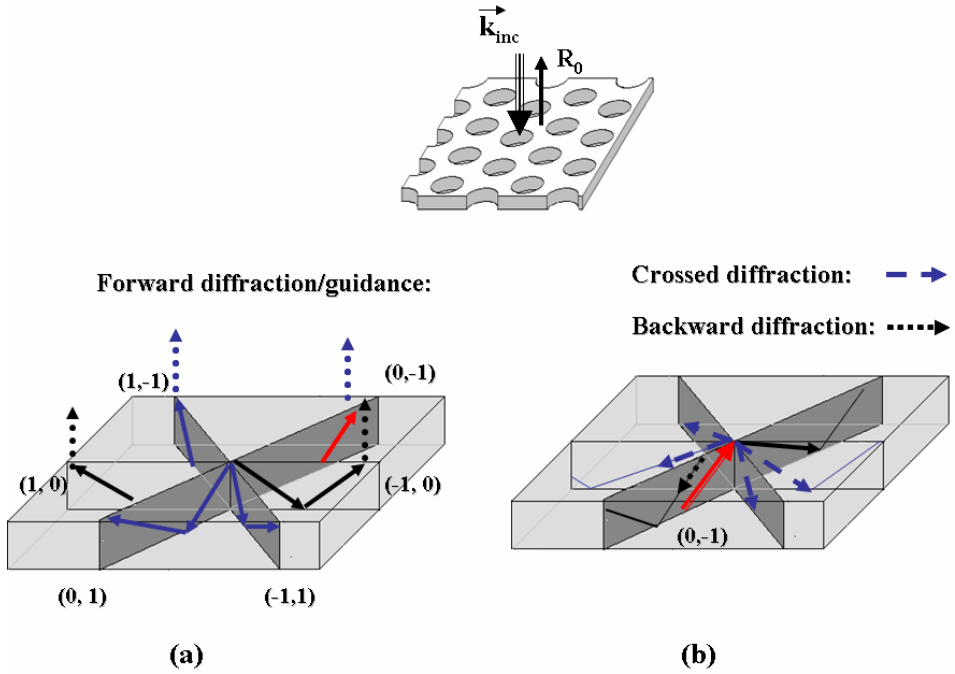

Figure 4.18: Scattering of field inside the structure with a hexagonal-lattice grating at resonance (a) forward diffraction (b) backward and crossed diffraction.

For a regular hexagonal-lattice grating ($\Lambda_a = \Lambda_b$ and $\zeta = 30^\circ$), the incident beam is partially coupled to all of the six first-order waves having the same tangential wave vectors. These waves contribute to the resonances unless some of the diffracted waves are polarized orthogonal to the resonant-mode polarization. In general, the coupling characteristics of an unpolarized incident beam can be considered as the decomposition of the field corresponding to TE and TM modes along the diffraction/guidance planes, $\vec{E}_{inc} = E_{a1}\,\hat{a}_1 + E_{a2}\,\hat{a}_2 + E_{a3}\,\hat{a}_3$. The drawing in Figure 4.19 is for the case of coupling to the TE resonant mode, where the unit vectors, a_1, a_2 and a_3, are perpendicular to each plane. Conceptually, the unpolarized beam is totally reflected at resonances as long as all of the field components are directly coupled to the resonant modes without rotating the polarization.

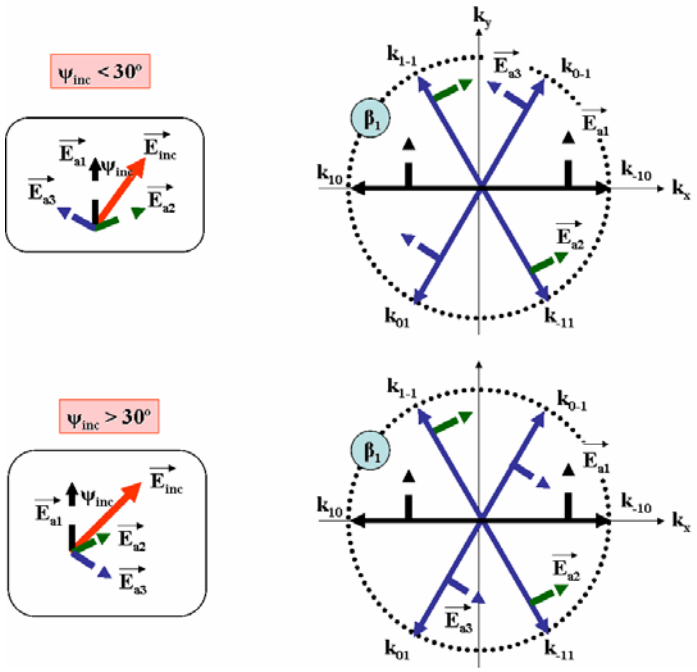

Figure 4.19: Phase matching diagram of TE resonant modes (β_1) in 2-D GMR using a regular hexagonal-lattice grating for the unpolarized beam

Due to the non-orthogonal periodicity in the hexagonal-lattice grating, the incident beam is diffracted into each wave with a slight rotation of the polarization and change in the coupling strengths ($\eta_{d,\perp,(p,q)}$ for TE modes and $\eta_{d,//,(p,q)}$ for TM modes) proportional to the incident beam polarization direction, as plotted in Figure 4.20. The structure calculated here applies the same design as in Section 4.2 but using the regular hexagonal-lattice grating with the same dimensions (periods, hole-radius, and depth.) The calculation results report small rotations of the diffracted-wave polarization when the incident beam is polarized at $\psi_{inc} = 0^\circ, 30^\circ, and\ 90^\circ$, with respect to one of the diffraction planes, by $\Delta\psi \sim 0.1^\circ, 0.7^\circ, and\ 0.7^\circ$, respectively. As a result, these additional polarization components of the diffracted waves are phase matched to the resonant modes and contribute to the constructive interference at the incident region. This reflected wave

becomes elliptically polarized with slightly reduced magnitude. The reduction of reflectivity is directly proportional to the degree of rotation.

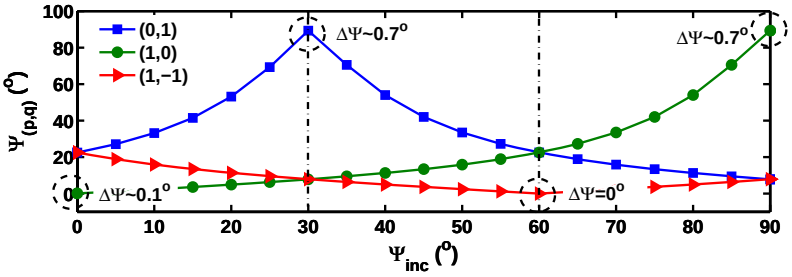

(a)

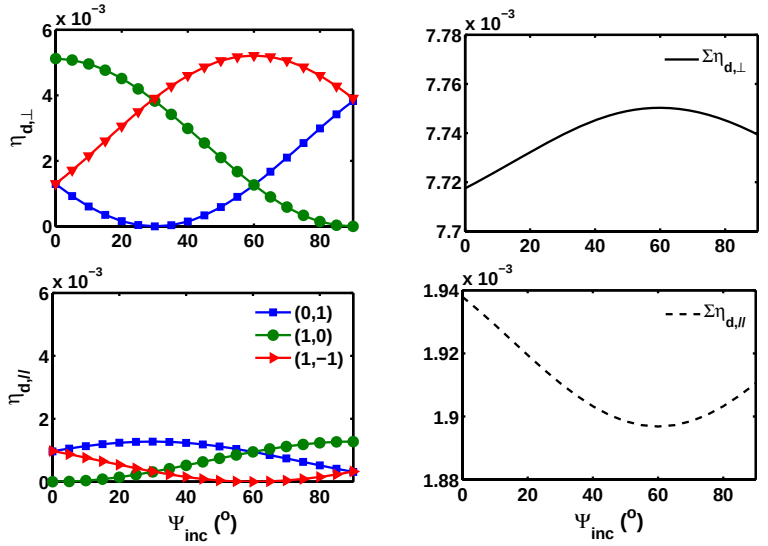

(b)

Figure 4.20: Plots of (a) polarization direction and (b) normalized powers dissipated to first-order waves by the regular hexagonal-lattice grating at normal incidence versus ψ_{inc}

While rotating the incident beam polarization, the total coupling strengths ($\sum \eta_{d,\perp}$ and $\sum \eta_{d,//}$) remain almost constant. The deviation becomes slightly larger when coupling to the TM resonant mode. Therefore, resonances have linewidths almost independent of the incident polarization.

The resonance locations however might be slightly shifted due to the phase mismatch when coupling to three non-orthogonal planes.

Obtaining both TE_0 and TM_0 resonances located at the same wavelength can be achieved in the 2-D GMR by shifting the film thickness to satisfy the phase matching of the particular resonant mode while keeping the other dimensions constant. The resonance responses are calculated and plotted versus the incident beam polarization in Figure 4.21.

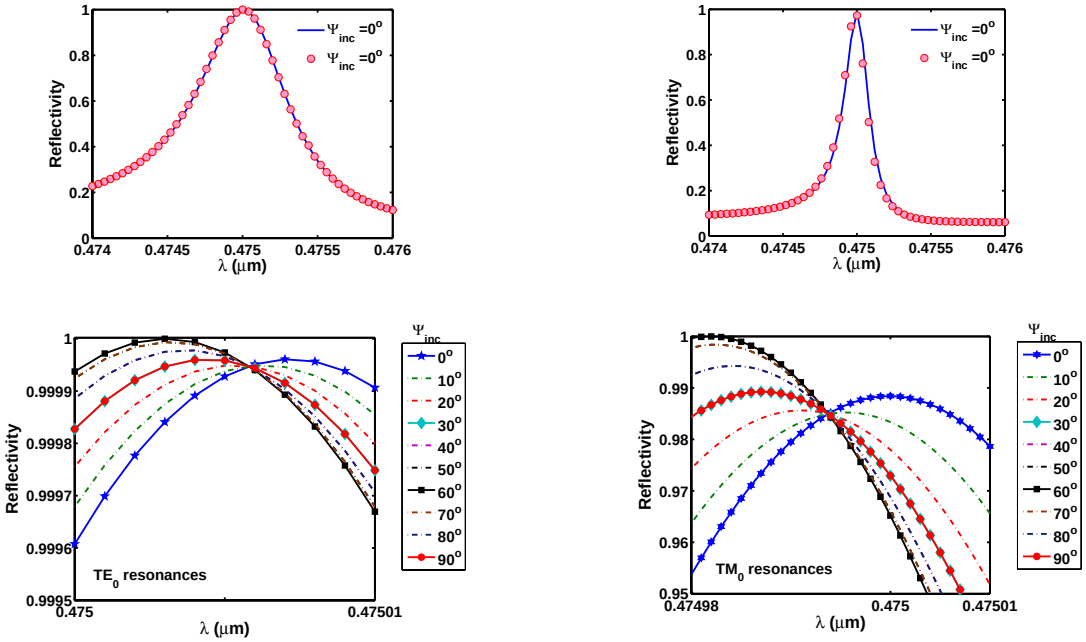

(a) (b)

Figure 4.21: Spectral responses versus the polarization direction $\psi_{inc} = 0^o$ to 90^o (a) TE_0 resonance: $t_f \sim 0.107 \mu m$ (b) TM_0 resonance: $t_f \sim 0.155 \mu m$.

The RCWA calculations show an almost invariant spectral response to the incident polarization. The shift of resonance response is more noticeable when coupling to the TM_0 resonance. The zoom-in plots of both cases agree in the fact that total reflection is accomplished only when

$\psi_{inc} = 60^{\circ}$. That indicates no phase mismatch and no rotation of the polarization (Figure 4.20a), as the incident beam is totally coupled into resonant modes along two planes. The reduction of reflection appears more significant when the polarization deviated away from 60 degrees, especially in the TM_0 resonance case. That corresponds to the fact that the polarization is rotated by the diffraction of the grating. The partial reflected beam has a polarization slightly deviated from the incident beam (Figure 4.22a) in addition to the change of the polarization state (Figure 4.22b.)

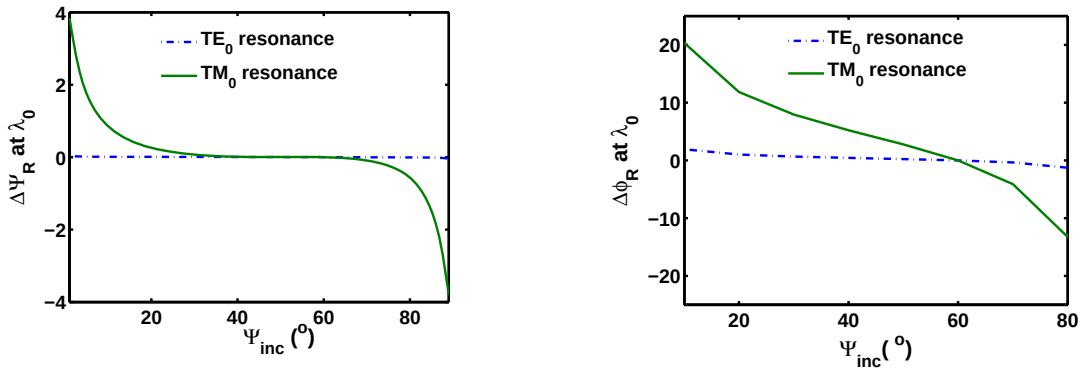

(c) (d)

Figure 4.22: Plot of (a) polarization rotation ($\Delta\psi_R = \psi_R - \psi_{inc}$) and (b) phase ($\Delta\phi_R = \phi_{E_{r,//}} - \phi_{E_{r,\perp}}$) of the reflected beam at λ_0 versus ψ_{inc}.

The crossed coupling between these resonant modes in three crossed planes instead of two reduces the phase mismatches. Therefore, this polarization dependence is not as significant as the case when coupling to modes propagating along single plane in 1-D GMR or propagating along two-tilted planes in 2-D GMR with rectangular-lattice grating at oblique incidence or with an arbitrary crossed grating, as discussed earlier.

Using an irregular hexagonal-lattice grating ($\Lambda_a \neq \Lambda_b$), the resonance is sensitive to the incident polarization due to the shift of the propagation constants of the resonant modes (β_1) along a plane (±1,0) away from that of the resonant modes (β_2) along two tilted planes (0,±1) and (1,-1)/(-1,1). The phase matching diagram of TE resonant mode (β_1) is depicted in Figure 4.23a. Hence, the unpolarized beam is partially reflected at resonant wavelength, as in the case of counter-propagation resonant modes in 2-D GMR using a rectangular lattice grating. In addition, the fact that the incident beam is also coupled to modes propagating along two tilted planes, polarization issues can be removed when designing the structure properly as discussed.

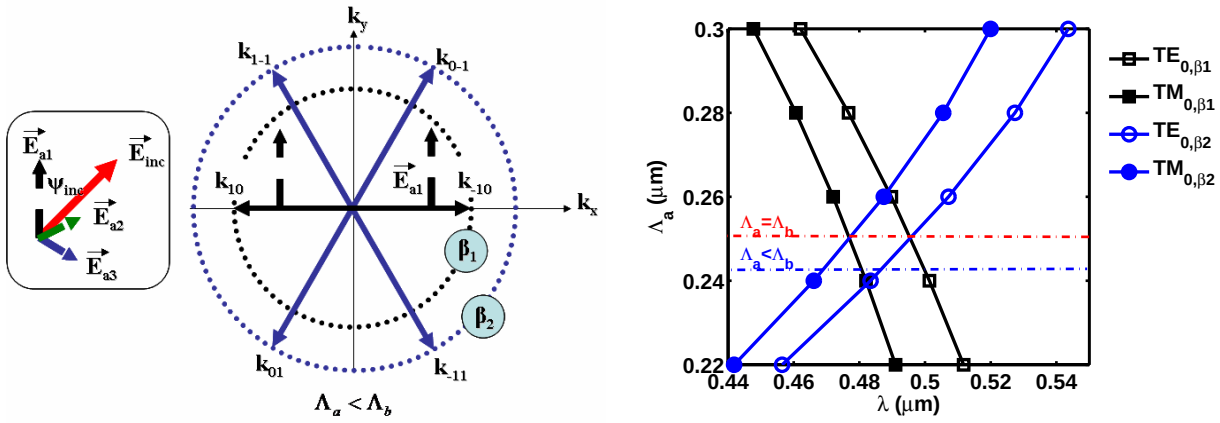

(a) (b)

Figure 4.23: (a) Phase matching diagram of TE resonant mode (β_1) for an unpolarized incident beam, when $\Lambda_a < \Lambda_a$ (b) plots of resonances versus shift of period Λ_a, calculated by HWA

Using the HWA calculations, resonances relating to each resonant mode are calculated in Figure 4.23b when shifting one period Λ_a. That produces four fundamental resonances. Changing one of the periodicities results in the shift of the tangential wave vectors of the all first-order waves simultaneously. Therefore, all resonances are shifted in manners defined by the change of the

modal propagation constants. As seen, the tangential wave vectors $k_{xy,\pm 10}$ (Eq. (4.3)) increase when designing the grating with larger period Λ_a. Consequently, the related resonances move toward the shorter wavelengths.

The main advantage of this structure is that at least three fundamental resonances, instead of two, with total reflections are formed when the incident beam is polarized normally or in plane of the diffracted waves (-1,0) and (1,0). One resonance is a contribution of TE_0 or TM_0 mode with a propagation constant β_1 via the diffracted waves (-1,0) and (1,0). The others are due to both fundamental modes with propagation constants β_2 via the diffracted waves (0, 1), (0,-1), (-1, 1), and (1,-1).

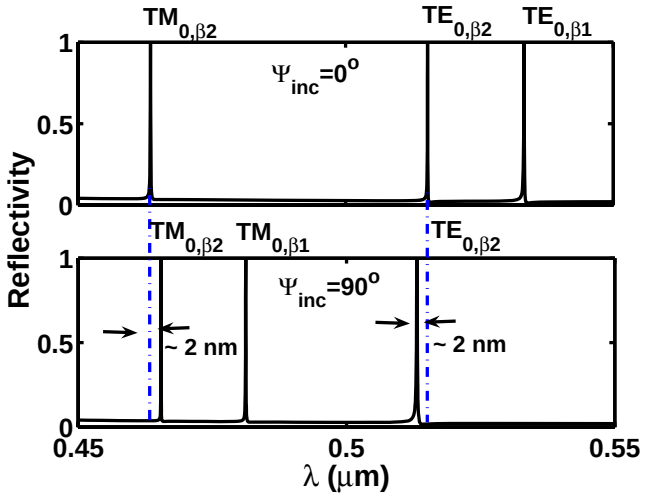

Figure 4.24: Spectral responses of the structure in Figure 4.19b having $\Lambda_a < \Lambda_a$, when incident polarization is ψ_{inc}=0º and 90º

Using the RCWA calculations, the resonance responses of both incident polarizations are plotted in Figure 4.24. The graphs show a slight shift of the resonances for modes having propagation constant β_2, when rotating the incident polarization by 90º.

4.4.2 Coupling of resonant modes at oblique incidence

In the hexagonal-lattice grating design, there exists six possible planes of incidence along which total reflection at oblique incidence is guaranteed when the incident beam is polarized along one of the diffraction planes (solid line in Figure4.25a) or one of the planes between them (dash line in Figure 4.25a.) In any case, the tangential wave vectors are deviated while the symmetry of diffraction is maintained around the plane of incidence. The phase matching diagram for $\varphi_{inc} = 0^\circ$ and $\varphi_{inc} = 90^\circ$ are exhibited in Figures 4.25b and 4.25c respectively.

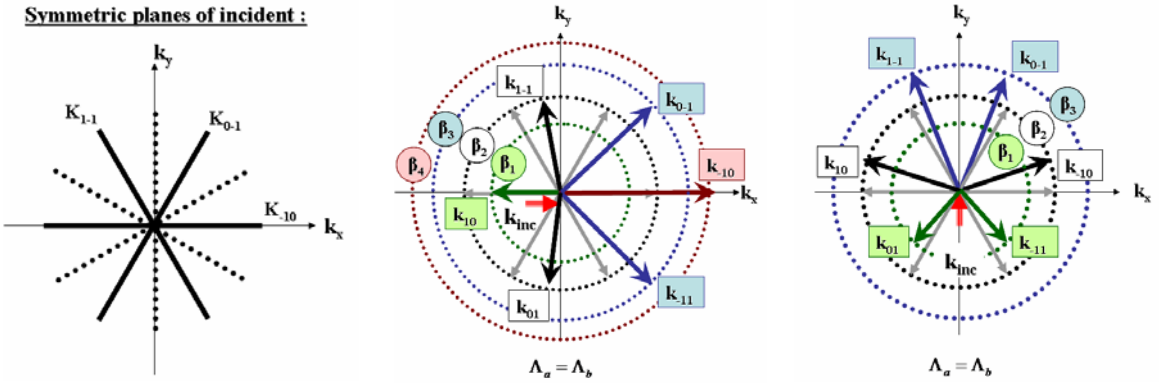

(a) (b) (c)

Figure 4.25: (a) Symmetric planes of incidence; phase matching diagram of the resonant modes in 2D-GMR with a regular hexagonal-lattice grating at oblique incidence (b) $\varphi_{inc} = 0^\circ$; (c) $\varphi_{inc} = 90^\circ$

Resonant modes with four possible propagation constants created when $\varphi_{inc} = 0^\circ$ can contribute to eight fundamental resonances. However, not all of them are phase matched due to the presences of two single-propagation modes along the waves (1,0) and (-1,0). Thereby, the resonances with total reflection at this setting are located at six wavelengths instead, and so are the ones when $\varphi_{inc} = 90^\circ$. Six fundamental resonances are formed by the phase matching of

resonant modes propagating along three pairs of first order waves when $\varphi_{inc} = 90^{\circ}$. In both cases, the separation of resonances is further broadened and noticeable for large incident angle as shown in Figure 4.26. Two fundamental resonances (TE_0 and TM_0) relating to each propagating constants are calculated versus the change of the incident angle (θ_{inc}) using the homogeneous waveguide approach. Resonances move toward the longer wavelengths when decreasing the modal propagation constants. As a result, the higher-order resonances might appear near resonances at a shorter wavelength. That can be seen in the calculation results in Figure 4.26b (dash plots).

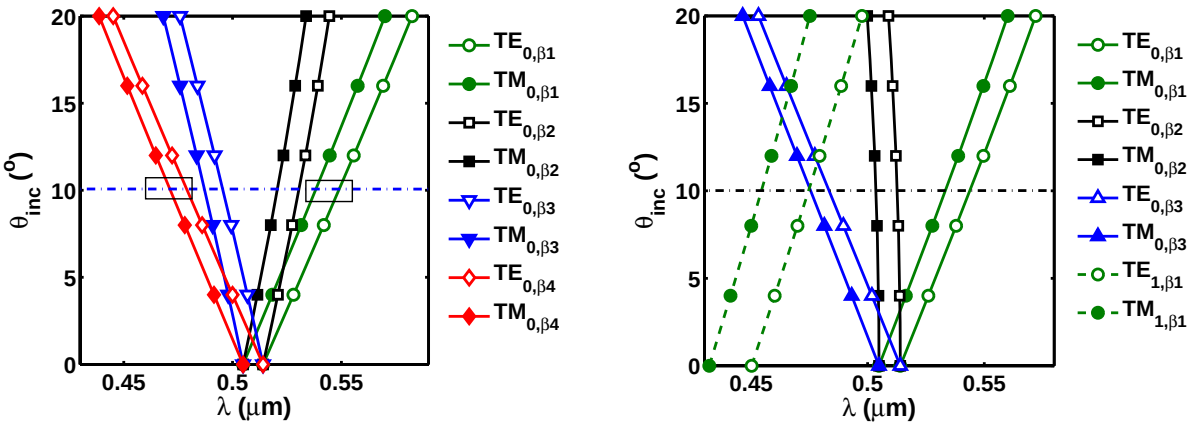

(a) (b)

Figure 4.26: Plots of resonances in of GMR with hexagonal-lattice grating ($\Lambda_a = \Lambda_b$) at (a) $\varphi_{inc} = 0^{\circ}$ (b) $\varphi_{inc} = 90^{\circ}$ versus θ_{inc}, calculated by HWA.

That explains the presence of the extra resonance when calculating the spectral responses using RCWA in Figure 4.27. In this calculation, the plane of incident is set at $\varphi_{inc} = 90^{\circ}$ and the incident angle is $\theta_{inc} = 10^{\circ}$. Like the other structures at oblique incidence, resonances are

inherently polarization dependent. Remove this dependency requires optimizing the grating design to eliminate the phase mismatches.

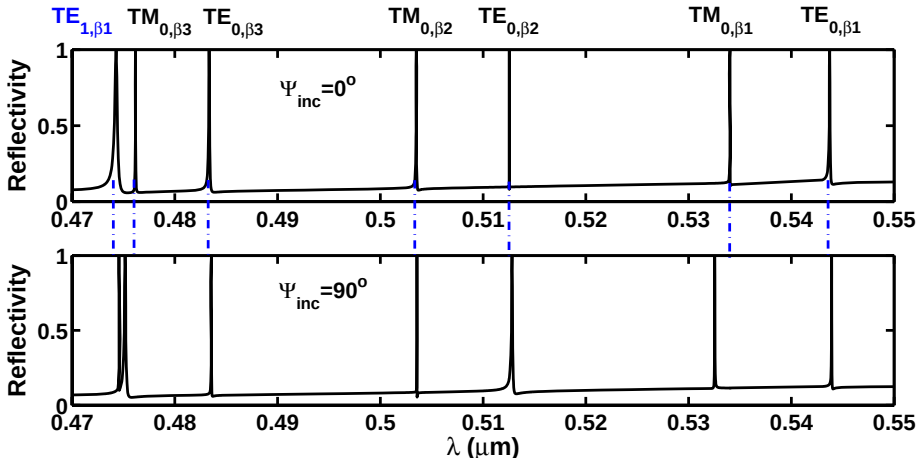

Figure 4.27: Reflectivity spectrum of GMR with hexagonal-lattice grating ($\Lambda_a = \Lambda_b$) at $(\theta_{inc}, \varphi_{inc}) = (10^\circ, 90^\circ)$

In advantage, the first-order diffraction in this structure at oblique incidence can be manipulated in a number of symmetric manners. Coupling to four resonant modes with the same propagation constant is possible. This is accomplished by properly adjusting the periodicities and the incident angle. The coupling characteristics then perform similarly to the polarization independent GMR filter using a square-lattice grating at normal incidence, as displayed in Figure 4.28. The resonant modes do not propagate in perpendicular directions to each other, hence the phase mismatches when applying TE and TM polarized beams still exist.

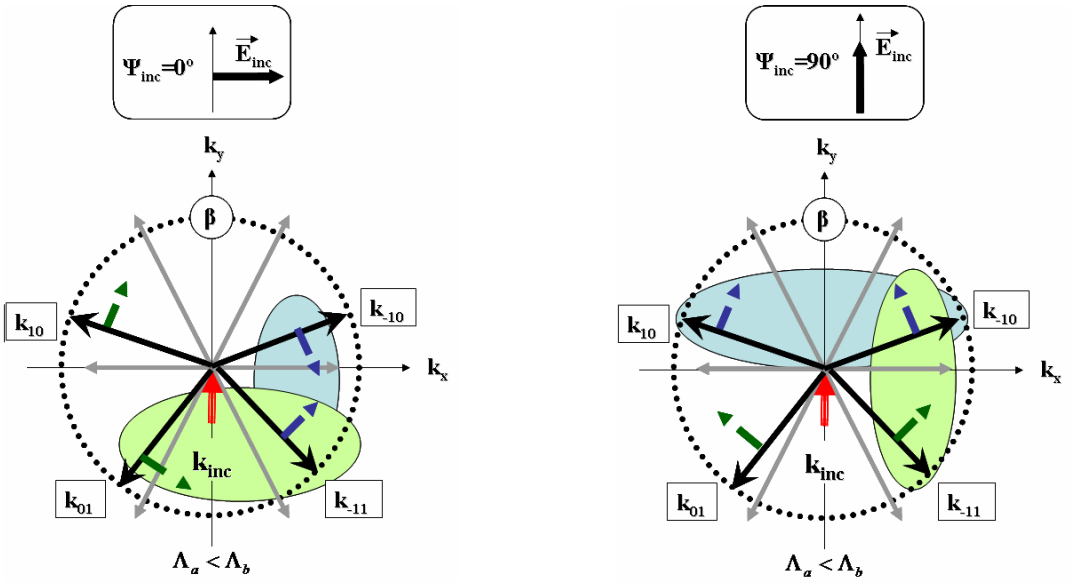

Figure 4.28: Phase matching diagram of four resonant modes in 2-D GMR using an irregular lattice grating at oblique incidence $\varphi_{inc} = 90^{\circ}$ and coupling characteristics for (a) TE and (b) TM polarized beam

The interaction of the forward waves (1,0)/(-1,0) and the backward waves (0,1)/(-1,1) with respect to the plane of incidence prevents the phase matching of all of the four resonances from forming at the same wavelength. The graph in Figure 4.29 shows the opening of the resonant band gap (calculated by RCWA: solid-line plots) around the pre-determined resonant angle $\theta_{inc} \sim 10^{\circ}$ (using HWA: dash-lines plots.) As a result, resonances are located at the upper and lower resonant band. The shift of the band for TE and TM polarizations incident beam is noticeable. Achieving polarization-independent resonances is then possible and can be even more practical compared to the previous designs. As seen in the plot, at the proper incident angle, the resonances at the upper resonant band of the TE beam and the lower resonant band of

the TM beam are shifted and properly intersect at the same wavelength. The phase mismatches are then removed without the need of a precise grating filling factor optimization.

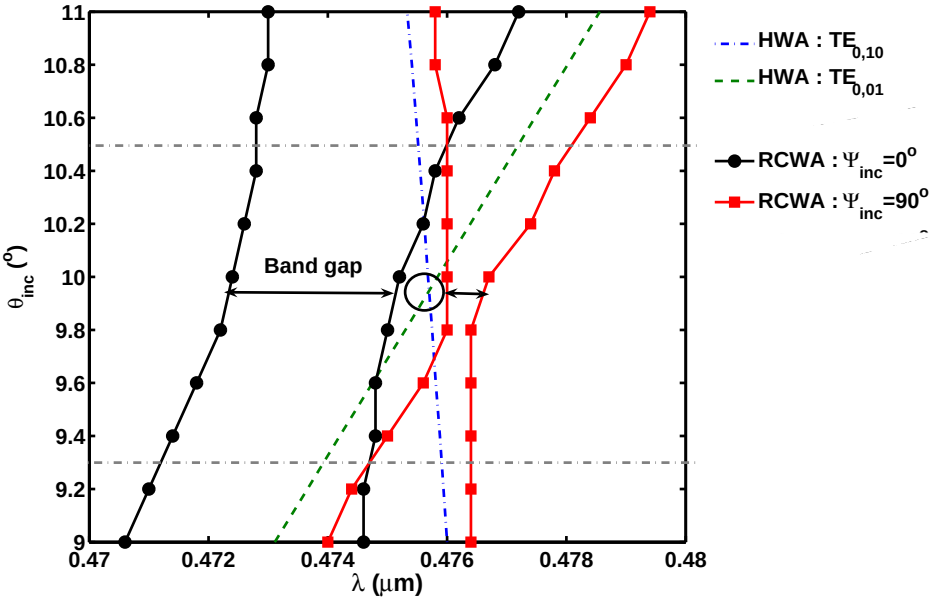

Figure 4.29: Plots of TE_0 resonant wavelengths as a contribution of waves (1,0)/(-1,0) and (0,1)/(-1,1) versus the incident angle θ_{inc} in 2-D GMR using an irregular hexagonal-lattice grating ($\Lambda_a = 0.25\mu m$ and $\Lambda_a = 0.27\mu m$)

The resonance responses of the structure at three incident angles in Figure 4.30 indicate the shift of the TE_0 resonances for TE and TM incident beams. The resonances overlap at the proper angle. The spectral linewidths on the other hand can be adjusted via the grating dimensions independently without introducing phase mismatches as was the situation for the other cases mentioned earlier.

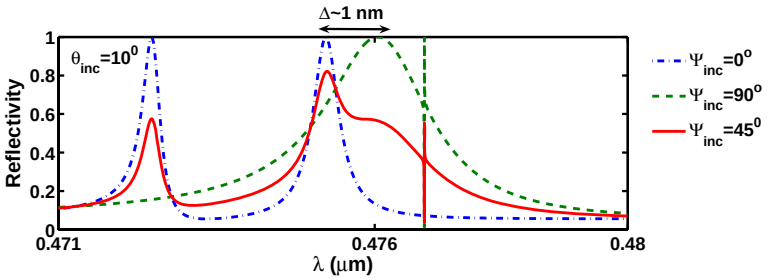

(a)

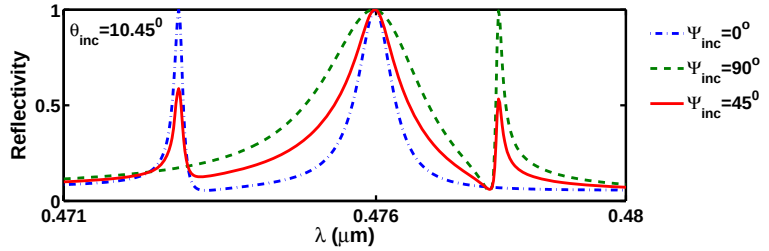

(b)

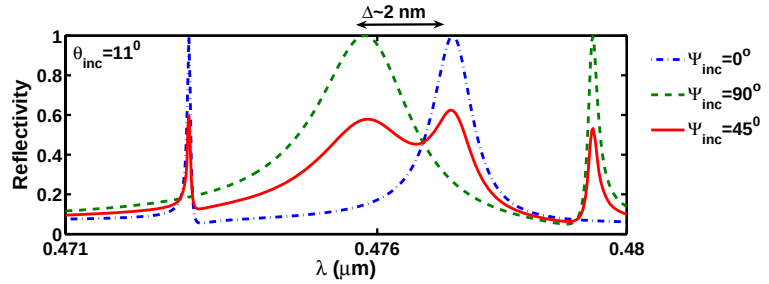

(c)

Figure 4.30: Reflectivity spectrum of GMR in Figure 4.29 at (a) $\theta_{inc} = 10^{\circ}$ (b) $\theta_{inc} 10.45^{\circ}$ and (c) $\theta_{inc} = 11^{\circ}$

4.5 Calculations of the leaky mode dispersion

Leaky-mode means having a complex propagation constant and that can be directly related to the resonance linewidth as discussed earlier. For the 2-D structure, there are a number of coupling characteristics reliant on the incident beam (polarization and incident direction) and the grating

pattern. Therefore, the resonance-linewidth calculations through the complex propagation constant (Eq. (3.2)) only may be not accurate as was the case in 1-D GMR. The linewidth depends on the grating coupling strengths regarding to the incident beam polarization as well. Nevertheless, the calculation of the modal dispersion is of interest. This demonstrates the actual interaction between the modes as well as the active resonant modes for a particular incident angle.

The Bloch mode approach (Section 2.3.2) is used to calculate the complex propagation constants of the leaky modes in 2-D GMR using a rectangular-lattice grating. Using this approach requires engineering the calculation unit cell along the direction of propagation. Hence, the calculation is effective only for modes propagating in an individual diffraction/guidance plane when the grating has different periods ($\Lambda_a \neq \Lambda_b$). The interactions of the modes in the orthogonal plane are also taken into consideration while forming the scattering matrix within the unit cell. To simplify the calculations, the surface grating used here has a rectangular groove profile. Besides, the unit cell is selected in a symmetric manner as shown in Figure 4.31. There exist three individual slides within the unit cell. Two of them are identical. The scattering matrix along the calculation region is then formed by the symmetric S-matrix multiplication as mentioned in Section 2.3.2. For the 2-D case, the sub-S-matrix is individually calculated by considering each one of these slides to be periodic along y- and z-axis. The propagations of the Bloch modes are determined by solving the Eigen value problem in Eq. (2.53) and (2.54). Only complex propagation constants with small imaginary parts actually propagate and may cause resonances.

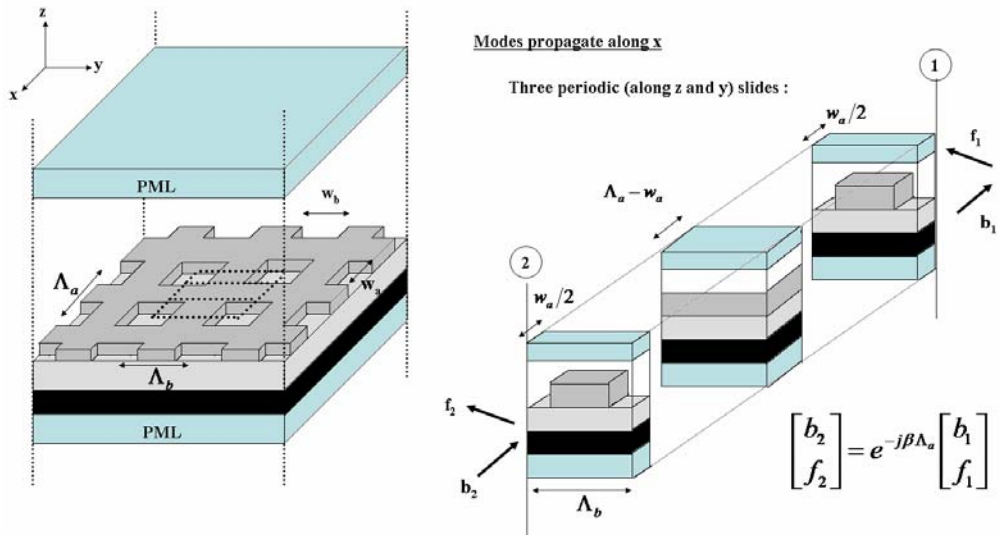

Figure 4.31: Unit cells of 2D-GMR with a rectangular-lattice grating (rectangular-shape hole)

Calculating the complex propagation constants of the leaky modes supported by a 2-D GMR with square-lattice grating ($\Lambda_a = \Lambda_b = 0.25\mu m$) in Section 4.2.1, the circular-hole grating ($r = 0.1\mu m$ or FF=0.5) is transformed to be a square-hole grating with dimensions of 177.2 x 177.2 nm maintaining the grating effective index. The dispersion graphs in Figure 4.32 represent the modes supported in this structure. The calculation results are plotted in term of the real and the imaginary parts of the normalized modal indices (n_{eff}) to the ratio Λ_a/λ when each one of them propagates in opposite directions, called the forward and the backward modes. It is shown that the structure supports two fundamental modes, TE_0 and TM_0. The dispersion plots of each mode demonstrate the formation of the band gap due to the interaction of the forward and the backward modes in the calculation plane. The additional band gap is due to the modes counter-propagating along the orthogonal plane. This band-gap is shifted from the actual ones under the calculation. The dispersion plots also exhibit the overlap of the forward-TM_0 mode and the

backward-TE_0 mode indices at the same wavelength where the resonant band gap is generated when applying the proper setting.

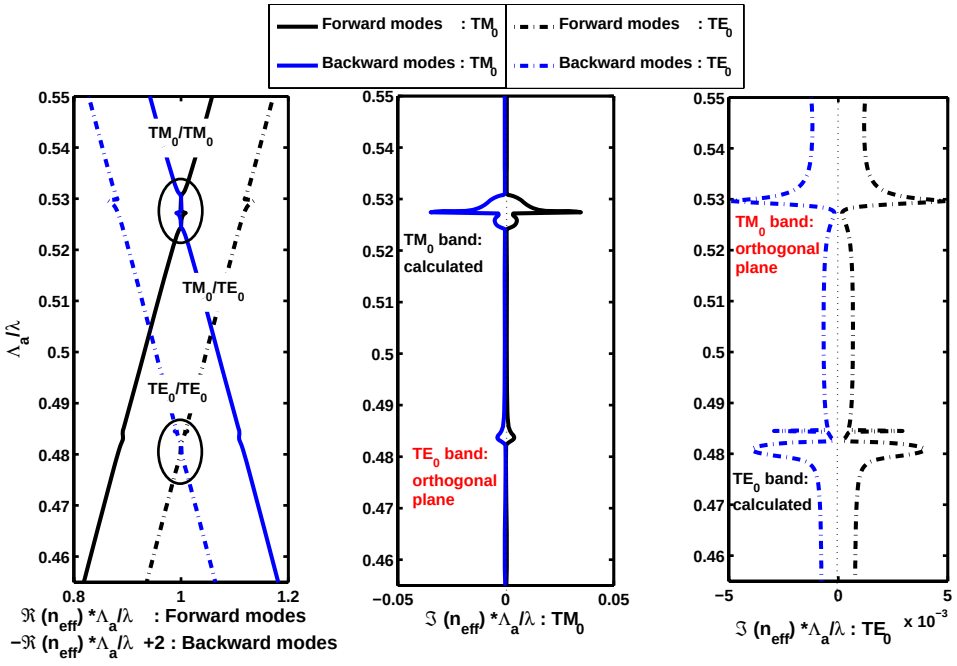

(a) (b) (c)

Figure 4.32: Dispersion of leaky modes (a) normalized $\Re\{n_{eff}\}$ $\mathrm{Re}\{n_{eff}\}$ (b) normalized $\Im\{n_{eff}\}$ of TM_0 guided modes (c) normalized $\Im\{n_{eff}\}$ of TE_0 guided modes

Achieving the resonances correlating to the normalized modal indices, the incident direction can be simply estimated using the phase matching condition of the first-order waves and the leaky modes as

$$\Re\{n_{eff}\}\times\frac{\Lambda_a}{\lambda}\bigg|_{\pm 10} \cong n_{inc}\sin\theta_{inc}\cos\varphi_{inc}\frac{\Lambda_a}{\lambda}\mp 1,$$

and

$$\Re\{n_{eff}\}\times\frac{\Lambda_b}{\lambda}\bigg|_{0\pm 1} \cong n_{inc}\sin\theta_{inc}\sin\varphi_{inc}\frac{\Lambda_b}{\lambda}\mp 1 \qquad (4.3)$$

At normal incidence, equation (4.3) insures that two resonances are located around the TE_0 and TM_0 band gaps, where the normalized modal indices of the leaky modes equal to 1. Both first-order counter-propagating waves ($\pm 1,0$) or (0, ± 1) are coupled to the leaky mode. Achieving resonance by coupling to the forward and backward modes with orthogonal polarizations, the normalized modal indices happen to be ~1.057 and ~0.943. In this case, the plane of incidence needs to be set at $\varphi_{inc} = 45^\circ$ in order that the polarized incidence beam can coupled to both TE and TM mode. Thus, the first order waves (-10/0-1) and (10/01) are phase matched to the forward TE_0 modes and backward TM_0 mode, respectively. The incident angle calculated from Eq.(4.3) is $\theta_{inc} = 9.14^\circ$. The RCWA calculations in Figure 4.33 demonstrate the agreement of the resonant responses to the modal dispersion and the phase matching condition in Eq. (4.3) for both the cases at normal (Figure 4.33a) and oblique (Figure 4.33c) incidences.

The coupling characteristics at oblique incidence however are polarization selective especially when the incident plane is along one of the fundamental diffraction/guidance planes, as discussed earlier in this chapter. Figure 4.34 illustrates resonances at oblique incidence $(\theta_{inc}, \varphi_{inc}) = (10^\circ, 0^\circ)$ relating to the modal dispersion plot, when the incident beam is TE polarized. As shown, only TE resonances are formed by (-1, 0) and (1,0) waves. They are phase matched to TE_0 forward and backward modes and located at different wavelengths. The first order waves (0, ±1) on the other hand are phase matched to both TE and TM modes located nearby their individual band gaps. That reports the existence of the interaction between the forward and the backward modes at these resonances.

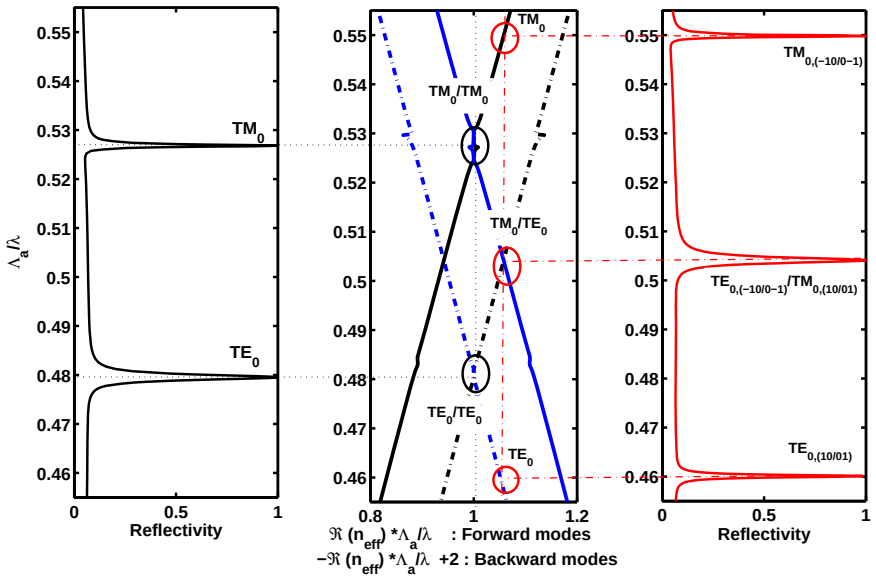

(a) (b) (c)

Figure 4.33: Spectral response of the resonances at (a) normal incidence/(c) at $(\varphi_{inc}, \theta_{inc}) = (45^{\circ}, 9.14^{\circ})$ and (b) band diagram of structure in Figure 4.32

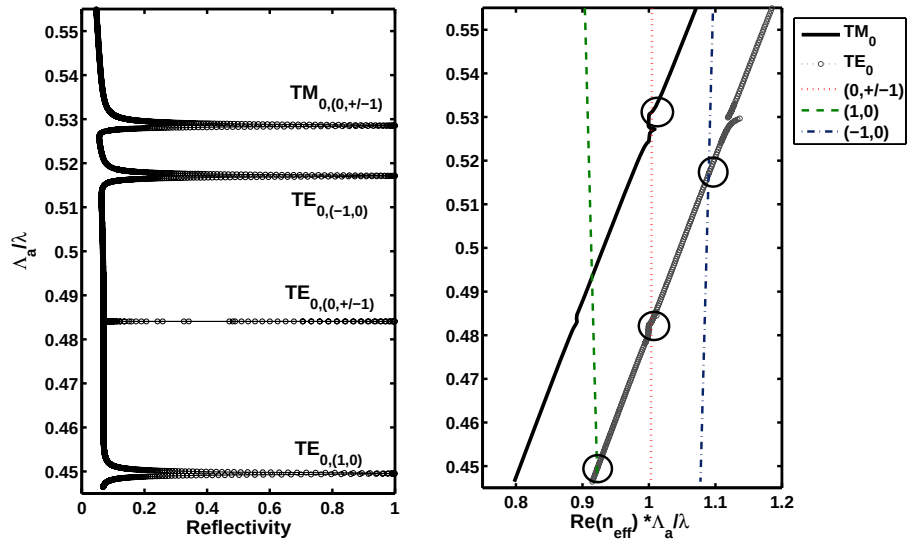

(a) (b)

Figure 4.34: (a) Spectral response and (b) matching plots of normalized modal index (TE_0/TM_0) and the normalized ±1 waves (calculated from Eq.(4.3)) at $(\theta_{inc}, \varphi_{inc}) = (10^{\circ}, 0^{\circ})$, and TE-polarized beam.

4.6 Summary

In this chapter, the coupling characteristics of the incident beam to the leaky modes contributing to the resonances of the 2-D GMR structure using three grating patterns: rectangular lattice, arbitrary cross lattice and hexagonal lattice were demonstrated. In all cases, the discussions are simplified based on the decomposition of the incident beam with respect to the first-order diffraction pattern and the resonant mode. Therefore, resonance with total reflection occurs once all components of the incident beam are phase matched to the leaky modes propagating in a common plane or different planes at the same wavelength. The polarization of the reflected beam remains unchanged.

Using symmetric grating patterns, a square- or a regular hexagonal-lattice grating, at normal incidence, the total reflection is obtained at resonances, and resonances are polarization independent as well. Due to the slight rotation of the diffraction-wave polarization by the regular hexagonal-lattice grating, the incident beam is simultaneously coupled to the leaky modes propagating along the three tilted planes instead of two planes based on the incident beam decomposition. This introduces a rotation of the reflected beam polarization, however the reduction of the reflectivity is not that significant (<1%) as well as the spectral responses remain almost unchanged while rotating the incident beam polarization.

The incident beam polarization becomes the main concern once the symmetry of diffraction is broken by either periodicity or the incident direction. It is necessary to select the plane of incident in such a way that the polarized incident beam is symmetrically diffracted around it. The phase mismatches when coupling the TE and TM beams to the same resonance mode can be removed by controlling the grating fill factor. Another approach presented was the

use of the irregular hexagonal-lattice grating to couple the incident beam along four diffracted waves with equal tangential wave vectors. The interaction of these modes forms the resonant band gaps but shifted when utilizing orthogonal polarized incident beam. At the proper incident angle, the intersection of the upper and the lower bands of the TE and TM beams, respectively or vice versa, introduces resonance independent of the incident polarization. The requirements of achieving the precise grating fill factor are then minimized.

In addition to the polarization issue, the advantage of having multiple diffraction/guidance planes in 2-D GMR was shown to have more degree of freedom in achieving multiple fundamental resonances with total reflections at both normal and oblique incidence. A number of fundamental resonances increase proportional to the diffraction/guidance planes. Resonance locations are adjustable directly through the grating periods or the incident direction when applying the proper polarized beam. The controllability of resonance responses is practical. Therefore, in next chapter, 2-D GMR will be proposed as controllable multi-line narrow-band spectral filters. The design methodology including the limitation will be demonstrated.

CHAPTER 5 : MULTI-LINE GMR FILTERS

In this chapter, multiple wavelength narrow-band reflection filters are developed based on the resonance anomaly in the guided-mode resonant (GMR) structure. Multiple resonances are produced once the structure supports multiple leaky modes that could include the higher-order waveguide modes or only the fundamental waveguide modes when using a 2-D grating for instance. The capability of controlling resonances is necessary and very useful in many applications. The 2-D GMR is proposed and demonstrated for the controllable multi-line spectral filters with spectral separation in a wide range which is not possible with 1-D GMR as the limitation of the structure material.

5.1 Overview

Multi-line resonant filters have been generated using 1-D GMR structure [36-38], where the multiple resonances are achieved by coupling to multimode leaky waveguide structures. These have been done by increasing the thickness of the guiding region or adding either thin-film layers or gratings into the original GMR structure. Multi-line resonances are achieved by insuring that each diffracted order is coupled to a guided mode in this structure. However, as will be shown, it is not possible to control the location of all the resonances (and their separation in a broad spectral range) without requiring specific change in the material refractive index which may not be feasible.

Multi-line reflection GMR filters are developed and the resonance locations are controlled by adjusting the physical dimensions of the structures (thickness, and periods, etc) and not its material properties (refractive index). This is accomplished by utilizing the diffraction properties of 2-D GMR filters, where the presence of multiple planes of diffraction generated by the 2-D grating makes multiple fundamental resonances. The locations of these resonances can be controlled by adjusting the periodicities of the two-dimensional grating structure and the geometric shape of the unit cell.

First, the limitations of 1-D GMR structures in specifying the location of the multi-line resonances owing to the requirement to specify the refractive index of the material for a given resonance location is demonstrated. Meanwhile, the material dependency of a controllable multi-line 1-D GMR filter is also briefly discussed. The utilization of multi-plane diffraction characteristics in 2-D GMR structures will be investigated and contrasted with 1-D GMR structures. A design approach and methodology is presented for multi-line filters in 2-D GMR structures. Two-line reflection filter designs in the visible spectrum with spectral line widths less than 1 nm and a controllable spectral separation up to 30 % of the short resonant wavelength are presented using rectangular-lattice grating GMR structures. Three-line filters are designed in a hexagonal-lattice grating GMR structure. Finally, the resonance characteristics and the advantages of each approach are discussed. In addition, the last section investigates the fabrication tolerance and the impact of each structure dimension on the resonance linewidth as well as the resonance location.

5.2 Multi-line 1-D GMR Filters

As discussed in Chapter 3, the resonances depend on the guided modes supported in the structure as well as the diffraction characteristics of the grating. One dimensional grating at an in-plane incidence ($\varphi = 0^\circ$) diffracts the incident beam along a common plane regardless of the direction of each diffracted order as shown in Figure 3.4. This restricts all of the leaky modes in the GMR structure to propagate along the same plane. Hence, the implementation of multiple-resonance structure is accomplished by coupling each first-order diffracted wave to a different guided (higher) order mode. At oblique incidence, two fundamental resonances via +1 and -1 waves are individually formed as a contribution of a single-propagation mode. Resonances however are not tolerant to the incident direction. Designing the structure at normal incidence is more desirable and mainly implemented in this work. The symmetry of the diffraction pattern results in phase matching of counter-propagation resonant modes with the same propagation constant. This can be initially defined by the grating period.

Like the traditional three-layer slab waveguide, the number of guided modes depends on the geometry and material properties of the structure. More modes propagate as the waveguide normalized frequency, or V number [72], increases.

$$V = k_0 t_f \sqrt{n_f^2 - n_s^2} \tag{5.1}$$

This can be done by increasing the thickness of the guiding region (t_f), or enhancing the index contrast between the film (n_f) and the substrate (n_s). The design approach [21] is to numerically optimize various structure parameters, such as the grating period, the refractive index contrast of

the structure and the thickness of the guiding region, to obtain the resonances at the desired locations.

Figure 5.1 shows the spectral response of a 1-D GMR that supports the first two leaky modes (TE_0 and TE_1) within the visible spectrum. In this graph, a TE polarized normal incident beam is considered. Then, the first resonance ($\lambda_1 = 475\,nm$) is due to the phase matching between the first order diffracted waves and the TE_1 mode. The second resonance ($\lambda_2 = 522\,nm$) corresponds to the TE_0 mode.

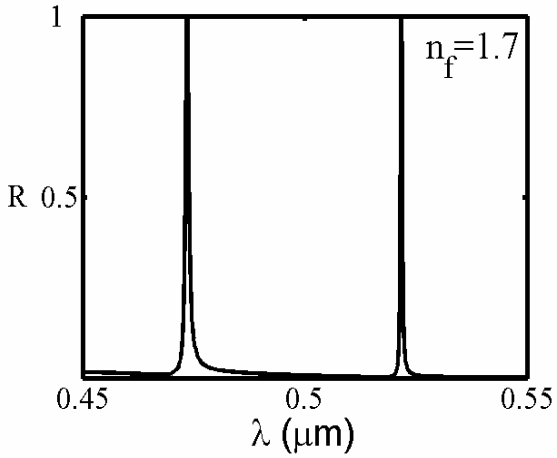

Figure 5.1: The spectral response of the two-line 1-D GMR filter at normal incidence: grating (n_g=1.5, Λ_a=320 nm FF=0.6, t_g=105 nm), high index film (n_f=1.7, t_f=353 nm), an AR coating ($n_{AR} = \sqrt{n_f n_s}$, $t_{AR} = \lambda_1 / 4n_{AR}$), a substrate ($n_s$=1.47), and an air superstrate (n_c=1)

The separation between these two resonances depends on the modal dispersion of the structure. When using a shallow grating (weak grating strength), the GMR structure can be considered as a three-layer slab waveguide, where the propagation constants of the modes are defined by the grating equation (2.2). The phase matching condition can be re-written as

$$\mathrm{Re}\{\beta_{+1}\} \cong \frac{2\pi}{\lambda} n_c \sin\theta_{inc} - \frac{2\pi}{\Lambda_a} \qquad \text{and} \qquad \mathrm{Re}\{\beta_{-1}\} \cong \frac{2\pi}{\lambda} n_c \sin\theta_{inc} + \frac{2\pi}{\Lambda_a} \tag{5.2}$$

At normal incidence, both propagation constants coincide. Modes propagate in opposite directions with the same propagation constants. To determine the separation between the resonance wavelengths due to two successive modes, one needs to solve the derivative of the TE mode characteristic equation (2.34) to (2.39)) when $dm = 1$.

$$t_f \, d\kappa - \frac{1}{\kappa^2 + \gamma_c^2}\left(\kappa \, d\gamma_c - \gamma_c \, d\kappa\right) - \frac{1}{\kappa^2 + \gamma_s^2}\left(\kappa \, d\gamma_s - \gamma_s \, d\kappa\right) = \pi \tag{5.3}$$

Considering two successive modes with the same propagation constant, $d\beta = 0$,

$$d\kappa = \frac{k_0 n_f^2 dk_0}{\kappa}, \quad d\gamma_c = -\frac{k_0 n_c^2 dk_0}{\gamma_c}, \quad \text{and} \quad d\gamma_s = -\frac{k_0 n_s^2 dk_0}{\gamma_s} \tag{5.4}$$

The wavelength separation ($d\lambda$) is then estimated by substituting $d\kappa$, $d\gamma_s$, and $d\gamma_c$ from Eq. (5.4) in Eq. (5.3).

$$\frac{d\lambda}{\lambda} = -\frac{dk_0}{k_0} = -\frac{\pi\kappa}{\left(t_f k_0^2 n_f^2 + \beta^2\left(\frac{1}{\gamma_c} + \frac{1}{\gamma_s}\right)\right)} \tag{5.5}$$

It is shown that the wavelength separation is not only inversely proportional to the high index film parameters (both refractive index and thickness) but also to the propagation constant as well. This implies that the more modes supported inside the structure, the narrower the

separation of resonances can be. Changing each of these parameters will change the resonance wavelengths; however the separation of resonances is limited by the index contrast of the structure that will be seen in next section.

5.2.1 Design of controllable multi-line 1-D GMR filters

While it is possible to obtain multiple resonances in 1-D GMR structures, it is critical to be able to control the location of (and the separation between) each resonant wavelength. As pointed out, the resonance locations depend on the modal dispersion of the structure. Both the thickness of the guiding layer and its material properties influence the resonance. In 1-D GMR structures, controlling the locations of the resonances in a broad spectrum requires changing the refractive indices of the film or the substrate according to the thickness of the high index film.

A typical approach in designing a multi-line 1-D GMR filter is to initially estimate the structure parameters under the cut-off conditions for the first resonance wavelength. For example, a two-line reflection filter can be designed by allowing only the first two guided modes (TE_0 and TE_1). To achieve the first resonance at 475 nm, and to guarantee that the second resonance corresponds to the lower guided mode at the desired wavelength, one needs to adjust the grating period and the film thickness while fixing the other parameters. The second resonance appears at a longer wavelength in this case. To control the second resonance while fixing the first resonance, the thickness of the high index film is reduced while increasing the grating period. The wavelength separation increases when reducing the thickness of the high index film as seen in Eq. (5.5). The limitation of the index contrast between the film and the substrate restricts the location of the second resonance. This can be seen in Figure 5.2. Varying

the grating period within the resonant range ($\lambda_1/n_f < \Lambda_a < \lambda_1/n_s$, Eq. (3.8)) from 290 to 320 nm increases the second resonance separation from 3% to 10% of the first resonance wavelength when the film refractive index is 1.7. For a film with higher refractive index of 2.5, the resonant range of the grating period is broadened and hence the separation changes from 4% up to 40%. The approximated results, calculated using Eq.(5.5), show similar trend when changing these two parameters (t_f and Λ_a). A maximum error of ~8% is experienced at larger periods.

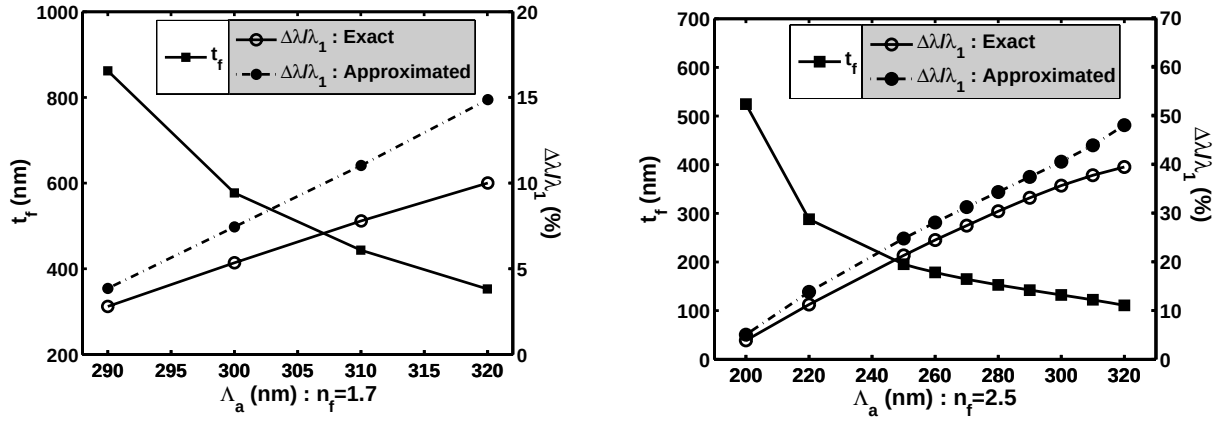

(a) (b)

Figure 5.2: Resonance separation ($\Delta\lambda/\lambda_1$) calculations of TE_0 and TE_1 resonances in two-line 1D-GMR filters (Figure 5.1) versus period of the grating (Λ_a) and film thickness (t_f) (a) film index (n_f)=1.7 (b) film index (n_f)=2.5

To be able to control the second resonance over a broader range from few nanometers up to hundreds nanometers, one needs to optimize the film thickness, film index and the grating period. The structure with higher film index gives a tunable range of the second resonance in a broader separation. However, the limitation of the cut-off resonant range prevents the resonances to have very narrow separation (< 10 nm.) Figure 5.3 shows the effect of changing both the film thickness and the film index when designing a two-line filter with the first resonance fixed at 475

nm. The grating has period at the minimum resonant range (290 nm) for the film index 1.7. The graphs show resonance separations in a broader spectrum from 3 % to 40 % of the first resonance. Likewise, the approximated calculations show similar trend (maximum error of 5 %).

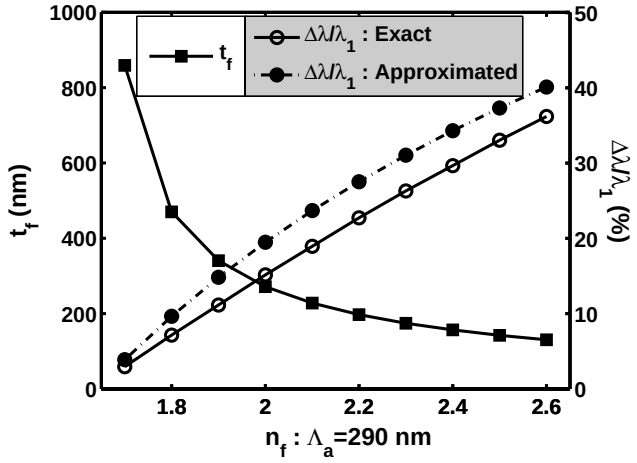

Figure 5.3: Resonance separation ($\Delta\lambda/\lambda_1$ for both exact and approximated Eq. (5.5) for two-line 1D-GMR filters (in Figure 5.1) versus film refractive index (n_f) and film thickness (t_f)

Realization of these structures, however, requires materials with refractive indices between 1.7 and 2.6. This, in addition to changing the physical dimensions of the structure, make multi line 1-D GMR filters not practical. The resonances tend to be more independent if each leaky mode is completely guided along a separate plane. GMR structure with a crossed grating adds more degrees of freedom to manipulate resonances as will be presented in the next section.

5.3 Multi-line 2-D GMR Filters

In 2-D GMR filters, multiple resonances appear intrinsically due to the multiple planes of diffraction. As discussed in Chapter 4, the number of the fundamental resonances increases

depending on the degree of symmetry in the grating grid geometry. As a result, modes corresponding to multiple resonances do not necessarily share the same planes of guidance. This eases the controllability of the resonances. Each resonance can be manipulated by modifying the value of the propagation constant independently through the periodicities of the grating at any incident direction.

These multiple planes of diffraction increase the degree of freedom in coupling the incident wave to both TE and TM guided modes of the structure. The normal components of diffraction waves potentially have phase matched to the TE guided mode, and vice versa for the TM guided mode case. Like the analysis of 1-D GMR, the wavelength separation between successive modes can be calculated by differentiating the characteristic equation, when the structure is considered as a three-layer slab waveguide. The analysis of 2-D GMR here copes with crossed-polarization modes instead. Then, the characteristic equation is generally written as

$$\kappa t_f - \tan^{-1}\left\{\left[p\left(\frac{n_f^2}{n_c^2}-1\right)+1\right]\frac{\gamma_c}{\kappa}\right\} - \tan^{-1}\left\{\left[p\left(\frac{n_f^2}{n_s^2}-1\right)+1\right]\frac{\gamma_s}{\kappa}\right\} = m\pi \qquad (5.6)$$

Where p indicates the polarization of the guided modes ($p = 0$ for TE_m modes, and $p = 1$ for TM_m modes). The constant m is the mode number.

Considering the separation of resonance wavelength between TE_m and TM_m modes with the same mode number, the derivative of Eq. (5.6) is presented in Eq. (5.7), where $dm = 0$ and $dp = 1$.

$$d\{\kappa\, t_f\} - \frac{1}{1+I^2}\, d\{I\} - \frac{1}{1+II^2}\, d\{II\} = 0 \tag{5.7}$$

where

$$I = \left[p\left(\frac{n_f^2}{n_c^2} - 1 \right) + 1 \right] \frac{\gamma_c}{\kappa}, \text{ and} \qquad II = \left[p\left(\frac{n_f^2}{n_s^2} - 1 \right) + 1 \right] \frac{\gamma_s}{\kappa} \tag{5.8}$$

At normal incidence, propagation constants of both resonant TE_m and TM_m modes are fixed by the grating periods. Having the same propagation constant, $d\beta = 0$, $d\kappa$, $d\gamma_c$, and $d\gamma_s$ are initially defined in Eq. (5.4). The wavelength separation calculated with respect to the TM mode resonance ($p = 1$) is shown in Eq. (5.9). λ_1 is the resonance wavelength relating to the TM mode and $k_0 = 2\pi/\lambda_1$.

$$\frac{\Delta\lambda_{wg}}{\lambda_1} = -\frac{\kappa^2}{k_0^2 n_f^2} \frac{\dfrac{n_c^2\gamma_c}{C} + \dfrac{n_s^2\gamma_s}{S}}{t_f + \beta^2\left(\dfrac{n_c^2}{\gamma_c C} + \dfrac{n_s^2}{\gamma_s S} \right)},$$

$$C = \beta^2\left(n_f^2 + n_c^2\right) - k_0^2 n_f^2 n_c^2,$$

and

$$S = \beta^2\left(n_f^2 + n_s^2\right) - k_0^2 n_f^2 n_s^2. \tag{5.9}$$

The wavelength separation between TE and TM modes of the same waveguide is significantly dependent on the structure parameters. With the same mode number, the wavelength separation is narrower compared to two successive modes with the same polarization. The wavelength separation is inversely proportional to the high index film parameters (both index and thickness).

The larger the propagation constant is, the narrower the separation can be. Fixing the first resonance at λ_1 requires reducing the high index film thickness and increasing the grating period.

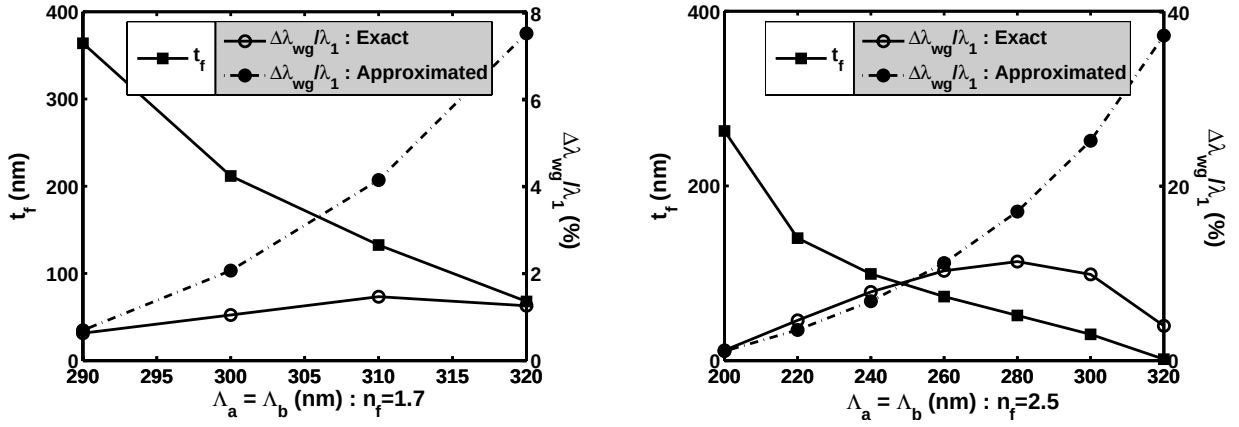

(a) (b)

Figure 5.4: Resonances separation ($\Delta\lambda/\lambda_1$) calculations of TE_0 and TM_0 resonances in 2-D GMR filters using a square-grid grating versus grating period and film thickness (t_f) (a) film index (n_f)=1.7 (b) film index (n_f)=2.5

Figure 5.4 shows a comparison between the approximated spectral separation between TE_0 and TM_0 resonances and the exact RCWA calculations when increasing the periods of the grating over the resonance range. The structure considered here is extended from the 1-D GMR in Figure 5.2, where the 1-D grating is replaced by a square-lattice 2-D grating having 100-nm depth and ~0.2 filling factor (ratio of air-hole and unit cell area). This approximation indicates more significant errors especially when the grating periods approach the upper limit of the resonance range. In this case, the resonance separation tends to be narrower when increasing the grating period. This is not trivial for the waveguide concept due to the complexity of coupling along two planes in the GMR structure. The RCWA results for two 2-D GMR structures with film indices n_f = 1.7 and 2.5 agree in the fact that the resonance separation is adjustable via the

grating period. However, the separation is limited when applying the low index contrast structure.

Controlling resonances in 2-D GMR confronts the same constraints unless each one of these fundamental resonant modes relies on a separate first-order wave. Thereby, it is possible to independently adjust the modal propagation constant within the desired spectra by changing the physical dimensions of the structure (grating period, geometry, and depth; and film thickness if it is necessary) without the need to change the refractive index of the structures as in the case of multi-line 1-D GMR filters.

5.3.1 Design of controllable multi-line 2-D GMR filters

Avoiding the dependency of the mode propagation constants that contribute to the resonances, the multi-line 2-D GMR filter is set at normal incidence. Thus, the incident beam can be coupled to the individual leaky modes along different fundamental diffraction planes for the proper polarizations.

For a rectangular-lattice crossed grating [49-50] with equal periods, the structure consists of two identical planes of diffraction orthogonal to each other. This implies that modes propagating along one of these planes have the same propagation constant at normal incidence. Both (TE and TM) guided-mode resonances present at any incident wave input polarization. It is possible to separate these two modes to be guided along different orthogonal planes if the incident beam is polarized along either one of these periodicities. Then, the resonance characteristic is equivalent to two superimposed 1-D GMR filters and the incident wave could be guided into both TE and TM waveguides at each resonance wavelength at orthogonal directions.

However, since one waveguide supports a TE mode and the other supports TM modes, equal propagation constants require different resonance wavelength. The spectral shift depends on the dispersion of the wave guiding structure. Changing the grating period in one direction, the diffraction in that plane results in a different mode propagation constant and hence shifts the resonance wavelength. Increasing the period, which corresponds to the TE mode (second resonance), has an effect on the broader resonance separation and vice versa. The shift of the film thickness in order to maintain the first resonance may not be necessary here as long as the cross coupling between modes is negligible. The minor shift of the first resonance (TM mode) is always compensated by the grating period related to that resonance.

For a regular hexagonal-lattice crossed grating, the structure has three planes of diffraction with hexagonal symmetry that corresponds to the fundamental diffracted orders. The resonance characteristic is equivalent to the square-lattice crossed grating, but the incident beam could be guided into each of the three planes of diffraction. An extra resonance will occur if the skew angle (ζ) of the hexagonal grid symmetrically slants from 30 degrees. The symmetry of the skew angle depends on the periodicities of the hexagonal grid, where $\zeta = \sin^{-1}\left(\Lambda_a / 2\Lambda_b\right)$. Thus, changing the skew angle will change the periodicities. Unlike the rectangular-grid crossed grating, the guidance along two symmetrically tilted planes (k_y' and k_y'' directions in Figure 4.2c) are not completely independent. The third resonance is created if the period along y-direction (Λ_a, in Figure 4.1) is distorted from the periods along x' and x" directions (Λ_b in Figure 4.1). Consequently, two resonances due to TE and TM guided modes along k_y'-k_z and k_y''-k_z diffraction planes are generated when the incident electric field is aligned on or normal to k_x-k_z diffraction plane. The diffracted waves along k_x-axis cause the third resonance, where this

resonance is controllable by adjusting one of the grating periods corresponding to the skew angle (ζ).

In either case, the resonances are roughly determined by applying the homogeneous waveguide approach [21] for each plane of diffraction. The exact locations of the resonances are determined by adjusting the periodicity along each diffraction plane.

5.3.2 Results and discussion

Using two approaches discussed in the previous section results in multiple resonances at the desired wavelengths. Here, the filters are designed at normal incidence considering an infinite incident plane wave and infinite GMR structure. The structure is comprised of a grating, a film and an AR coating deposited on the substrate with a refractive index of 1.47 as depicted in Figure 4.1. The grating (with refractive index of 1.5) is also designed to behave as an AR coating[51] to reduce the Fresnel refection at the air-grating interface. In addition, the grating is designed such that the power transferred to the diffracted waves is small enough to narrow the spectral linewidth at each resonance [21.] The thickness of the AR coating between the film and the substrate is designed as a quarter-wave film. A two-line reflection filter at any arbitrary wavelengths is designed with rectangular-grid grating ($\zeta = 0^\circ$) GMR structure. Controllable three resonances are achieved using the hexagonal-grid grating ($\zeta = \sin^{-1}\left(\Lambda_a / 2\Lambda_b\right)$) GMR filter.

The grating region of the multi-line 2-D GMR structure is designed to eliminate the Fresnel reflection at the air-grating interface. This requires a grating depth of 100 nm and a hole-radius of 50 nm for the 1.5 grating index. Two resonances will occur in the structure due to the first two guided modes (TE_0 and TM_0). The 2-D GMR filter consists of a waveguide with both

TE and TM guided modes. TM mode refers to the case where the guided wave is polarized in the plane of diffraction where the mode is guided. TE mode is when the guided wave is polarized normal to the plane of diffraction. Each waveguide is optimized to correspond to one resonance. Since both single-mode waveguides have the same film refractive index and film thickness, the location of the two resonances are controlled by adjusting the grating periods. The ability to adjust the crossed grating periodicity in an asymmetric manner makes it feasible to design arbitrary resonances. It is important to note that the two resonances are caused by coupling one input polarization (TE or TM) into the TE and TM guided modes. It is necessary that the incident field is either TE or TM polarized to achieve 100% reflectivity. Otherwise, the reflection peaks will be formed at four locations with reflectivity less than 100% when the periods are different. In the following calculations, the incident beam is polarized along the x-axis as depicted in Figure 4.1.

5.3.2.a Controllable two-line 2-D GMR filters using a rectangular-lattice grating

In the rectangular-lattice GMR filter, the two planes of diffraction are orthogonal. The structure is initially designed to achieve the first resonance (λ_1) at 475 nm as a result of the TM_0 mode (guided wave polarized in the plane of diffraction). Here, the film with a refractive index of 2.5 has a fixed thickness of 50 nm. Therefore, the grating periodicity parallel to the incident electric field relating to the TM_0 resonance is defined at 281 nm. The second resonance due to the mode propagating along the orthogonal plane (TE_0) occurs at a longer wavelength (guided wave polarized normal to the plane of diffraction). Increasing the period of the grating in the

orthogonal direction (Λ_b) up to λ_1/n_s ~320 nm, the second resonance is maximally shifted from the first resonance. The spectral response of two-line GMR filter is shown in Figure 5.5a to 5.5d.

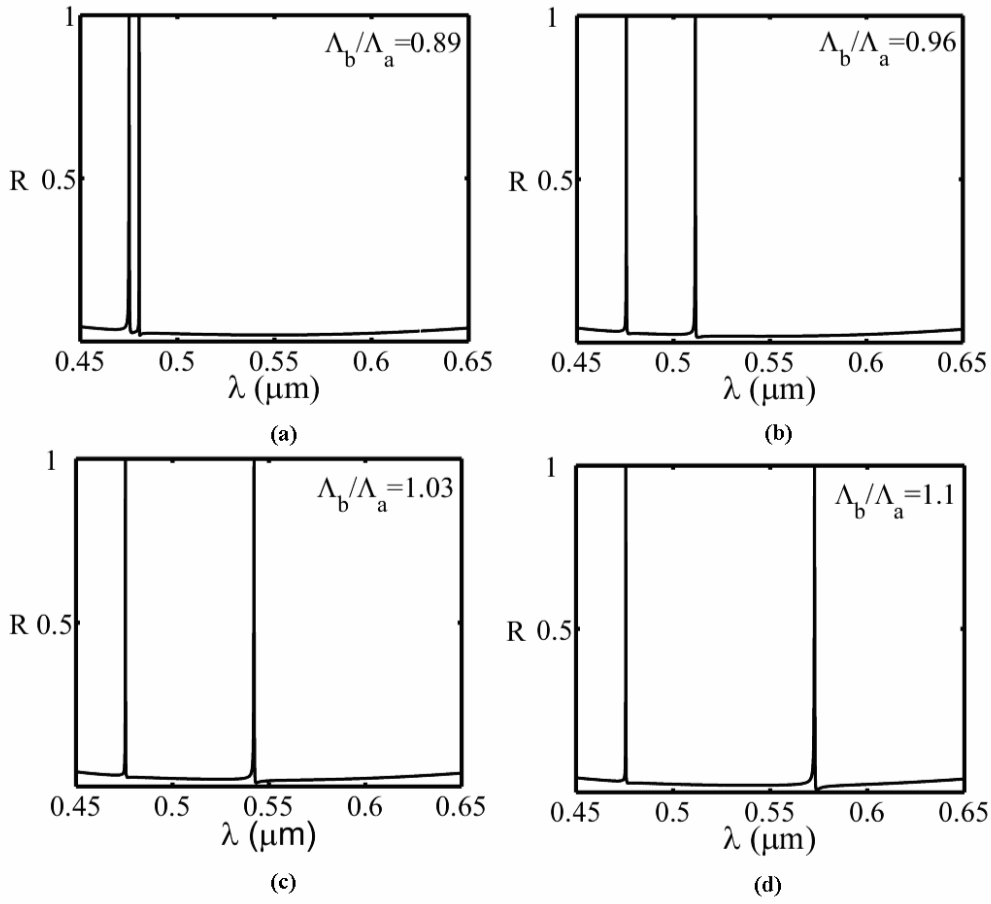

Figure 5.5: Spectral response of the two-line 2-D GMR filters with a rectangular-lattice structure. (a) Λ_b/Λ_a= 0.89; (b) Λ_b/Λ_a = 0.96; (c) Λ_b/Λ_a = 1.03; (d) Λ_b/Λ_a = 1.1

The response is symmetric with low side lobe (< 10 %) with very narrow line width (less than 1 nm). Spectral separations of 3 nm up to 110 nm are shown. That is about <1% to 23% of the short resonance wavelength. This is achieved by changing the grating period in one orthogonal direction relative to the other.

Figure 5.6a shows the shift of the second resonance as a function of the ratio of the two grating periods in the orthogonal direction ($\Lambda_a = 281$ nm and $\lambda_1 = 475$ nm).

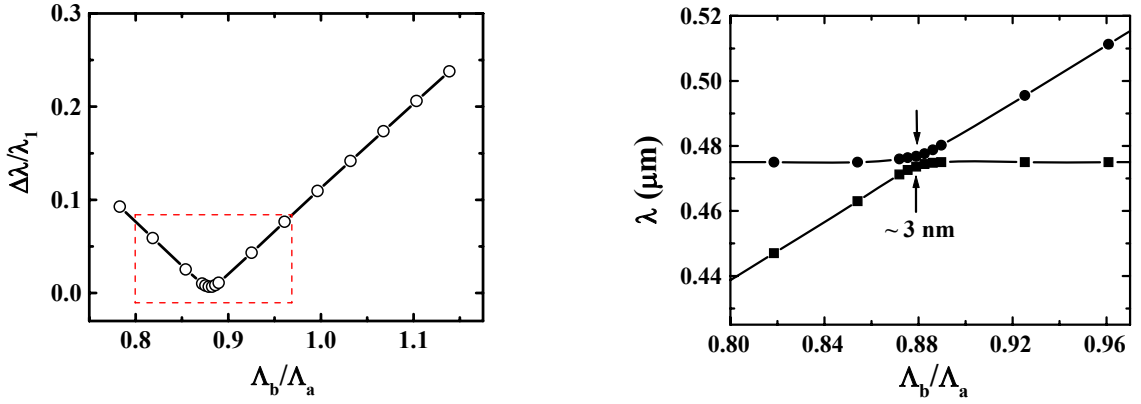

(a) (b)

Figure 5.6: (a) Shift in the location of the second resonance (b) resonance locations in two-line 2-D GMR filters with a rectangular-lattice structure versus the ratio of grating periods ($\Lambda_a = 281\ nm$)

The spectral separation may be approximated by:

$$\frac{\Delta\lambda}{\lambda_1} = C\left\{\frac{\Lambda_b}{\Lambda_a} - 1\right\} + \frac{\Delta\lambda_{wg}}{\lambda_1}, \qquad C = \frac{1}{\lambda_1}\frac{d(\Delta\lambda)}{d(\Lambda_b/\Lambda_a)} \tag{5.10}$$

$\Delta\lambda_{wg}$ is the spectral separation when the ratio of the two grating periods are equal. $\Delta\lambda_{wg}$ and C depend on the modal dispersion of the waveguide between the TE_0 and the TM_0 modes with the same propagation constant. For the structure presented here, C is 0.91 and $\Delta\lambda_{wg}/\lambda_1$ is 0.11. Near zero spectral shift occurs when $\Lambda_b = \Lambda_a\left(1 - \Delta\lambda_{wg}/C\lambda_1\right)$. Due to the interaction of resonant modes which are phase matched at the same wavelength, resonances do not coincide as shown in Figure 5.6b. The existence of a band structure results in a minimum spectral separation for a

structure with $\Lambda_b = 247\ nm$ of ~ 3 nm or <1% of the short resonance wavelength. The maximum spectral shift is determined by the maximum useable grating period which is $\Lambda_b = \lambda_1 / n_s$. This is to insure that the diffraction orders in the input region and the substrate are suppressed. For the structure considered here, the maximum spectral separation is 23% of the short resonance wavelength. This is achieved by changing the grating period and without the need to change neither the refractive index nor the thickness of the wave guiding region. Wider spectral separation is possible with further optimized the waveguide structure.

Designing a structure with grating periods that cover the resonance range, $\lambda_1 / n_f < \Lambda < \lambda_1 / n_s$, can broaden the spectral separation up to 30-40 % of the short wavelength. The graph in Figure 5.7 represents the resonance locations in a structure designed with the grating period Λ_a set at the minimum limit (220 nm.) The second resonance at a longer wavelength, ~ 200-nm larger than the first resonance, is achieved when shifting the grating period Λ_b to the maximum limit (320 nm.) However, the presence of the higher-order resonance (TE_1) at a shorter wavelength limits the maximum period Λ_b to ~280 nm only, and hence the maximum separation is ~140 nm or ~ 30% of the TE_0 resonance wavelength.

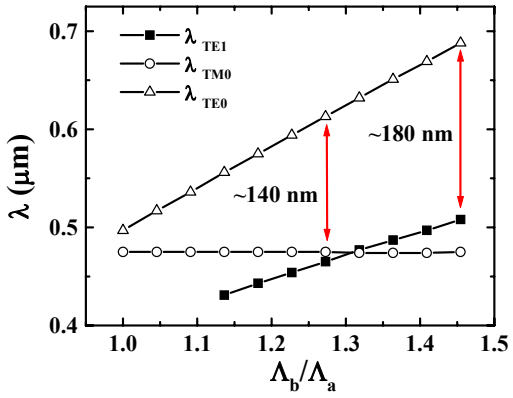

Figure 5.7: Resonance locations in two-line 2-D GMR filters with a rectangular-lattice structure versus the ratio of grating periods ($\Lambda_a = 220\ nm$)

5.3.2.b *Controllable three-line 2-D GMR filters using a hexagonal-lattice grating*

In the hexagonal-lattice grating GMR structure, there are two identical diffraction/ waveguide planes symmetrically slanting with arbitrary angle in addition to the fundamental diffraction plane (k_x-k_z plane). Therefore, three resonances will occur in the GMR structure if the incident field is polarized perpendicular to or in the fundamental diffraction plane x-z. The first and the second resonances, due to the slanted waveguides (k_y'-k_z plane and k_y"-k_z plane), can be explained by the decomposition of the incident polarization into two components. One component is parallel to each of the diffraction planes producing a TM_0 guided mode and the other component is normal to the two diffraction planes producing a TE_0 guided mode. The first resonance, (designed to be at 475 nm), is then due to the guided TM_0 mode. The resonance due to the TE_0 mode of these gratings appears at a longer wavelength of ~520 nm. The propagation constants of these two modes are identical. The spectral shift depends on the modal dispersion of the waveguides. Meanwhile, the third resonance is due to the fundamental diffraction plane (k_x-

k_z plane). This resonance is adjustable by changing one of the periodicities (Λ_b), which significantly shifts the propagation constant of the mode along this plane. However, a slight shift of the propagation constants of the first two modes is always found. This can be explained by the grating equation (4.2). In the reciprocal plane, the wave vectors of the diffracted waves are not orthogonal. Fixing the two resonances due to the modes propagating along the tilted planes requires optimizing the other grating period Λ_a while keeping the other structure dimensions (film thickness) constant. The film thickness is fixed at ~95 nm. A structure with equal grating periods of 280 nm produces two resonances. Controlling the third resonance by changing Λ_b requires a slight shift of the period Λ_a inversely proportional to Λ_b as shown in Figure 5.8a.

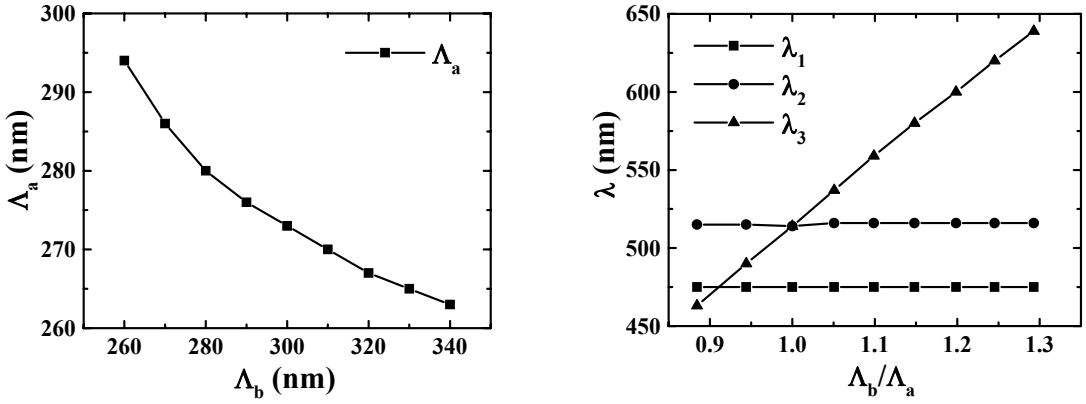

(a) (b)

Figure 5.8: (a) The change of the grating periods Λ_b versus Λ_a to fix two resonances (λ_1 and λ_2), while shift the other (λ_3). (b) The location of resonances in three-line 2-D GMR filters using a hexagonal-lattice grating versus the ratio of the two grating periods (Λ_b/Λ_a).

The calculation results in Figure 5.8b show the shift of the third resonance when the incident filed is polarized normal to the k_x-k_z diffraction plane. This makes the third resonance to be

caused by the TE_0 mode of the third diffraction plane. The third resonance can have a wavelength at a short wavelength, between the first two resonances, or even at a longer wavelength.

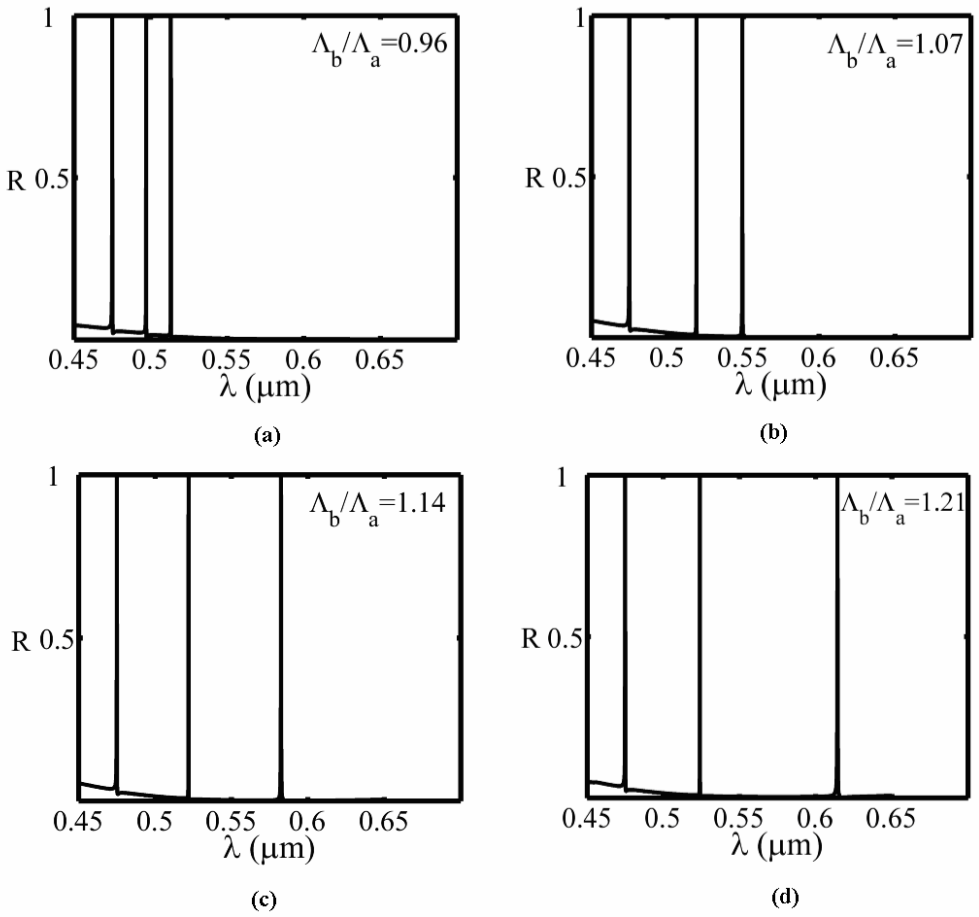

Figure 5.9: Spectral response of the three-line 2-D GMR filters using a hexagonal-lattice structure (a.) Λ_b/Λ_a= 0.96; (b.) Λ_b/Λ_a= 1.07; (c.) Λ_b/Λ_a= 1.14; (d.) Λ_b/Λ_a= 1.21

It is shown in Figure 5.9a through Figure 5.9d that the resonance response of each design with different period along x'-axis (Λ_b) has symmetric and narrow (less than 1 nm) spectrum around each resonance wavelength. Equation (5.10) may be used to estimate the spectral separation between the resonances caused by the non-slanted waveguide and any of the other two

from the slanted waveguides. $\Delta\lambda_{wg}$ is the separation between TE_0 and TM_0 guided modes of the slanted waveguides.

The advantages of the double periodicity of the two-dimensional gating GMR structures are that the guidance properties of the leaky-waveguide structure (GMR filter) can be completely controlled by adjusting the periods of the gratings in order to achieve the desired resonances. The dependency of two resonances due to the non-orthogonal waveguides limits the design of the three-line reflection filters. However the locations of the three resonances are much better controlled using the hexagonal 2-D grating GMR structure compared to the 1-D GMR filter. In all these structures, a shift of resonance always exists due to the fabrication error. Trade-off between the structure dimensions helps to sustain the desired resonances, as will be discussed in next sections.

5.4 Fabrication tolerances of Multi-line 2-D GMR Filters

The error in fabricating these structures might cause a deviation in the locations of the resonances including their spectral responses as well. Hence, it is necessary to study the fabrication tolerance of each individual structure parameter and its effect on the resonance locations and spectral response. As presented previously, the locations of the resonances are sensitive to the grating period and the high index film thickness. Good control of the grating fabrication including film deposition is required. In practice, precise control of the film thickness might require costly growth techniques (EBM). Using cheaper techniques such as E-beam or thermal evaporation are usually accompanied with certain errors. These errors can be corrected for by the changing the grating parameters such as grating period and air-hole radius as will be

shown later in this section. Besides, the difficulty of fabricating a high aspect ration grating with vertical side walls can be always compensated by altering the grating-hole radius.

Here, 2-D GMR structure with a square-grid grating (air hole grating) is investigated. The grating is etched in a material with refractive index of 2. The high index film refractive index is n_f =2.5. The AR film ($n_{AR} = \sqrt{n_f n_s}$) with quarter wave thickness is inserted between the high index film and the substrate (refractive index n_s=1.47) to neglect the Fresnel reflection at the film/substrate interface. The structure is designed to support two fundamental modes (TE_0 and TM_0) within the visible spectrum. The first resonance is located at $\lambda_1 = 475\ nm$ and the second one is at $\lambda_2 = 501.6\ nm$. The high index film is 102.8 nm thick. The grating has a period of 230 nm with an air-hole radius of 65 nm, and a grating depth of 80 nm. The beam is normally incident from free space to the GMR structure. To determine the fabrication tolerances of each structure dimension, one calculates the resonance response while shifting each one of these structure dimensions from the original design. That is shown in Figure 5.10 and 5.11.

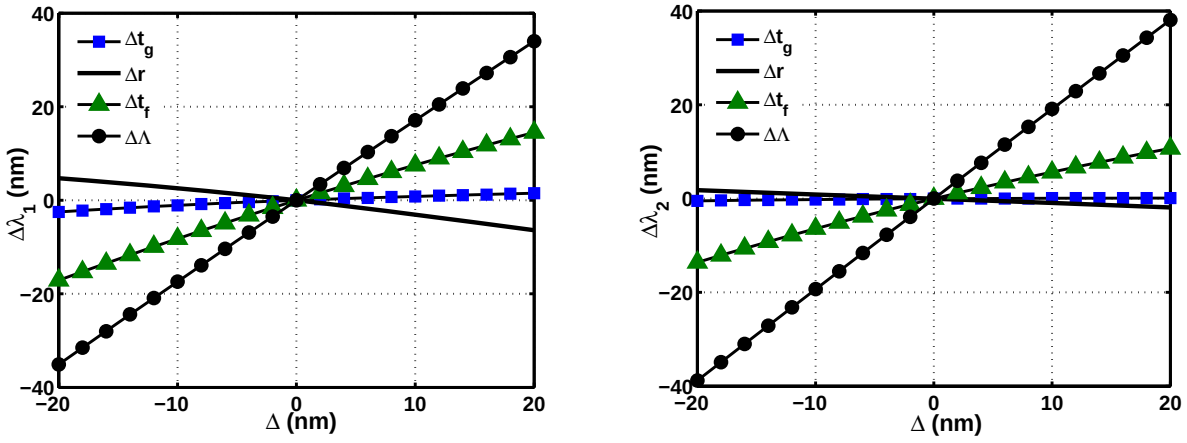

(a) (b)

Figure 5.10: Deviation of the resonant wavelengths while changing one of each structure dimension from the design (a) TM_0 resonance (b) TE_0 resonance

The calculations in Figure 5.10 show the shifts of resonance locations when changing the structure parameters (a grating depth: t_g, an air-hole radius: r, thickness of a high index film: t_f, and a grating period: Λ) from the original design. Figures 5.10a and 5.10b are the shifts of TM_0 (λ_1) and TE_0 (λ_2) resonances, respectively. Both graphs show linear shift of resonances with the most significant shift by changing the grating period ($\left|\Delta\lambda_1/\Delta\Lambda\right|$ is ~1.7 and $\left|\Delta\lambda_2/\Delta\Lambda\right|$ is ~1.9). Besides, resonances are also sensitive to the thickness of the high index film ($\left|\Delta\lambda_1/\Delta t_f\right|$ is ~0.8 and $\left|\Delta\lambda_2/\Delta t_f\right|$ is ~0.6). Changing the grating depth and air-hole radius shows the least effect. The results point out some shift of the TM_0 resonance ($\left|\Delta\lambda_1/\Delta r\right|$ is ~0.3 and $\left|\Delta\lambda_2/\Delta r\right|$ is ~0.09) when changing the air-hole radius. The change in air-hole radius affects the effective index of the grating. The phases of the TM guided modes are more sensitive to the structure refractive indices than the TE ones. Then, changing the grating fill factor or air-hole size in this case has more significant impact on the location of the TM resonance than the TE resonance.

The plots in Figure 5.11 illustrate the deviation of the spectral linewidth ($\Delta\lambda_{FWHM}$). The data are calculated at the relocated resonances when changing each individual parameter. It is seen that the spectral linewidth increases dramatically with the air-hole radius. This is, however, obviously formed in the TE resonance. The depth and period of the grating show no major influence in altering the spectral linewidth.

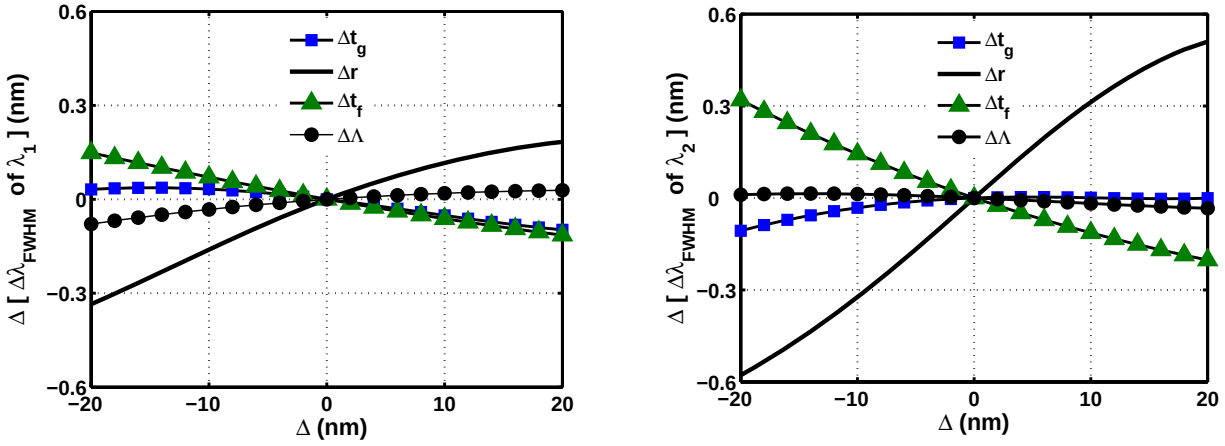

(a) (b)

Figure 5.11: Deviation of the spectral linewidth while changing one of each structure dimension from the design (a) TM_0 resonance (b) TE_0 resonance

The calculation results correspond to the previous discussion in Chapter 3. The spectral linewidths of the resonances rely on the leakage of the modes ($\mathrm{Im}\{\beta\}$) or the grating strength (η_d). This is mainly adjusted by the grating parameters (depth and fill factor). Therefore, the spectral linewidth tends to be sensitive to the grating depth and fill factor. The calculation results in Figure 5.11 show that the spectral linewidth is more tolerant to the grating depth compared to the fill factor. In addition to the grating strength, the thickness of the high index film also influences the spectral linewidth of the resonances.

It is seen that the thickness of the high index film is critical to both resonance location and its spectral linewidth. This, however, can be compensated by the grating parameters (period and fill factor). For example, if the thickness of the high index film is off by +10 nm, the first resonance is relocated at a wavelength ~7.4-nm longer than the design. Achieving the resonance at the desired wavelength can be done by reducing the grating period by ~4 nm. The data is analyzed by the curve-fitting equation: $\Delta\lambda_1 \sim 1.73\Delta\Lambda - 0.2095$. Meanwhile, the spectral linewidth

is also slightly narrowed by ~0.06 nm. The air-hole radius needs to be ~5-nm bigger than the original design ($\Delta(\Delta\lambda_{FWHM}) \sim -0.0002\Delta r^2 + 0.0134\Delta r - 0.0019$.)This fixes both the resonance location and the spectral linewidth as well.

Fabrication process would always cause some error in the dimensions of the structure, especially the thickness of each layer. Figure 5.12 show that this error can always be corrected by the grating fill factor (air-hole radius in this design). The contour plot in Figure 5.12a and 5.12b shows the shift of the TM_0 resonance while changing the grating depth versus the air-hole radius and changing the thickness of high index film versus the air-hole radius, respectively. The plots show that the resonance location can be fixed at the desired wavelength by adjusting the hole-radius for a specific thickness. As mentioned in the previous paragraph, the resonance location is more tolerant to the grating depth. Then, it requires a slight shift of the air-hole radius from the original design.

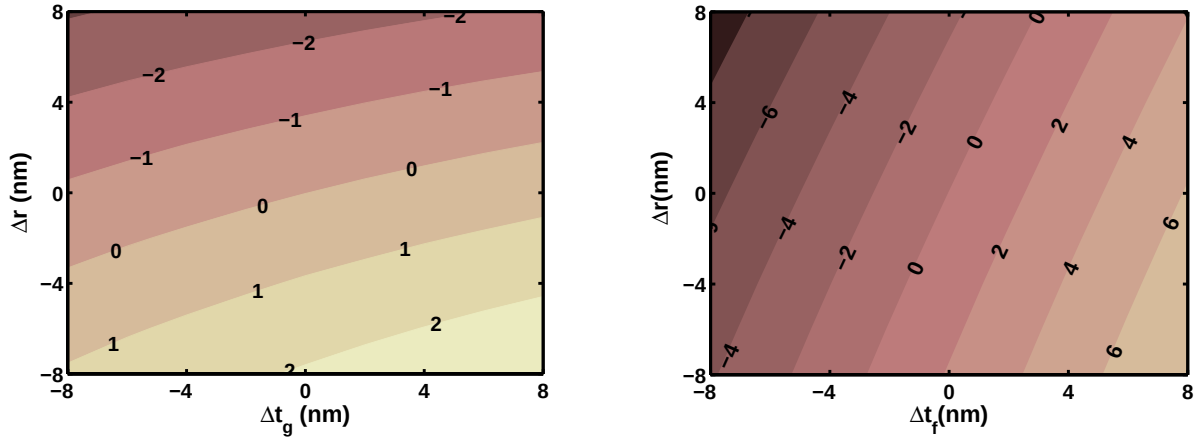

(a) (b)

Figure 5.12: Contour plot of the shift (nm) of TM_0 resonance (a) deviation of grating depth (Δt_g) and air-hole radius (Δr) (b) deviation of high index film thickness (Δt_f) and air-hole radius (Δr).

The other concern of the grating fabrication is the difficulty to achieve vertical side walls. A cone shape grating (Figure 5.13a) is usually formed when the grating is designed to have high aspect ratio (depth: air-hole diameter).

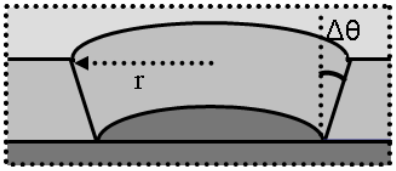

(a)

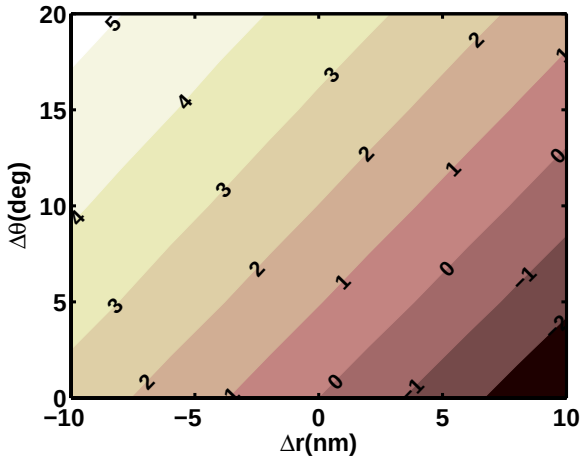

(b)

Figure 5.13: (a) A configuration of the grating with slanted side wall (b) the contour plot of the shift (nm) of TM_0 resonance with the change of air-hole radius (Δr) and slanted side wall angle ($\Delta\theta$).

In this case, the resonance is potentially shifted from the design. The effective index of the subwavelength grating depends on the percentage of the material left within the unit cell. The cone shape grating has more grating material, and hence, a higher effective index. Therefore, increasing the grating-hole size can compensate for the cone shape. The resonance appears at the same wavelength as long that the absolute grating material is conserved within the unit cell. The

previous discussion is confirmed by the contour plot of the shift of the TM_0 resonance in Figure 5.13b. With the cone shape grating, the resonance remains at the same wavelength only if the air-hole has larger radius from the design.

5.5 Summary

A novel multi-line filter using two-dimensional guided mode resonant (GMR) filter was proposed. The filter concept utilizes the multiple planes of diffraction produced by the two-dimensional grating. Multiple resonances are obtained by matching the guided modes in the different planes of diffraction to different wavelengths. It was shown that the location and the separation between the resonances can be specifically controlled by modifying mainly the periodicity of the grating and other physical dimensions of the structure if it is necessary. It was shown that one-dimensional GMR filters where multiple resonance are obtained by coupling to higher order modes, where the location of the resonances is material refractive index dependent, are impractical. Two types of two-dimensional gratings GMR designs, rectangular grid and hexagonal grid, were presented to obtain controllable two-line and three-line reflection filters, respectively. For the rectangular grid grating, a two-line GMR filter was constructed where the resonance separation was controlled over the region from <1% to 30% of the short resonance wavelength by changing one of the grating periods in the resonant range $\lambda_1/n_f < \Lambda < \lambda_1/n_s$ while keeping the other structure parameters constant. Finally, a three-line GMR filter using the hexagonal grating structure was presented. Similarly, the line separations were controlled through altering the periodicity of the grating corresponding to the skew angle (ζ).

The locations of the resonances are significantly dependent on the period of grating and the thickness of the high index film. The grating depth and hole-size have more influence on the spectral linewidth of each resonance. In practice, precise structure dimensions are not always guaranteed. This definitely results in the distortion of the resonances from the design. However, slight shift of the dimensions can always be compensated by the fill factor of the grating. As shown, the errors from both thicker dielectric film and the cone shape grating were corrected by increasing the grating-hole size.

CHAPTER 6 : BROADENING THE ANGULAR TOLERANCES IN 2-D GMR AT OBLIQUE INCIDENCE

Important consideration in the GMR devices is to have large angular tolerance in order to insure high reflection for finite beams. While these devices have been observed to possess an angular bandwidth broad enough to accommodate incident finite beams at normal incidence, the angular bandwidth of the resonant response at oblique incidence is considerably narrower. In this chapter, broadening of the angular response of 2-D GMR spectral filters at oblique incidence is investigated. Two different approaches are considered. The first is by coupling into multiple fundamental guided resonant modes having the same propagation constant and enhancing the second Bragg diffraction of the 2-D grating structure. A second approach utilizing a dual 2-D grating configuration with a second grating on the substrate side is proposed and demonstrated.

6.1 Overview

In the literature, there exist some attempts [22, 44-46] to broaden the angular linewidth while maintaining a narrow spectral linewidth. At normal incidence, the tangential components of both the +1 and -1 diffracted orders are phase-matched to leaky modes with equal magnitude propagation constants traveling in opposing directions. In this situation, the spectral bandwidth of the resonant grating remains very narrow, in the order of a few angstroms, while the angular bandwidth can often become quite broad, many angular degrees. Having a counter propagation resonant mode results in forming the resonant band gap and a dispersionless resonant mode is localized at the upper or lower frequency of the resonant band gap. This condition of resonant

mode always occurs at normal incidence due to the symmetry of the diffraction. The angular tolerances are further improved by enhancing a strong second Bragg diffraction like the case of the doubly periodic structure proposed by Lemarchand *et al* [44] or by optimizing the grating dimensions to have a strong backward coupling as presented by Jacob *et al* [22.] Broader angular response can be formed by merging the side bands in multimode structures[11] where resonance is a contribution of a higher-order waveguide mode.

At oblique incidence, the diffraction orders are not symmetric and the resonant band gap is formed by two counter-propagating complex modes of differing magnitudes. Recently, Sentenac *et al* [46] proposed a design of 1-D GMR multimode structure to match two first-order waves individually to higher-order TE_1 and TE_2 modes. This concept was extended to the 2-D structure in order to achieve polarization independent resonances and high angular tolerance [54.] Resonance is achieved by coupling the incident wave ($\varphi_{inc} = 45^{\circ}$) to two pairs of higher resonant modes propagating in different planes. Having different propagation constant resonant modes, resonance was not as tolerant as at normal incidence.

In 2-D GMR devices, the two-dimensional grating is used to control the resonant mode propagation constants, and hence the resonance locations, by adjusting the periodicity and the incident direction [63] as demonstrated in Chapter 5. In this chapter, broadening of the angular response of 2-D GMR narrow spectral filters at oblique incidence is investigated and demonstrated. Coupling to multiple fundamental resonant modes having the same propagation constant but propagating in different planes is shown to produce significant broadening of the angular tolerance at oblique incidence while maintaining the narrow spectral linewidth. The phase mismatch between these first-order diffraction waves at off- resonant angles is minimized,

and that substantially improves the angular tolerances. Broadening of the angular tolerances is symmetric when coupling to four resonant modes in a structure with an irregular hexagonal grating pattern. Further broadening is obtained by enhancing the second Bragg diffraction of the 2-D grating structure. That is done by adjusting the grating's physical dimensions. A second approach utilizing a dual 2-D grating configuration with a second grating on the substrate side is investigated. The improvement in the lateral confinement results in merging of two successive resonant bands and further improvement of the angular/spectral linewidth ratio.

6.2 Coupling characteristics to enhance the angular tolerances of 2-D GMR

In 2-D GMR structure, the fundamental diffraction/guidance planes are along two orthogonal planes for the rectangular-lattice grating and along three crossed planes for the hexagonal-lattice grating. Resonance could be caused by multiple waves propagating in different planes. The resonant modes are controlled by the grating periodicities along the incident direction. Achieving resonant response with broad angular linewidth, the incident beam is coupled to resonance modes having de-phases compensated at off resonant angle. Hence, the incident beam is simultaneously coupled to the forward and backward propagating modes corresponding to the incident plane. They do not essentially coincide in the same plane. This intrinsically occurs at normal incidence, where de-phases are absolutely compensated at off resonance. Oblique incidence, on the other hand, requires that the incident plane be along a symmetric plane (parallel to one of the grating vectors or in the middle between two of them.) Coupling of the forward and the backward propagating modes can be in various manners. Multiple resonant modes, where

each mode has the same propagation constant, at oblique incidence can be achieved only in two configurations.

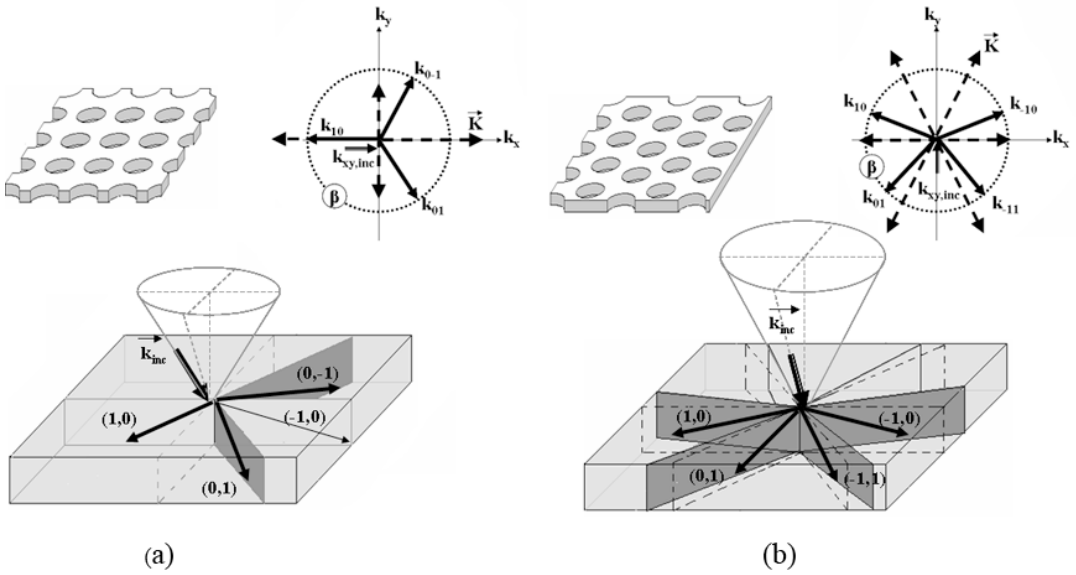

Figure 6.1: Configurations of diffraction/guidance planes at oblique incidence and phase matching diagram of resonant modes with the same β in the 2-D GMR with (a) a rectangular-(b) a hexagonal-lattice grating

In the first configuration, the resonant modes propagate along three first-order diffraction waves as in Figure 6.1a for the rectangular-lattice grating. Second, the resonant modes propagate along four first-order diffraction waves as in Figure 6.1b for the hexagonal-lattice grating.

For the rectangular-lattice grating, the incident wave has to be along one of the two fundamental planes. One of the resonant modes is then in the same plane via the diffracted wave (1,0). The other resonant mode propagates along the planes of the two identical diffracted waves (0,1) and (0,-1) as shown in Figure 6.1a. All of these three waves can have the same propagation constant and contribute to a resonance at the same wavelength once the periodicities and the incident direction meet the following condition

$$\sin\theta_{inc} = \frac{\lambda_0}{2\Lambda_b}\left[1-\left(\frac{\Lambda_b}{\Lambda_a}\right)^2\right] \tag{6.1}$$

For the hexagonal-lattice grating, the incident plane has to be aligned in the middle of two of the three crossed fundamental planes (dash planes in Figure 6.1b.). The resonant modes then propagate along two pairs of symmetric diffracted waves (1,0/-1,0 and 0,1/-1,1). In order to couple them simultaneously to the waveguide mode with the same propagation constant, the grating periods and the direction of incidence need to satisfy the following equation:

$$\sin\theta_{inc} = \frac{\lambda_0}{2\Lambda_a}\left[1-\frac{3}{4\left(\frac{\Lambda_b}{\Lambda_a}\right)^2-1}\right] \tag{6.2}$$

In both cases, the resonant modes are located in different planes. The de-phasing at off-resonant angle is in an asymmetric manner due to the diffraction and not the waveguide modes ($\Delta\beta$). Although the de-phasing compensation is less than that at normal incidence, the angular tolerance at oblique incidence is expected to be improved compared to the resonant modes with different propagation constants as will be illustrated in Section 6.3.

6.3 Multiple resonant modes with the same β in 2-D GMR at oblique incidence

In 2-D structures, the de-phasing mismatch exists due to the asymmetry of the diffraction, but it is less than that of the case of 1-D GMR. The degree of symmetry is proportional to the diffraction pattern. That will be chronically discussed in Section 6.3.1 for the rectangular-lattice

grating and in Section 6.3.2 for the hexagonal-lattice grating. The resonant responses of both cases will be presented in Section 6.3.3.

6.3.1 Three resonant modes with the same β in a rectangular-lattice grating

In this case, these resonant modes propagate with the same propagation constant along three diffraction planes as in Figure 6.1a. The de-phasing at off-resonant angle is demonstrated in Figure 6.2a for on-incident plane and Figure 6.2b for off-incident plane where the dash-diffraction planes and thin dot- wave vectors represent the case at resonance.

For the on-incident plane case, the de-phasing compensation behaves similarly to the 1-D structure, but along two pairs of waves, (1,0/0,1) and (1,0/0,-1). The de-phasing mismatch is formed due to the diffraction and not due to coupling to different modes. The forward waves (0, 1) and (0,-1) have identical de-phasing rate which is different from the backward waves (1, 0). That can be approximately written as

$$\frac{d\phi_{+}}{d\theta_{inc}} \approx \frac{k_0 \sin\theta_{inc}}{k_{xy,+}} k_0 \cos\theta_{inc} \frac{d\phi}{d\beta},$$

and

$$\frac{d\phi_{-}}{d\theta_{inc}} \approx k_0 \cos\theta_{inc} \frac{d\phi}{d\beta} \tag{6.3}$$

where the subscript +/- represent the forward (0,1) and (0,-1) /backward (1,0) waves. $k_{xy,+} = \sqrt{(k_0 \sin\theta_{inc})^2 + (2\pi/\Lambda_a)^2}$ is the forward wave vectors with respect to the incident plane. As shown, the mismatch reduces when the grating has larger period or the resonant mode has smaller propagation constant.

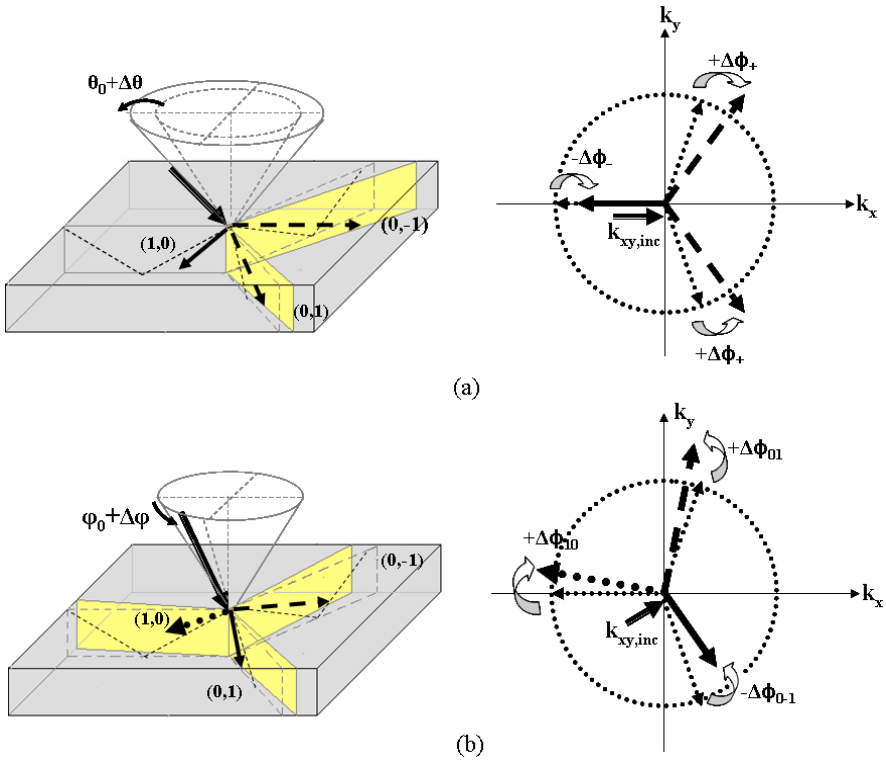

Figure 6.2: Configurations of diffraction/guidance plane and phase matching diagram of three resonant modes at off-resonant angle (a) on- (b) off-incident plane.

For the off-incident plane case, the de-phasing rates of both forward waves and the backward wave are not exactly the same. However, the symmetric diffraction along the waves 01/0-1 results in slightly deviating de-phasing rates accumulating in opposite signs. They are noticeably larger than the (1,0)-wave de-phasing rate as approximately written in Eq. (6.4).

$$\frac{d\phi_{0\pm1}}{d\varphi_{inc}} \approx \mp \frac{k_0 \sin\theta_0 \cos\varphi_{inc}}{k_{xy,0\pm1}} \frac{2\pi}{\Lambda_a} \frac{d\phi}{d\beta},$$

and

$$\frac{d\phi_{10}}{d\varphi_{inc}} \approx \frac{k_0 \sin\theta_0 \sin\varphi_{inc}}{k_{xy,10}} \frac{2\pi}{\Lambda_b} \frac{d\phi}{d\beta}. \qquad (6.4)$$

The de-phasing compensations are along two pairs of waves, 10/01 and 01/0-1. Due to less de-phasing accumulation along the wave (1,0) compared to the others, the de-phasing compensation

at off-incident plane are degraded from that at on-incident plane causing asymmetric angular responses.

6.3.2 Four resonant modes with the same β in a hexagonal-lattice grating

In the hexagonal grating GMR structure, the resonant modes propagate along four diffraction planes as shown in Figure 6.1b. The de-phasing at off-resonant angle is shown to be more symmetric as depicted in the drawings in Figure 6.3a for on-incident plane and Figure 6.3b for off-incident plane.

The de-phasing at off-angle along the plane of incidence is compensated via four different pairs of waves, (0,1/10), (0,1/-10,), (-1,1/-1,0), and (-1,1/1,0). The forward waves (1, 0) and (-1, 0) have the same de-phasing rate, but different from the backward waves (0, 1) and (-1, 1). These rates can be approximately written as

$$\frac{d\phi_+}{d\theta_{inc}} \approx \frac{k_0 \sin\theta_{inc}}{k_{xy,+}} k_0 \cos\theta_{inc} \frac{d\phi}{d\beta},$$

and

$$\frac{d\phi_-}{d\theta_{inc}} \approx \frac{k_0 \sin\theta_{inc} - \left(\frac{2\pi}{\Lambda_a}\right)}{k_{xy,-}} k_0 \cos\theta_{inc} \frac{d\phi}{d\beta}. \qquad (6.5)$$

where the forward wave vectors are $k_{xy,+} = \sqrt{\left(4\pi/\sqrt{4\Lambda_b^2 - \Lambda_a^2}\right)^2 + \left(k_0 \sin\theta_{inc}\right)^2}$ and the backward wave vectors are $k_{xy,-} = \sqrt{\left(2\pi/\sqrt{4\Lambda_b^2 - \Lambda_a^2}\right)^2 + \left(k_0 \sin\theta_{inc} - 2\pi/\Lambda_a\right)^2}$. The de-phasing rate of the backward waves is somewhat smaller than that of Section 6.3.1 under the similar circumstances

(incident angle θ_{inc} and grating periods). Hence the de-phasing between the forward and backward waves is better compensated. Resonances are then expected to be more angular tolerant along the incident plane than the rectangular structure.

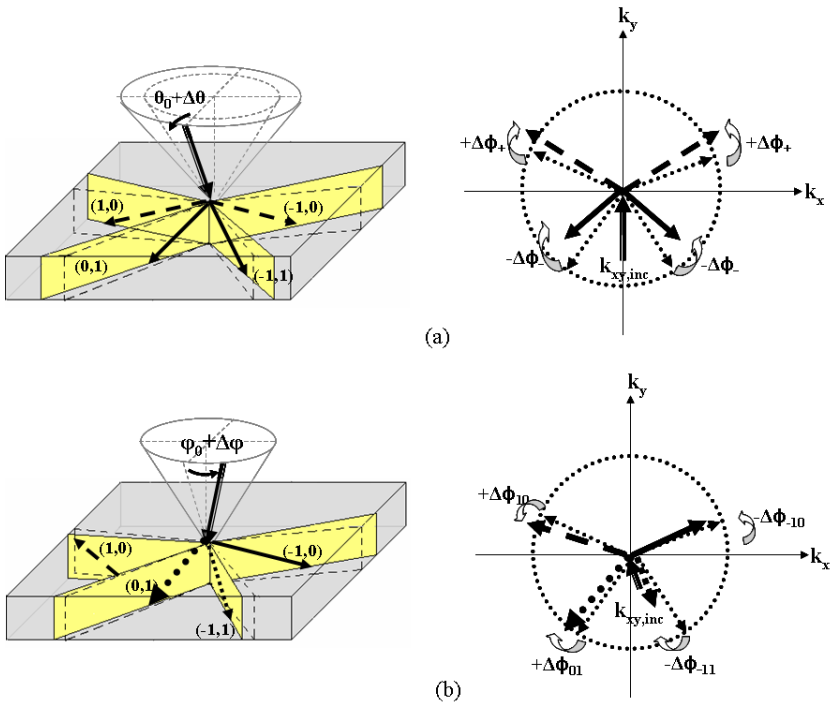

Figure 6.3: Configurations of diffraction/guidance plane and phase matching diagram of four resonant modes at off-resonant angle (a) on- (b) off-incident plane.

The degree of de-phasing compensations at off-incident plane tends to improve as well when having four pair of waves, (0,1/-1,0), (0,1/-1,1), (1,0/-1,0) and (1,0/-1,1) in spite the fact that the de-phasing rates are slightly different. The de-phasing compensation of diffraction waves are more effective along the symmetric diffraction waves (1,0/-10,) and (0,1/-1,1) where the de-phasing rates are approximately defined by Eq. (6.6).

$$\frac{d\phi_{\pm 10}}{d\varphi_{inc}} \approx \frac{k_0 \sin\theta_0}{k_{xy,\pm 10}} \left(\mp \frac{4\pi}{\sqrt{4\Lambda_b^2 - \Lambda_a^2}} \sin\varphi_{inc} \right) \frac{d\phi}{d\beta},$$

and

$$\frac{d\phi_{01/-11}}{d\varphi_{inc}} \approx \frac{k_0 \sin\theta_0}{k_{xy,01/-11}} \left[\pm \frac{2\pi}{\sqrt{4\Lambda_b^2 - \Lambda_a^2}} \sin\varphi_{inc} - \frac{2\pi}{\Lambda_a} \cos\varphi_{inc} \right] \frac{d\phi}{d\beta}. \qquad (6.6)$$

Consequently, the asymmetry of the angular responses is minimized in this configuration which is more desirable in broadening of the angular tolerances of GMR structure at oblique incidence.

6.3.3 Results and discussions

In this section, the resonant responses of the design approaches mentioned in Section 6.3.1 are calculated and compared to the one in Section 6.3.2. To show the improvement of the angular tolerance; the structure in Section 6.3.2 is also modified to have forward and backward waves with different β. For all cases, the structures are designed to have resonances located at a wavelength λ_0= 0.98 μm with almost identical spectral linewidth ($\Delta\lambda_{FWHM}$).

The structure is comprised of a refractive index film of 2 deposited on a substrate with a refractive index of 1.47. The grating is directly fabricated on the film as depicted in Figure 4.1. The grating has air circular-holes with radius *r* and depth t_g. The actual thickness of the main guiding layer is t_f. In these calculations, the Fresnel reflection (that causes an asymmetric and high sidelobe resonant lineshape) at the film/substrate interface is minimized by inserting an anti-reflection (AR) film with a refractive index of $n_{AR}=\sqrt{n_f n_s}$ and thickness $t_{AR}=\lambda_0/4n_{AR}$. The calculated resonance linewidths of three different designs are presented in Table 6.1.

Table 6.1: Spectral and angular linewidth of resonances (λ_0=0.98 μm) by a counter-propagation resonant mode in 2D-GMR at oblique incidence

GMR #	Incident beam			Structure parameters (μm)						$\Delta\lambda_{FWHM}$ (nm)	$\Delta\theta_{FWHM}$ at φ_0	$\Delta\varphi_{FWHM}$ at θ_0
	Θ_0	φ_0	Ψ_0	Λ_a	Λ_b	ζ	r	t_g	t_f			
1	9º	0º	90º	0.54	0.48	0º	0.11	0.19	0.334	0.12	1.08º	1.12º
2	10.9º	90º	0º	0.55	0.6	27.3º	0.07	0.21	0.305	0.18	0.85º	2.45º
3	11.5º	90º	0º	0.57	0.58	29.4º	0.1	0.21	0.826	0.16	0.68º	0.82º

In Table 6.1, GMR #1 and #2 match the first-order diffracted waves to the TM_0 mode by the grating structure and the settings in Section 6.3.1 and 6.3.2, respectively. The grating periods of these GMRs are selected in order to achieve an identical modal index. The third design on the other hand matches the (1,0/-1,0) and (0,1/-1,1) waves to the TM_0 and TM_1 modes at the same wavelength, respectively. The grating has the same pattern as GMR #2 but different grating periods. The spectral and angular responses of each case are shown in Figure 6.4. To estimate the minimum beam size allowed in the structures, the angular responses are calculated here as a function of the deviation Δk along ($// k_{inc}$) and perpendicular to ($\perp k_{inc}$) the incident direction.

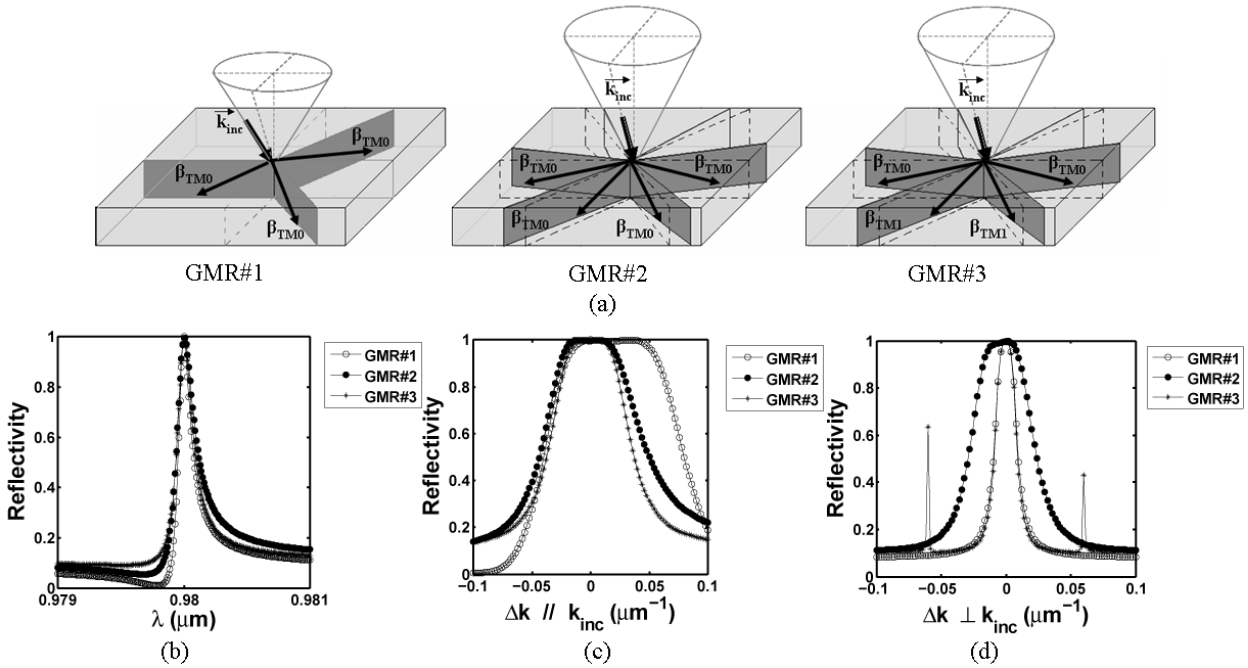

Figure 6.4: (a) Phase matching conditions (b) spectral (c) and (d) angular resonant response along and perpendicular to plane of incidence of 2-D GMRs in Table 6.1

The calculation results in Table 6.1 show an improvement of the angular tolerances when the resonant modes have the same β as in GMR #1 and GMR #2. The angular linewidths ($\Delta\theta_{FWHM}$ and $\Delta\varphi_{FWHM}$) are about twice of that in GMR #3 when the resonant modes have different β. That is in agreement with Eqs. (6.3)/ (6.4) and (6.5)/ (6.6) where the de-phasing mismatches at off-resonance are minimized. Based on the equations, the de-phasing compensation in GMR#1 and GMR#2 at off-resonant angle is plotted in Figure 6.5a for on-incident plane and in Figure 6.5b for off-incident plane.

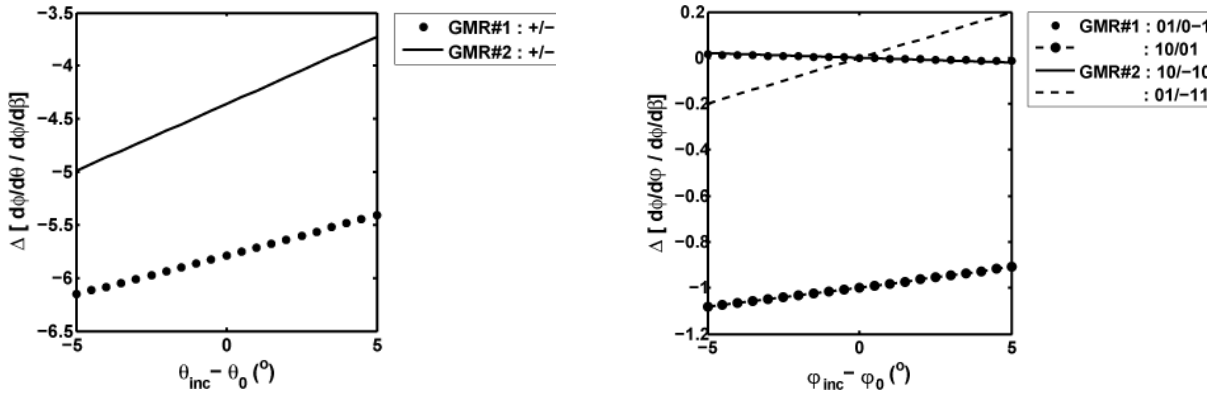

(a) (b)

Figure 6.5: Comparison of de-phasing compensations in GMR#1 and GMR#2 (Figure 6.4) calculated from Eqs. (6.3)-(6.6) (a) on- incident plane (b) at off-incident plane

The calculations in Figure 6.5a indicate better de-phasing compensation in GMR#2 with the hexagonal structure although its angular linewidth $\Delta\theta_{FWHM}$ in Table 6.1 is narrower than that of GMR#1 with the rectangular structure. This represents more interaction between modes in GMR#1 when the grating has a strong second Bragg diffraction as will be discussed in Section 6.4. In spite of the broader angular linewidth of GMR #1 (3 modes with the same β), the asymmetric angular response shown in Figures 6.4c and 6.4d limits the minimum size of the incident beam to $\ln(2)/\Delta k_{FWHM} \sim$ 34-μm in diameter. This is also observed in GMR #3 (different β). A more symmetric diffraction pattern in the hexagonal structure results in less de-phasing mismatches between 10/-10 and 01/-11 in Figure 6.5b for off-incident planes. The angular response (Figure 6.4) then appears more symmetric for GMR #2 (4 modes with the same β). This broad angular tolerance allows an incident beam as small as 13-μm diameter, which is about half of the other two designs.

Like the resonances at normal incidence, the angular tolerances at oblique incidence could be even broader by strengthening the second Bragg diffraction of the grating. Therefore, in Section 6.4 and 6.5, resonances by four modes with the same β in GMR #2 will be further implemented.

6.4 Broadening the angular tolerances in a single- grating 2-D GMR

The approach developed for the normal incidence [22] case is used to increase the angular tolerances of resonances at oblique incidence. However, the asymmetric diffraction at oblique incidence must be taken into consideration.

As in normal incidence, the resonance has a broader angular linewidth when the resonant mode is more laterally confined [22.] That requires a grating with a strong second Bragg diffraction. The resonant modes at oblique incidence are in four planes. They are cross-diffracted and coupled to each other once the grating has a strong second Bragg diffraction as depicted in Figure 6.6a. The strength of this diffraction can be approximately measured in term of the backward diffraction efficiency (η_B), where the film is assumed as a half-space.

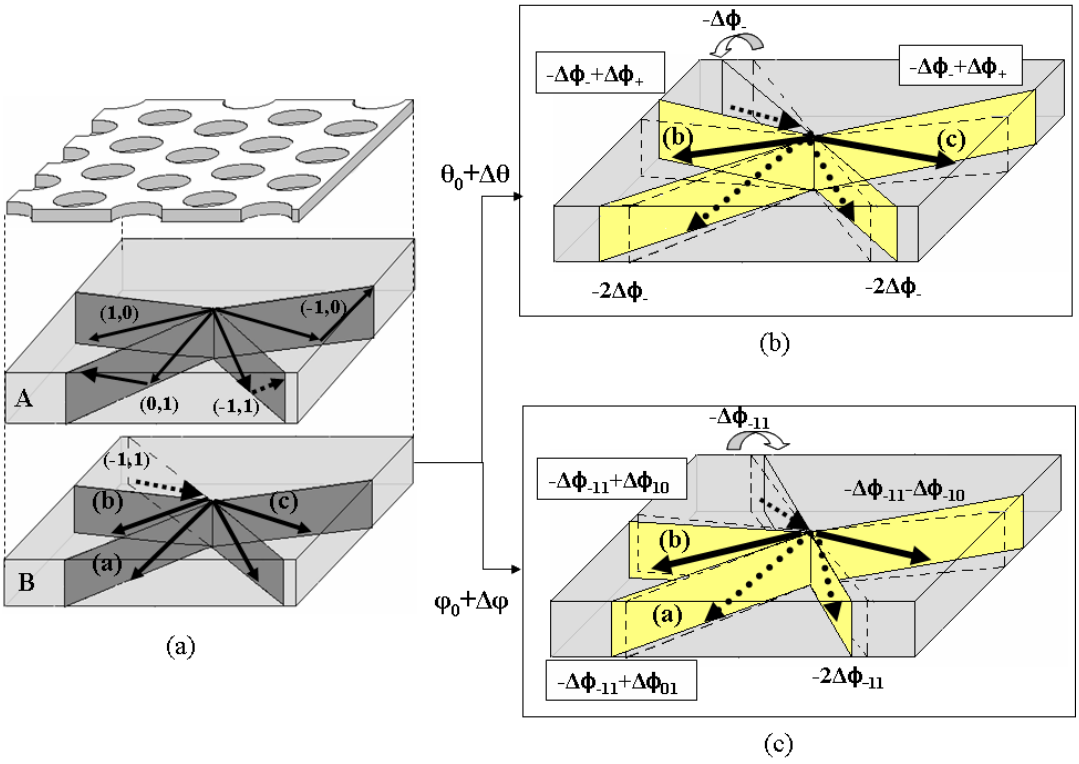

Figure 6.6: (a) Scattering of four resonant modes at resonance (A: forward diffraction, B: a crossed diffraction) and de-phasing manners of a crossed diffraction at off-resonance (b) $\theta_0+\Delta\theta$ (c) $\varphi_0+\Delta\varphi$

At off-resonant angle along the incident plane ($\theta_0+\Delta\theta$) (as shown in Figure 6.6a,) the crossed diffractions of the diffracted wave (-1, 1) are illustrated in Figure 6.6b. The diffracted wave has accumulated a de-phasing of $-\Delta\phi_-$ as presented in Figure 6.3a. As a result, the crossed diffractions experience less de-phases ($\Delta\phi = -\Delta\phi_- + \Delta\phi_+$) along two backward diffracted waves, (b) and (c). At an off-resonant angle which is deviated away from the incident plane ($\varphi_0+\Delta\varphi$ in Figure 6.3b), the diffracted wave (-1, 1) de-phases by $-\Delta\phi_{-11}$. The crossed diffractions add less de-phasing along the backward diffracted waves (a) and (b) as shown in Figure 6.6c. Broadening the angular tolerances in this structure behaves in a symmetric manner if the three η_{Bs} are

simultaneously maximized. $\eta_{B,(a)}$ mainly impacts the angular linewidth $\Delta\varphi_{FWHM}$ and $\eta_{B,(c)}$ broadens the angular linewidth $\Delta\theta_{FWHM}$. Broadening the angular linewidth can be done by optimizing the grating dimensions. Changing the grating dimensions modifies the grating strength (η_d), and hence the spectral linewidth [21.] Thus the grating is designed to have strong backward diffraction efficiencies and weak grating strengths in order to further improve the angular tolerance while keeping a narrow spectral linewidth.

The influence of the crossed diffraction on the resonant response is investigated by calculating the resonance response while gradually increasing the grating depth. The structure considered in this section has similar design as GMR #2 (Table 6.1,) but without the AR film is inserted between the film and the substrate. Therefore, resonances with high baseline and asymmetric lineshape are expected. The incident direction which corresponds to the grating periodicities can be estimated from Eq. (6.2). In order to achieve a resonant mode by the same waveguide mode (TM_0) at λ_0=0.98μm, the incident direction, θ_{inc}, has to be ~10.4º. At this setting, the backward diffraction efficiencies ($\eta_{B,(a)/(b)/(c)}$) and the grating strengths ($\eta_{d+/-}$), where the subscript + represents the diffracted waves (-1,0) and (1,0) and the subscript – represents the diffracted waves (-1,1) and (0,1), are calculated and plotted versus the grating depth in Figure 6.7. Based on the calculations, the desired range of the grating depth that broadens the angular linewidth not the spectral linewidth is from 0.4 to 0.6 μm ($t_g \geq \lambda_0/2$).

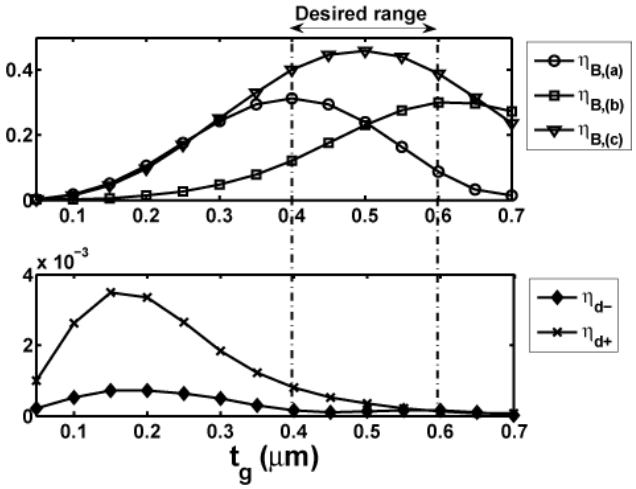

Figure 6.7: η_B and η_d of the grating structure of GMR#2 in Table 6.1 versus the grating depth, where grating has r=0.13 μm, λ_0=0.98μm θ_{inc}~10.4º.

In the calculations, the resonant mode as well as the resonant wavelength is fixed which requires changing the film thickness when increasing the grating depth. The film thicknesses and their resonant responses are exactly determined using the RCWA calculation. For the structure with a shallow grating, t_g=0.05 μm, the angular response exhibits resonance separation as shown in Figure 6.8a. The result indicates a phase mismatch between the two pairs of the resonant modes, + and -, due to the scattering by the grating. That is investigated by plotting the dispersion of the resonances in Figure 6.8b versus the wavelength (λ) and the incident angle (θ_{inc}). In comparison to the homogeneous waveguide approach [21] (Figure 6.8c.), the intersections of the resonances as a contribution of + and – resonant modes are opened due to the scattering by the grating creating a band gap which is referred to in this thesis as the *"resonance band gap"*. This band gap shows that the homogeneous waveguide approach, Eq. (6.2), is no longer an accurate tool. The results indicate a resonance at $\lambda_0 \sim 0.98\mu m$ located nearby the shorter wavelength side of the desired band gap (TM_{0+}/TM_{0-}). The scattering by the grating shifts

the resonant band gap towards a longer wavelength. Therefore, the design resonance is not exactly at the top of the lower resonance band. The shift increases with the grating strength as seen in Figures 6.8d and 6.8e for a structure with t_g=0.15 μm.

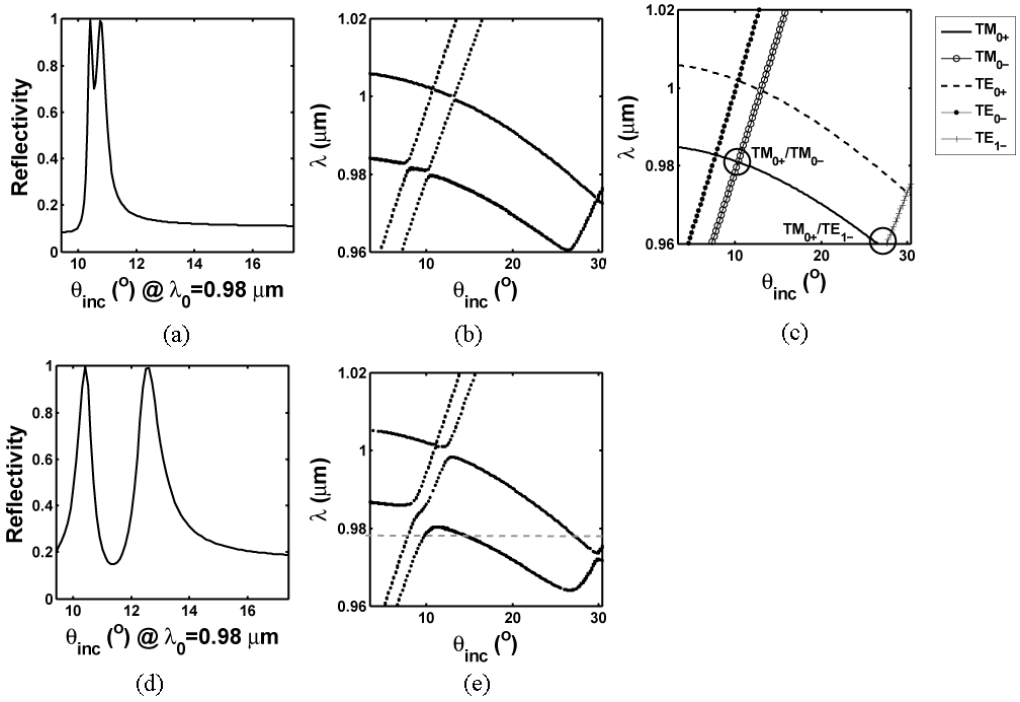

Figure 6.8: (a)/(e) Angular responses of four TM_0 resonant modes located at λ_0=0.98μm, θ_{inc}=10.4º and dispersion plots calculated by RCWA (a)-(b) t_g=0.05 μm, t_f=0.503 μm and (e)-(d) when t_g=0.15 μm, t_f= 0.44μm (c) dispersion plot calculated by HWA for t_g=0.05 μm

The grating strength on the other hand opens the resonant band gap wider and the band is flattened. This insures broader angular tolerances for deeper-grating structures when moving the resonance to the top of the lower band by changing the incident angle. This is shown in Table 6.2 where slightly tilting the incident direction (θ_0) and simultaneously changing the grating depth and film thickness results in significant improvement in the ratio between the angular tolerance to the spectral linewidth.

Table 6.2: Spectral and angular linewidth of resonances (λ_0= 0.98 μm) in a hexagonal-lattice grating resonance structures (Λ_a =0.55 μm, Λ_b=0.6 μm, and r =0.13 μm) at oblique incidence (φ_0=90º, ψ_0=0º)

GMR #	θ_0(º)	Structure parameters (μm)		$\Delta\lambda_{FWHM}$ (nm)	$\Delta\theta_{FWHM}$ at φ_0 (º)	$\Delta\varphi_{FWHM}$ at θ_0 (º)	$\Delta\theta/(\Delta\lambda/\lambda_0)$ (rad)	$\Delta\varphi/(\Delta\lambda/\lambda_0)$ (rad)
		t_g	t_f					
1	10.6	0.05	0.503	0.23	0.6	0.5	44.62	37.18
2	12.4	0.25	0.388	0.65	2.05	4.32	53.94	113.68
3	13.2	0.35	0.347	0.41	1.5	3.06	62.58	127.66
4	**14.2**	**0.55**	**0.278**	**0.16**	**1.15**	**4.26**	**22.94**	**455.4**
5	14.6	0.65	0.245	0.41	2.15	21.4	89.7	892.76

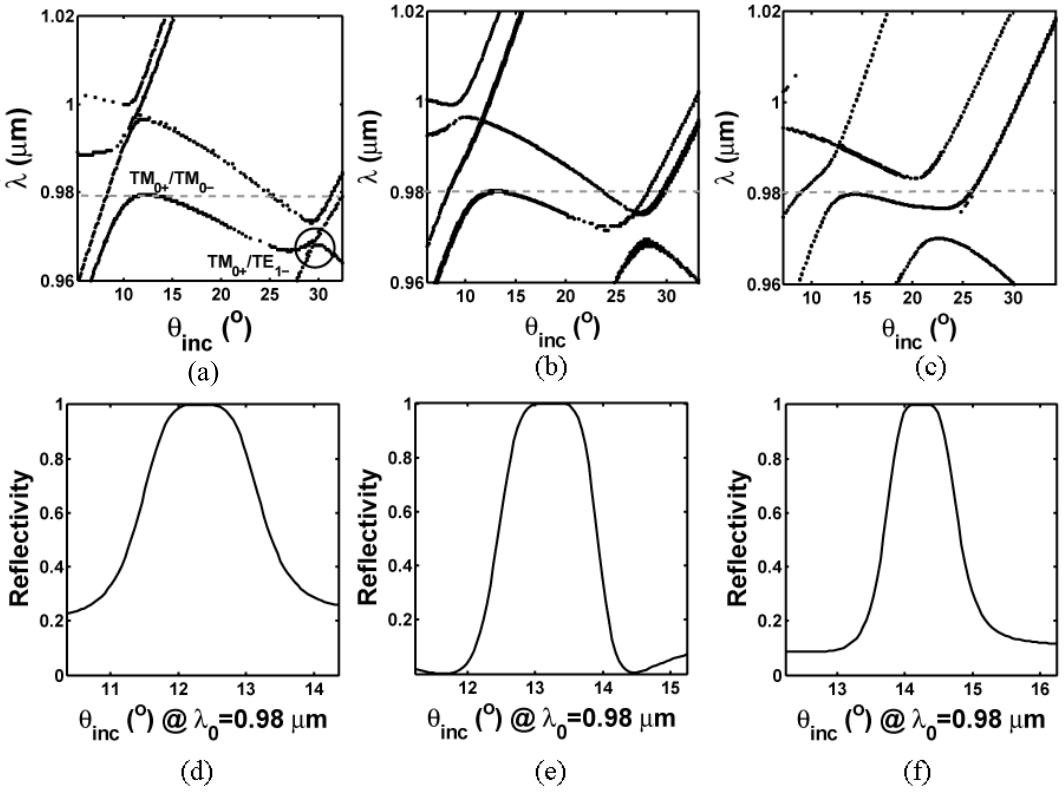

Figure 6.9: Resonant band diagram of the structure in Table 6.2 calculated by RCWA and angular responses at λ_0, (a)-(d) t_g=0.25 μm, (b)-(e) t_g=0.35 μm, and (c)-(f) t_g=0.55 μm

The flattening of the resonant band is shown in Figures 6.9a- 6.9c for grating depths 0.25, 0.35, and 0.55 μm respectively. The graphs illustrate a gradual opening of the band gap belonging to TM_{0+}/TE_{1-}. The upper band of this band gap slowly moves and aligns almost at the same wavelength as the lower band of the TM_{0+}/TM_{0-} band gap. The angular responses, in Figure 6.9d-6.9f, show a flat-top lineshape. Figure 6.10 shows the calculated angular/spectral linewidth ratios ($\Delta\theta/(\Delta\lambda/\lambda_0), \Delta\varphi/(\Delta\lambda/\lambda_0)$). The plots indicate that structures with grating depth between 0.45 and 0.55 μm have good resonance performances in agreement with the initial estimation of the grating strengths in Figure 6.7.

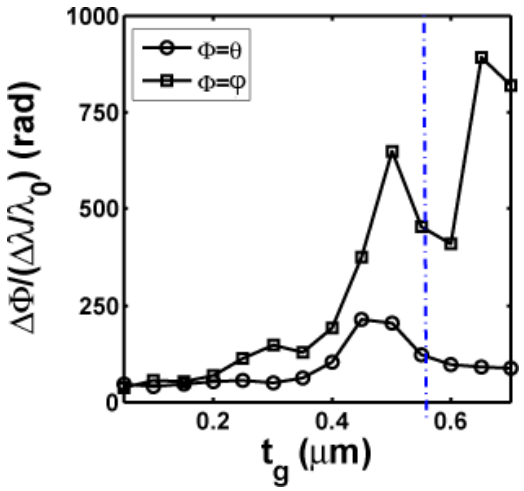

Figure 6.10: The angular -wavelength linewidth ratio vs. grating depth (resonances in Table 6.2)

In addition to a wide angular tolerance ($\Delta\theta$,) it is important to have a symmetric angular response. For an angle of incidence around 14°, symmetric response is achieved for an angular linewidth ratio $\Delta\varphi:\Delta\theta=\cos\theta_{inc}/\sin\theta_{inc}:1\approx 4:1$. For a 0.55-μm deep grating, the optimum design has resonance with a very narrow spectral linewidth ~0.2 nm and angular linewidth as large as $\Delta\theta$~1.15º and $\Delta\varphi$~4.3º. These angular linewidths correspond to a beam waist as small

as ~6-μm diameter. The angular/spectral linewidth ratios $(\Delta\theta/(\Delta\lambda/\lambda_0), \Delta\varphi/(\Delta\lambda/\lambda_0))$ are (~175%, ~1130%). This ratio for a deep grating is much larger than that for a very shallow-grating structure where the angular width is proportional to the spectral line width.

6.5 Broadening the angular tolerances in a dual- grating 2-D GMR

Dual-grating 2-D GMR structures considered in this section are comprised of gratings with the same periodicities located above and beneath the high index film as depicted in Figure 6.11. The resonant mode is scattered by both gratings. This modifies the spectral and angular linewidths. Better resonance performances can be obtained as will be discussed in this section.

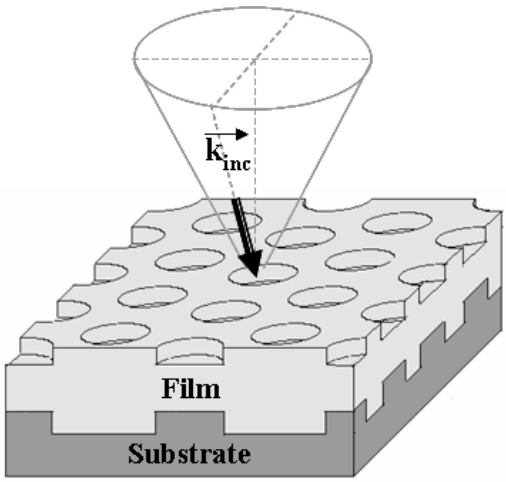

Figure 6.11: Dual-grating 2-D GMR configuration

Dual-grating 1-D GMR structures were proposed to control the spectral linewidth by Jacob *et al*. [74] Due to the difficulty of achieving the desired grating dimensions, the spectral linewidth is controlled via the film thickness. Having two gratings along the slab waveguide, the mode excitation at resonances is simultaneously executed by both gratings where the leaking fields have phase differences accumulated by the non-diffracted wave inside the film. Therefore,

the effective leakage, and hence the spectral linewidth, can be adjusted proportionally to this phase. This is controlled by the film thickness.

Increasing the second Bragg diffraction may increase the grating strength and degrades the resonance performance as mentioned in Section 6.4. This constraint was removed once the grating was properly designed to have $t_g \approx \lambda_0/2$. In dual grating structures, the spectral linewidth could be narrowed without the limit of the grating thickness. Besides, the double scatterings by two gratings with the same periodicity enhance the lateral confinement of the resonant mode if the substrate grating is sufficiently strong. This improves the resonance performances compared to the single grating GMR structure. The lateral confinement by the substrate grating is accomplished differently from the superstrate grating due to the extraordinary backward scattering paths as depicted in drawing B in Figure 6.12a at resonance and in Figure 6.12b and 6.12c at off-resonant angles $\Delta\theta$ and $\Delta\varphi$. At resonance, the mode is simultaneously excited by the superstrate and the substrate gratings. The ordinary scattering by the superstrate grating is illustrated in the diffraction/guidance planes A (Figure 6.12a.) As the substrate grating has a strong second Bragg diffraction, the first diffracted waves by the superstrate grating (dash arrows in Figure 6.12a) are cross-diffracted to the others with a total phase of ~2mπ, as demonstrated in the diffraction/guidance plane B (Figure 6.12a.) At off-resonant angle (both $\Delta\theta$ and $\Delta\varphi$), each one of these waves de-phases by a half cycle ($\Delta\phi/2$). The phase mismatch in the excited mode is nearly compensated by the crossed diffractions which are along waves (b)/(c) in Figure 6.12b and along waves (a)/ (b) in Figure 6.12c. The de-phasing is reduced to roughly half of that of the single grating. This effectively flattens the resonant band as will be seen in following calculations.

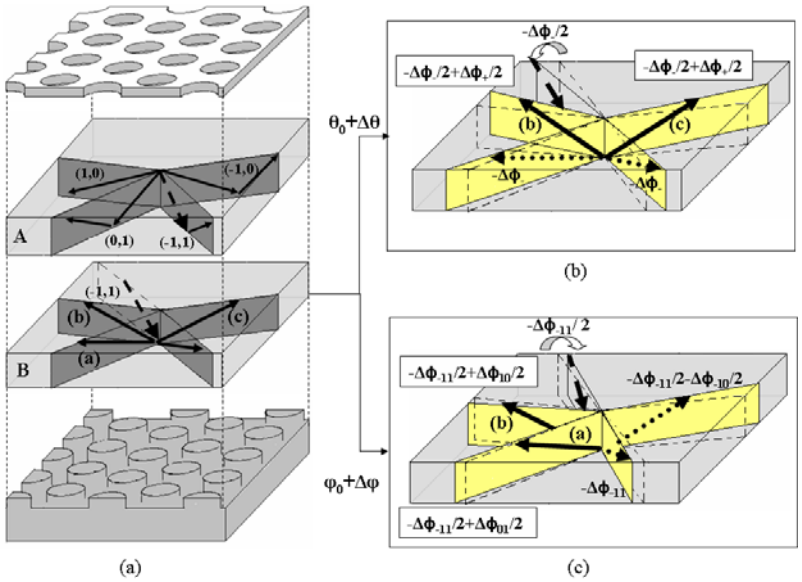

Figure 6.12: (a) Scattering of four resonant modes at resonance (A: forward diffraction, B: a crossed diffraction by the substrate grating) and de-phasing manners of a crossed diffraction (B) at off-resonance (b) $\theta_0+\Delta\theta$ (c) $\varphi_0+\Delta\varphi$

The structures considered here are similar to those analyzed in the previous section. The substrate grating is directly fabricated on the substrate before depositing the film. The superstrate grating has the optimum dimensions in Section 6.4 (t_g = 0.55 μm). The crossed diffraction of the substrate grating is improved by increasing the grating depth. Similar to the calculations in Section 6.4, the resonance band diagram and the angular response at resonant wavelength are calculated. The structure dimensions including the spectral/angular linewidths are shown in Table 6.3 for different substrate grating thicknesses (0-0.35 μm).

Table 6.3 shows that both angular linewidths along the incident plane ($\Delta\theta$) and its orthogonal plane ($\Delta\varphi$) simultaneously increase. This maintains the symmetry of the angular response. The spectral linewidth of this structure grating is sufficiently narrow regardless of the

substrate grating. The substrate grating does not significantly modify the spectral linewidths. In spite of the spectral/angular dependency, the resonance performances are significantly improved as depicted in Figure 6.13 when the substrate grating has an adequately strong second Bragg diffraction (depth ~ 0.3-μm.)

Table 6.3: Spectral and angular linewidth of resonances (λ_0=0.98 μm) in a dual hexagonal-lattice grating resonance structures (Λ_a = 0.55 μm, Λ_b=0.6 μm, superstrate grating: nH/nL=2/1, t_{g1}=0.55 μm, r_1 =0.13 μm, substrate grating: nH/nL=2/1.47, r_2=0.21 μm) at oblique incidence (φ_0=90º, ψ_0=0º, θ_0=14 º)

GMR#	Structure parameters (μm)		$\Delta\lambda_{FWHM}$ (nm)	$\Delta\theta_{FWHM}$ at φ_0 (º)	$\Delta\varphi_{FWHM}$ at θ_0 (º)	$\Delta\theta/(\Delta\lambda/\lambda_0)$ (rad)	$\Delta\varphi/(\Delta\lambda/\lambda_0)$ (rad)
	t_{g2}	t_f					
1	0	0.278	0.16	1.15	4.26	122.9	455.4
2	0.15	0.223	0.18	1.18	8.95	112.1	850.5
3	0.25	0.208	0.15	1.06	9	120.9	1026.3
4	**0.33**	**0.201**	**0.16**	**1.96**	**7.35**	**216.3**	**811**
5	0.34	0.2	0.16	1.48	6.4	163.3	706.2
6	0.35	0.2	0.15	0.88	6	100.3	684.2

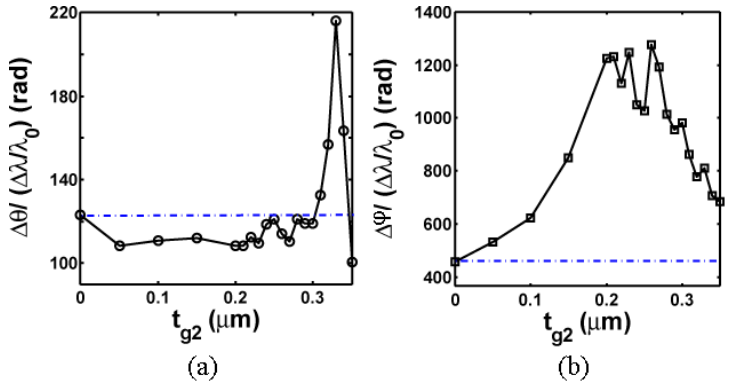

Figure 6.13: The angular-wavelength linewidth ratio vs. substrate grating depth, t_{g2}, (resonances in Table 6.3)

As discussed earlier, the influences of the crossed diffraction in dual-grating structure on the resonant response is different from that in the single grating due to the additional scattering

caused by the substrate grating. As a result, the flattening of the resonance band is expected to be different as well. Here, the resonance band diagrams when gradually increasing the depth of the substrate grating (t_{g2}= 0.15, 0.25 and 0.34 μm), are presented in Figure 6.14(a), (b), and (c), respectively. The angular responses at resonance are plotted versus the substrate-grating depth, t_{g2}, in Figure 6.14(d).

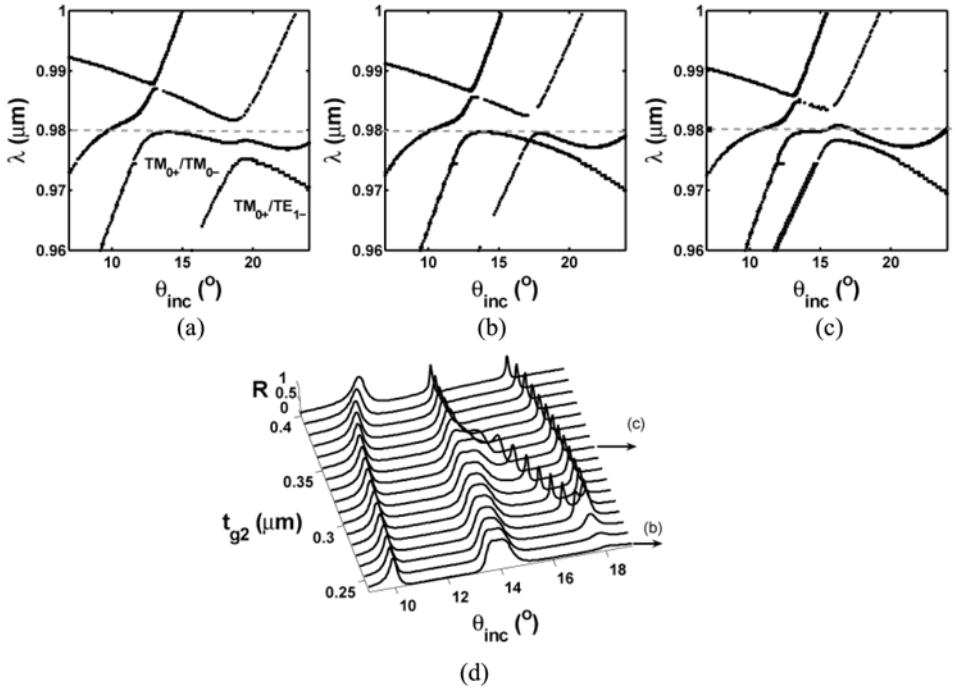

Figure 6.14: Resonant band diagram of the structure in Table 6.3 calculated by RCWA (a) t_{g2}=0.15 μm (b) t_{g2}=0.25 μm (c) t_{g2}=0.34 μm (d) plot of angular responses at λ_0 of the structures with t_{g2}= 0.25-0.4 μm

It is shown that the resonance band diagram of the structure with a very shallow substrate grating (as in Figure 6.14a) remains almost the same as the ones without the substrate grating (Figure 6.9c.) However, a side band by TM_{0+}/ TE_{1-} slightly shifts toward the designed resonance band by TM_{0+}/TM_{0-}. The shift is more significant in the structures with deeper gratings. The

structure can be designed such that the bands are merged at the same wavelength creating a substantially flat resonant band as shown in Figure 6.14c when the substrate grating is ~ 0.34-μm deep. The angular spectra calculated at the resonance wavelength (Figure 6.14d) clearly indicate the appearance of the side-band (TM_{0+}/TE_{1-}) resonance at λ_0 when the substrate grating is ~0.25-μm deep. It moves closer to the main resonance and they are merged when the substrate grating is 0.33-μm deep. That dramatically improves the resonance response. Resonance in the optimum design has angular linewidths ($\Delta\theta, \Delta\varphi$) broadened up to (2º, 7º) and spectral linewidth ~0.16 nm. The angular/spectral linewidth ratios increase ~80% larger than the single-grating structure.

Realizing the potential difficulty to fabricate the deep grating, another design of the dual-grating GMR structure using shallower superstrate grating, t_{g1}=0.35 μm in Table 6.2, is calculated here. The structure dimensions including the spectral/angular linewidths are noted in Table 6.4 for different substrate grating thicknesses (0-0.45 μm).

Table 6.4: Spectral and angular linewidth of resonances (λ_0=0.98 μm) in a dual hexagonal-lattice grating resonance structures (Λ_a = 0.55 μm, Λ_b=0.6 μm, superstrate grating: nH/nL=2/1, t_{g1}=0.35 μm, r_1 =0.13 μm, substrate grating: nH/nL=2/1.47, r_2=0.21 μm) at oblique incidence (φ_0=90º, ψ_0=0º)

GMR#	θ_{inc} (º)	Structure parameters (μm)		$\Delta\lambda_{FWHM}$ (nm)	$\Delta\theta_{FWHM}$ at φ_0 (º)	$\Delta\varphi_{FWHM}$ at θ_0 (º)	$\Delta\theta/(\Delta\lambda/\lambda_0)$ (rad)	$\Delta\varphi/(\Delta\lambda/\lambda_0)$ (rad)
		t_{g2}	t_f					
1	13.24	0	0.347	0.41	1.5	3.06	62.6	127.7
2	13.14	0.05	0.324	0.21	0.98	3.2	82.2	268.3
3	13.14	0.25	0.28	0.16	0.82	3.5	87.7	374.2
4	13.66	0.35	0.273	0.17	0.98	3.4	99.8	346.2
5	**14.16**	**0.4**	**0.27**	**0.1**	**1.83**	**2.2**	**326**	**392**
6	14.16	0.45	0.266	0.08	0.2	1.85	45	416.4

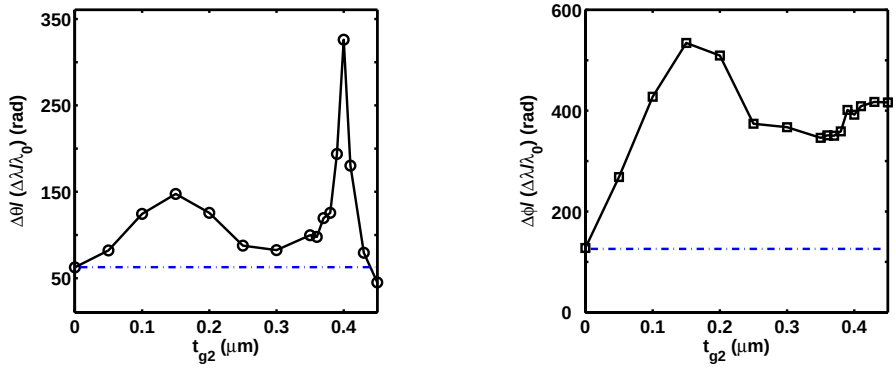

Figure 6.15: The angular-wavelength linewidth ratio vs. substrate grating depth, t_{g2}, (resonances in Table 6.4)

In this structure, the superstrate grating has weaker second Bragg diffraction, but it has sufficiently strong coupling strength. The contribution of the diffraction by the substrate grating narrows the spectral linewidths as seen in Table 6.4. The spectral/angular dependency at resonance is slightly improved as illustrated in the graph in Figure 6.15. The improvement is not dramatically noticed until the substrate grating has an adequately strong second Bragg diffraction (depth ~ 0.35-μm.) The dispersion plots in Figure 6.16 show the flattening of the resonant band due to the merging of two successive resonant bands as in the previous structure. Using the shallower superstrate grating may require deeper substrate grating in order to create a side band at the same wavelength.

For the optimum design with ~ 0.4-μm deep substrate grating, resonance has angular/spectral linewidth ratio as high as that in the previous structure but it comprises of shallower gratings. That eases the fabrication processes. The main drawback in this particular structure dimensions calculated here is the fact that the superstrate grating has unequal backward diffraction efficiencies as reported in Figure 6.7. This causes an asymmetric angular linewidths similar to the angular responses when using the superstrate grating only. This asymmetry can be

removed by optimizing the dimensions (filling factor and periods) of the shallow superstrate grating.

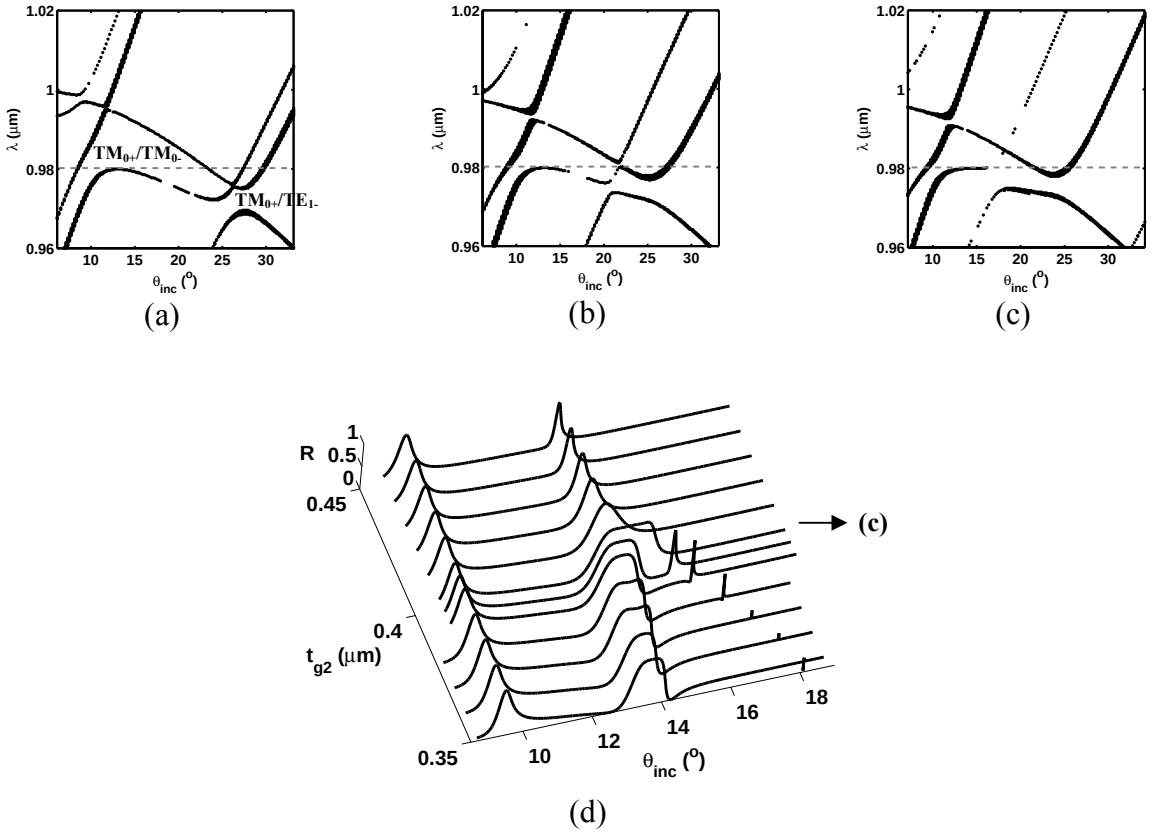

Figure 6.16: Resonant band diagram of the structure in Table 6.4 calculated by RCWA (a) t_{g2}=0.05 μm (b) t_{g2}=0.25 μm (c) t_{g2}=0.4 μm (d) plot of angular responses at λ_0 of the structures with t_{g2}= 0.35-0.45 μm

Based on both calculations, the crossed diffraction by the substrate grating is shown to flatten the resonant band in a different fashion compared to the single-grating structure due to the extra scattering by the substrate grating. Merging the side-bands broadens the angular tolerances compared to the single grating structure while the spectral linewidth remains narrow. Symmetric and broad angular response is achieved by insuring the symmetric backward coupling strengths

of the superstrate. The resonant mode is more laterally confined and the angular tolerance is further improved when utilizing two gratings with a strong second Bragg diffraction.

6.6 Summary

In this work, we investigated broadening of the angular response of narrow band two-dimension guided mode resonant spectral filters at oblique incidence while maintaining a narrow spectral response. The angular response was broadened by coupling into multiple fundamental guided resonant modes having the same propagation constant but propagating in different planes inherent in multiple planes of diffraction of the 2-D gratings. The propagation constants of the guided resonant modes are determined from the physical dimensions of the grating (periodicity and duty cycle) and the incident direction. The de-phasing mismatch resulting from the asymmetric diffraction at oblique incidence was effectively minimized by using an irregular hexagonal-lattice grating. The angular tolerances were almost twice that obtained by matching resonant modes with different propagation constants. Further improvement in the angular tolerance is achieved using a strong grating in order to produce a crossed diffraction or second Bragg diffraction. That was formed in a deep grating ($t_g > \lambda_0/2$.) The resonant mode had a high lateral confinement and hence high angular tolerance. For the optimum design, the angular/spectral linewidth ratios were improved up to (~175%, ~1130%) compared to the very shallow-grating structure.

A dual grating structure where a second grating is located on the substrate side was investigated. The presence of a double scattering by the two gratings sustained a narrow spectral linewidth while increasing the angular linewidth. This required a substrate grating with

sufficiently strong second Bragg diffraction. The extraordinary backward scattering by the substrate grating caused two successive resonant bands to merge producing a resonance with angular/spectral linewidth ratios (~80%) larger than the ones in the first approach. The angular tolerances were broadened in a symmetric manner when the superstrate grating had a strong crossed diffraction in both orthogonal planes.

CHAPTER 7 : CONCLUSION

In this dissertation, the unique nature of the resonant anomaly in GMR structures with two-dimensional (2D) periodic perturbation was studied in detail based on the coupling characteristics in different geometries of the grating unit cell and the incident beam properties (direction and polarization.) The interaction between these non-collinear guides and its impact on spectral and angular responses of GMR devices was investigated. Clear understanding of the resonance phenomenon was developed and novel 2D-GMR structures were proposed to provide new device functionality and to significantly improve the performance of narrow spectral filters. The analysis was carried using the approach where the homogenous waveguide approach (HWA), which does not account for the leaky mode, is used to develop a very good estimate for the structure dimension and the resonance location, and the rigorous coupled analysis (RCWA) is used to determine the exact structure parameters and the spectral/angular responses.

In 2D grating diffraction, each diffracted order inherently propagates in its distinct diffraction plane. This allows for coupled polarization dependent resonant leaky modes with one in each diffraction plane. With the magnitudes of the first-order waves directly connected to the resonance modes propagation constants, resonances locations were practically managed through the grating periods and the other structure dimensions (if necessary.) The resonances lineshape was controlled by the scattering and the de-phasing manners of the resonance modes. Based on this concept, we illustrated that coupling into multiple resonant modes for which the de-phasing is compensated at off resonances improves the angular tolerance. The resonance sustained a

narrow, symmetric and low side-bands spectrum for weak grating coupling strength (η_d) and low Fresnel reflection. Further, GMR with multi-level AR grating was introduced to improve the resonance responses.

The analysis in Chapters 3 and 4 showed a strong dependence of the resonance on the grating geometry and periodicities. That allowed us to demonstrate several polarization independent 2-D GMR filters. The polarization independence was shown to be achieved when having at least two resonant modes to which both orthogonal polarized beams can be coupled. This was demonstrated when using the 1-D structure at fully conical setting and in 2-D structure using symmetric grating patterns (a square- or a regular hexagonal-lattice grating) at normal incidence. At oblique incidence, the incident plane was aligned along any of the symmetric planes. At oblique incidence, there are some phase mismatches between the modes causing a shift of resonances (of TE and TM beams.) This shift deforms the resonance responses of the unpolarized beam. Using the proper grating dimensions, the structure was shown to remove the phase mismatches and maintain symmetric spectral linewidth. In the second approach, an irregular hexagonal-lattice grating was used to couple the incident beam along four diffracted waves with equal magnitude. Resonant band gaps were created but at the shifted spectra for the orthogonal polarized incident beams. Polarization independent resonances were exhibited at the proper incident angle where these bands were overlapped without optimizing other grating dimensions.

The unique characteristics of 2D grating lead to two new devices. First, a novel controllable multi-line narrow-band 2D-GMR filter was proposed. The filter concept utilized the multiple planes of diffraction produced by the 2-D grating at normal incidence. Multiple

resonances were obtained by matching the guided modes in the different planes of diffraction to different wavelengths. It was shown that the location and the separation between the resonances can be specifically controlled by modifying the periodicity of the grating and other physical dimensions of the structure not through changing the material as it was the case for the multi-line 1-D GMR filters. Two types of 2-D grating GMR designs, rectangular and hexagonal grid, were presented to obtain controllable two-line and three-line reflection filters, respectively. The resonance separation was controlled over spectra from <1% to 30% of the short resonance wavelength by modifying only the grating periods in the resonance range $\lambda_1/n_f < \Lambda < \lambda_1/n_s$. It was shown that the locations of the resonances were significantly dependent on the period of grating and the thickness of the high index film while the grating depth and hole-size had more influence on the spectral linewidth of each resonance.

Finally, broadening of the angular response in 2-D GMR at oblique incidence, while maintaining a narrow spectral response, was investigated. Resonances by coupling into multiple fundamental modes having the same propagation constant but propagating in different planes using an irregular hexagonal-lattice grating were addressed having the angular tolerance increased by factor of two of that obtained by matching resonant modes with different propagation constants. A five-fold improvement in the angular tolerance was achieved using a grating with strong second Bragg diffraction in order to produce a crossed diffraction. For the optimum design (using a deep grating, $t_g > \lambda_0/2$), resonance with a narrow spectral linewidth ($\Delta\lambda_{FWHM}$~$1.6\times10^{-14}\lambda_0$) and angularly tolerant to a ~6-μm beam diameter were obtained. A novel dual hexagonal-lattice grating structure with a second grating located on the substrate side was proposed to further broaden the angular tolerance of the spectral filter without degrading its

spectral response. This strong second Bragg backward diffraction from the substrate grating causes two successive resonant bands to merge producing a resonance with symmetric broad angular response. The angular/spectral linewidth ratios were enhanced by ~80% larger than the ones in the first approach.

LIST OF REFERENCES

1. R. W. Wood, "On remarkable case of uneven distribution of light in a diffraction grating spectrum," Phil. Mag. **4**, 396-402 (1902.)
2. Lord Rayleigh, "On the dynamical theory of gratings," Proc. Roy. Soc. (London) A **79**, 399 (1907.)
3. R. W. Wood, "Diffraction gratings with controlled groove form and abnormal distribution of intensity," Phil. Mag. **23**, 310-317; (1912.)
4. U Fano, "The theory of intensity anomalies of bending (in German)," Ann. Phys. **32**, 393; (1938.)
5. C. H. Palmer, "Parallel diffraction grating anomalies," J. Opt. Soc. Am. **42**, 269-276; (1952.)
6. B.A. Lippmann, "Note on the theory of gratings," J. Opt. Soc. Am, **43**, 408, (1953.)
7. V.Twersky, J. Appl. Phys. **23**, 1099, (1952.)
8. V.Twersky, "Multiple scattering of waves and optical phenomena," J. Opt. Soc. Am, **52**, 145, (1962.)
9. A. Hessel and A. A. Oliner, "A new theory of Wood's anomalies on optical gratings," Appl. Opt. **4**, 1275-1297 (1965.)
10. M. Neviere, "Electromagnetic Theory of Gratings," R. Petit, ed. (Springer-Verlag, Berlin, 1980), Chap. 5.
11. M. Neviere, R. Petit, and M. Cadilhac, "About the theory of optical grating coupler-waveguide systems," Opt. Commun. **8**, 113–117 (1973.)

12. M. Neviere, R. Petit, and M. Cadilhac, “Systematic study of resonances of holographic thin film couplers,” Opt. Commun. **9**, 48–53 (1973.)

13. E. Popov, L. Mashev, and D. Maystre, “Theoretical study of anomalies of coated dielectric gratings,” Opt. Acta **32**, 607–629 (1986).

14. A. Avrutsky and V. A. Sychugov, “Reflection of a beam of finite size from a corrugated waveguide,” J. Mod. Opt. **36**, 1527–1539 (1989.)

15. S. S. Wang, R. Magnusson, J. S. Bagby, and M. G. Moharam “Guided-mode resonances in planar dielectric-layer diffraction gratings,” J. opt. Soc. Am. A **7**, 1470–1474 (1990.)

16. R. Magnusson and S. S. Wang, “New principle for optical filters,” Appl. Phys. Lett. **61**, 1022–1024 (1992.)

17. S. M. Norton, T. Erdogan and R. M. Morris, “Coupled-mode theory of resonant-grating filters,” J. opt. Soc. Am. A **14**, 629-639 (1997.)

18. A. Sharon, S. Glasberg, D. Rosenblatt, and A. A. Friesem, “Metal-based resonant grating waveguide structures,” J. Opt. Soc. Am. A **14**, 588–595 (1997.)

19. A. Sharon, D. Rosenblatt, and A. A. Friesem, “Resonant grating-waveguide structures for visible and near infrared radiation,” J. Opt. Soc. Am. A **14**, 2985–2993 (1997.)

20. D. Rosenblatt, A. Sharon, and A. A. Friesem, ‘‘Resonant grating waveguide structures,’’ IEEE J. Quantum Electron. **33**, 2038–2059 (1997.)

21. D. K. Jacob, S. C. Dunn, and M. G. Moharam, “Design considerations for narrow-band dielectric resonant grating reflection filters of finite length,” J. Opt. Soc. Am. A **17**, 1241–1249 (2000.)

22. D. K. Jacob, S. C. Dunn, and M. G. Moharam, "Normally incident grating reflection filters for efficient narrow-band spectral filtering of finite beams," J. Opt. Soc. Am. A **18**, 2109-2120 (2001.)

23. T. Tamir, and S. Zhang, "Resonant scattering by multilayered dielectric gratings," J. Opt. Soc. Am. A **14**, 1607-1616 (1997.)

24. Y. Ding and R. Magnusson "Band gaps and leaky-wave effects in resonant photonic-crystal waveguides," Opt. Exp. **15**, 680-694 (2007.)

25. David L. Brundrett, Elias N. Glytsis, Thomas K. Gaylord, and Jon M. Bendickson S. Tibuleac and R. Magnusson, "Effects of modulation strength in guided-mode resonant subwavelength gratings at normal incidence," J. opt. Soc. Am. A **17**, 1221-1230 (2000.)

26. Z. S. Lie, S. Tibuleac, D. Shin, P.P. Young and R. Magnusson, "High efficiency guided-mode resonance filter," Opt. Lett. **23**, 1556-1558 (1998.)

27. S. M. Norton, G. M. Morris and T.Erdogan, "Experimental investigation of resonant-grating filter lineshapes in comparison with theoretical models," J. Opt. Soc. Am. A **15**, 464-472 (1998.)

28. Z. S. Lie, S. Tibuleac, D. Shin, P.P. Young and R. Magnusson, "Normal-incidence guided-mode resonant grating filters: design and experimental demonstration," Opt. Lett. **23**, 700-703 (1998.)

29. S. S. Wang and R. Magnusson, "Design of waveguide-grating filters with symmetrical line shapes and low sidebands," Opt. Lett. **19**, 919–921 (1994.)

30. S. S. Wang and R. Magnusson, "Multilayer waveguide grating filters," Appl. Opt. **34**, 2414–2420 (1995.)

31. S. Tibuleac and R. Magnusson, “Reflection and transmission guided-mode resonance filters,” J. opt. Soc. Am. A **14**, 1617-1626 (1997.)
32. Donald K. Jacob, Steven C. Dunn, and M. G. Moharam, “Flat-Top Narrow-Band Spectral Response Obtained from Cascaded Resonant Grating Reflection Filters,” App. Opt. **41**, 1241-1245 (2002.)
33. Samuel T. Thurman and G. Michael Morris, “Controlling the Spectral Response in Guided-Mode Resonance Filter Design,” App. Opt. **42**, 3225-3233 (2003.)
34. Y. Ding and R. Magnusson “Doubly resonant single-layer bandpass optical filters,” Opt. Lett. **29**, 1135-1137 (2004.)
35. D. Lacour, G. Granet, J-P Plumey, and A. Mure-Ravaud, “Polarization independence of a one-dimensional grating in conical mounting,” J. opt. Soc. Am. A **20**, 1546-1552 (2003.)
36. D. Shin, S. Tibuleac, T. A. Maldonado and R. Magnusson, “Thin-film optical filters with diffractive elements and waveguides,” Opt. Eng. **37**, 2634-2646 (1998).
37. S. Tibuleac, R. Magnusson, T. A. Maldonado, P.P. Young, and T.R. Holzheimer, "Dielectric Frequency-Selective Structures Incorporating Waveguide Gratings," IEEE trans. Microwave Theory Tech. **48**, 553-561 (2000).
38. Z. S. Liu and R. Magnusson, "Concept of multiorder multimode resonant optical filters," IEEE Photon. Technol. Lett. **14**, 1091-1093 (2002).
39. D. Wawro, S. Tibuleac, R. Magnusson and H. Liu, “Optical fiber endface biosensor on resonances in dielectric waveguide gratings,” Proc. of SPIE **3911**, 86-94 (2000.)

40. R. Magnusson, Y. Ding, K.J. Lee, D. Shin, P.S. Priambodo, P.P. Young, and T. A. Maldonado, "Photonics devices enabled by waveguide-mode resonance effects in periodically modulated films," Proc. of SPIE **5225**, 20-34 (2003.)
41. G. Niederer, H. P. Herzig, J. Shamir, H. Thiele, M. Schnieper, and C. Zschokke, "Tunable, oblique incidence resonance grating filter for telecommunications," Appl. Opt. **43**, 1683–1694 (2004.)
42. T. Katchalski, G. Levy-Yurista and A. A. Friesem "Light modulation with electro-optics polymer-based resonant grating waveguide structures," Opt. Exp. **13**, 4645-4650 (2005.)
43. B. Bai, J. Tervo and J. Turunen "Polarization conversion in resonant magneto-optic gratings," New J. Phys. **8**, 1-12 (2006.)
44. F. Lemarchand, A. Sentenac, and H. Giovannini, "Increasing the angular tolerance of resonant grating filters with doubly periodic structures," Opt. Lett. **22**, 1149-1151 (1998.)
45. F. Lemarchand, A. Sentenac, E. Cambril, and H. Giovannini , "Study of the resonant behavior of waveguide gratings: increasing the angular tolerance of guided-mode filters," J. Opt. A: Pure Appl. Opt. **1**, 545-551 (1999).
46. A. Sentenac and A-L Fehrembach, "Angular tolerant resonant grating filters under oblique incidence," J. Opt. Soc. Am. A **22**, 475-480 (2004.)
47. J. Saarrinen, E.Noponen and J. Turunen, "Guided-mode resonance filters of finite aperture," Opt. Eng. **34**, 2560-2566 (1995.)
48. R. R. Boye and R. K. Kostuk, "Investigation of the effect of finite grating size on the performance of guided-mode resonance filters," Appl. Opt. **39**, 3649–3653 (2000.)

49. S. Peng and G. M. Morris, “Experimental demonstration of resonant anomalies in diffraction from two-dimensional gratings,” Opt. Lett. **21**, 549-551 (1995.)

50. S. Peng and G. M. Morris, “Resonant scattering from two-dimensional gratings,” J. opt. Soc. Am. A **13**, 993-1005 (1996.)

51. A. Mizutani, H. Kikuta, K. Nakajima, and K. Iwata, “Non-polarizing guided-mode resonant grating filter for oblique incidence,” J. opt. Soc. Am. A **18**, 1261-1266 (2001.)

52. A. Fehrembach, D. Maystre, and A. Sentenac, “Phenomenological theory of filtering by resonant dielectric gratings,” J. opt. Soc. Am. A **19**, 1136-1144 (2002.)

53. A. Fehrembach and A. Sentenac, “Study of waveguide grating eigenmodes for unpolarized filtering applications,” J. opt. Soc. Am. A **20**, 481-488 (2003.)

54. A-L Fehrembach, and A. Sentenac, “Unpolarized narrow-band filtering with resonant gratings,” Appl. Phys. Lett. **86**, 121105-1-121105-3 (2005.)

55. T. Clausnitzer, A. V. Tishchenko, E-B Kley, H-J Fuchs, D. Schelle, O. Parriaux and U. Kroll, “Narrowband polarization-independent free-space wave notch filter,” J. opt. Soc. Am. A **22**, 2299-2803 (2005.)

56. M. G. Moharam, E. B. Grann, D. A. Pommet, and T. K. Gaylord, “Formulation for stable and efficient implementation of the rigorous coupled-wave analysis of binary gratings,” J. opt. Soc. Am. A **12**, 1068-1076 (1995.)

57. M. G. Moharam and T. K. Gaylord, “Coupled-wave analysis of two-dimensional gratings,” in Holographic Optics: Design and Applications, I. Cindrich, ed., Proc. SPIE **883**, 8–11 (1986.)

58. L.Li, “New formulation of the fourier model for crossed surface-relief gratings,” J. opt. Soc. Am. A **14**, 2758-1767 (1997.)

59. P. Lalanne, “Improved formulation of the coupled-wave method for two-dimensional gratings,” J. opt. Soc. Am. A **14**, 1592-1598 (1997.)

60. M. G. Moharam, D. A. Pommet, E. B. Grann, and T. K. Gaylord, “Stable implementation of the rigorous coupled-wave analysis for surface-relief gratings: enhanced transmittance matrix approach,” J. opt. Soc. Am. A **5**, 1077-1086 (1995.)

61. Q. Cao, P. Lalanne and J-P Hugonin, “Stable and efficient Bloch-mode computational method for one-dimensional grating waveguides,” J. opt. Soc. Am. A **19**, 335-338 (2002.)

62. P. Lalanne, “Electromagnetic analysis of photonic crystal waveguides operating above the light cone,” IEEE J. Quan. Elec. **38**, 800-804 (2002.)

63. S. Boonruang, A. Greenwell, and M. G. Moharam, “Multiline two-dimensional guided-mode resonant filters,” Appl. Opt. **45**, 5740–5747 (2006.)

64. E. Hecht, Optics, (Addison Wesley Longman, 1998), Chap 10.

65. A. Papoulis, Systems and Transforms with applications in optics, (McGraw-Hill, 1968), Chap 4.

66. S-D Wu, T. K. Gaylord, E. N. Glytsis, and Y-M Wu, “Three-dimensional converging-diverging Gaussian beam diffraction by a volume grating,” J. opt. Soc. Am. A **11**, 2695-2703 (1994.)

67. E. B. Grann, M. G. Moharam, and D. A. Pommet, “Artificial uniaxial and biaxial dielectrics with use of two- dimensional subwavelength binary gratings,” J. opt. Soc. Am. A **11**, 2695-2703 (1994.)

68. A. Yariv, Optical electronics in modern communications, (Oxford, New York, 1997), Chap 13.

69. N. P. K. Cotter, T. W. Preist, and J. R. Sambles, "Scattering-matrix approach to multilayer diffraction," J. opt. Soc. Am. A **12**, 1097-1103 (1995.)

70. J. P. Berenger, "A perfectly matched layer for the absorption of electromagnetic waves," J. Comput.Phys. **114**, 185-200 (1994.)

71. E. B. Grann and M. G. Moharam, "Comparison between continuous and discrete subwavelength grating structures for antireflection surfaces," J. opt. Soc. Am. A **13**, 988-992 (1996.)

72. L. Young, "Synthesis of multiple antireflection films over a prescribed frequency band," J. opt. Soc. Am. A **51**, 967-974 (1961.)

73. Marcuse, Dietrich, Theory of Dielectric Optical Waveguides, (Academic Press, New York and London, 1974), Chap 1.

74. D. K. Jacob, S. C. Dunn, and M. G. Moharam, "Interference approach applied to dual-grating dielectric resonant grating reflection filters," Opt. Lett. **26**, 1749-1751 (2001.)

75. C. Kappel, A. Selle, M. A. Bader and G Marowsky, "Resonant double-grating waveguide structures as inverted Fabry-Perot interferometers," J. opt. Soc. Am. B **21**, 1127-1136 (2004.)